Étude expérimentale et modélisation multi-échelle du comportement de poudres métalliques mécaniquement activées : des systèmes binaires aux alliages à haute entropie.

Adrien Fourmont

THESE DE DOCTORAT DE L'ETABLISSEMENT UNIVERSITE BOURGOGNE FRANCHE-COMTE

PREPAREE AU LABORATOIRE INTERDISCIPLINAIRE CARNOT DE BOURGOGNE

École doctorale n°553

École doctorale Carnot Pasteur

Doctorat de Chimie Physique

Par

M. Fourmont Adrien

Étude expérimentale et modélisation multi-échelle du comportement de poudres métalliques mécaniquement activées : des systèmes binaires aux alliages à haute entropie.

Thèse présentée et soutenue à Dijon, le 6 décembre 2021

Composition du Jury :

Y. Le Bouar	DR CNRS, Onera	Président
J. M. Chaix	DR CNRS, Université Grenoble Alpes	Rapporteur
M. Laurent-Brocq	CR CNRS HDR, Université Paris Est Créteil	Rapporteure
A. S. Rogachev	PR, Russian Academy of Sciences	Examinateur
S. Le Gallet	MCF, Université de Bourgogne	Directrice de Thèse
O. Politano	MCF HDR, Université de Bourgogne	Directeur de Thèse
F. Baras	CR CNRS HDR, Université de Bourgogne	Invitée
C. Desgranges	Ingénieure de recherche, Safran Tech	Invitée

Remerciements

Les travaux présentés dans ce document sont le résultat de nombreuses collaborations, discussions et contributions de toutes sortes. Je tiens à remercier dans ces quelques lignes toutes les personnes qui y ont pris part.

Mes premiers remerciements vont aux membres du jury pour avoir évaluer mon travail. Merci à Y. Le Bouar, Directeur de recherche à l'Onera, pour avoir présidé le jury. Merci aux rapporteurs, J.M. Chaix, Directeur de recherche à l'Université Grenoble Alpes, et M. Laurent-Brocq, Chargée de recherche à l'Université Paris Est Créteil, qui ont su déterminer les forces et faiblesses de ce travail.

I would like to say Спасибо to A. S. Rogachev. Thank you for your relevant commentary during the defense and thank you for this fruitful collaboration. These thanks are also due to all my Russian collaborators, especially to A. Nepapushev and A. S. Sedegov for their warm welcome.

Je tiens à adresser des remerciements tous particuliers à mes encadrants de thèse. Un doctorat a toujours des hauts et des bas et ils ont su m'accompagner durant l'intégralité de celui-ci. Merci à O. Politano pour ses conseils et questionnement, même sur l'aspect expérimental hors de son expertise. Merci à S. Le Gallet pour toutes ces discussions prolifiques qui ont souvent apporté autant de réponses que d'autres passionnantes questions. Merci à F. Baras pour son encadrement certes non-officiel, mais très présent et efficace. La rédaction des articles et donc de ce document serait très différent sans sa participation grandement appréciée.
Travailler avec vous trois a été une expérience extrêmement riche tant sur le plan personnel que professionnel et scientifique. Merci également pour toutes les opportunités que vous m'avez offertes et la confiance que vous avez placé en moi.

Je souhaite remercier C. Desgranges, Ingénieure de recherche à Safran Tech, pour ses conseils concernant les calculs thermodynamiques et les résultats d'oxydation à haute température. La collaboration avec un acteur industriel a été très intéressante.

J'adresse mes remerciements à l'équipe s'occupant de la Sonde Atomique Tomographique à Marseille ; notamment, M. Descoins et K. Hoummada. Ils m'ont accueilli et guidé avec bienveillance pour tirer le maximum cette technique si extraordinaire.

Merci aux Ingénieurs du DTAI qui m'ont apporté leur soutien pour caractériser mes échantillons. Merci tout particulièrement à F. Herbst pour les nombreuses discussions, O. Heintz pour la mise en place de la mesure sous vide et N. Geoffroy pour son aide à la DRX. Du côté du personnel de l'ESIREM, je remercie J.M. Dachicourt et M.L. Léonard pour leur soutien sans faille concernant le matériel de l'école.

Je voudrais remercier tous les stagiaires qui ont participé à la préparation de cette thèse. M. François, M. Garnier, N. Haglon et A. Uyanik, vos contributions ont réellement apporté une pierre l'édifice.

Merci à M. Bouley pour les corrections et suggestions très pertinentes concernant l'anglais scientifique de mes documents.

Je remercie les membres de l'équipe BH2N notamment N. Millot pour avoir participé à mon comité de suivi de thèse, ainsi que L. Maurizi, J. Boudon et L. Saviot pour les discussions au café.

J'adresse mes remerciements aux membres de l'équipe M4Oxe notamment I. Popa et C. Siri, pour leur aide en oxydation à haute température. Je souhaiterais également remercier L. Combemale pour m'avoir guidé dans mes premiers pas d'enseignant.

Merci à tous les membres de l'équipe MaNaPI, et notamment ceux à l'I3M, je pense surtout à F. Bernard pour ses conseils avisés, ainsi qu'à F. Bussiere et M. Moser qui ont partagé les soucis scientifiques et techniques liés au broyage.

Je voudrais également remercier certaines personnes aujourd'hui loin de l'Université qui m'ont transmis le flambeau. Ces remerciements vont particulièrement à L. Minier et S. Lorand pour leur expertise du SPS ainsi qu'à Y. Kchaou pour sa savoureuse compagnie.

J'adresse un remerciement tout particulier à mes collègues de bureau B. Ravry, L. Convert et Q. Bizot. Vous avez été des acteurs importants dans le bon déroulement de ce travail en participant chacun à votre manière à la bonne ambiance de l'étage.

Enfin, je remercie les membres de ma famille pour leur soutien indéfectible. Ce travail de longue haleine porte leur empreinte discrète mais primordiale.

Pour terminer, je voudrais remercier Célia pour sa présence au quotidien. Merci d'avoir accepté de partager mes doutes et mes espoirs concernant ce travail. J'ai pu traverser cette épreuve en toute sérénité grâce à elle.

List of publications

- **Mechanical activation of metallic powders and reactivity of activated nanocomposites: a molecular dynamics approach**
  F. Baras, Q. Bizot, A. Fourmont, S. Le Gallet, O. Politano
  Applied Physics A, 127, 555, 2021

- **Reactivity of Ni–Al nanocomposites prepared by mechanical activation: A molecular dynamics study**
  A. Fourmont, O. Politano, S. Le Gallet, C. Desgranges, F. Baras
  Journal of Applied Physics, 129, 065301, 2021

- **Effects of planetary ball milling on AlCoCrFeNi high entropy alloys prepared by Spark Plasma Sintering: Experiments and molecular dynamics study**
  A. Fourmont, S. Le Gallet, O. Politano, C. Desgranges, F. Baras
  Journal of Alloys and Compounds, 820, 153448, 2020

- **Effects of mechanical activation on chemical homogeneity and contamination level in dual-phase AlCoCrFeNi high entropy alloy**
  A. Fourmont, S. Le Gallet, K. Hoummada, M. Descoins, C. Desgranges, O. Politano, F. Baras
  Materials Chemistry and Physics, 272, 125000, 2021

- **Thermal Stability of Medium- and High-Entropy Alloys of 3d-Transition Metals**
  A. Fourmont, A.S. Rogachev, S. Le Gallet, O. Politano, D.Yu. Kovalev, N.A. Kochetov, N.F. Shkodich, S.G. Vadchenko, F. Baras
  Journal of Phase Equilibria and Diffusion, 2021

Contents

General introduction

Preamble

The objective of this thesis is twofold. First, it is part of an approach at the core of Materials Science: understanding the interplay between key parameters during the progress of a particular process, namely, high energy ball milling and the subsequent behavior of metallic powders. This approach is made all the more relevant by taking into consideration computer simulation. This powerful tool has two advantages: it is able to provide answers where no other techniques are available and it sheds new light on former issues. In addition, this approach is a direct continuation of the work of the ICB teams involved in metallurgy research. Since 2011, a considerable effort to both simulate and experimentally study the reactivity of Ni-Al has been undertaken. The milling of this particular system and the resulting features are one core aspect of this research.
Secondly, this project deals with a new kind of innovative material, namely High Entropy Alloys. New kinds of materials emerge all the time, from the MAX phases in 1996 to the single-layer materials such as graphene in 2004, for instance. Yet a tremendous amount of work is required between the first elaboration and the actual industrial application of these new materials. Among other things, it is necessary to thoroughly identify what differs between these new materials and other comparable materials. One obvious question is: do established elaboration processes still work the same way for these new materials?
In this introduction, we will explain how these two objectives are complementary and how they led to the present work.

1. Background

As illustrated in Figure 1, the basis of materials science is understanding the relation between structure, process and properties [1]. Simply put, the structure corresponds to how atoms organize themselves; the process is how atoms are forced to organize that way and properties

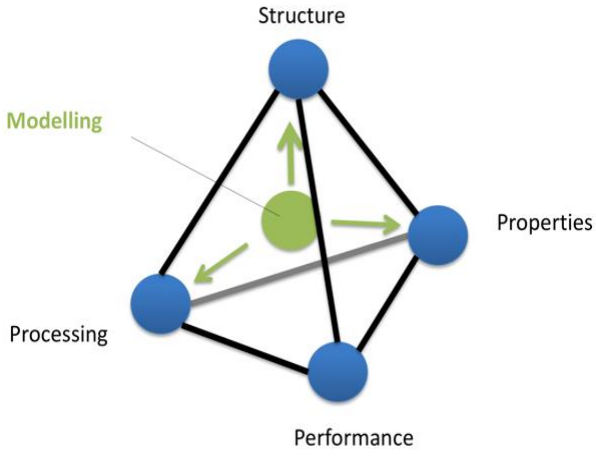

Figure 1: The tetrahedron of Materials Science.

are what can be quantitatively measured from this material. The combination of these factors determines the performance of materials: is this material better than others for this application? Are the properties sufficient? Is the process low-cost? One difficulty is to take into account all relevant features and their interdependence, even if they span different size and time scales. Scientific modelling of chemical-physical systems, such as the laws of thermodynamics for instance, provide the framework for the study and improvement of materials.

1.1. Modelling and computer simulation

Beyond scientific modelling, which can be considered as a simple mathematical description of the laws of nature in a given framework, computer simulations allow assessment of these mathematical models in more detail and complexity [2]. In materials science, a great variety of simulations exist. They primarily fulfill two roles: predicting materials features such as properties and/or illustrating complex mechanisms which are not necessarily possible to study experimentally. The present work aims to devise a multi-scale modelling of the synthesis of High Entropy Alloys by high energy ball milling: two specific simulations are used: Molecular Dynamics (MD) at the atomic scale and the CALculation of PHAse Diagrams method (Calphad) at the macroscopic level.

Since Alder *et al.* introduced their work on a new method used to calculate equilibrium properties of hard spheres in 1957, Molecular Dynamics has come a long way [3]. Based on Newton's equations of motion, this computer simulation method examines the physical and chemical properties of materials at the nanoscale. These kinds of observations are often impossible to study experimentally but their implications can often be experimentally verified. Nowadays, simulations containing millions of atoms are able to describe extremely fast phenomena which directly influence the material behavior at a macroscopic scale.

Molecular Dynamics is well-suited for the study of metals and related processes. For instance, in his PhD thesis [4], Turlo studied Self-propagating high-temperature synthesis (SHS) in nanometric metallic multilayers. It is a complex process involving many phenomena occurring at different length scales such as dissolution processes or phase transformations at the microscopic level. MD simulations of an SHS in Ni-Al nanometric metallic multilayers led to the precise characterization of several features of the process as well as of the corresponding microstructures. The methodology developed could be used to study other nano-scale phenomena such as the structural transformations resulting from quenching.

The CALculation of PHAse Diagrams (Calphad) method was introduced in the 1960s by Larry Kaufman [5]. The principle of this method lies in the laws of thermodynamics. More precisely, the Gibbs energy of each considered phase is mathematically described through thermodynamic optimization and experimental data capture. In practical terms, reliable phase diagrams of simple systems can be generated, and the thermodynamic properties of more complex systems can be extrapolated. Calphad calculation and results allow for significant time and cost reduction in producing a material of a specific composition and phase constitution for a given

application. Calphad is also widely used nowadays to perform high throughput screening to design new alloys.

Calphad is a particularly sharp tool in metallurgical analysis. For instance, for the design of a new Ni-based superalloy, the experimental test matrix was considerably reduced, the influence of thermo-mechanical treatments was simulated and then experimentally assessed. Hence, the method provided an efficient experimentation route that allowed critical features of the alloy to be quantitatively designed on the computer [6].

1.2. Metallurgy and powder metallurgy

Metals form the majority of the elements in the periodic table. They are defined by their specific chemical bond: metallic bonding, in which electrons are delocalized. This specificity explains their high thermal and electrical conductivity for instance. One other particularity, shared with ceramics, is the arrangement of their atoms in crystal structures. As a result, metals are easy to work with and exhibit an interesting combination of strength and ductility.
Metallurgy is the part of materials science that studies these metals, alongside intermetallics and alloys. The study of the interplay between structure and properties corresponds to the discipline named physical metallurgy, whereas the methods of extraction of metals from their natural mineral deposits correspond to the other main metallurgical discipline: extractive metallurgy [7]. Physical metallurgy therefore deals with the precise characterization of the material at each step of its synthesis.

Although one of the oldest materials science fields studied by mankind, metallurgy is still particularly relevant today. In addition to long-term developments or disruptive innovations such as technologies for nuclear fusion [8], industrial Research & Development focuses on three main objectives of iterative innovations [9]:

- improving the robustness of metallurgical processes (property dispersion, product quality) and lowering the manufacturing costs (raw material consumption, energy efficiency).
- improving the predictability of processes based on progress in multi-scale modelling.
- improving the environmental performance of processes: reductions in gaseous emissions or solid waste, for instance.

To tackle these objectives, the study of powder metallurgy is pertinent. Contrary to other, more classical, metallurgical processes, there is neither complete melting nor solidification during powder metallurgy. The transformation from powders to bulk materials occurs by sintering, for instance. Sintering is the consolidation which happens by fusing small particles together at elevated temperature (but below the melting temperature of the considered material).
Compared to other metallurgical processes, powder metallurgy has several unique features [10]:

- the process ensures uniformity of part dimensions and properties, as pressing and sintering are repetitive

- the raw materials are almost fully used, as there is little waste at each of the manufacturing steps
- the synthesis of unique, high-performance materials is made possible. Some examples are custom-made, multi-phase materials with predetermined textures or materials with very high melting temperatures such as WC-Co composites.
- since sintering can be performed rapidly, out of equilibrium materials and nanostructured materials can be easily synthetized.

Powder metallurgy has a wide range of applications. In the aerospace field for instance, Ni-based superalloys were specifically designed to manufacture turbine parts such as disks. The study of the relationships between the process parameters, microstructure and mechanical properties provided relevant data to efficiently increase disk life. More specifically, the powder metallurgy route enables production of higher content of refractory metals while chemical segregations are minimized. The process involving hot extrusion has led to an improvement in the high temperature properties of the alloy [11,12].

2. High Energy ball milling and subsequent behavior of metallic powders

One field in powder metallurgy research corresponds to the milling of powders prior to sintering.

In this work, we will differentiate between mechanical alloying and mechanical activation, both of which may be considered as mechanical milling (also termed mechanochemistry or mechanochemical synthesis). Mechanical milling is transferring mechanical energy to materials by means of a milling medium, often balls. This transfer leads notably to the creation of lattice defects, the decrease in powder particle size and the chemical mixing of the different powders.

- Mechanical alloying corresponds to mechanical milling until full homogenization of the powders is reached.
- Mechanical activation corresponds to mechanical milling to the point of partial homogenization. Full homogenization is achieved by a subsequent transformation. This transformation can be initiated by heating, for instance.

In practical terms, the effective main difference between mechanical activation and mechanical alloying is often the milling time. Mechanical activation and mechanical alloying will be intensively compared throughout this manuscript and examples will be given, especially in Chapters I, III and IV.

Mechanical milling can be performed by High Energy Ball Milling (HEBM). In the present work, the main milling device is a planetary ball mill. In theory, the device we used at ICB is one of the high energy ball milling systems. Compared to recent milling devices however, the transferred energy is low; thus, it is sometimes referred to as “medium energy ball milling”. It should be noted that the mechanisms involved have been considered as identical. These notions are detailed in Chapters I and III.

In the literature, the term “mechanical alloying” often replaces “mechanical milling” when the powder being milled is metallic.

Benjamin was the first to develop the mechanical milling of metallic powders in 1970. In the original article, he combined yttrium oxide and a nickel-base superalloy to produce oxide-dispersion strengthened (ODS) alloys. He milled 10kg of reactant in an attritor-grinding mill originally designed for paint and ink production. The bulk alloy was produced by hot extrusion at 1200°C and exhibited high strength and remarkable high temperature resistance [13].

Mechanical milling involves repeated cold welding, fracturing and rewelding powder particles and is useful to prepare supersatured solid solution, metastable crystalline phases and nanostructures. Contamination from the milling media is often considered as the main drawback of this process. It is, overall, a very versatile technique which still attracts much attention [14].

The mechanisms occurring during mechanical milling are still only partially understood. Currently, most models are based on the assumption that milling ball collisions are the main factor which influences microstructure and reactivity in the powder mixtures. However, direct experimental observations and analysis of microstructures indicate that friction and shear deformation may be major activating influences. As a result, the elemental mechanisms responsible for the unique features of the process are still poorly understood.

Mechanical milling may seem archaic but high-performance nanostructured materials can be elaborated by means of this technique. In his PhD thesis, Paris studied the synthesis of dense and nanostructured intermetallics [15]. Indeed, intermetallics are often brittle and nanostructuration is a way to improve the mechanical properties of such compounds. Consequently, the development of new processes is required in order to produce these peculiar materials. The Mechanical Activation and the subsequent Pressure-Assisted Field-Activated Synthesis of FeAl were analyzed. The relevant parameters were determined to elaborate a dense compound with a fine microstructure. He determined that a short milling time was enough to enhance the formation of FeAl by reactive sintering. The developed methodology could be extended to other binary intermetallics or to more complex systems.

3. High Entropy alloys

Millenia ago, the first alloy was developed: bronze. This invention corresponded to the addition of a small amount of tin to copper. The same approach has been applied to develop new alloys ever since. First, a base element is selected for its interesting properties, then small quantities of alloying elements are added to improve and balance the properties. Centuries later, the production of steel was standardized, by precisely controlling small carbon additions to an iron base. In the 1950s, titanium was the last metallic element exploited as a major alloy base. With the progress of metallurgy, alloy design became more and more complex. Superalloys for instance, may have as many as 12 meticulously controlled alloying elements. Nowadays, some findings report that this approach may be reaching a limit, although metallurgical challenges

still arise [16]. Reducing the need for rare and strategic elements and improving the recyclability of alloys are excellent examples of challenges for the beginning of the century.

High Entropy Alloys (HEAs) represent a new class of materials that are composed of 5 – 10 elements in near-equiatomic concentrations in one phase, as opposed to traditional metallic alloys based on one major element doped by a set of minor elements. Beyond the promising properties that this new class of materials could exhibit, there is also a strong interest in exploring the center of phase diagrams and the resulting materials. Indeed, the elaboration of such complex materials encompasses significant challenges: meeting the industry criteria in terms of quality and reproducibility or transferability between two alloy compositions.

As detailed in Chapter I, the High Entropy Alloys concept can be extended to Concentrated Complex Alloys (CCAs) or Multi-Principal Elements Alloys (MPEAs). However, we chose to adopt the term HEA because it is still the most commonly used. The alloys studied in the present work would not necessarily exhibit High Entropy, the same way than Spark Plasma Sintering does not necessarily exhibit Plasma.

Most HEAs are produced from raw elemental materials using liquid-phase methods with arc melting. Melted and cast HEAs usually present segregated microstructures with the presence of dendritic and inter-dendritic regions, which are difficult to remove with homogenization due to the peculiar diffusion of HEAs. Only a small fraction of HEAs is synthetized by solid state processing.

The number of possible combinations of elements in the HEA is practically infinite. Among all these possibilities, we chose to investigate HEAs composed mainly of Al, Co, Cr, Fe and Ni in order to provide a system that can be compared to results emanating from a substantial body of research. Indeed, $Al_xCoCrFeNi$ alloys are among the most widely studied systems. High entropy alloys such as equimolar AlCoCrFeNi may exhibit very interesting properties such as high temperature oxidation resistance. In addition, the presence of light elements lowers the total density of the alloy for applications in aerospace materials.

4. Aims of this project

This introduction has argued that powder metallurgy elaboration applied to High Entropy Alloys is a particularly relevant topic in regard to the current state of metallurgy. In order to obtain a new class of materials able to valuably replace existing alloys, it is necessary to develop appropriate routes for its preparation. This project aimed at developing an efficient and reliable synthesis method to produce HEAs with unique features. The preparation of alloys by powder metallurgy often exhibits two drawbacks: long preparation times and undesired contamination. Considerable efforts will be made in the present work to deal with these issues. The study of mechanical activation instead of mechanical alloying seems especially promising in this context.

However, to efficiently evaluate the relation between process and microstructure, a first study carried out on simplified systems had to be initiated. In the first part of this work, simulations will be used to understand the role of the process in the synthesis. The progress of ball milling and mechanical activation will be investigated at the atomic scale. The purpose is to thoroughly describe the elemental mechanisms responsible for the unique behavior of mechanical activated powder in order to select the most relevant elaboration parameters. Until now, most of the studies on mechanical activation have concerned reactive bi-metallic systems. The situation is more complex in the case of 5 element powders and a major effort has to be made to develop a comprehensive understanding of powders ranging from 2 to 5 and more elements. This thesis is intended to lay the first foundations on this topic.

Although the direct MD simulation of HEAs is premature, many questions call for a multi-scale modelling approach. Based on a phenomenological perspective, the Calphad method should reveal the macroscopic behavior of HEAs, including the phase stability and phase composition as a function of temperature. Molecular dynamics simulations will be developed in order to follow the elemental mechanisms governing the kinetic aspects at the microscopic level, including friction between metallic particles, diffusion and creation of defects during ball milling.

Industrial renewal is intimately related to the development of innovative materials. This is especially the case in metallurgy because of the demand for materials with tailored characteristics. High-entropy alloys represent an alternative to traditional alloy systems (steel, aluminum, copper, etc.) or superalloys which are all based on one principal metallic element. In this work, the alloy design is of a lesser importance since one of the main goals is to understand how complex systems involving 5 powders with different characteristics will behave during milling and sintering -not to design a specific material for a particular application. In this context, the present work was supported by Safran as technological watch.

This project seeks to determine a well-suited route for the elaboration of HEAs. The process-structure relation will be investigated since the properties of HEAs are primarily related to the formation of microstructures at nanoscale.

5. Presentation of articles

We chose the journal thesis format because one of the main topics of this thesis -High Entropy Alloys- is a current and highly visible topic. Figure 2 illustrates the idea that High Entropy Alloys attract a lot of attention compared to other similar classes of materials. Consequently, it was important to rapidly publish and position the ICB laboratory as an active player in this innovative research.

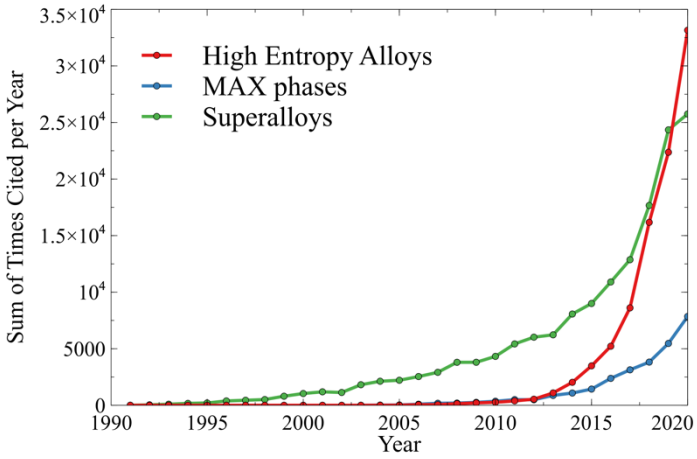

Figure 2: Bibliography data about various classes of materials. Source: Web of Science.

The journal thesis format necessarily involves some repetition, especially between the state-of-the-art presentation in Chapter I and the introductions of each article-chapter. Certain parts of the literature review will be referred to in the corresponding article introduction.

Chapter II is entitled “Mechanical Activation of Metallic Powders: A Molecular Dynamics Approach” [17]. This chapter deals mainly with the effect of high energy ball milling on metallic powders at a sub-microscopic level. In this chapter, only binary mixtures were considered, as numerous questions remain unanswered even for simple systems. The effects induced by the mechanical treatment were closely analyzed in regard to the structure and mechanical properties of the elemental powders.

Chapter III examines the “Reactivity of Ni-Al nanocomposites prepared by mechanical activation: a molecular dynamics study” [18]. This chapter deals with the behavior of metallic powders after mechanical milling. This study follows a thorough experimental study led by Russian collaborators. The aim of this study is to evaluate one of the possible activating factors of the heightened reactivity after mechanical milling: nano-scale mixing of the reagents.

Chapter IV presents the “Effects of planetary ball milling on AlCoCrFeNi high entropy alloys prepared by Spark Plasma Sintering: Experiments and molecular dynamics study” [19]. The chapter deals with the alternative way to produce HEAs: mechanical activation. The objective of this chapter is to experimentally evaluate the influence of the key processing parameters such as milling speed, sintering temperature, or powder size on the prepared HEAs. A multi-scale approach leads to the fine characterization of the material at each step of the process.

Chapter V deals with the “Effects of mechanical activation on chemical homogeneity and contamination level in dual-phase AlCoCrFeNi High Entropy Alloy” [20]. The in-depth characterization of HEAs produced by the route developed in this work is detailed in this chapter. Experimental atomic scale characterizations are used to evaluate the chemical homogeneity of the sintered HEAs. Special attention is paid to the contamination originating from the process.

Chapter VI is entitled “Thermal stability of Medium and High Entropy Alloys of 3d-transition metals” [21]. This chapter deals with one very important feature of materials: thermal stability. This question is all the more important in the case of HEAs prepared by mechanical milling since out of equilibrium states are often reached after powder metallurgy routes.

Given the specific format of the present manuscript, a number of interesting results were not published and do not appear in the main chapters. Five Appendices have been added at the end of the manuscript to report these results that will require complementary investigations before publication.

The first Appendix, “Comparison of Mechanical Alloying and Mechanical Activation in AlCoCrFeNi High Entropy Alloy synthesis,” deals with the comparison of powders obtained by means of two different mills. Both the powder characteristics and their temperature-induced reactivity are investigated.

Appendix II, “Influence of milling and sintering scale change,” focuses on the effect of some parameters of the process including the size of the milling jars and sintering dies. This study is particularly useful since Appendices III, IV and V are all based on the results reported there.

Appendix III, “Influence of the initial elemental particle size on the milling progress,” deals with one critical parameter during milling: the size of each elemental particle before milling begins. The influence of initial chromium size was evaluated in Chapter IV; this study focuses on the influence of Al, Fe and Ni initial size.

Appendix IV, “Investigation of new High Entropy Alloy compositions elaborated by Mechanical Activation and Spark Plasma Sintering,” deals with the influence of Mn and Al content on the milling progress and sintered alloy microstructure. Among other things, the aim of this study was to assess the process by investigating the well-known MnCoCrFeNi Cantor Alloy.

The intent of the investigations reported in Appendix V, “High temperature behavior of High Entropy Alloys elaborated by mechanical activation,” was to evaluate the thermal stability and high temperature oxidation properties of sintered alloys elaborated by the process developed in the present thesis. The influence of Al content on the oxidation products was especially investigated.

References

[1] W. Callister, D. Rethwisch, Materials Science and Engineering – An Introduction, 8th ed., John Wiley and Sons, 2009.

[2] R. LeSar, Introduction to Computational Materials Science: Fundamentals to Applications, 1st ed., New York: Cambridge University Press., 2013.

[3] B.J. Alder, T.E. Wainwright, Phase Transition for a Hard Sphere System, J. Chem. Phys. 27 (1957) 1208–1209. https://doi.org/10.1063/1.1743957.

[4] V. Turlo, Etudes par dynamique moléculaire de multicouches nanométriques métalliques de Ni-Al : processus de dissolution, transformations structurales et propagation d'une onde réactive, Université de Bourgogne, 2017.

[5] P.J. Spencer, A brief history of CALPHAD, Calphad. 32 (2008) 1–8. https://doi.org/10.1016/j.calphad.2007.10.001.

[6] N. Saunders, M. Fahrmann, C.J. Small, The Application of Calphad Calculations to Ni-Based Superalloys, in: Superalloys 2000 Ninth Int. Symp., TMS, 2000: pp. 803–811. https://doi.org/10.7449/2000/Superalloys_2000_803_811.

[7] J.J. Moore, Chemical metallurgy, 2nd ed., Elsevier, 2013.

[8] S. Sgobba, S.S. Lourenço, I.A. Santillana, P. Libeyre, T. Reagan, C. Wooten, Metallurgical assessment of large size tensioning components for the precompression structure of the ITER central solenoid, Fusion Eng. Des. 170 (2021) 112543. https://doi.org/10.1016/j.fusengdes.2021.112543.

[9] B. Dubost, F. Mudry, A. Greliier, R&D industrielle en métallurgie, Techniques de l'Ingénieur, 2011.

[10] M. Eudier, Métallurgie des poudres - Généralités, 2nd ed., Techniques de l'Ingénieur, 1994.

[11] C. Ducroq, Superalloy compositions with a Nickel base, U.S. Patent USOO5104614A, 1992.

[12] D. Locq, P. Caron, On some advanced nickel-based superalloys for disk applications, Aerosp. Lab. (2011) 1–9.

[13] J.S. Benjamin, Dispersion strengthened superalloys by mechanical alloying, Metall. Trans. (1970) 9.

[14] C. Suryanarayana, Mechanical alloying and milling, Prog. Mater. Sci. 46 (2001) 1–184. https://doi.org/10.1016/S0079-6425(99)00010-9.

[15] S. Paris, Mécanismes réactionnels induits par frittage "flash" réactif activé mécaniquement (Application au système Fe / Al), Université de Bourgogne, 2005.

[16] S. Gorsse, J.-P. Couzinié, D.B. Miracle, From high-entropy alloys to complex concentrated alloys, Comptes Rendus Phys. 19 (2018) 721–736. https://doi.org/10.1016/j.crhy.2018.09.004.

[17] F. Baras, Q. Bizot, A. Fourmont, S. Le Gallet, O. Politano, Mechanical activation of metallic powders and reactivity of activated nanocomposites: a molecular dynamics approach, Appl. Phys. A. 127 (2021) 555. https://doi.org/10.1007/s00339-021-04700-9.

[18] A. Fourmont, O. Politano, S. Le Gallet, C. Desgranges, F. Baras, Reactivity of Ni–Al nanocomposites prepared by mechanical activation: A molecular dynamics study, J. Appl. Phys. 129 (2021) 065301. https://doi.org/10.1063/5.0037397.

[19] A. Fourmont, S. Le Gallet, O. Politano, C. Desgranges, F. Baras, Effects of planetary ball milling on AlCoCrFeNi high entropy alloys prepared by Spark Plasma Sintering: Experiments and molecular dynamics study, J. Alloys Compd. 820 (2020) 153448. https://doi.org/10.1016/j.jallcom.2019.153448.

[20] A. Fourmont, S. Le Gallet, K. Hoummada, M. Descoins, C. Desgranges, O. Politano, F. Baras, Effects of mechanical activation on chemical homogeneity and contamination level in dual-phase AlCoCrFeNi high entropy alloy, Mater. Chem. Phys. (2021) 125000. https://doi.org/10.1016/j.matchemphys.2021.125000.

[21] A. Fourmont, A.S. Rogachev, S. Le Gallet, O. Politano, D.Yu. Kovalev, N.A. Kochetov, N.F. Shkodich, S.G. Vadchenko, F. Baras, Thermal Stability of Medium- and High-Entropy Alloys of 3d-Transition Metals, J. Phase Equilibria Diffus. (2021). https://doi.org/10.1007/s11669-021-00903-y.

Chapter I: Literature review

Introduction

This chapter, presenting a literature review, will focus on High Entropy Alloys since this class of materials has appeared very recently and since the review of the literature on milling mechanisms will be covered in the introductions to Chapters II and III.

High Entropy Alloys (HEA) are new materials that were described simultaneously in 2004 by Yeh *et al.* [1] and Cantor *et al.* [2]. They were first defined as the mixture of at least 5 metal elements in a proportion of between 5 and 35 at.%. This mixture has thus a high configurational entropy (unlike conventional alloys composed of a main base). Entropy is a property of a thermodynamic system, characterizing the disorder of the system: here, the multiplicity of configurations limits the appearance of intermetallic phases and favors the formation of a limited number of multi-elemental solid solutions (i.e., a crystal composed of all the elements, homogeneous on the mesoscopic scale). Because of the wide choice of potential compositions, a considerable number of microstructures and therefore properties can be tailored.

Two main categories of HEA have emerged today: alloys composed of transition metals in the fourth row of the periodic table and refractory alloys.

- The first category may be considered as an extension of stainless steels and superalloys, generalizing their concept to *N* constituents in almost equal proportions. The most widely studied composition in this category corresponds to the Cantor alloy: CoCrFeMnNi [2]. The interest of this family is to combine a high yield strength with good thermal stability as well as remarkable resistance to wear and corrosion. As the literature is expanding on this branch and as the cost of the constituent elements is moderate [3], this family will be explored in this thesis work.
- The second category is less studied than the first one; it is composed of alloys like WNbMoTaV [4] which have very good mechanical properties at high temperature, and thus meet needs that conventional alloys no longer satisfy in current operating conditions (in aircraft engines for example).

The microstructure of HEAs depends on the manufacturing process. There are two main ways of preparing these alloys: the liquid or the solid route.

- Most HEAs are synthesized by means of the liquid route, in particular via the method of arc fusion. This method consists in creating an electric arc between an electrode and the crucible containing the mixture in a high-vacuum chamber. Each component melts and then mixes with the others. The first HEAs were elaborated using this method. Its main interest is that it allows for the synthesis of the high entropy solid solution with very few secondary phases. This technique also has the advantage of being fast, although several remeltings are

necessary to ensure the chemical homogeneity of the alloy. The limit of the process lies in the cooling step, which is difficult to control. This process results in various microstructures, mainly dendrites (fragile and thus unwanted).

- Since 2008, the preparation of solid route HEA has been explored [5]. It consists in the co-milling of the powders leading to the formation of the solid solution. We speak of mechanical alloying. This process has the advantage of avoiding solidification and the drawbacks related to cooling. Nevertheless, milled mixtures frequently show traces of contamination from the mill components. Finally, the HEA synthesized via this route are in powder form. The technique most often used to elaborate them in massive form is Spark Plasma Sintering (SPS). This method involves passing a strong electric current through the sample while applying an uni-axial pressure. The SPS is therefore similar to hot pressing, except that the heat source is internal to the material and the heating rate is very high.

We focus on the aforementioned technique in this thesis. Indeed, in addition to providing better control of the microstructure, improving our understanding of the phenomena related to mechanical alloying is of great interest.
High-entropy alloys constitute a rapidly expanding subject of research, which is tackled in many ways: the influence of the composition, the impact of the manufacturing process or the response mechanisms to mechanical stress and the environment in general (corrosion, radiation, etc.).
Several industrial sectors are interested in HEA: aeronautics (Safran for example) for their possible mechanical strength and high temperature resistance (essential in improving the performance of critical parts of turboshaft engines); the defense sector (Nexter-Munitions, ...) for their density and hardness (in order to improve the perforating nature of projectiles for instance) or the nuclear sector (CEA, etc.) for their mechanical strength coupled with their resistance to radiation.

This chapter aims to present an overview of the literature relevant to the High Entropy Alloy topic of this thesis and to determine the relevant remaining questions and issues. In the first part, we will present the concepts necessary to an understanding of HEAs. Then, we will present the chosen composition AlCoCrFeNi and the influence of relevant metallic elements and synthesis route on phase formation. The Powder Metallurgy preparation of multicomponent alloys will be covered in a third part. Finally, a brief summary of molecular dynamics simulation studies related to this topic will be presented.

1. Main concepts

In thermodynamics, the equilibrium of a system is reached when its Gibbs free energy G is at a minimum. At constant pressure and fixed temperature, the free energy is expressed as:

$$G = H - T.S \quad (1)$$

where H is the enthalpy, T is the temperature and S is the entropy of the system. In the case of a mixture (and in particular for a solid metal alloy), the variation of the Gibbs free energy between the reference state in which the components are separated, and the state of the system is:

$$\Delta G_{mix} = \Delta H_{mix} - T.\Delta S_{mix} \quad (2)$$

In conventional alloys, the energy term ΔH_{mix} ensures the stability of the mixture by minimizing free energy. For high entropy alloys, the entropy term $T.\Delta S_{mix}$ ensures stability. More precisely, the configurational entropy is defined by the Boltzmann formula:

$$S_{conf} = k_B.\ln(\omega) \quad (3)$$

where k_B is the Boltzmann constant and ω is the number of configurations. In the case of a mixture passing from the elementary state to a random solid solution, the entropy variation can be expressed as:

$$\Delta S_{mix} = -R.\sum_{i=1}^{N} c_i.ln(c_i) \quad (4)$$

where R is the ideal gas constant and c_i is the molar fraction of each constituent of the N-element mixture. This last relation makes it possible to specify quantitatively the notion of an alloy with high entropy: a high entropy alloy is defined as a mixture of metals whose entropic term exceeds the enthalpic term. In their first article on HEA [1], Yeh *et al.* define them as alloys composed of at least 5 elements whose concentration is between 5 and 35 at. %.

According to Yeh *et al.* [6], it seems that four main effects are responsible for the remarkable properties of HEA.

• Entropic effect

The multi-elemental mixture forms a simple disordered solid solution (often BCC or FCC). The entropic effect associated with the intimate mixing of the elements in the solution avoids the spontaneous formation of complex microstructures.

• Effect of lattice distortion

The resulting solid solution does not have a conventional crystalline structure: it presents a strong distortion of the lattice as shown in Fig. 1. This has the notable effect of modifying the mechanical behavior, the thermal behavior, etc.

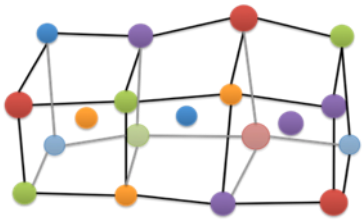

Figure 1: Schematic representation of a random multicomponent BCC lattice.

• Effect of sluggish diffusion

The distortion of the lattice will significantly reduce the number of diffusion paths at the atomic scale. We speak here of sluggish diffusion. This property has the effect of inhibiting a number of temperature-related phenomena such as phase transformations.

• Cocktail effect

HEA can be considered as composites on the atomic scales. By combining the characteristics of the elements of which they are composed, they have properties that are absent from the elements taken separately.

Although almost produced simultaneously, Cantor *et al.* did not suggest entropy to explain their results. They manufactured multicomponent alloys by casting and isolated the five components FeCrMnNiCo (known today as the Cantor alloy) as being single phase FCC. They also found that the number of phases formed for multicomponent alloys are always well below the maximum number given by the Gibbs phase rules. The authors underlined the absence of formation of glassy structures, even in the case of 20 elements in equimolar proportion [2].

Furthermore, Otto *et al.* demonstrated that high configurational entropy was not a real predictor of single-phase alloys. Indeed, they prepared several equiatomic quinary alloys by replacing individual elements in the Cantor alloy (thus keeping the same configurational entropy) and found that only the initial alloy exhibited single phase. They concluded that high configurational entropy was only useful to explain "after the fact" why a random multicomponent solid solution forms [7].

Using simulation methods like the Density Functional Theory (DFT), Schön *et al.* demonstrated that configurational entropy had a marginal effect. The authors suggested that the competition between conflicting interactions in the solid solution (what the authors called "configurational frustration") was in fact the parameter responsible for disordered solid solution stabilization. In addition, their results showed that diffusion was enhanced by the thermodynamic effect in the

case of high concentrated alloys and thus brought into question the role of sluggish diffusion [8].

In light of the articles presented above, Gorsse *et al.* suggested that the term "high entropy alloys" should be restricted to single-phase multicomponent alloys only and the other alloys in Yeh's definition should be named Complex Concentrated Alloys (CCA). Although the principal composition of this thesis is not single phase, the HEA term will be used in what follows (as it is in most of the literature) for the sake of uniformity and clarity [9].

Several criteria have been proposed to predict the stability of HEAs and the possible formation of various phases according to composition. In the following paragraph, a selection only of examples will be given.

Zhang *et al.* proposed an enthalpy of mixing ΔH_{mix} calculated with the Miedema model. This model is semi-empirical, and it is used to estimate the heat of formation of various compounds. It should be noted that the authors used the enthalpy for liquid systems in order to propose their criterion. They also tried to adapt Hume-Rothery rules to HEA. In this way, they introduced the mean square deviation δ_r of the atomic size of elements. They found that high entropy solid solutions are stable for $-15 < \Delta H_{mix} < 5$ kJ/mol and $\delta_r < 6.6\%$ [10].

To complete these two criteria, Guo S. *et al.* used the Valence Electron Concentration (VEC). They found that the respective stability of FCC and BCC is well defined using this tool. VEC < 6.87 would seem to favor the formation of a BCC single phase and VEC > 8 would seem to favor the formation of an FCC single phase [11].

1.1. Thermodynamic predictions of HEAs

Zhang *et al.* were among the first to investigate High Entropy Alloys using the Calphad approach (CALculation of PHAse Diagrams). As researchers in the CompuTherm company (Pandat^{TM} publisher), the authors developed their own database for Al-Co-Cr-Fe-Ni. They assessed the effect of each element on the FCC/BCC transition and confirmed the experimental observations (covered in section 2.1.). It should be noted that they always compared their thermodynamic calculations to fully homogenized alloys (24h, 1100°C). The AlCoCrFeNi equimolar composition is predicted to exhibit an ordered BCC + disordered BCC+ FCC microstructure at 1100°C (which is different from as-cast AlCoCrFeNi HEA, see section 2.2.1) [12].

In another article, Zhang *et al.* addressed the common discrepancies observed between Calphad calculations and experimental results (e.g., missing ordered phases). They suggested that there were two main reasons for such discrepancies: periods of heat treatment which were too short--according to the authors heat treatment should last at least 50h--and the difficulties in distinguishing ordered and disordered phases [13].

Manzoni *et al.* used the Thermo-Calc TCNi7 database to investigate compositions derived from AlCoCrCuFeNiTi. They tried to reach 3 main goals: decrease Cu content (which often segregates), increase oxidation protective element content (Al and Cr) and arrive at the formation of a γ/γ' microstructure (a matrix/coherent precipitate-type of microstructure inspired by the popular Ni-based superalloy). Their results on the AlCoCrFeNi composition are in agreement with Zhang's work (fig. 8). The authors concluded that $Al_{10}Co_{25}Cr_8Fe_{15}Ni_{36}Ti_6$ (in at. %) was the stoichiometry most likely to meet their 3 criteria [14].

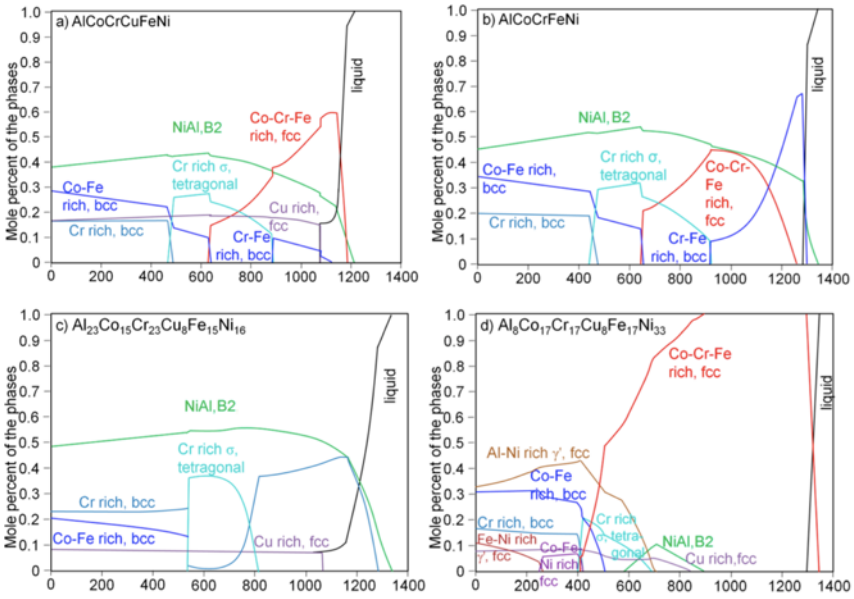

Figure 2: Calphad calculations on different AlCoCrCuFeNi compositions using ThermoCalc and the TTNi7 database [14].

Syed Ghazi and Ravi compared equilibrium phases after melting, equilibrium phases after mechanical alloying and Calphad calculations. They focused on the CoFeNi, CoCrFeNi and CoCuFeNi compositions and suggested that equilibrium of liquid-state processing routes can be effectively predicted by considering that the phase evolution is the result of cooling (the equilibrium moves from top to bottom), whereas the equilibrium of a solid-state process (i.e., MA but not sintering) is the result of heating (the equilibrium moves from bottom to top). In other words, the authors suggested that increasing milling time was equivalent to heating to a higher temperature in a phase diagram. This last consideration is rather meaningful in the case of a 2-element milling [15].

In their review, Gorsse and Tancret evaluated the use of Calphad in the case of HEAs. First, they demonstrated that the formation of an entropy-stabilized single solid solution was in fact an improbable event. Then, they showed that Calphad is a very useful tool, both for predicting equilibrium and for confirming experimental results. They outlined two challenges for thermodynamic calculations: the lack of description for most ternary systems within the whole compositional range and the immensity of data to explore. They suggested using complementary tools such as data mining. They recommended that future work should be focused on precipitation strengthening and twinning-induced or transformation-induced plasticity [16].

2. The AlCoCrFeNi alloy

As was stated in the Introduction, AlCoCrFeNi is a very common composition. It is thus interesting to carry out a brief statistical analysis of the literature with Web of Science. In this way, we can see the different possibilities of designating this alloy as well as the main research topics concerning the HEA containing these five elements.

First, let us describe the specific nomenclature which exists to designate equimolar and non-equimolar multi-principal element systems. Equimolar compositions are often designated as CoCrFeNiMn for instance, which corresponds to $Co_1Cr_1Fe_1Ni_1Mn_1$ where the molar ratio of each element is the same. Non-equimolar alloys are then designated as $Al_{0.3}$CoCrFeNi for instance, corresponding to $Al_{0.3}$(CoCrFeNi). The four elements in parentheses have the same molar ratio and there is 30 at. % Al of this amount. Thus, in at. %, $Al_{0.3}$CoCrFeNi corresponds to 7% Al, 23.25% Co, 23.25% Cr, 23.25% Fe, 23.25% Ni.

In general, when the subscript numbers exceed 5, the number corresponds to at. % and not molar ratio.

Fig. 3 shows that the most common way to designate this alloy is by arranging the elements in alphabetical order; this is the nomenclature adopted in this thesis as well. Only 5+5% of publications arrange the elements in the order of the periodic table. We can also see that Al is the main element of interest; indeed authors often end the HEA formula by a specific element to underline the studied parameter (the Al content in most of the cases). Apart from the equimolar composition, two other compositions are of interest: the eutectic composition $AlCoCrFeNi_{2.1}$ ([17] for instance) and the low content $Al_{0.3}$CoCrFeNi ([18] for instance) which is the maximum Al content to have a single FCC alloy.

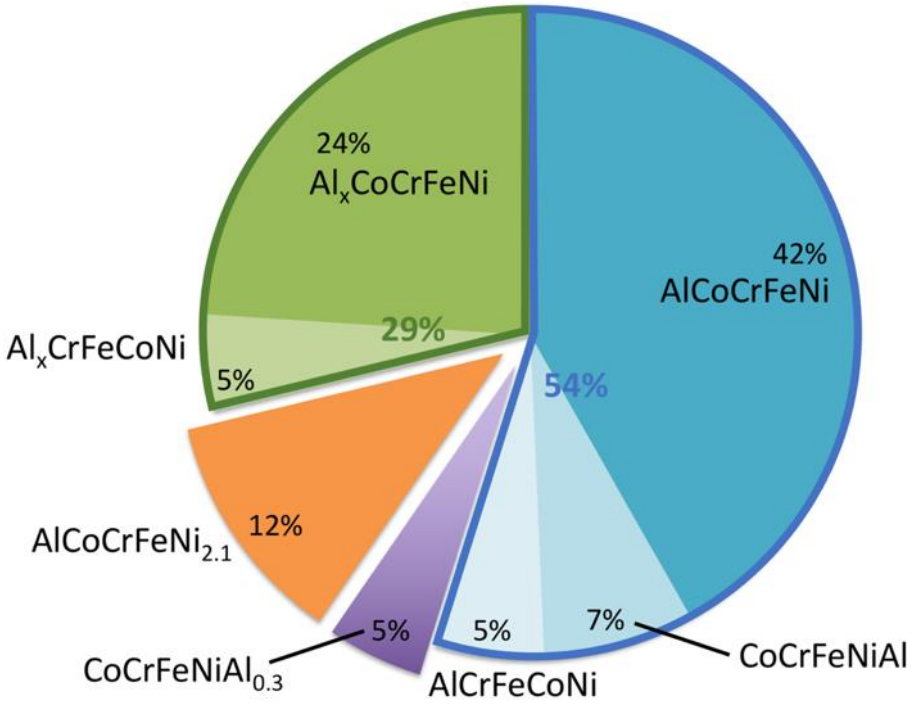

Figure 3: Statistical analysis of the literature concerning the AlCoCrFeNi alloy in 2019.

2.1. Influence of elements

A lot of work has been done to experimentally assess the influence of each element ratio on HEAs as compared to the equimolar composition. At the early stages of HEA research, these experimental and empirical assessments were very common and the present chapter takes this trend into consideration. Nowadays, Calphad investigations are more and more common and tend to replace such systematic studies.

Tung *et al.* experimentally checked the influence of each element for the arc melted AlCoCrCuFeNi. They found that Co, Cu and Ni enhance the formation of the FCC phase and that Cu tends to segregate easily. Al and Cr enhance the formation of the BCC phase [19].

2.1.1. The Role of Aluminum

Aluminum is definitely the highest impact element of the five. One of its important effects is the formation of intermetallic-like phases. Indeed, in the cases of binary Al-X (X being another metal such as Ni, Fe), ordered structures often form. Such structures also form in the case of multi-principal element systems. For example, an ordered BCC structure, designated as B2 in the Strukturbericht nomenclature, corresponds to the well-known structure CsCl: two simple cubic structures imbricated. The disordered BCC structure is designated as A2.

Wang *et al.* synthetized thirteen $Al_xCoCrFeNi$ cast alloys with the Al ratio varying between 0 and 20 at. %. Increasing the Al content indeed promotes the formation of the BCC phase (Fig. 2). The authors experimentally found that the single FCC phase is stable below 11% of Al and that BCC phases (A2 precipitates in a B2 matrix) are stable above 18.4% [20].
The role of Al as a stabilizer of the ordered B2 structure was confirmed by Yang *et al.* thanks to thorough TEM/SAED analysis [21].

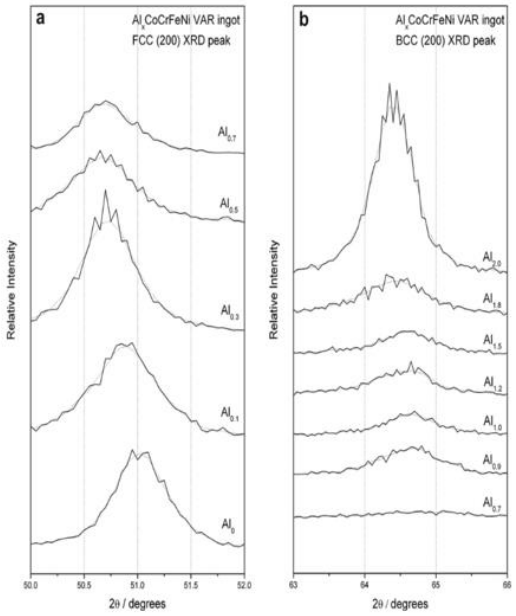

Figure 4: Evolution of main FCC and BCC XRD peaks with Al content for the $Al_xCoCrFeNi$ alloys [21].

2.1.2. The Role of Cobalt

Qin *et al.* studied the influence of Co content with the idea of increasing plasticity. They prepared several $(AlCoCrFeNi)_{100-x}Co_x$ cast alloys and found that Co is indeed an FCC stabilizer. The plasticity increased with the FCC phase volume which is closely linked to the Co content [22].

$Al_{0.6}CoCrFeNi$ and $Al_{0.6}CrFeNi$ alloys were prepared by a combination of milling and SPS or HIP. The milling of the composition with Co led to 60 vol. % BCC and 40 vol. % FCC while the elimination of Co led to a BCC increase (85 vol. %). After a 1273K sintering, the trend remained: $Al_{0.6}CoCrFeNi$ had more BCC than $Al_{0.6}CrFeNi$ [23].

2.1.3. The Role of Chromium

Shun and Yung investigated the influence of Cr for $AlCoCr_xFeNi$ cast alloys (from 0.3 to 1). They found that Cr is a BCC former and reported ordered BCC in every case [24].

2.1.4. The Role of Iron

Guo L. *et al.* investigated the influence of Fe addition using an original method. They mixed pure Fe powders and AlCoCrFeNi starting powders using high-energy ball milling. Thus, they studied $(AlCoCrFeNi)_{100-x}Fe_x$ (x=5,15 and 20) sintered by SPS at 1100°C. They found that increasing Fe leads to an increase in the FCC phase volume fraction and simultaneously to the formation of Fe-Cr rich BCC nanoprecipitates [25]. They explained the formation of the Fe-Cr rich precipitates in the Al-Ni rich matrix by spinodal decomposition, quoting previous articles [26].

2.1.5. The Role of Nickel

Surprisingly, there are no similar publications on the influence of Ni in the 3d-element HEA. However, it has been shown that increasing the Ni content leads to an interesting class of materials: eutectic high entropy alloys.

Lu *et al.* investigated $AlCoCrFeNi_{2.0}$, $AlCoCrFeNi_{2.1}$ (the true eutectic composition) and $AlCoCrFeNi_{2.2}$ prepared by vacuum induction melting (2.5 kg ingots). The eutectic microstructure exhibits the fine lamella of the Fe-Cr rich $L1_2$ phase and the Ni-Al rich B2 phase. The hypoeutectic composition shows more B2 phase and the hypereutectic one shows more FCC phase. Ni seems indeed to be an FCC stabilizer [17].

2.2. Microstructure and properties of the AlCoCrFeNi alloy.

2.2.1. Liquid route synthesis of AlCoCrFeNi

Most HEAs are prepared by arc-melting. This processing route leads to a dendritic/interdentritic region and A2+B2 phases. Thermomechanical processes can result in more homogeneous materials and are often applied.

Ren *et al.* investigated the formation conditions of high entropy disordered solid solution for several compositions including AlCoCrFeNi. The arc melted alloy exhibits a disordered BCC phase and the NiAl intermetallic compound (B2). The authors use radius mismatch and mixing enthalpy criteria to explain/predict that this composition will form intermetallics [27].

Wang *et al.* were among the first to transition from the composition AlCoCrCuFeNi to AlCrFeCoNi to test whether the Cu was really mandatory for alloy ductility. The alloy was prepared by arc-melting and was composed only of a BCC phase. The dendritic area was found to be Al-Ni rich and the interdentritic zone is Cr-Fe rich. The fracture mechanisms found were both cleavage fractures (brittle) and slip separations (ductile) [28].

Manzoni *et al.* investigated the AlCoCrFeNi composition at the nanoscale (TEM, atom probe tomography) to complete Wang's work. The arc-melted alloy exhibits a single BCC phase with an Al-Ni rich matrix and Cr-Fe rich precipitates. Contrary to the Al-Ni rich phase, an alternation of Fe and Cr clusters are observed in the other phase [29]. The authors suggest that spinodal decomposition is the reason for these fluctuations, quoting previous work carried out with Atom Probe Tomography [30].

Several studies report the influence of temperature on the formation of FCC and sigma phases. The effect of heat treatment on the arc melted AlCoCrFeNi alloy was studied by Munitz *et al.* The as-cast alloy exhibits BCC phases (A2+B2) with an Al-Ni rich dendrite core and Co-Cr-Fe rich interdentritic regions. A sigma phase and an FCC phase formed in the interdendritic regions with heat treatments of between 650 and 975°C. Heating to 1100°C caused some of the sigma and the FCC phases to transform back into a BCC phase. The FCC and the sigma phase disappear completely from the diffractogram after a 1200°C heat treatment [31]. The phase changes and transitions in the AlCoCrFeNi system were assessed by Strumza *et al.* The alloy was prepared by arc melting under a Ti-getter and heat treated under an argon atmosphere. The FCC phase seems to precipitate from the B2/BCC matrix at about 590 °C. The authors suggested that the high-energy interphase at the FCC/BCC boundary leads to the σ phase precipitation at around 640°C [32]. Lim *et al.* focused their work on the advantages of the dual phase structure (A2+B2) and its high-temperature behavior. The as-cast alloy indeed exhibits both these phases but a solid-solid transformation occurs at around 773K: an FCC and a sigma phase are formed. These phases formed preferentially in the Cr-Fe rich region (or interdendritic region). The authors suggested that controlling the initial microstructural morphology (i.e. reducing interdendritic volume fraction) could hinder the formation of unwanted phases [33].

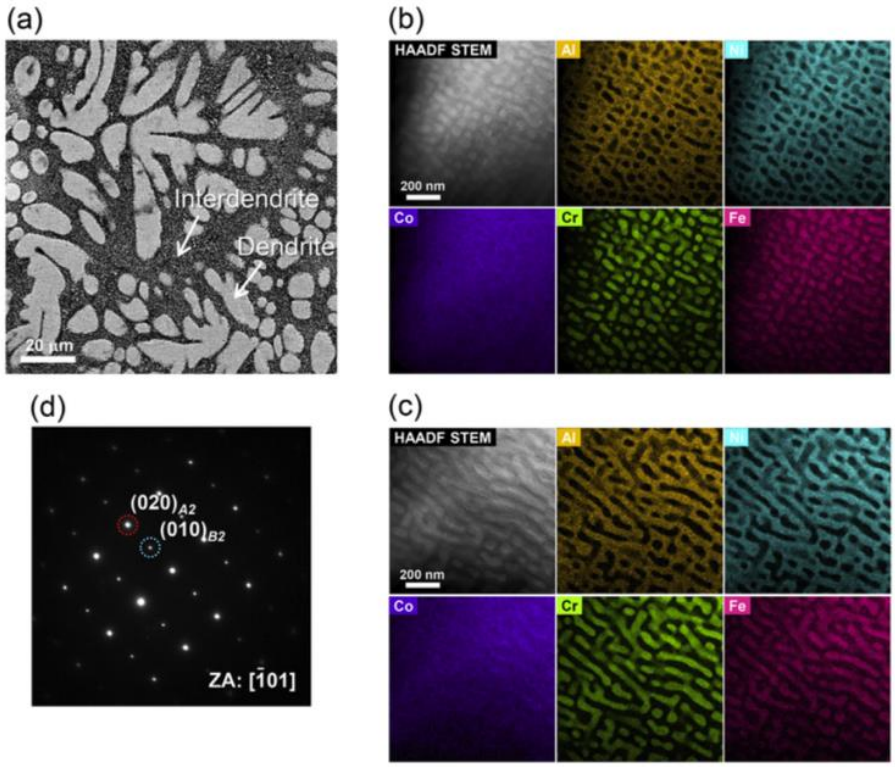

Figure 5: Classical microstructure of a cast AlCoCrFeNi alloy, a mix of a A2+B2 phases [33]. (a) SEM image of as-cast AlCoCrFeNi, Elemental maps of (b) dendritic (c) interdendritic regions, (d) Selected area diffraction pattern showing the A2+B2 dual-phase structure.

Preliminary investigations on the influence of the elaboration process and post-treatments have also been conducted. For instance, Uporov *et al.* investigated the influence of different thermal processing methods on the synthesis of the AlCoCrFeNi alloy. They studied as-cast, quenched (suction cast), slowly remelted (1600K and cooling with 5K/min) and homogenized (1400K for 50h) samples. All the samples exhibit a combination of FCC and BCC. The FCC is the main phase only in the homogenized samples; the authors supported another study's findings [34] which suggested that very long heat treatments (>100h) are required for HEAs to reach equilibrium [35]. Cieslak *et al.* compared the arc melting and the traditional hot uniaxial pressing (sintering) of AlxCoCrFeNi. The amount of FCC phase increased by lowering the Al content for both methods. After a 50h annealing at 1000°C, the FCC and BCC ratios are similar in both methods. However, the microstructures are different: the cast alloy presents dendritic regions and the sintered alloy shows large and regular grains. A sigma phase formed in the case of the sintered AlCoCrFeNi sample annealed at 1000°C [36].

Gangireddy *et al.* focused their work on the dual phase (FCC+BCC) microstructure. Arc-melted and thermomechanically processed $Al_{0.7}$CoCrFeNi alloys exhibit a BCC phase and an FCC phase. This alloy showed good mechanical properties due to a lamellar microstructure with many interphase boundaries. An ageing procedure leads to the formation of $L1_2$ precipitates which increase the yield strength, among other things [37]. Lee *et al.* focused their work on the impact of high temperature compression of the suction cast AlCoCrFeNi HEA. At 1100°C and

deformation from 0.055 to 0.7, a FCC phase is generated and this phase and the B2 phase grain sizes are intensely refined from several hundred microns to a few microns [38].

2.2.2. Solid route synthesis of AlCoCrFeNi

Most powder metallurgy elaboration of HEAs combines Mechanical Alloying (MA) via High Energy Ball Milling and consolidation (or sintering) via SPS [39,40]. Most of the HEBM devices used are planetary ball mills. This kind of mill consists of a rotating sun disk on top of which are placed rotating jars. The difference in speeds between the balls and grinding jars releases high dynamic energies. The final result is highly dependent on the milling parameters. In this chapter, they are noted as 'speed of the disc (rpm)'/'relative speed of the jar (rpm)'/'duration'/'ball to powder mass ratio'/'process control agent' e.g., 250/-500/30h/15:1/N-heptane. Process Control Agents are surfactants used during milling in order to modify the balance between cold welding and fracturing [41]. In practical terms, PCA are often used to prevent excessive agglomeration and oxidation. As PCA are organic liquids, resulting contamination is inevitable.

Ji *et al.* focused on the evolution of the microstructure with annealing and sintering of the AlCoCrFeNi composition. After a 250/-500/30h/15:1/N-heptane treatment, they obtained one single BCC phase agglomerate (Fig. 5). They report the formation of an FCC phase after annealing above 500°C for 1h and the complete transformation from BCC to FCC at 900°C. Spark Plasma sintering at 900°C for 10 min, however, leads to the coexistence of an FCC and a BCC phase [42].

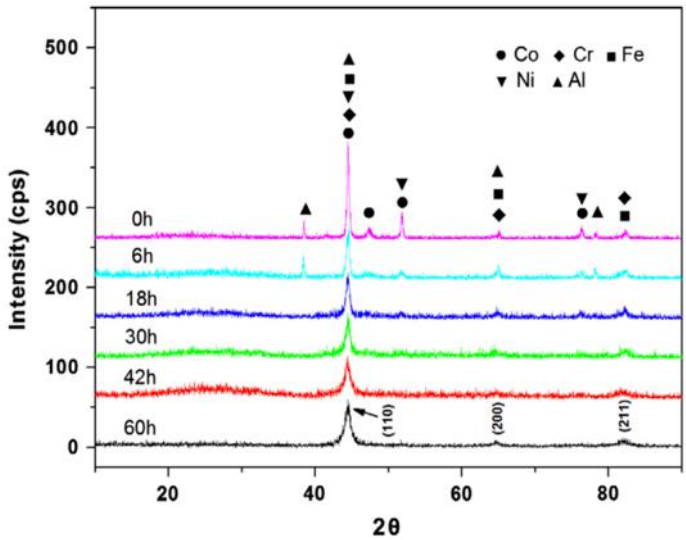

Figure 6: XRD of AlCoCrFeNi with different milling times. These diffractograms show the disappearance of the FCC phase with milling time [42].

Mohanty *et al.* investigated the mechanical properties of sintered AlCoCrFeNi alloy. After a 200/-400/60h/20:1/none treatment, they obtained FCC and BCC solid solutions. After a sintering step between 973 and 1273K, the alloy exhibits an Al-Ni rich $L1_2$ phase, a sigma phase and a Cr-Fe-Co rich FCC phase. TEM analysis revealed that the $L1_2$ may form from the

decomposition of the supersaturated BCC solution obtained during the milling step. The authors suggested that the sigma phase was responsible for the high level of hardness and helped the densification process [43].
Colombini *et al.* investigated field assisted powder metallurgy routes (namely SPS and microwave heating) for producing AlCoCrFeNi. They studied mechanically activated (250/-500/3x20min/10:1/none) and mechanically alloyed powders (250/-500/35h/10:1). The MA step did not lead to the complete disappearance of the FCC phase. Both the mechanically activated powders and the MA ones exhibit an FCC+BCC phase after a 1000°C Spark Plasma sintering. A post heat treatment at 1200°C caused the BCC phase to transform into FCC, but only in the case of the MA powders. However, two nuances are observed: an Al-Ni rich one and a Fe-Cr one [44].

Zhang *et al.* tried to sinter AlCoCrFeNi starting from pure metal powders (average particle size of 45 μm). They only mixed the blended powders in a mechanical mixer for 5h. There were no signs of MA after the mixing step. They report the formation of an FCC phase and BCC phases (A2+B2) after a 1200°C Spark Plasma Sintering (Fig. 6). The alloy exhibits interesting mechanical properties (see Table 1) which may be due to the effective combination of the FCC and the BCC phases [45].

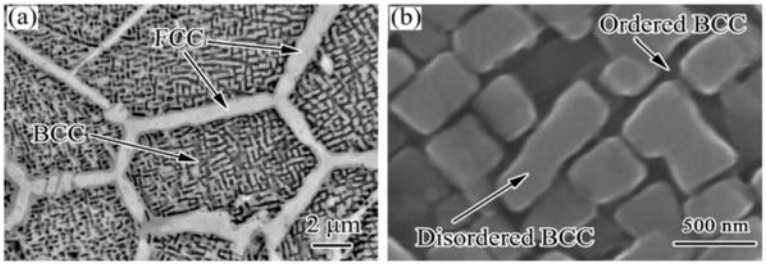

Figure 7: SEM pictures of the microstructure of pure metal powder sintered at 1200°C [45]. (a) BSE contrast, (b) SE contrast of the BCC phase.

Thanks to these findings, we note that the MA step leads either to the formation of a single BCC phase and or to the coexistence of an FCC and a BCC phase inside the agglomerates. In addition, the sintering always leads to the formation of an FCC phase. More complex phases such as sigma or ordered FCC ($L1_2$) may also form after heating. Table 1 summarizes the phases observed after different routes and treatments.

	Liquid route synthesis			Solid route synthesis		
Routes / Treatments	Arc-melting	Annealing > 600°C	Annealing > 1200°C [31]	Milling	Sintering > 600°C	Annealing > 1200°C [44]
Phases formed	A2+B2	+ FCC (+ sigma)	- FCC (- sigma)	A2(+FCC)	+ FCC (+ sigma) (+ $L1_2$)	- A2

Table 1: Summary of phases formed after different routes and treatments.

2.2.3. *Some AlCoCrFeNi properties*

Butler *et al.* investigated high temperature oxidation behaviors of arc melted $Al_xCoCrFeNi$ HE alloys. Low Al HEAs are found to be mainly FCC and the transition occurs at around 15 at. %. During oxidation at 1050°C under ambient laboratory air, a combination of Al_2O_3 and AlN formed beneath an external Cr_2O_3 scale (Fig. 7) [46].

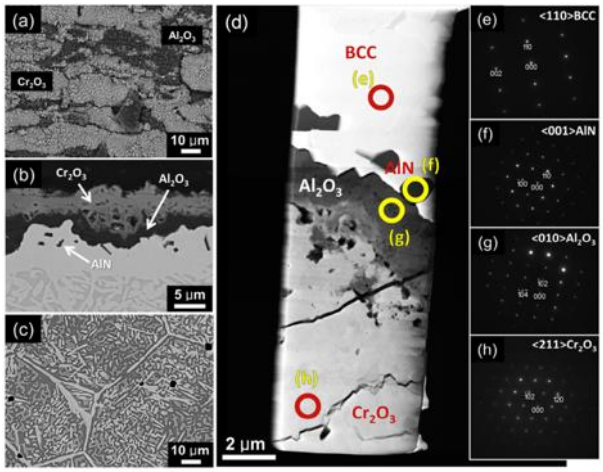

Figure 8: SEM pictures and TEM analysis showing the evolution of the AlCoCrFeNi alloy under aggressive atmosphere and high temperature [46]. (a) Plan-view, cross-sectional and internal SEM images (BSE) of the sample. (d) TEM observation and (e-h) corresponding SADPs.

On average, melted AlCoCrFeNi exhibits better mechanical properties than the more classic counterparts, such as M-Cr-Al alloys. Sintered (nanocrystalline and more polluted) HEAs exhibit even better properties. Table 2 summarizes some data concerning mechanical properties. Another, similar table can be found in [31].

		Hardness (HV)	Yield strength (MPa)	Ultimate tensile strength (MPa)	Strain (%)	Fracture toughness ($MPa.m^{1/2}$)	Observations
Liquid route	[28]		1251	2004	32.7		B2 (+A2?)
	[31]	510	1380	2065	10		As-cast value, A2+B2
			1450	2500	20.1		Annealed at 1200°C, A2+B2+residual FCC
	[33]		1384	1912	16.7		
Solid route	[43]	816				3.9	$L1_2$ precipitates
	[45]	518	1262				
	[42]	625		1907	11.3		
	[44]	450					Single FCC

Table 2: Summary of mechanical properties of the equimolar AlCoCrFeNi alloy.

2.3. Drawbacks of the AlCoCrFeNi composition

There are other, unwanted phases. These may be formed as a result of the composition or the powder metallurgy process. In the following paragraph, we will overview what phases are likely to appear and how they form.

2.3.1. The Sigma phase

As has been noted in the previous section concerning composition, an intermetallic Cr-rich quadratic phase: sigma (σ), often forms.

Zhu *et al.* investigated the effect of annealing on the phase stability of $(FeNiCrMn)_{(100-x)}Co_x$. The alloys were prepared by arc-melting and the annealing was carried out at 850°C. They found that the sigma phase formed for the low Co contents (5 and 10 at. %) and not for the higher one (20 at. %). The sigma chemical composition was close to at. %: Cr 45, Fe 20, Mn 15, Co 10, Ni 10 [47].

Tsai *et al.* suggested effective criteria to predict the formation of the sigma phase using a method based on the valence electron concentration (VEC) of the composition. They fabricated 32 HEAs and studied their phase composition. They introduced the concept of PSFE (paired sigma-forming element) which principally involves the enumeration of sigma-forming elements such as Cr, Mo, V and their affinity with other sigma-forming elements present in the alloy composition. They found that PSFE completes the initial VEC criterion (fig. 9.) [48,49]. The composition AlCoCrFeNi has a VEC of 7.2 and a PSFE of 40% and therefore is likely to exhibit a sigma phase.

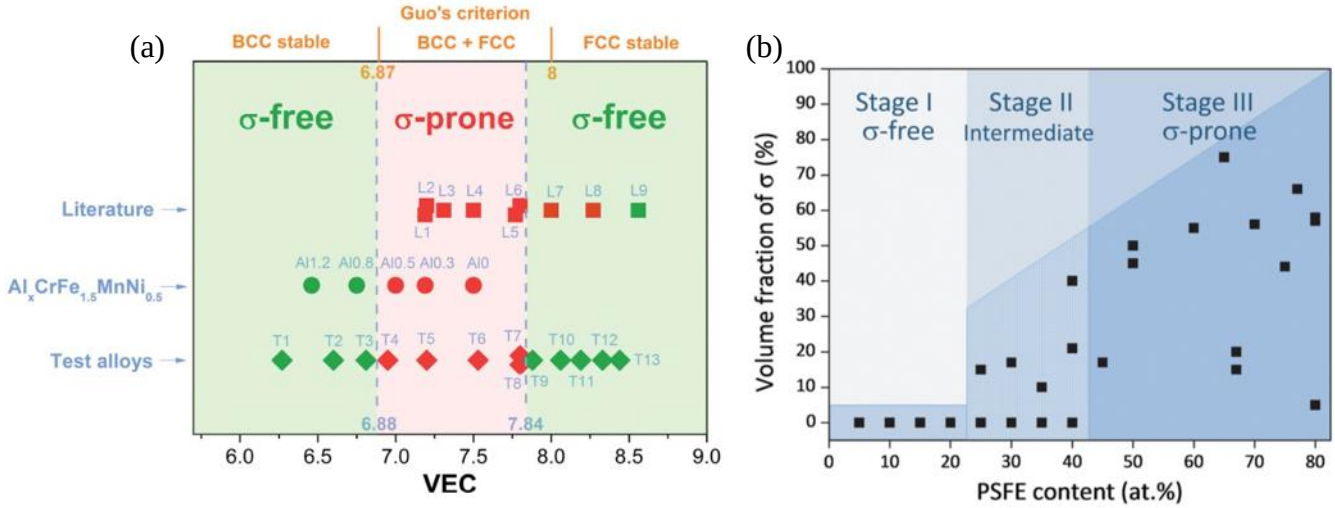

Figure 9: Stability domain of the sigma phase with Tsai's criteria [48,49]. (a) Relationship between the VEC and the presence of sigma after aging, (b) PSFE content and sigma phase volume fraction.

Zhang *et al.* suggested that the formation of a nanoscale sigma phase could be beneficial. A non-equiatomic CoCrNiAlW high entropy alloy was prepared by arc melting and thermomechanical procedures and exhibited an FCC matrix and nanoscale σ particles. The alloy showed extremely good mechanical features due to the interactions between the σ particles, deformation twins and dislocations [50].

2.3.2. Carbides and oxides

This composition, containing Al and Cr, is prone to oxide and carbide formation. However, carbides and oxides are primarily formed because of the process rather than the composition. Indeed, during milling, Process Control Agents are often a significant source of contamination. In addition, since SPS dies are made of graphite, carbides are often formed in Spark Plasma Sintered alloys. This is also the case for HEAs prepared by SPS. The topic of contamination, as well as the recent, analogous and trendy topic of oxide dispersed high entropy alloys, will be meticulously covered in Chapter V. The following paragraph aims to give a brief overview of the problematic.

Moravcik *et al.* reported the observation of oxides formed in sintered HEAs. Their work focused on the heat treatment of the sintered $AlCoCrFeNiTi_{0.5}$. After a MA+SPS preparation (250/-500/24h/10:1/-), they observed Al_2O_3 nanocrystallites with TEM, which were not observable in XRD (fig. 11). The authors suggested that the nano-oxides could come from air exposure before the elaboration or from the PCA (methanol) [51].

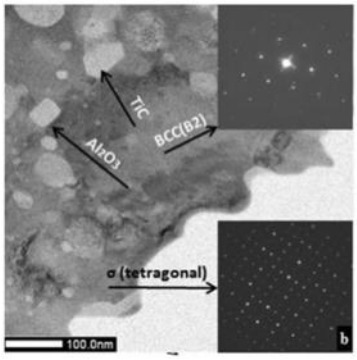

Figure 10: TEM results on Spark Plasma Sintered $AlCoCrFeNiTi_{0.5}$, showing Aluminum oxides [51].

The effects of different PCAs (namely: methanol, n-heptane and stearic acid) on particle features were investigated by Ruiz-Esparza-Rodríguez *et al.* in the case of $Al_xCoCrFeMnNi$ high-entropy powders. They used a SPEX shaker mill to perform their study, demonstrating that PCA chemical decomposition generated residual oxygen and carbon in the powders. They also showed that particle size distribution and microstructure were highly dependent on PCA properties such as vapor pressure [52].

Joo *et al.* studied, among other things, the effect of contamination on the microstructure of sintered CoCrFeMnNi. They used very high milling parameters 1100/-/20min/10:1/- with ZrO_2 balls and SPS. They observed the formation of $Cr_{23}C_6$ after sintering at 900°C and Cr_7C_3 at 1100°C. They found that a longer milling (1h) hinders the formation of carbides. To explain this finding, the authors suggested that phase stability was higher, thus limiting carbide formation. The distribution of carbides showed that the carbon came from the SPS graphite mold (fig. 10) [53].

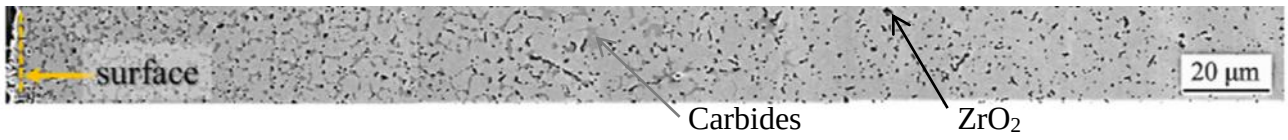

Figure 11: SEM pictures (BSE) of milled (1100°C/-/20min/10:1/-) and Spark Plasma Sintered (1100°C) HEA cross section. The carbides are more abundant to the left (surface of the sample) [53].

3. Powder Metallurgy preparation of High Entropy Alloys

3.1. Mechanical milling concepts

Mechanical milling and relative concepts will also be detailed in the introductions of Chapters II and III.

The main mill used for MA is a planetary ball mill. LeBrun *et al.* tried to investigate the ball trajectory in order to predict milling modes. They developed a theoretical approach based on kinetic equations. Several hypotheses were formulated: the ball is considered as a point mass (so friction is not treated), the force of gravity is neglected and there is only one ball. They found 3 regimes as a function of K (ratio between the speed of the main disk Ω and of the jars ω, $K^1 = \omega/\Omega$): chaotic for low K where the ball trajectory is not described; impact + friction for medium K where the ball leaves the wall, flies across the jar and impacts the wall on the other side; friction for high K where the ball never leaves the wall (fig. 12). The authors also carried out in-situ observations of milling and the impact+friction mode was never observed [54].

Abdellaoui and Gaffet developed their own model of planetary ball milling based on a kinematic approach (very close to that of LeBrun). They suggested that injected shock power alone was responsible for powder transformation. Their suggestion, although questionable considering the in-situ observations presented later, is a very common point of view even to this day [55].

[1] The definition of K varies depending on the source and it is not always clear which definition is used. It is sometimes defined as $K_2 = \omega/\Omega - 1$.

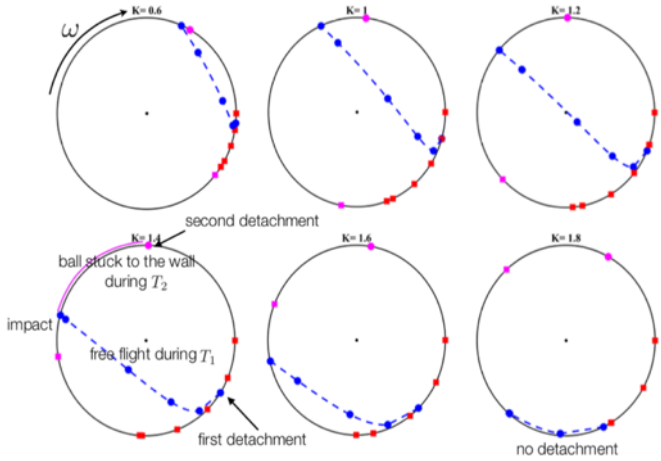

Figure 12: Schematic representation of ball motion depending on K values according Abdellaoui and Gaffet model.

Rosenkranz *et al.* performed in-situ observations of ball motion during planetary ball milling. They investigated the influence of the speed ratio, the ball filling ratio and the friction conditions (by trying different powder types). They investigated the effect of K_2 from 1 to 3 and observed no difference in ball motion; in all cases the regime was cascading. This result can be explained by the absence of mill feed. Friction was demonstrated to have a tremendous effect and thus invalidated previous kinetic models. The Discrete Element Model was used to model the milling and the results are in agreement with in-situ observations [56].

Rogachev *et al.* also performed in-situ observations of the ball motion by means of high-speed video recording. Their study confirms the findings reported by Rosenkranz. Three milling regimes were identified (depending on the speed ratio K_2): cascading (K_2=1), cataracting ($1.5<K_2<1.9$) and centrifugal ($K_2 \geq 2$) (fig. 13). The authors concluded that shear deformation was the key player in microstructure transformation and thus that the cascading regime was the most effective [57].

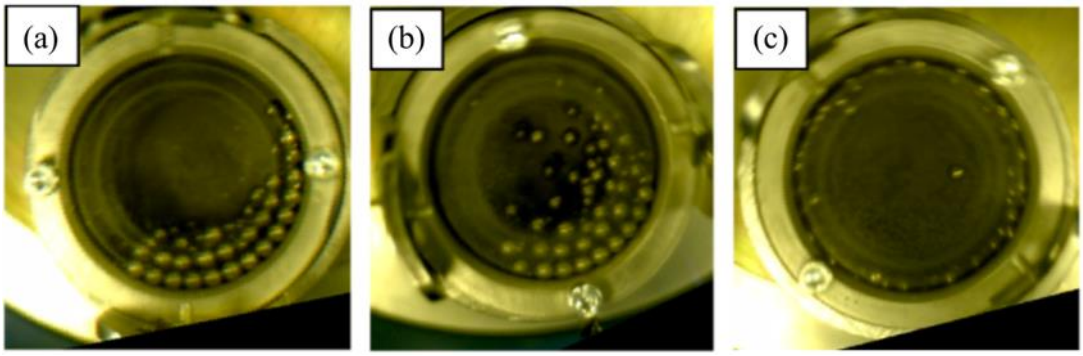

Figure 13: In-situ observations of instant ball distribution in the grinding jar depending on K_2 values. K_2=1, cascading regime (a), 1.8, cataracting regime (b) and 2.0, centrifugal regime (c) [57].

3.2. Milling of HEAs

The milling of HEAs, and especially the comparison between Mechanical Alloying and Mechanical Activation of HEAs, will also be covered in Chapters IV and V.

Varalakshmi *et al.* (Prof. Murty's group) were the first to synthesize HEA solid solution by Mechanical Alloying. They milled different compositions from AlFe to AlFeTiCrZnCu at 300/-600/20h/10:1/toluene. They assessed the formation of solid solution by XRD analysis only (disappearance of elemental peaks). They always obtained a single BCC phase at the end and the crystallite size was around 10 nm. After sintering at 800°C, the material was still only BCC, 99% dense and exhibited a hardness of 200 HV [5].

Sriharitha *et al.* reported the influence of Al on the $Al_xCoCrCuFeNi$ system during milling (-/-/20h/-/toluene) and on the thermal stability of the milled powders. Low content systems exhibit two FCC phases and a BCC phase. High content Al alloys exhibit a B2 phase only (Al thus showing the same BCC stabilizing trend as in casting). DSC measurements revealed that the FCC phases were Fe-Ni rich and Cu-Ni rich. The milled powders were nanocrystalline (10 nm) and remained so after DSC (~70 min). The authors also demonstrated that Zhang's empirical criteria [10] are unable to predict the phase formed by MA [58].

Yang *et al.* fabricated AlCoCrFeNi HEA using metallic glasses as precursors. They milled commercial elemental powders until they reached nearly 100% amorphous phase (as seen in XRD). The authors do not provide any details about the milling parameters they used. Then they "sintered" the powders at 1523K (85% of Fe melting temperature). They measured the crystallization temperature T_x at 926K and the glass transition temperature T_g at 782K by DSC (fig. 14). The bulk material exhibits two BCC phases, both composed of matrix + precipitates. One exhibited an Al-Ni rich matrix and Cr-Fe rich precipitates and the second one the other way around. The HEA exhibits ultra-high fracture strength and excellent ductility (measured by compression test) [59].

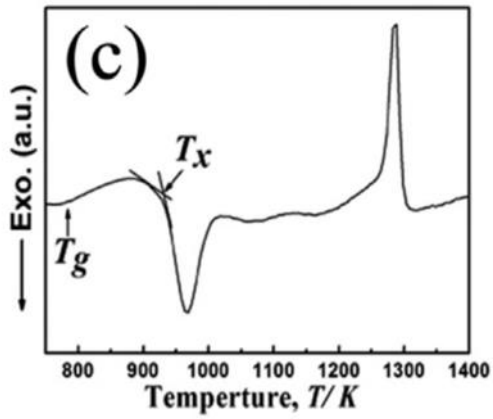

Figure 14: DSC curve of the amorphous HEA powder at a heating rate of 20 K min^{-1} [59]. This measurement gives the value of the temperature of crystallization Tx and of the glass transition temperature Tg.

Portnoi *et al.* focused their work on the reaction steps during milling (mechanochemical synthesis). They worked on the AlCoCrFeNiTi system and they used a rather high-energy milling (Fritsch P7/8:1/-). They studied the amorphisation rate of their system and found that an amorphous phase already begins to form after 4h. In the early stage, an ordered phase formed but then disappeared and the initial hcp-Cobalt transformed into fcc-Co. The remainder of the powders exhibits a BCC structure. 25h milling led to the transformation of 90% of the powders to the amorphous phase. Heating up to 1200°C revealed the formation of B2 at 450°C, the formation of $L1_2$ at 650°C (mainly due to the Ti) and of a sigma phase at 850°C [60].

Alcalá *et al.* studied the effect of milling time and Al content on the microstructure of FeCoNiCrMn(Al) HEAs prepared by a pressureless sintering. They used high milling parameters 600/-600/14h/18:1/NaCl and were original in their choice of NaCl as PCA. They verified the formation of the single FCC solid solution by a statistical analysis of the XRD peaks. They measured the skewness and the kurtosis (assuming that the XRD peaks were described by a Gaussian function) and observed that the skewness decreased with milling time. Such an approach is rather uncommon, especially since XRD peaks are rarely described by a Gaussian function but rather by a Voigt function, for instance. The use of NaCl seems to result in a decrease in the size of agglomerates. However, the elimination of Na and Cl atoms from inside the metallic powder is not clearly demonstrated. The sintering between 1200°C and 1400°C led to relative densities of between 82 and 92% and hardness up to 305 HV. Increasing Al content favored Cr segregation and the formation of a Cr-Mn rich phase [61].

Vaidya *et al.* introduced sequential alloying, i.e., adding elemental powders one by one to attain the AlCoCrFeNi composition during milling with WC balls (fig. 14). They used rather standard milling parameters 300/-600/20h-70h/10:1/toluene and first compared pre-milled nanocrystalline and as-received microcrystalline powders. Alloying kinetics proved faster in the case of pre-milled powders. Indeed, elemental XRD peaks disappear after shorter milling times in the case of nanosized crystallites (pre-milled powders). However, traces of WC are found in the case of Cr. The authors made several valuable observations concerning the role of each element during milling: Al and Cr heavily favor a BCC phase whereas Co, Fe and Ni tend to favor an FCC phase. The authors noted that Co is slower to dissolve due to its hcp structure. They also suggested that during the milling of the 5 elements, the FCC would be FeNi at first and then the other elements would dissolve into this matrix [62].

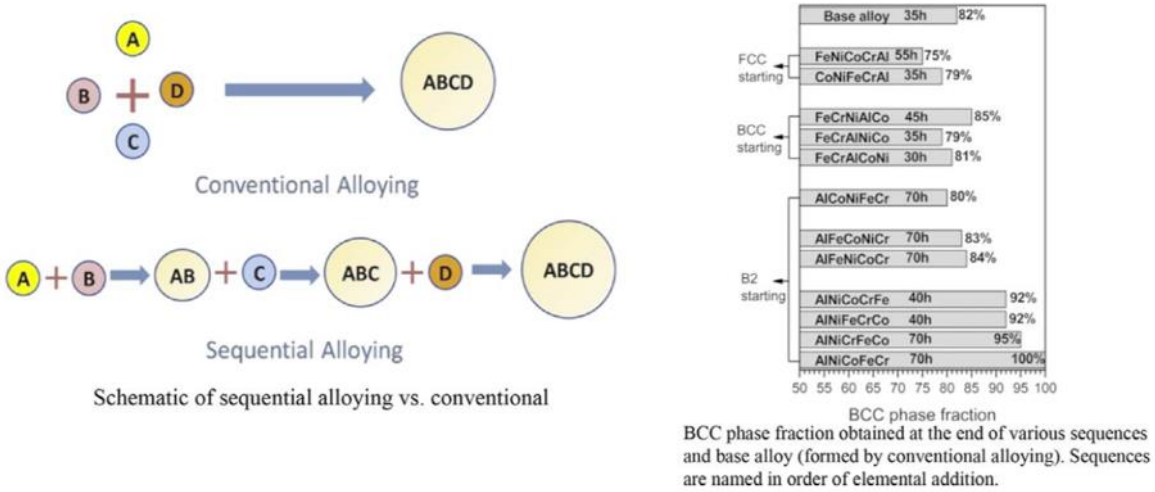

Schematic of sequential alloying vs. conventional

BCC phase fraction obtained at the end of various sequences and base alloy (formed by conventional alloying). Sequences are named in order of elemental addition.

Figure 15: Graphic abstract from Vaidya *et al.* concerning sequential alloying [62].

Ang *et al.* used mechanical alloying followed by plasma spraying for AlCoCrFeNi and MnCoCrFeNi. They milled at 300/-600/10h/10:1/toluene and obtained a mixture of FCC and BCC for both the Al-alloy and Mn-alloy. Al is confirmed here to be a BCC stabilizer, as the BCC phase is more abundant in the case of the AlCoCrFeNi composition. The average particle size (in volume) for the Al-alloy is approximately 15 µm. The major phase of the sprayed Al-alloy is FCC; it has been reported elsewhere that a higher content of Al was necessary to reach BCC majority in laser-clad coatings (in the case of $Al_xFeCoNiCuCr$). Some oxides formed during spraying, which appeared to be Al_2MO_4 ($M=Cr_{0,5}+Fe_{0,5}$) [63].

Praveen *et al.* investigated the densification behavior in regard to the phase evolution of several MA HEAs ($Co_xCr_xCu_xFe_xNi$). These researchers milled at 300/-600/15h/10:1/toluene and obtained mixtures of FCC and BCC, except in the case of the system without Cr which was FCC only. In the case of CrCoFeNi, they observed the progressive shifting of the (200) FCC during milling (Fig. 17). They suggested that this behavior resulted from the formation of a new Fe-based FCC phase instead of the dissolution of other elements into the Ni matrix. Indeed, in this case, all 4 elements have very similar atomic radii but the main peak of γ-Fe (which is FCC) is close to 43.7° 2θ [64].

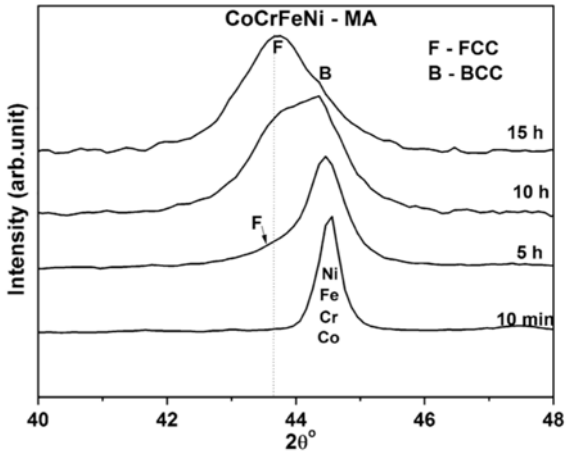

Figure 16: XRD of the CoCrFeNi alloys with different milling times. These diffractograms show the "shifting" of the FCC phase with milling [64].

The influence of the pre-milling of Ni and Cr prior to the milling of CoFe(CrNi)Mn was investigated by Suprianto and Chen. They attempted to form a stable solid solution in order to hinder the formation of Cr oxide during the PM route. The milling parameters were 300/-600/8h+16h/10:1/stearic acid. They found that pre-milling promotes the formation of nanostructured Ni-Cr particles which favor the nucleation of nano-oxide during sintering. However, they suggested that the final amount of oxides would seem to be of a lesser magnitude compared to regular milling [65].

A comparison between a SPEX shaker mill and a planetary ball mill was performed by Stasiak *et al*. They worked with the uncommon composition AlCrFeMnMo. The planetary ball mill parameters were 300/-600/70h/10:1/stearic acid and the SPEX shaker mill parameter was 18 Hz. Judging from the resulting powder features, they suggested that use of the SPEX shaker mill led to higher energy shocks compared to the planetary ball mill. They concluded that homogeneity and contamination increased as a function of shock energy and suggested optimized milling parameters involving the combination of the two mills [66].

A thorough comparison between the PM and casting routes was initiated by Moravcikova-Gouvea *et al.* They produced the $Al_{0.2}Co_{1.5}CrFeNi_{1.5}Ti$ high-entropy alloy and demonstrated that the PM route has a tendency to form carbides because of process control agents they deemed essential to the process. As a result, the PM alloy exhibited a fine-grained microstructure composed mostly of FCC, whereas the cast HEA exhibited a coarse-grained microstructure containing an FCC matrix, a BCC phase and a mixture of complex intermetallic phases including σ. They suggested that the formation of intermetallics was inhibited in the case of the PM route thanks to the rapid heating and cooling of the SPS [67].

3.3. Spark Plasma Reactive Sintering

Reactive sintering can be very interesting for certain syntheses. These syntheses often concern drastic crystalline and exothermic transformations such as the formation of intermetallics starting from elemental powders. Nonetheless, this terminology can also be used in the case of the formation of a multi-component solid solution during sintering. Some studies addressing the reactive sintering problematic are thus of interest here.

Orrù *et al.* formed $MoSi_2$ by Spark Plasma reactive sintering starting from Mo and Si powders which were milled separately, co-milled and non-milled. The reaction is Mo(BCC)+Si(Diamond)=$MoSi_2$(tetragonal). The co-milling of the powders was not supposed to correspond to mechanical alloying but was nevertheless very powerful and comparable to parameters chosen to carry out MA: 300/-600/9h/21:1/None. They obtained traces of $MoSi_2$ and a mixture of pure Si (very low crystallinity) and pure Mo. Nanocrystalline $MoSi_2$ was formed during sintering only in the case of co-milled powders [68].

Paris *et al.* formed an AlFe intermetallic by mechanical activation + SPS. The reaction is Al(FCC)+Fe(BCC)=AlFe(B2). The milling parameters were 150/-350/4h/7:1/None. They obtained mostly composite Al-Fe agglomerates (Fig. 15) and some regions seem to be mechanically alloyed. The authors found that the mechanically alloyed phases act as heterogeneous nucleation sites and favored the formation of the desired phase during sintering [69,70].

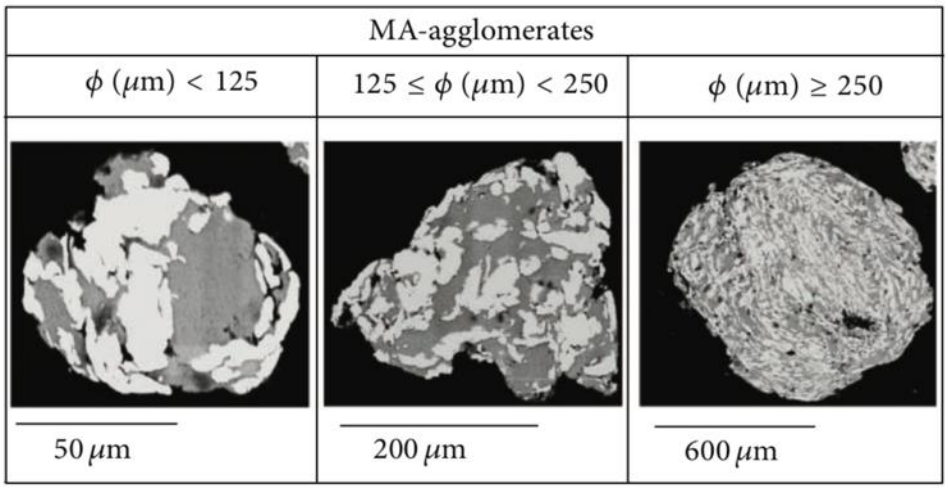

Figure 17: SEM pictures (BSE) of three classes of Al-Fe agglomerates obtained by Paris *et al.* [70]. Bright zones correspond to Fe and dark ones to Al.

3.4. Spark Plasma Sintering of HEAs

As has been noted, the sintering step is often viewed as secondary compared to the milling step. As a consequence, few articles concentrate on the sintering mechanism of HEAs.

In their first study, Mane and Panigrahi investigated the sintering mechanism of the CoCrFeNi alloy. They compared as-milled (300/-600/15/15:1/toluene) and milled+annealed powders (1100°C). The authors said that the milled powders exhibit FCC+BCC+sigma whereas annealed powders exhibit FCC+sigma. Annealed powders seem to have a higher activation energy. The authors suggested that the milled powders presented a mixed response: grain boundary diffusion + volume diffusion whereas single phase annealed powders were sintered mainly by volume diffusion [71,72].

In their second study, Mane and Panigrahi studied densification behaviors as a function of alloying order. They studied as-milled CoFeNi (3E), CoFeNiCr (4E), CoFeNiCrMn (5E) and CoFeNiCrMnAl (6E) sintered by means of a dilatometer. CoFeNiCrMnAl powders exhibited BCC+FCC whereas all the other powders and sintered samples exhibited mostly FCC. The authors found that sinterability decreases with the number of elements (Fig. 16) [73].

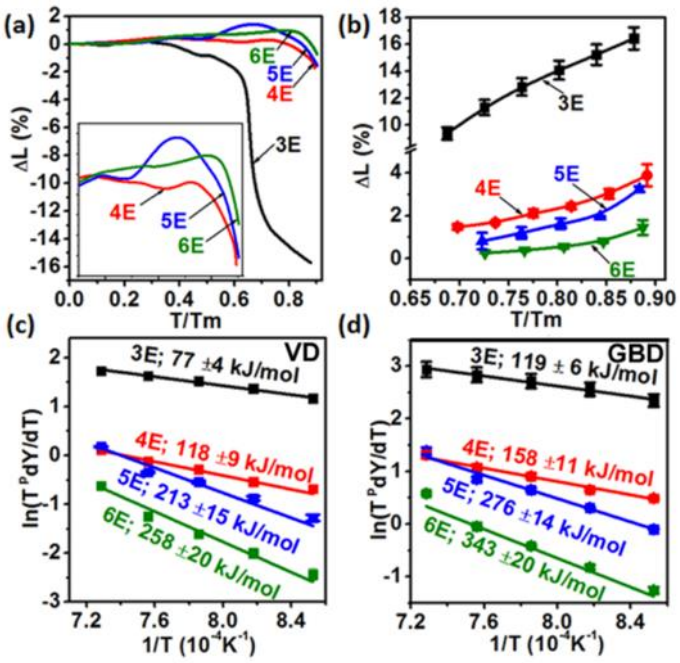

Figure 18: Dilatometer curves as a function of homologous temperature (a), Measured shrinkage as a function of homologous temperature (b), Arrhenius plots for volume diffusion (c) and grain boundary diffusion (d) [73]. The homologous temperature being T/Tm (Tm: melting temperature measured by DSC)

Praveen *et al.* investigated densification behavior in regard to the phase evolution of several MA HEAs ($Co_xCr_xCu_xFe_xNi$). Concerning the sintering mechanism (by SPS), they observed a delayed densification in the case of CrCrFeNi and linked this observation to the transformation of the BCC phase into the sigma phase at 550°C. They concluded that the sigma phase played a major role in nanosize retention and high hardness [64].

4. Molecular Dynamics simulations of multi-component solid solutions

One of the main challenges of Molecular Dynamics simulation is to have access to a proper potential. The works presented below tackle this issue: simulations with numerous metallic elements or HEAs.

When we began the present work in 2017, the only interatomic potential database available to simulate a complex mixture of many metals was proposed by Zhou. Interatomic interactions were fitted by an Embedded Atom potential (EAM) and normalized for certain pure metals: Cu, Ag, Au, Ni, Pd, Pt, Al, Pb, Fe, Mo, Ta, W, Mg, Co, Ti, and Zr. The cross-potential for multi-component systems is obtained by a simple rule based on weighted averages of elemental components. The mechanical properties of a wide range of single metallic elements are correctly described, including those of Al, Co, Fe, Ni. In their article, Zhou *et al.* studied vapor-deposited NiFe/CoFe/Cu multilayers and found that edge dislocations were formed and increased the mismatch strain energy [74]. Later, Lin *et al.* published a potential for Cr which is compatible with the Zhou formulation [75]. The main drawback of the Zhou potential is the lack of optimization for binary or higher order compounds.

In 2018, Choi *et al.* developed a second nearest-neighbor modified embedded atom method (2NN MEAM) potential for the CoCrFeNiMn system. This kind of potential requires parameters for unary, binary and ternary systems involved in the quinary. They completed the missing ternary systems and used this potential to suggest that the large number of vacant sites with high migration energy barriers was the reason for sluggish diffusion [76].

More recently, Farkas and Caro developed several sets of EAM interatomic potentials to represent HEAs. However, they labeled their potentials “toy model” potentials since they are not designed to precisely model all kinds of HEAs, but only to depict FCC FeNiCrCoCu or FCC $Al_x(CoCrFeNi)_{1-x}$. At the same time, they argue that this approach captures some of the most relevant features of multi-component alloys. They found that static distortion magnitudes are in agreement with calculations based on size differences. They concluded that Molecular Dynamics is particularly useful in that case because it shows that individual atoms are subjected to very high atomic strains and that stress has a significant effect on mechanical properties. In addition, since stacking value relies on local configuration, large variations are observed and they impact dislocation behavior [77,78]. Interestingly enough, the set of potentials concerning $Al_x(CoCrFeNi)_{1-x}$ seems to be able to predict $L1_2$ and B2 phases in agreement with experimental results. In addition, they showed that the lattice parameter of the FCC $Al_x(CoCrFeNi)_{1-x}$ phase increased linearly with the Al content [79].

Molecular Dynamics simulation of refractory High Entropy Alloys has also increasingly attracted attention. This attention is evidenced by the growing number of interatomic potentials recently developed to consider these systems, including TaHfZrTi [80], HfNbTaZr [81] or NbMoTaW [82]. These studies focused on chemical SRO and strengthening mechanisms.

Other works use the aforementioned developed interatomic potentials to investigate the behavior of multi-elementary solid solutions. For instance, Anand *et al.* generated dozens of configurations of some five element compositions by means of a genetic algorithm, ensuring that the energy of these configurations followed a Maxwell-Boltzmann distribution. Then, they measured the thermodynamic parameters such as enthalpy using Molecular Dynamics and the Zhou potential. The authors showed that the stability of FCC over BCC (or vice versa) was indeed due to the configurational entropy. In addition, they suggested that the minor presence of an FCC phase in the AlCoCrFeNi composition was caused by the variation in configurational entropy with temperature [83].

The dislocation mechanism and grain boundary mobility of multi-principal element alloys are increasingly common focuses in MD simulations in the field of High Entropy Alloys. For instance, the BCC $Co_{16.67}Fe_{36.67}Ni_{16.67}Ti_{30}$ composition was simulated using the Zhou potential. The comparison between this alloy and a standard BCC alloy demonstrated that local variation in composition hindered dislocation motion [84]. On the contrary, local chemical fluctuations were demonstrated to play a minor role in the migration behavior of a symmetrical tilt grain boundary in a 4-component CuNiCoFe FCC high-entropy alloy. However, a hypothesis explaining the reduced grain growth in FCC HEAs (c.f. sluggish diffusion) resulted from this study. Indeed, grain boundary migration seems to be suppressed by the inevitable segregation occurring at the grain boundary [85].

Interestingly, Deluigi et *al.* investigated the radiation resistance of FeNiCrCoCu. Among other things, they compared this High Entropy composition to pure Ni and confirmed that HEAs may exhibit enhanced radiation resistance. However, the mechanisms responsible for this interesting feature are yet to be thoroughly studied [86].

The evaluation of the influence of the elaboration process on High Entropy Alloy behavior is still a niche concern. However, Xie *et al.* studied the AlCoCrCuFeNi HEA film growth on a silicon substrate by DM using the Zhou potential. They observed that the final crystallinity

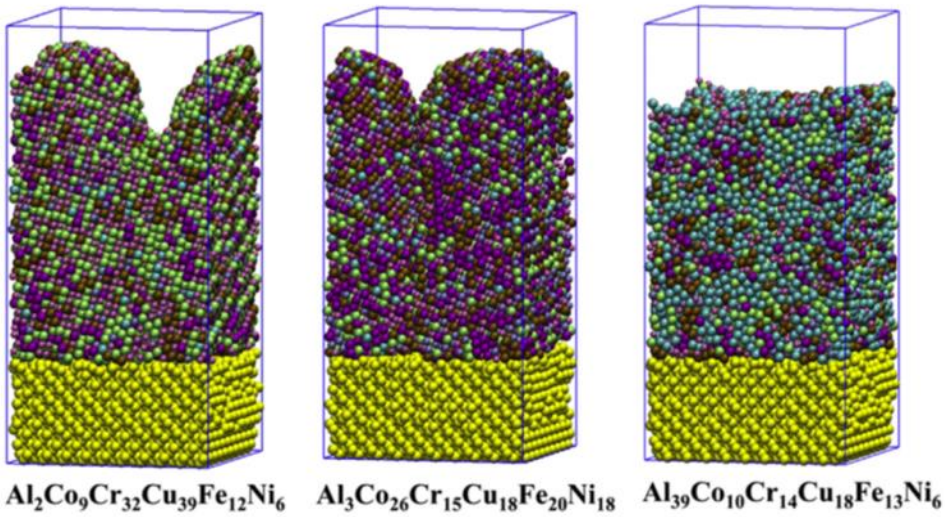

Figure 19: Snapshots of HEA films deposited on Si substrate [87].

depended on the Al content: indeed, low Al content led to a crystalline structure whereas high Al content led to bulk metallic glass (Fig. 17). The authors concluded that DM results were in agreement with Zhang's criterion (see section 1) [87].

Conclusion

The idea of exploring the center of multi-dimensional phase diagrams emerged in Oxford and Taiwan at the same time, naturally embodying the next step forward in Metallurgy. The concept of the High Entropy Alloy, based on a multi-component disordered solid solution, is very recent but very promising. Materials scientists quickly realized the potential revolution in the initial concept and have already generalized it to a broader topic: Complex Concentrated Alloys (CCA) or Multi-Principal Element Alloys (MPEA), alloys with no obvious base element.
Indeed, the High Entropy approach could be considered reductive. The basic core effects, such as sluggish diffusion, have not yet resulted in consensus in the research community. In addition, recent articles suggest that introducing precipitates into the high entropy solid solution could enhance mechanical properties. Both the concept of High Entropy and the requirement of a single disordered solution are being extended to involve a larger class of alloys.

We have seen throughout this chapter that numerous angles of approach exist. These include alloy design, mechanical properties, influence of the elaboration method – to name but a few. However, these approaches principally involve short studies leading to easy publications. Indeed, evaluating the microstructure of one of the thousands of potential systems never treated elsewhere is the core of almost every article on HEAs. In addition, the evaluation of mechanical properties is often reduced to quick and simple compression tests. Today, basic studies about alloy durability are lacking, as is research into high temperature oxidation resistance, corrosion resistance, thermal stability and fatigue behavior.

Concerning the AlCoCrFeNi alloy, which is among the top 5 most studied HEAs, this chapter has shown that a very wide range of microstructures has been reported. The thermal stability of the microstructure is an essential issue that must be systematically investigated. Another important parameter leading to the large number of microstructures could be the presence of impurities, such as oxygen, carbon or azote, and yet almost no work strictly reports the amount of these unwanted elements.

Recently, the Calphad method seems to have replaced the empirical criteria which held sway in the first studies on HEAs. This method results in efficient alloy design and confirms that equilibrium has been reached. The ThermoCalc software has proven to be a powerful tool in the High Entropy Alloy domain. It is now essential to use this kind of software in order to have an idea of what kind of microstructure the alloy may have and to identify the discrepancies--that is, to assess one's results.

The vast majority of HEAs are elaborated by means of a melting-related method. The Powder Metallurgy route appears to be an interesting alternative. The Indian group led by Prof. Murty

seems to heavily dominate the subject. Nonetheless, there are few high-quality articles about how the sintering of a 5-element system occurs, and few articles about variants of MA+simple densification. In addition, this chapter has highlighted the lack of consensus on the first step (MA) mechanism. Indeed, High Energy Ball Milling modeling seems outdated and new techniques, such as the Discrete Element Method or Molecular Dynamics, are poised to provide new answers.

Finally, simulation studies are rare in the HEA field. We have seen that the main reason for this is the lack of adequate multi-element interatomic potentials. However, inaccurate understanding of some nanoscale mechanisms could be corrected by using slightly flawed potentials or model alloys mimicking HEA features. Considering these last two points, atomistic analysis of the milling process is an appropriate undertaking.
This chapter has identified a number of gaps in the research field of HEAs. In response, this thesis will focus on the influence of one of the powder metallurgy route variants: mechanical activation. This work will also address issues lacking in existing studies such as the thermal stability of HEAs, the evaluation of impurities, and multi-scale modelling.

References

[1] J.-W. Yeh, S.-K. Chen, S.-J. Lin, J.-Y. Gan, T.-S. Chin, T.-T. Shun, C.-H. Tsau, S.-Y. Chang, Nanostructured High-Entropy Alloys with Multiple Principal Elements: Novel Alloy Design Concepts and Outcomes, Adv. Eng. Mater. 6 (2004) 299–303. https://doi.org/10.1002/adem.200300567.

[2] B. Cantor, I.T.H. Chang, P. Knight, A.J.B. Vincent, Microstructural development in equiatomic multicomponent alloys, Mater. Sci. Eng. A. 375–377 (2004) 213–218. https://doi.org/10.1016/j.msea.2003.10.257.

[3] X. Fu, C.A. Schuh, E.A. Olivetti, Materials selection considerations for high entropy alloys, Scr. Mater. 138 (2017) 145–150. https://doi.org/10.1016/j.scriptamat.2017.03.014.

[4] O.N. Senkov, G.B. Wilks, D.B. Miracle, C.P. Chuang, P.K. Liaw, Refractory high-entropy alloys, Intermetallics. 18 (2010) 1758–1765. https://doi.org/10.1016/j.intermet.2010.05.014.

[5] S. Varalakshmi, M. Kamaraj, B.S. Murty, Synthesis and characterization of nanocrystalline AlFeTiCrZnCu high entropy solid solution by mechanical alloying, J. Alloys Compd. 460 (2008) 253–257. https://doi.org/10.1016/j.jallcom.2007.05.104.

[6] J.-W. Yeh, Recent progress in high-entropy alloys, Ann. Chim. Sci. Matriaux. 31 (2006) 633–648. https://doi.org/10.3166/acsm.31.633-648.

[7] F. Otto, Y. Yang, H. Bei, E.P. George, Relative effects of enthalpy and entropy on the phase stability of equiatomic high-entropy alloys, Acta Mater. 61 (2013) 2628–2638. https://doi.org/10.1016/j.actamat.2013.01.042.

[8] C.G. Schön, T. Duong, Y. Wang, R. Arróyave, Probing the entropy hypothesis in highly concentrated alloys, Acta Mater. 148 (2018) 263–279. https://doi.org/10.1016/j.actamat.2018.01.028.

[9] S. Gorsse, J.-P. Couzinié, D.B. Miracle, From high-entropy alloys to complex concentrated alloys, Comptes Rendus Phys. 19 (2018) 721–736. https://doi.org/10.1016/j.crhy.2018.09.004.

[10] Y. Zhang, Y.J. Zhou, J.P. Lin, G.L. Chen, P.K. Liaw, Solid-Solution Phase Formation Rules for Multi-component Alloys, Adv. Eng. Mater. 10 (2008) 534–538. https://doi.org/10.1002/adem.200700240.

[11] S. Guo, C. Ng, J. Lu, C.T. Liu, Effect of valence electron concentration on stability of fcc or bcc phase in high entropy alloys, J. Appl. Phys. 109 (2011) 103505. https://doi.org/10.1063/1.3587228.

[12] C. Zhang, F. Zhang, S. Chen, W. Cao, Computational Thermodynamics Aided High-Entropy Alloy Design, JOM. 64 (2012) 839–845. https://doi.org/10.1007/s11837-012-0365-6.

[13] C. Zhang, F. Zhang, H. Diao, M.C. Gao, Z. Tang, J.D. Poplawsky, P.K. Liaw, Understanding phase stability of Al-Co-Cr-Fe-Ni high entropy alloys, Mater. Des. 109 (2016) 425–433. https://doi.org/10.1016/j.matdes.2016.07.073.

[14] A. Manzoni, S. Singh, H. Daoud, R. Popp, R. Völkl, U. Glatzel, N. Wanderka, On the Path to Optimizing the Al-Co-Cr-Cu-Fe-Ni-Ti High Entropy Alloy Family for High Temperature Applications, Entropy. 18 (2016) 104. https://doi.org/10.3390/e18040104.

[15] S. Syed Ghazi, K.R. Ravi, Phase-evolution in high entropy alloys: Role of synthesis route, Intermetallics. 73 (2016) 40–42. https://doi.org/10.1016/j.intermet.2016.03.002.

[16] S. Gorsse, F. Tancret, Current and emerging practices of CALPHAD toward the development of high entropy alloys and complex concentrated alloys, J. Mater. Res. 33 (2018) 2899–2923. https://doi.org/10.1557/jmr.2018.152.

[17] Y. Lu, Y. Dong, S. Guo, L. Jiang, H. Kang, T. Wang, B. Wen, Z. Wang, J. Jie, Z. Cao, H. Ruan, T. Li, A Promising New Class of High-Temperature Alloys: Eutectic High-Entropy Alloys, Sci. Rep. 4 (2015). https://doi.org/10.1038/srep06200.

[18] S.G. Ma, S.F. Zhang, J.W. Qiao, Z.H. Wang, M.C. Gao, Z.M. Jiao, H.J. Yang, Y. Zhang, Superior high tensile elongation of a single-crystal CoCrFeNiAl0.3 high-entropy alloy by Bridgman solidification, Intermetallics. 54 (2014) 104–109. https://doi.org/10.1016/j.intermet.2014.05.018.

[19] C.-C. Tung, J.-W. Yeh, T. Shun, S.-K. Chen, Y.-S. Huang, H.-C. Chen, On the elemental effect of AlCoCrCuFeNi high-entropy alloy system, Mater. Lett. 61 (2007) 1–5. https://doi.org/10.1016/j.matlet.2006.03.140.

[20] W.-R. Wang, W.-L. Wang, S.-C. Wang, Y.-C. Tsai, C.-H. Lai, J.-W. Yeh, Effects of Al addition on the microstructure and mechanical property of AlxCoCrFeNi high-entropy alloys, Intermetallics. 26 (2012) 44–51. https://doi.org/10.1016/j.intermet.2012.03.005.

[21] T. Yang, S. Xia, S. Liu, C. Wang, S. Liu, Y. Zhang, J. Xue, S. Yan, Y. Wang, Effects of AL addition on microstructure and mechanical properties of AlxCoCrFeNi High-entropy alloy, Mater. Sci. Eng. A. 648 (2015) 15–22. https://doi.org/10.1016/j.msea.2015.09.034.

[22] G. Qin, W. Xue, C. Fan, R. Chen, L. Wang, Y. Su, H. Ding, J. Guo, Effect of Co content on phase formation and mechanical properties of (AlCoCrFeNi)100-Co high-entropy alloys, Mater. Sci. Eng. A. 710 (2018) 200–205. https://doi.org/10.1016/j.msea.2017.10.088.

[23] Z. Fu, W. Chen, H. Wen, Z. Chen, E.J. Lavernia, Effects of Co and sintering method on

microstructure and mechanical behavior of a high-entropy Al 0.6 NiFeCrCo alloy prepared by powder metallurgy, J. Alloys Compd. 646 (2015) 175–182. https://doi.org/10.1016/j.jallcom.2015.04.238.

[24] T.-T. Shun, W.-J. Hung, Effects of Cr Content on Microstructure and Mechanical Properties of AlCoCr $_x$ FeNi High-Entropy Alloy, Adv. Mater. Sci. Eng. 2018 (2018) 1–7. https://doi.org/10.1155/2018/5826467.

[25] L. Guo, D. Xiao, W. Wu, S. Ni, M. Song, Effect of Fe on microstructure, phase evolution and mechanical properties of (AlCoCrFeNi)100-xFex high entropy alloys processed by spark plasma sintering, Intermetallics. 103 (2018) 1–11. https://doi.org/10.1016/j.intermet.2018.09.011.

[26] L. Guo, W. Wu, S. Ni, Z. Wang, M. Song, Effects of annealing on the microstructural evolution and phase transition in an AlCrCuFeNi2 high-entropy alloy, Micron. 101 (2017) 69–77. https://doi.org/10.1016/j.micron.2017.06.007.

[27] M. Ren, B. Li, H. Fu, Formation condition of solid solution type high-entropy alloy, Trans. Nonferrous Met. Soc. China. 23 (2013) 991–995. https://doi.org/10.1016/S1003-6326(13)62557-1.

[28] Y.P. Wang, B.S. Li, M.X. Ren, C. Yang, H.Z. Fu, Microstructure and compressive properties of AlCrFeCoNi high entropy alloy, Mater. Sci. Eng. A. 491 (2008) 154–158. https://doi.org/10.1016/j.msea.2008.01.064.

[29] A. Manzoni, H. Daoud, R. Völkl, U. Glatzel, N. Wanderka, Phase separation in equiatomic AlCoCrFeNi high-entropy alloy, Ultramicroscopy. 132 (2013) 212–215. https://doi.org/10.1016/j.ultramic.2012.12.015.

[30] S. Singh, N. Wanderka, K. Kiefer, K. Siemensmeyer, J. Banhart, Effect of decomposition of the Cr–Fe–Co rich phase of AlCoCrCuFeNi high entropy alloy on magnetic properties, Ultramicroscopy. 111 (2011) 619–622. https://doi.org/10.1016/j.ultramic.2010.12.001.

[31] A. Munitz, S. Salhov, S. Hayun, N. Frage, Heat treatment impacts the micro-structure and mechanical properties of AlCoCrFeNi high entropy alloy, J. Alloys Compd. 683 (2016) 221–230. https://doi.org/10.1016/j.jallcom.2016.05.034.

[32] E. Strumza, Comprehensive study of phase transitions in equiatomic AlCoCrFeNi high-entropy alloy, J. Alloys Compd. (2021) 12.

[33] K.R. Lim, K.S. Lee, J.S. Lee, J.Y. Kim, H.J. Chang, Y.S. Na, Dual-phase high-entropy alloys for high-temperature structural applications, J. Alloys Compd. 728 (2017) 1235–1238. https://doi.org/10.1016/j.jallcom.2017.09.089.

[34] E.J. Pickering, R. Muñoz-Moreno, H.J. Stone, N.G. Jones, Precipitation in the equiatomic high-entropy alloy CrMnFeCoNi, Scr. Mater. 113 (2016) 106–109. https://doi.org/10.1016/j.scriptamat.2015.10.025.

[35] S. Uporov, V. Bykov, S. Pryanichnikov, A. Shubin, N. Uporova, Effect of synthesis route on structure and properties of AlCoCrFeNi high-entropy alloy, Intermetallics. 83 (2017) 1–8. https://doi.org/10.1016/j.intermet.2016.12.003.

[36] J. Cieslak, J. Tobola, K. Berent, M. Marciszko, Phase composition of Al x FeNiCrCo high entropy alloys prepared by sintering and arc-melting methods, J. Alloys Compd. 740 (2018) 264–272. https://doi.org/10.1016/j.jallcom.2017.12.333.

[37] S. Gangireddy, B. Gwalani, V. Soni, R. Banerjee, R.S. Mishra, Contrasting mechanical behavior in precipitation hardenable AlXCoCrFeNi high entropy alloy microstructures:

Single phase FCC vs. dual phase FCC-BCC, Mater. Sci. Eng. A. 739 (2019) 158–166. https://doi.org/10.1016/j.msea.2018.10.021.

[38] K.S. Lee, J.-H. Kang, K.R. Lim, Y.S. Na, Influence of compressive strain on the microstructural evolution of an AlCoCrFeNi high entropy alloy, Mater. Charact. 132 (2017) 162–168. https://doi.org/10.1016/j.matchar.2017.08.010.

[39] J.M. Torralba, P. Alvaredo, A. García-Junceda, High-entropy alloys fabricated via powder metallurgy. A critical review, Powder Metall. 62 (2019) 84–114. https://doi.org/10.1080/00325899.2019.1584454.

[40] M. Vaidya, G.M. Muralikrishna, B.S. Murty, High-entropy alloys by mechanical alloying: A review, J. Mater. Res. 34 (2019) 664–686. https://doi.org/10.1557/jmr.2019.37.

[41] A. Nouri, C. Wen, Surfactants in Mechanical Alloying/Milling: A Catch-22 Situation, Crit. Rev. Solid State Mater. Sci. 39 (2014) 81–108. https://doi.org/10.1080/10408436.2013.808985.

[42] W. Ji, Z. Fu, W. Wang, H. Wang, J. Zhang, Y. Wang, F. Zhang, Mechanical alloying synthesis and spark plasma sintering consolidation of CoCrFeNiAl high-entropy alloy, J. Alloys Compd. 589 (2014) 61–66. https://doi.org/10.1016/j.jallcom.2013.11.146.

[43] S. Mohanty, T.N. Maity, S. Mukhopadhyay, S. Sarkar, N.P. Gurao, S. Bhowmick, K. Biswas, Powder metallurgical processing of equiatomic AlCoCrFeNi high entropy alloy: Microstructure and mechanical properties, Mater. Sci. Eng. A. 679 (2017) 299–313. https://doi.org/10.1016/j.msea.2016.09.062.

[44] E. Colombini, R. Rosa, L. Trombi, M. Zadra, A. Casagrande, P. Veronesi, High entropy alloys obtained by field assisted powder metallurgy route: SPS and microwave heating, Mater. Chem. Phys. (2017).

[45] A. Zhang, J. Han, J. Meng, B. Su, P. Li, Rapid preparation of AlCoCrFeNi high entropy alloy by spark plasma sintering from elemental powder mixture, Mater. Lett. 181 (2016) 82–85. https://doi.org/10.1016/j.matlet.2016.06.014.

[46] T.M. Butler, M.L. Weaver, Oxidation behavior of arc melted AlCoCrFeNi multi-component high-entropy alloys, J. Alloys Compd. 674 (2016) 229–244. https://doi.org/10.1016/j.jallcom.2016.02.257.

[47] Z.G. Zhu, K.H. Ma, X. Yang, C.H. Shek, Annealing effect on the phase stability and mechanical properties of (FeNiCrMn)(100−x)Cox high entropy alloys, J. Alloys Compd. 695 (2017) 2945–2950. https://doi.org/10.1016/j.jallcom.2016.11.376.

[48] M.-H. Tsai, K.-C. Chang, J.-H. Li, R.-C. Tsai, A.-H. Cheng, A second criterion for sigma phase formation in high-entropy alloys, Mater. Res. Lett. 4 (2016) 90–95. https://doi.org/10.1080/21663831.2015.1121168.

[49] M.-H. Tsai, K.-Y. Tsai, C.-W. Tsai, C. Lee, C.-C. Juan, J.-W. Yeh, Criterion for Sigma Phase Formation in Cr- and V-Containing High-Entropy Alloys, Mater. Res. Lett. 1 (2013) 207–212. https://doi.org/10.1080/21663831.2013.831382.

[50] L. Zhang, X. Huo, A. Wang, X. Du, L. Zhang, W. Li, N. Zou, G. Wan, G. Duan, B. Wu, A ductile high entropy alloy strengthened by nano sigma phase, Intermetallics. 122 (2020) 106813. https://doi.org/10.1016/j.intermet.2020.106813.

[51] I. Moravcik, J. Cizek, P. Gavendova, S. Sheikh, S. Guo, I. Dlouhy, Effect of heat treatment on microstructure and mechanical properties of spark plasma sintered

AlCoCrFeNiTi0.5 high entropy alloy, Mater. Lett. 174 (2016) 53–56. https://doi.org/10.1016/j.matlet.2016.03.077.

[52] M.A. Ruiz-Esparza-Rodríguez, Influence of process control agent and Al concentration on synthesis and phase stability of a mechanically alloyed AlxCoCrFeMnNi high-entropy alloy, J. Alloys Compd. (2021) 11.

[53] S.-H. Joo, H. Kato, M.J. Jang, J. Moon, E.B. Kim, S.-J. Hong, H.S. Kim, Structure and properties of ultrafine-grained CoCrFeMnNi high-entropy alloys produced by mechanical alloying and spark plasma sintering, J. Alloys Compd. 698 (2017) 591–604. https://doi.org/10.1016/j.jallcom.2016.12.010.

[54] P. Le Brun, L. Froyen, L. Delaey, The modelling of the mechanical alloying process in a planetary ball mill: comparison between theory and in-situ observations, Mater. Sci. Eng. A. 161 (1993) 75–82. https://doi.org/10.1016/0921-5093(93)90477-V.

[55] M. Abdellaoui, E. Gaffet, The physics of mechanical alloying in a planetary ball mill: mathematical treatment, Acta Metall. Mater. 43 (1995) 1087–1098.

[56] S. Rosenkranz, S. Breitung-Faes, A. Kwade, Experimental investigations and modelling of the ball motion in planetary ball mills, Powder Technol. 212 (2011) 224–230. https://doi.org/10.1016/j.powtec.2011.05.021.

[57] A.S. Rogachev, D.O. Moskovskikh, A.A. Nepapushev, T.A. Sviridova, S.G. Vadchenko, S.A. Rogachev, A.S. Mukasyan, Experimental investigation of milling regimes in planetary ball mill and their influence on structure and reactivity of gasless powder exothermic mixtures, Powder Technol. 274 (2015) 44–52. https://doi.org/10.1016/j.powtec.2015.01.009.

[58] R. Sriharitha, B.S. Murty, R.S. Kottada, Phase formation in mechanically alloyed AlxCoCrCuFeNi (x = 0.45, 1, 2.5, 5 mol) high entropy alloys, Intermetallics. 32 (2013) 119–126. https://doi.org/10.1016/j.intermet.2012.08.015.

[59] C. Yang, J. Lin, J. Zeng, Shenggua. Qu, X. Li, W. Zhang, D. Zhang, High-Strength AlCrFeCoNi High Entropy Alloys Fabricated by Using Metallic Glass Powder as Precursor., Adv. Eng. Mater. 18 (2016) 348–353. https://doi.org/10.1002/adem.201500339.

[60] V.K. Portnoi, A.V. Leonov, S.E. Filippova, A.N. Streletskii, A.I. Logacheva, Mechanochemical synthesis and heating-induced transformations of a high-entropy Cr-Fe-Co-Ni-Al-Ti alloy, Inorg. Mater. 50 (2014) 1202–1211. https://doi.org/10.1134/S0020168514120188.

[61] M.D. Alcalá, C. Real, I. Fombella, I. Trigo, J.M. Córdoba, Effects of milling time, sintering temperature, Al content on the chemical nature, microhardness and microstructure of mechanochemically synthesized FeCoNiCrMn high entropy alloy, J. Alloys Compd. 749 (2018) 834–843. https://doi.org/10.1016/j.jallcom.2018.03.358.

[62] M. Vaidya, A. Prasad, A. Parakh, B.S. Murty, Influence of sequence of elemental addition on phase evolution in nanocrystalline AlCoCrFeNi: Novel approach to alloy synthesis using mechanical alloying, Mater. Des. 126 (2017) 37–46. https://doi.org/10.1016/j.matdes.2017.04.027.

[63] A.S.M. Ang, C.C. Berndt, M.L. Sesso, A. Anupam, P. S, R.S. Kottada, B.S. Murty, Plasma-Sprayed High Entropy Alloys: Microstructure and Properties of AlCoCrFeNi and MnCoCrFeNi, Metall. Mater. Trans. A. 46 (2015) 791–800.

https://doi.org/10.1007/s11661-014-2644-z.
[64] S. Praveen, B.S. Murty, R.S. Kottada, Phase Evolution and Densification Behavior of Nanocrystalline Multicomponent High Entropy Alloys During Spark Plasma Sintering, JOM. 65 (2013) 1797–1804. https://doi.org/10.1007/s11837-013-0759-0.
[65] C.-L. Chen, Study of (Ni,Cr) pre-milling for synthesis of CoFe(NiCr)Mn high entropy alloy by mechanical alloying, Mater. Sci. (2021) 10.
[66] T. Stasiak, Novel Multicomponent Powders from the AlCrFeMnMo Family Synthesized by Mechanical Alloying, Adv Eng Mater. (2019) 5.
[67] L. Moravcikova-Gouvea, I. Moravcik, M. Omasta, J. Veselý, J. Cizek, P. Minárik, J. Cupera, A. Záděra, V. Jan, I. Dlouhy, High-strength Al0.2Co1.5CrFeNi1.5Ti high-entropy alloy produced by powder metallurgy and casting: A comparison of microstructures, mechanical and tribological properties, Mater. Charact. 159 (2020) 110046. https://doi.org/10.1016/j.matchar.2019.110046.
[68] R. Orrù, J. Woolman, G. Cao, Z.A. Munir, Synthesis of dense nanometric MoSi2 through mechanical and field activation, J. Mater. Res. 16 (2001) 1439–1448. https://doi.org/10.1557/JMR.2001.0201.
[69] S. Paris, E. Gaffet, F. Bernard, Z.A. Munir, Spark plasma synthesis from mechanically activated powders: a versatile route for producing dense nanostructured iron aluminides, Scr. Mater. 50 (2004) 691–696. https://doi.org/10.1016/j.scriptamat.2003.11.019.
[70] S. Paris, E. Gaffet, F. Bernard, Control of FeAl Composition Produced by SPS Reactive Sintering from Mechanically Activated Powder Mixture, J. Nanomater. 2013 (2013) 1–11. https://doi.org/10.1155/2013/150297.
[71] R.B. Mane, B.B. Panigrahi, Comparative study on sintering kinetics of as-milled and annealed CoCrFeNi high entropy alloy powders, Mater. Chem. Phys. 210 (2018) 49–56. https://doi.org/10.1016/j.matchemphys.2017.11.047.
[72] R.B. Mane, B.B. Panigrahi, Sintering mechanisms of mechanically alloyed CoCrFeNi high-entropy alloy powders, J. Mater. Res. 33 (2018) 3321–3329. https://doi.org/10.1557/jmr.2018.225.
[73] R.B. Mane, B.B. Panigrahi, Effect of alloying order on non-isothermal sintering kinetics of mechanically alloyed high entropy alloy powders, Mater. Lett. 217 (2018) 131–134. https://doi.org/10.1016/j.matlet.2018.01.092.
[74] X.W. Zhou, R.A. Johnson, H.N.G. Wadley, Misfit-energy-increasing dislocations in vapor-deposited CoFe/NiFe multilayers, Phys. Rev. B. 69 (2004). https://doi.org/10.1103/PhysRevB.69.144113.
[75] Z. Lin, R.A. Johnson, L.V. Zhigilei, Computational study of the generation of crystal defects in a bcc metal target irradiated by short laser pulses, Phys. Rev. B. 77 (2008). https://doi.org/10.1103/PhysRevB.77.214108.
[76] W.-M. Choi, Y.H. Jo, S.S. Sohn, S. Lee, B.-J. Lee, Understanding the physical metallurgy of the CoCrFeMnNi high-entropy alloy: an atomistic simulation study, Npj Comput. Mater. 4 (2018) 1. https://doi.org/10.1038/s41524-017-0060-9.
[77] D. Farkas, A. Caro, Model interatomic potentials and lattice strain in a high-entropy alloy, J. Mater. Res. 33 (2018) 3218–3225. https://doi.org/10.1557/jmr.2018.245.
[78] D. Farkas, Grain boundary structure in high-entropy alloys, J Mater Sci. (2020) 11.
[79] D. Farkas, A. Caro, Model interatomic potentials for Fe–Ni–Cr–Co–Al high-entropy

alloys, J. Mater. Res. 35 (2020) 3031–3040. https://doi.org/10.1557/jmr.2020.294.
[80] P. Wang, Y. Bu, J. Liu, Q. Li, H. Wang, W. Yang, Atomic deformation mechanism and interface toughening in metastable high entropy alloy, Mater. Today. 37 (2020) 64–73. https://doi.org/10.1016/j.mattod.2020.02.017.
[81] X. Huang, L. Liu, X. Duan, W. Liao, J. Huang, H. Sun, C. Yu, Atomistic simulation of chemical short-range order in HfNbTaZr high entropy alloy based on a newly-developed interatomic potential, Mater. Des. 202 (2021) 109560. https://doi.org/10.1016/j.matdes.2021.109560.
[82] X.-G. Li, C. Chen, H. Zheng, Y. Zuo, S.P. Ong, Complex strengthening mechanisms in the NbMoTaW multi-principal element alloy, Npj Comput. Mater. 6 (2020) 70. https://doi.org/10.1038/s41524-020-0339-0.
[83] G. Anand, R. Goodall, C.L. Freeman, Role of configurational entropy in body-centred cubic or face-centred cubic phase formation in high entropy alloys, Scr. Mater. 124 (2016) 90–94. https://doi.org/10.1016/j.scriptamat.2016.07.001.
[84] S.I. Rao, C. Varvenne, C. Woodward, T.A. Parthasarathy, D. Miracle, O.N. Senkov, W.A. Curtin, Atomistic simulations of dislocations in a model BCC multicomponent concentrated solid solution alloy, Acta Mater. 125 (2017) 311–320. https://doi.org/10.1016/j.actamat.2016.12.011.
[85] D. Utt, A. Stukowski, K. Albe, Grain boundary structure and mobility in high-entropy alloys: A comparative molecular dynamics study on a 11 symmetrical tilt grain boundary in face-centered cubic CuNiCoFe, Acta Mater. (2020) 9.
[86] O.R. Deluigi, R.C. Pasianot, F.J. Valencia, A. Caro, D. Farkas, E.M. Bringa, Simulations of primary damage in a High Entropy Alloy: Probing enhanced radiation resistance, Acta Mater. 213 (2021) 116951. https://doi.org/10.1016/j.actamat.2021.116951.
[87] L. Xie, P. Brault, A.-L. Thomann, X. Yang, Y. Zhang, G. Shang, Molecular dynamics simulation of Al–Co–Cr–Cu–Fe–Ni high entropy alloy thin film growth, Intermetallics. 68 (2016) 78–86. https://doi.org/10.1016/j.intermet.2015.09.008.

Chapter II: Mechanical activation of metallic powders: a molecular dynamics approach

1. Introduction

Mechanical treatment of powders in planetary ball mills is a very common process used for several purposes including the synthesis of inorganic compounds and metallic nanocomposites, the formation of supersaturated solid solutions or metastable crystalline phases, and the elaboration of nanostructured materials or amorphous alloys [1]. Mechanosynthesis, also termed mechanochemistry or mechanical alloying, supposes that the reaction is completed during the mechanical treatment [2]. In contrast, preliminary mechanical activation is used to fabricate reactive materials [3], and the reaction follows the activation process. As an example, the combination of mechanical activation and reactive sintering leads to the formation of nanostructured intermetallics [4], and nanostructured high-entropy alloys [5]. Nanocomposites prepared by mechanical milling are also used in additive manufacturing [6,7], where attention is also paid to particle size and shape. Characterizing the reactive properties of activated powders is important to design reactive material with tailored reactivity and to choose the most adequate parameters for the elaboration process (e.g., milling speed).

In practice, powders processed in planetary ball mills are submitted to a series of transformations induced by contact with grinding balls. The different elemental load modes observed in milling experiments include compression, shear, shock, cutting, and impact. Beinert *et al.*[8] classified the contacts between beads or bead and wall into four contact types: impact, torsion, shearing, and rolling, as a function of the relative velocity of colliding bodies. In addition, in situ observations have demonstrated that milling balls undergo complex motions in the jar [9]. Three milling regimes were identified as a function of milling parameters in the case of a large number of grinding balls [10]. In cascading regime, the balls are taken along the container and unroll upon each other from the bulk top to its base. Friction between grinding balls is dominant. In cataracting regime, the balls detach from the wall and impact the other balls or the opposite wall with high intensity. In centrifugal regime, the balls are stuck to the inner wall of the vial and move together with the vial. The specific milling regime was found to influence the microstructure and reactivity of the final powder mixture [11]. The action of balls on the blended elemental powders is essential to control the effects of milling. The two main activation factors are the collision of grinding balls with one another and with the milling wall, and friction between the grinding balls.

The fundamental question is to determine how the mechanical energy delivered by the mechanical process is stored in the powder, leading to enhanced reactivity in activated powders. The most common explanation is to assert that mechanical energy is stored in defects created during severe plastic deformation associated with mechanical treatment. According to Hoffman

et al. [12], the defects due to mechanical treatment include: zero-dimensional point defects, such as vacancies; one-dimensional line defects, such as dislocations; two-dimensional area defects, such as stacking faults, grain boundaries, and contact areas with other phases. Three-dimensional volume defects include amorphous regions, pores, other phases, and metastable regions, corresponding to the development of structural transformations. The energy associated with different types of point defects, dislocations, and grain boundaries has been evaluated by Khina [13,14]. Low-dimensional defects appear to have a negligible effect on subsequent reactivity, in comparison with metastable phases, for which the formation mechanism is not yet understood.

In order to understand the effect of mechanical activation on reactivity, the Ni–Al system has been widely studied experimentally. It has been shown that high-energy ball milling (HEBM) affects the reaction kinetics of Ni/Al reactive composites [15,16]. Specifically, it was demonstrated that the effective activation energy of the reaction is significantly reduced after mechanical treatment [17]. This reduction may be attributed to structural refining that leads to an increase in the number of contact surfaces. In addition, microstructural analysis has shown that nanosized clusters are formed, which can serve as highly reactive precursors of new phases, and thus reduce the potential barrier to the initiation of exothermic reaction.

A problem of topical interest is to understand how impact and friction (the two prevalent actions during milling) act on the powder and modify microstructure evolution. Several studies have already been conducted at the atomic level. The plastic deformation induced by milling was modeled by cyclic deformation [18,19]. These studies have demonstrated that cyclic deformation forces chemical mixing due to dislocation gliding. The progressive amorphization and mixing of a binary system through extensive plastic straining has been studied in [20], by means of a strain-and-stack process similar to cold-rolling. Since the pioneering work of Holian and coworkers [21], the friction between sliding metallic blocks has been extensively studied (see for instance [22]). The frictional sliding of solid surfaces involves large plastic strains and strain gradients, high strain rates and strain rate gradients, and mechanical mixing from both contacting solids. Mechanical mixing was attributed to different mechanisms: interface instability that leads to local vorticity, dislocation and twin activity, and amorphization. Atomic mixing in metals under shear deformation has been studied at various interfaces in [23]. The mixing was found to be diffusive or “superdiffusive,” depending on the coherence between interfaces. Heat dissipation due to sliding was investigated by means of non-equilibrium molecular dynamics simulations [24,25]. Atomic-scale mechanical mixing and generation of mixing layer were observed in the regions near the contact interface. The enhanced reactivity of mechanical activated systems has also been considered in the literature. The mechanisms of loading and chemical processes resulting from shock compaction have been investigated in the case of Ni/Al composites by means of molecular dynamics simulations [26,27]. The role of porosities in such systems during deformation has been considered in [28]. The reactivity of Ni–Al composites prepared by mechanical activation has been studied in order to detect the role played by the nanoscale mixing of the reagents [29]. But, in these studies, a nano-laminated structure or premixing of reagents was assumed. So a complete description of the effects

induced by the mechanical treatment of elemental powders from activation to reaction is still lacking.

In the present work, we developed a set of molecular dynamics simulations mimicking the effects of grinding balls on powder particles, in order to obtain a better understanding of the mechanisms that take place during mechanical activation at the atomic level. We modeled the impact of grinding balls and their action on blended powders following Maurice and Courtney's idea [30]. Flat surface tools act on a large number of individual powder particles and cause uniaxial compression of the powder. Despite unavoidable limitations in system size and simulation time, large-scale molecular dynamics simulations are a useful tool to provide in situ observations during mechanical activation. We considered a set of metallic binary systems: Ni–Al, Ti–Al, Fe–Ni, and Fe–Cr. It is expected that a layered structure would be observed in ductile/ductile binaries. In the case of couples with dissimilar ductility, the resulting composite represents a metallic matrix with inclusions of the less ductile phase. The aim is to understand the specific behavior of each couple as a function of the mechanical and structural properties of its elemental constituents. Understanding the specific behavior of metallic couples during mechanical activation is important when this process is used to fabricate complex alloys. The efficiency of mechanically induced deformation will be investigated by measuring amorphization rate, chemical mixing efficiency, and the creation of defects.

2. Simulation details

All atomic simulations were performed with the Large-scale Atomic/Molecular Massively Parallel Simulator (LAMMPS) [31]. The LAMMPS is very well suited to study the properties of large-scale metallic systems by molecular dynamics and embedded atom method (EAM) potentials. The equations of motion of the atoms were integrated with a timestep of 1 fs. As shown in Fig. 1, we studied the mechanical deformation of a parallelepipedal simulation box filled with rounded particles[2]. The typical box size was 58.6 nm × 58.6 nm × 16.8 nm. To build this initial system, we randomly distributed 12 spheres of 16.6 nm diameter in the middle plane of the simulation box. Each sphere was filled with either a monocrystalline or polycrystalline metal. The polycrystalline systems were obtained by Voronoï tessellation [32,33]. The binary systems considered in the present study are listed in Table 1, with their corresponding EAM potentials. The number of atoms of each species and mole fraction are given in Table 2. The properties of the elements are summarized in Table 3.

The system was first equilibrated at 300 K by a run of 50 ps in the NVT (canonical) ensemble followed by 50 ps in the NPT (isothermal-isobaric) ensemble. After this preliminary step, the atoms are integrated in the NPT ensemble. In order to mimic high-energy ball milling in which the average impact velocity of grinding balls is typically between 2 and 14 m/s, the box was

[2] Here, "particle" means powder particle.

shrunk at the constant velocity of 13.17 m/s, corresponding to a compression rate of $\dot{\epsilon} = 4.5 \times 10^{10}$ s^{-1} along the x-direction [38]. The length of the simulation box was fixed along the *z*- direction and adjusted along the y- direction by the Nose-Hoover barostat to maintain zero pressure in the system. The system deformation was monitored by computing the relative compression $\epsilon_{xx} = |\Delta L/L_0| = |(L - L_0)/L_0|$. In the following, we will use ϵ instead of ϵ_{xx}, for simplicity. The system was deformed up to 80% of its initial length in 1.78 ns before studying its final state.

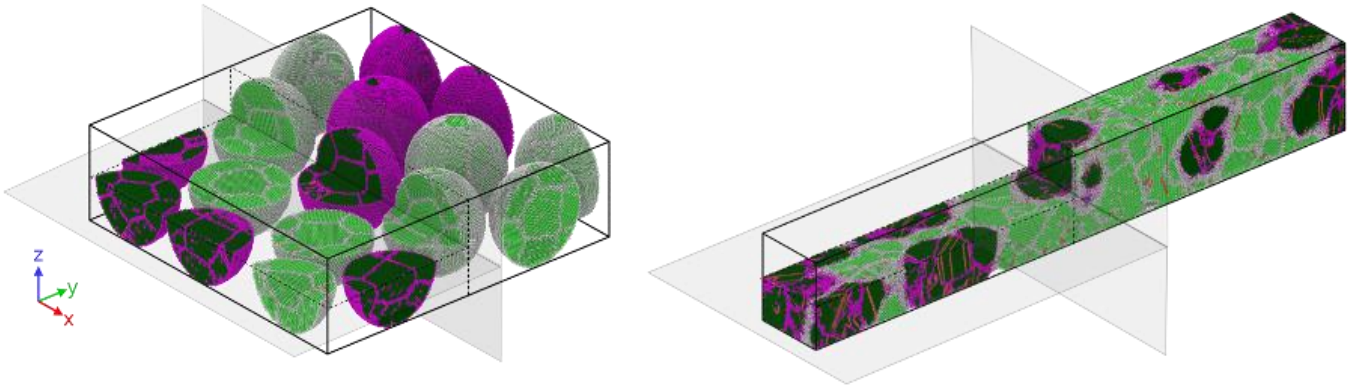

Figure 1: Simulated system. Initial state with fcc-Ni and fcc-Al polycrystalline particles (left). System elongated along the y-direction after deformation (right).

The mechanical alloying observed during high-energy ball milling is necessarily related to the mechanical properties (e.g., Young's modulus, hardness, and tensile strength) of the elemental metal. Some of these properties can be evaluated by computing stress–strain curves. Nevertheless, hardness calculations will require nanoindentation simulations, which are complex and beyond the scope of this study. As a first approximation, stress–strain curves give a rough estimate of the hardness in a given binary by using an empirical linear dependence, $H \approx 3\sigma$, reported between tensile strength and hardness [39]. The computed stress–strain curves are given in Supporting Information.

The atomic positions were visualized with the open-source software, OVITO [40]. The local environment (i.e., *fcc*, *bcc*, or unknown/amorphous) was determined for each atom, with the adaptative common neighbor analysis (a-CNA) [41]. In the initial configuration depicted in Fig. 1, each atom was tagged with an indicator referencing its type and local structure.

Metallic binary K-L	EAM potential
Ni-Al	Purja Pun and Mishin [34]
Ti-Al	Zope and Mishin [35]
Fe-Ni	Bonny *et al.* [36]
Fe-Cr	Bonny *et al.* [37]

Table 1: EAM potential used for the different binaries.

K-L	N	N(K)	N(L)	x (at. %)
Ni-Al mono	2,106,488	1,097,480	1,009,008	52
Ni-Al poly	2,110,942	1,099,995	1,010,947	52
Ti-Al mono	1,510,824	789,312	721,512	52
Ti-Al poly	1,658,148	866,526	791,622	52
Fe-Ni mono	2,440,686	1,170,390	1,270,296	48
Fe-Cr mono	2,329,662	1,170,390	1,159,272	50

Table 2: List of systems considered in the analysis.

N(K) is the number of atoms of element K, N is the total number of atoms, x = N(K)/N is the mole fraction

	Structure	Exp. T_m (K)	Sim. T_m (K)	Exp. T_{tr} (K)	Sim. σ (GPa)	Exp. H (Hv)
Al	*fcc*	933	1055 [34]		8.0 [34]	18
			889[a] – 870[b] [35]		6.6 [35]	
Ni	*fcc*	1728	1710 [34]		19.4 [34]	60
					14.6 [36]	
Fe	*bcc* → *fcc*	1811		1185	9.4 [36]	60
					9.4 [37]	
Ti	*hcp* → *fcc*	1713	1571[a] – 1531[b] [35]	1155	14.8 [35]	99
Cr	*bcc*	2180	Not given		13.5 [37]	100

Table 3: Structural, thermodynamics and mechanical properties: structure of pure elements at ambient temperature; melting temperature T_m of pure elements: experimental value and theoretical value corresponding to the specific potential; experimental value of the transition temperature T_{tr}; simulated tensile strength, σ; experimental value of hardness, H.

[a]Melting temperature evaluated using the sphere method
[b]Melting temperature evaluated using the two-phase method

3. Results and discussion

3.1. Study of deformation

We first describe the effect of deformation on the Ni–Al system. A progressive uniaxial compression was applied to the system of 12 polycrystalline particles of nickel and aluminum, as described in the previous section. Figure 2a presents snapshots of the system in the x−y plane at representative stages of the process. The simulation box shrank in the x-direction and elongated in the y-direction.

The particles were homogeneously distributed in the initial configuration. The compression applied to the simulation box induced modifications in the system as a function of deformation. Up ϵ = 10%, the particles moved freely, filling voids (stage I). At that deformation, the simulation box is equal to 12 $\times V_{cube}$, where V_{cube} is the volume of the cube in which a particle is inscribed. During compaction (stage II from ϵ = 10% to 49%), most of the empty space

between particles was removed. At ϵ = 35%, Al particles seem to be crushed by Ni particles, and some dislocation started to develop in Al particles. Compaction was complete at ϵ = 49% when the volume of the simulation box reached its inflection point. After compaction (stage III, ϵ > 49%), the powder was further compressed and underwent plastic deformation. The ductile Al particles deformed, whereas Ni particles remained spherical. The microstructure of the composite formed after compression (Fig. 2a at ϵ = 73 %) looks very similar to the samples

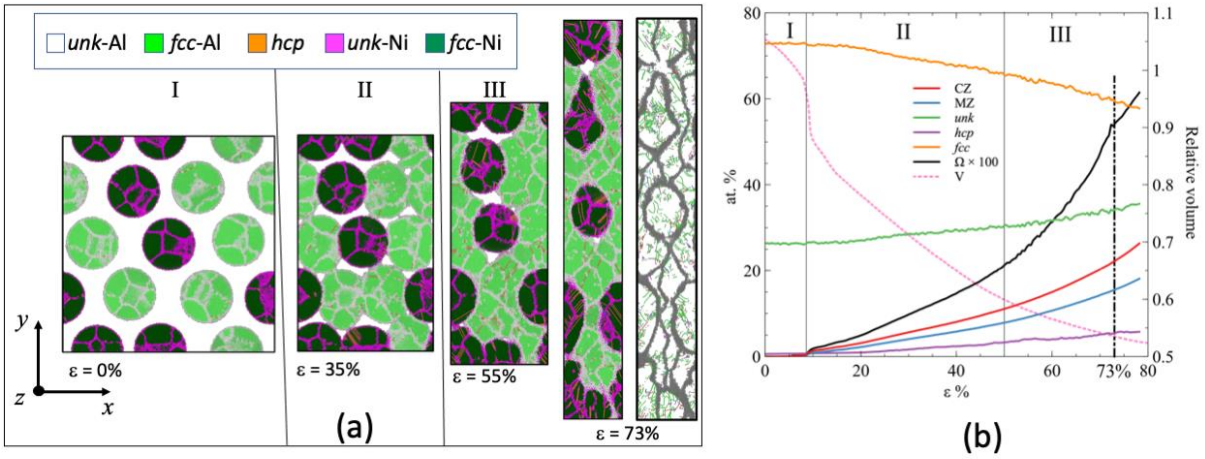

Figure 2: Evolution of the Ni–Al system composed of polycrystalline spheres during deformation. (a) Snapshots at different deformation rates: ϵ = 0%, ϵ = 35%, ϵ = 55% and ϵ = 73% and DXA (dislocation extraction algorithm) analysis at ϵ = 73% [42], (b) number of atoms (at%) in contact zones CZs, in mixing zones MZs, and in local configuration fcc, hcp or *unk* in the entire system as a function of deformation. Evolution of the mixing parameter Ω and of the relative volume of the simulation box. The relative volume is defined as the volume of the simulation box divided by 12 × d^3 with, *d*, the diameter of the particle.

obtained experimentally via HEBM [43], despite the difference in scale.

In what follows, we analyze the different stages of the microstructural changes during deformation. To do so, several indicators were tracked, including the fraction of atoms in relation to their chemical identity, their local configuration (*hcp*, *fcc*, *unk*), and the particle it belonged to initially. Figure 2b presents the evolution of the entire Ni–Al system as a function of deformation in terms of these indicators. A major consequence of mechanical activation (MA) is the formation of contact zones between particles. In order to study this aspect, we defined two types of regions:

- Contact Zone (CZ): an atom in particle *a* belongs to a CZ if one of its neighbors, in a sphere of radius r_{cut}, belongs to another particle *b*.
- Mixing Zone (MZ): an atom of type *i* in particle *a* belongs to an MZ if one of its neighbors, in a sphere of radius r_{cut}, belongs to another particle *b* and is of type *j*, with $i \neq j$.

The choice of r_{cut} = 3.25 Å is such that only nearest neighbors are selected. A group of atoms that will be in a particular region at the end of the deformation is noted "*end*-region." For instance, if we consider the group of atoms that will be in the MZ at the end (but not necessarily at any previous time except the end), the group is noted "*end*-MZ."

Figure 3 highlights, in the initial system, the position of atoms that participate in *end*-CZs and *end*-MZ.

Table 4 gives the characteristics of all $K-L$ systems at ϵ = 73 % (where K and L stand for Ti, Al, Fe, Ni, Cr):

- N_{MZ} is the total number of atoms in MZs;
- $N_{MZ}(K)$ is the number of atoms of species K in MZs;
- $n_{MZ} = N_{MZ}/N$ is the fraction of atoms in MZs;
- $x_{MZ} = N_{MZ}(K)/N_{MZ}$ is the mole fraction in mixing zones;
- $u_{MZ} = N_{MZ}(unk)/N_{MZ}$ is the fraction of *unk*-atoms inMZs;
- $\hat{u}_{MZ} = N_{MZ}(unk\text{-}L)/N_{MZ}(L)$ is the number of *unk*-atoms of species L over the number of atoms of species L in MZs.

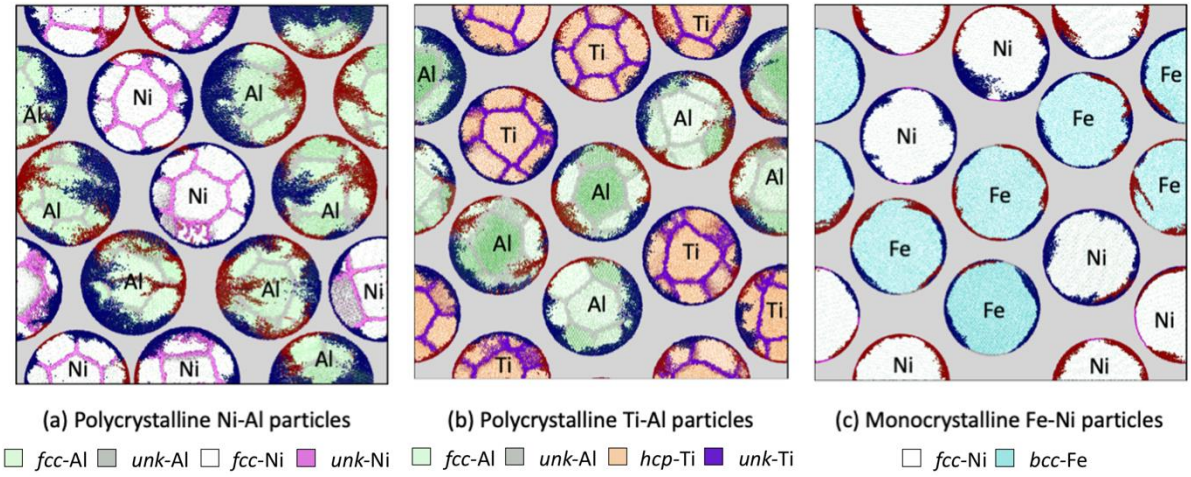

Figure 3: Snapshots of the initial system prior to deformation (x–z view). Atoms embedded in mixing zones after deformation are highlighted. Atoms in *end*-CZ are red, and atoms in *end*-MZ are blue.

ϵ = 73 %	Ni-Al poly	Ni-Al mono	Ti-Al poly	Ti-Al mono	Fe-Ni mono	Fe-Cr mono
n_{MZ} (at. %)	15.2	12.6	10.2	7.6	4.5	4.7
x_{MZ} (at. %)	47.0	44.8	45.7	45.3	48.5	51.0
u_{MZ} (at. %)	74.4	69.3	52.9	45.6	62.5	31.8
$\hat{u}_{MZ}$ (at. %)	88.6	86.3	60.4	54.7	54.2	23.3
Ω at 73%	0.54	0.36	0.32	0.30	0.25	0.24

Table 4: System characteristics at deformation ϵ = 73% for each binary K–L.

In the case of the Ni–Al polycrystalline system, the initial system already contained *unk*-atoms distributed at grain boundaries and on particle surfaces (see Fig. 2a). During deformation, the number of *fcc*-atoms decreased in relation to *unk*- and *hcp*-atoms: *unk*-atoms were observed at contact zones and *hcp*-atoms in the dislocation network. The number of atoms in CZs and MZs increased during compaction (stage II). This rise was slightly more pronounced during plastic deformation (stage III). The number of atoms in CZs reached 20 at% in the final sample with more atoms in CZs than in MZs. This indicates that only a fraction of atoms in CZs will lead to effective chemical mixing. Most of the atoms in MZs are amorphous (u_{MZ} = 74.4 at. %), with a large majority of *unk*-Al ($\hat{u}_{MZ}$ = 88 at. %) (see Table 4). The mole fraction in MZ (x_{MZ} = 47 at. %) is not strictly preserved in comparison with the overall mole fraction (x = 52 at. %). This

means that more Al atoms were trapped in the MZ during deformation. It appears that plastically deformable aluminum forms layers between Ni particles. Some Ni atoms were trapped in these amorphous Al layers. During compaction and compression of both Al and Ni particles, plastic deformation involved dislocations that can be quantified by the percentage of *hcp*-atoms in the system. As shown in Fig. 2a, plastic deformation is more noticeable in Ni particles, where the number of *hcp* atoms is greater after deformation.

The atomic-level mixing induced by mechanical activation is best appreciated by considering a simple non-dimensional order parameter. The short-range order parameter (SRO) is based upon nearest-neighbor atomic distribution:

$$\Omega = \frac{\frac{c}{1-c}N_i^j + \frac{1-c}{c}N_j^i}{N_i^j + N_j^i} \quad (1)$$

where N_i^j is the average number of neighbors of type *j* in a sphere of radius r_{cut} = 3.25 Å around atoms of type *i*, and *c* is the atomic fraction (*c* = 0.5 in an equiatomic system). Values of Ω between 0 and 1 indicate partial chemical segregation, and Ω = 1 corresponds to a randomly mixed system. Thus, Ω provides a sensitive measure of the state of chemical mixing in a given system [44]. Atoms located in *end*-MZs were identified, and the SRO Ω was then evaluated for this specific group of atoms as a function of deformation. Note that atoms that do not belong to *end*-MZs contribute to N_i^j if they are in the coordination sphere of radius 3.25 Å. The value of Ω at ϵ = 73% is given in Table 4. The evolution of Ω as a function of deformation is depicted in Fig. 2b. We observed that Ω increased with deformation but never reached the value corresponding to complete mixing.

We next considered the system of 12 polycrystalline particles of Ti and Al. The Ti–Al system behaves very differently from the Ni–Al system. After deformation, the number of atoms in MZs (n_{MZ}) is lower: only 10 at% in the Ti–Al system compared to 15 at% in the Ni–Al system. The nature of MZs is also different: only half of MZ-atoms are amorphous, with only a slight excess in Al atoms. In order to visualize behavior during deformation, we considered two Ti particles (Fig. 4a). The relative number of Ti atoms in MZs increased with deformation, but this evolution differs from one particle to another. As shown in Fig. 4b and c, particle #5 is surrounded by more Al particles than particle #12. As a consequence, the number of atoms in MZs is greater for particle #5. More Ti atoms were trapped in MZs during plastic deformation, with a substantial increase at ϵ = 45% (close to the compaction limit, Fig. 4a). For the entire system, the SRO reaches 0.49 in MZs after deformation, corresponding to partial mixing between Ti and Al.

Initially, Ti particles are in *hcp* local configuration except in their external shell. During compaction, we observed that a non-negligible number of *hcp*-atoms became *fcc*, as depicted in Fig. 4a. This tendency is more pronounced during plastic deformation (ϵ > 45%). The

increase in *fcc*-Ti can be attributed either to the occurrence of stacking faults in Ti particles or to structural transformations. Indeed, the structural transformation *hcp fcc* of Ti atoms has been observed in Ti–Al multilayers as a function of bilayer thick- ness and orientation at interfaces [45, 46]. Nanometric Ti–Al multilayers can nevertheless be very stable in specific conditions: the interface between (002)-Ti plane and (111)-Al plane is very stable because of the slight misfit between the two structures [47]. In this case, the solubility of Ti in Al is very limited in the solid state. In the simulation of deformation, the random contact between Ti and Al particles generated interfaces with different orientations that may present weak stability. Deformation induces emergence of *fcc*-Ti inside Ti particles and promotes mixing between Ti and Alat low temperatures.

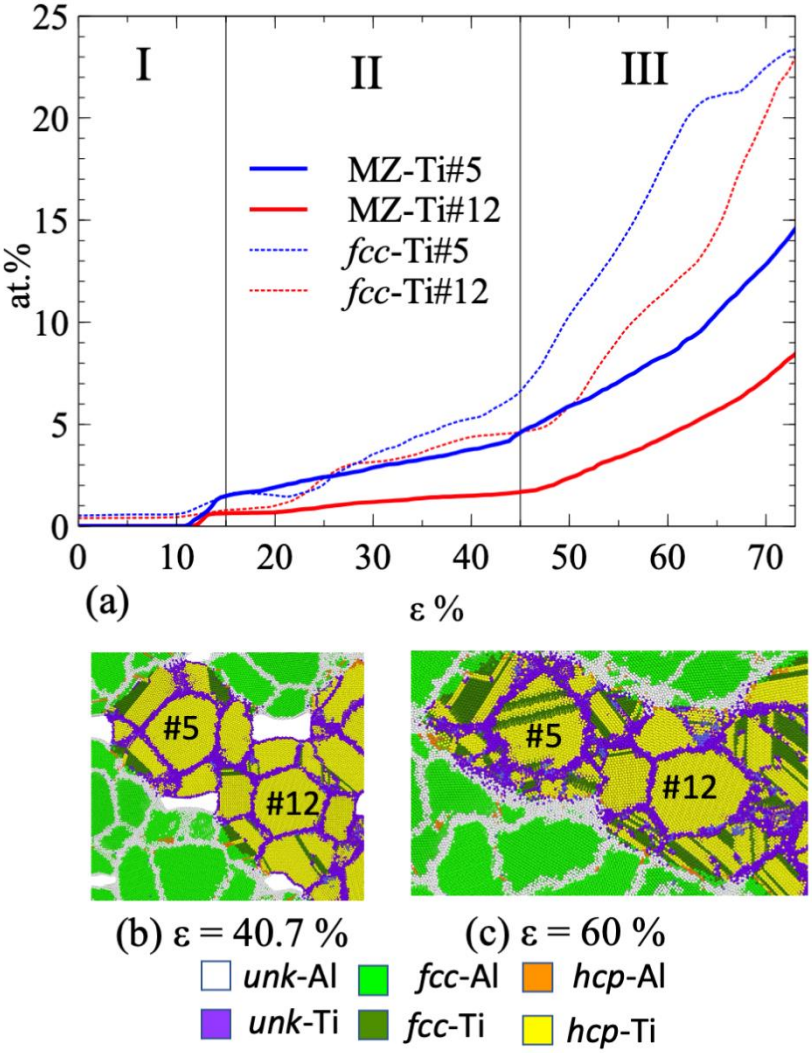

Figure 4: Evolution of two Ti particles as a function of deformation. (a) Number of Ti atoms in particles #5 and #12 (at%) in MZs and number of *fcc*-Ti in particles #5 and #12 (at%). (b) Snapshot of Ti particles #5 and #12 at ϵ = 40.7 % during stage I (compaction), (c) Snapshot of Ti particles #5 and #12 at ϵ = 60 % during stage II (plastic deformation).

3.2. Microstructure after deformation

We then studied the microstructure of the four binary systems Ni–Al, Ti–Al, Fe–Ni, and Fe–Cr after deformation using several indicators. Figure 5 shows the typical microstructure after deformation and the arrangement of atoms in MZs. The partial radial distribution functions (RDF), $g_{KL}(r)$, are presented in Fig. 6. Partial RDFs, in comparison with the solid configuration of pure elements, provide the degree of amorphization, and the local rearrangement of atoms. Figure 7 gives the histogram of potential energy per atom in MZs in comparison with pure elements. It allows us to appreciate the effect of mechanical activation on atom stability. Finally, Fig. 3 allows us to detect where atoms in *end*-MZs and *end*-CZs were initially located: in the core, in the shell, or in internal grain boundaries. In what follows, we analyze the case of monocrystalline particles, with comparison in some cases to polycrystalline particles.

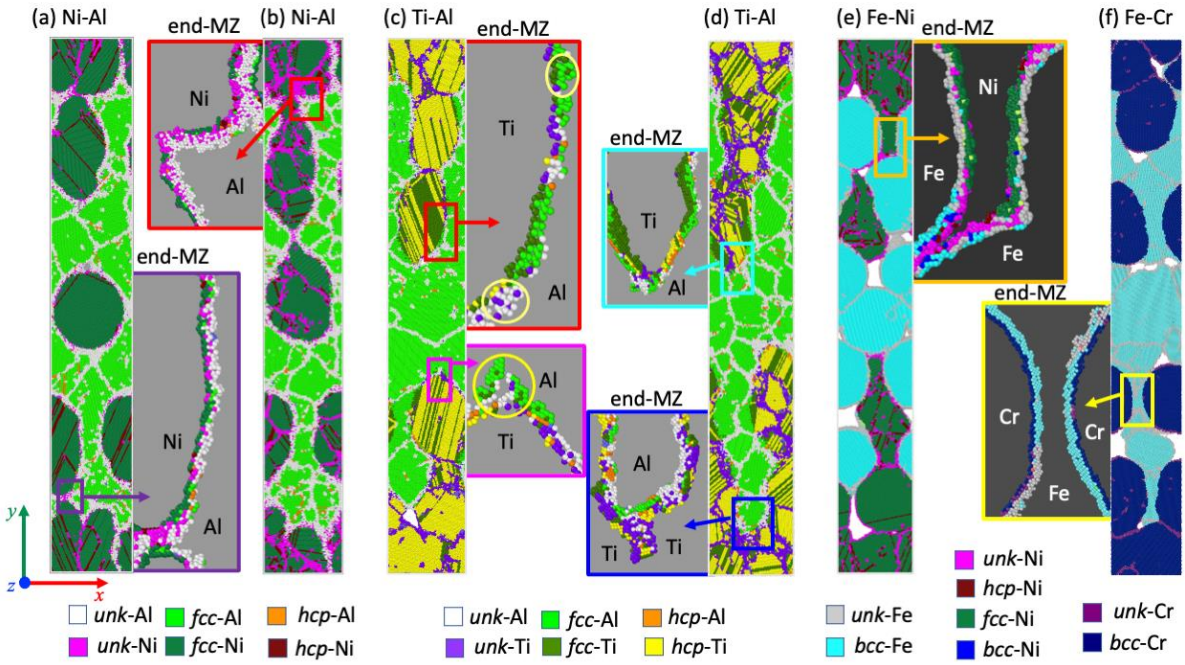

Figure 5: Snapshots of a slice of 10 Å, around z = 100 Å after deformation (ϵ = 73 %): (a) Ni–Al monocrystalline particles, (b) Ni–Al polycrystalline particles, (c) Ti–Al monocrystalline particles, (d) Ti–Al polycrystalline particles, (e) Fe–Ni monocrystalline particles, (f) Fe–Cr monocrystalline particles. Insets represent enlarged views of mixing zones after deformation (MZs).

3.2.1. Ni–Al system

In the case of the Ni–Al system, the mole fraction of MZ, x_{MZ}, is 45 at% after deformation compared to the global mole fraction, x, 52 at%. This means that MZs trapped more Al atoms than Ni atoms during deformation. The majority of atoms in MZs are amorphous (u_{MZ} = 70 at%), and most are Al atoms ($\hat{u}_{MZ}$ = 86 at%). In Fig.6a, we observe that the partial RDF, $g_{AlAl}(r)$, has the typical shape of an amorphous phase: the long-range order is lost. The first peak is shifted to the left in comparison with that of pure Al. The partial RDF $g_{NiNi}(r)$ keeps the typical order of pure *fcc*-Ni. At short range, the first nearest neighbors Ni–Al are located at the first

peak of pure *fcc*-Ni, but the second and subsequent neighbors indicate an amorphous phase. At short range, *fcc*-Al atoms are embedded in the *fcc*-Ni lattice.

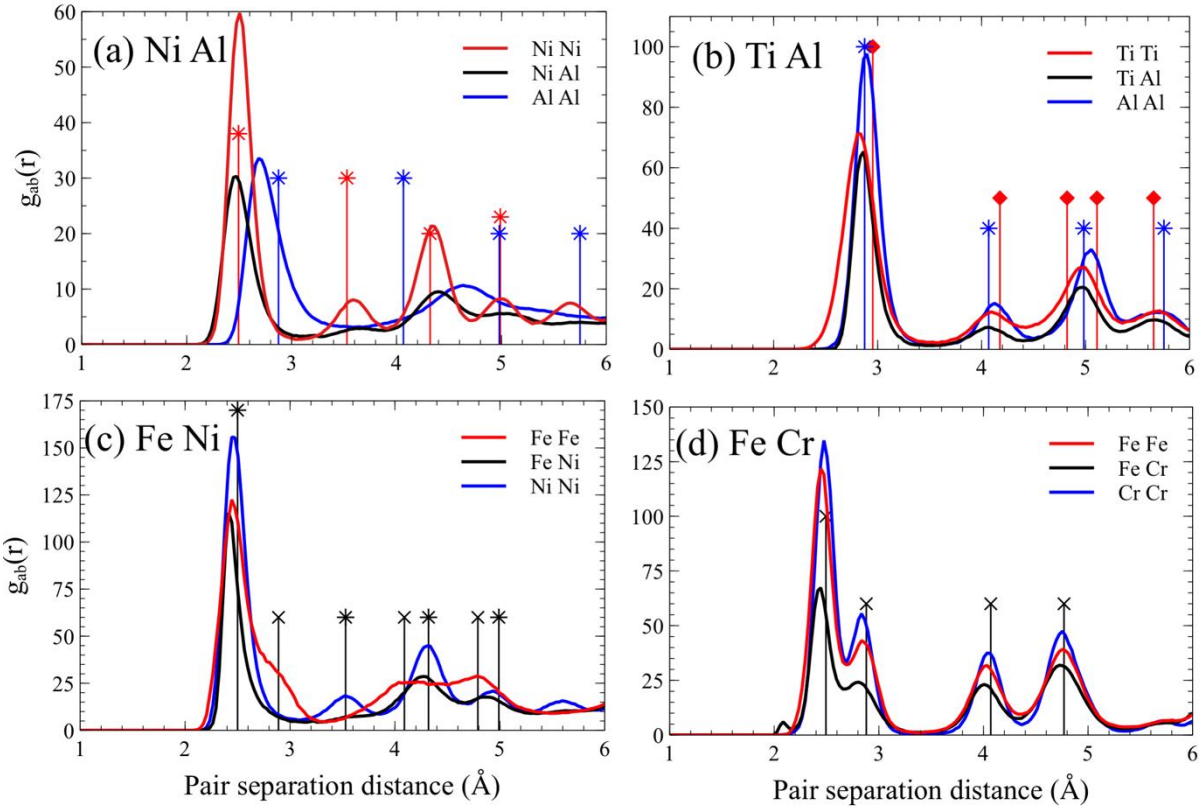

Figure 6: Partial radial distribution functions $g_{KL}(r)$ calculated in *end*-MZs at ϵ=73 % for the four systems: (a) Ni–Al, (b) Ti–Al, (c) Fe–Ni and (d) Fe–Cr. Vertical lines indicate the position of nearest neighbors in pure systems: star for *fcc*, cross for *bcc* and diamond for *hcp* structures.

The histogram of potential energy per atom provides supplementary information (Fig. 7a). Prior to deformation, Ni atoms in *end*-MZs are in a state corresponding to pure Ni, but some are less stable, as indicated by multiple small peaks to the right of the main peak. These atoms are actually located in the shell of Ni particles. In contrast, a large number of Al atoms in *end*-MZs correspond to pure Al. This result indicates that most of the Al in *end*-MZs are atoms that were initially located in the core of the particles, as shown in Fig. 3a. After deformation, the distribution of potential energy per atom is quite different. The Al-distribution expands to lower energies with a maximum value slightly shifted compared to that of Al atoms prior to deformation. The Ni-distribution expands to the right, but the main peak remains unchanged. These typical profiles with overlap are associated with the amorphization of Al, the partial dissolution of Ni into *unk*-Al atoms, and the substitution of Al atoms in the *fcc*-Ni lattice.

As shown in Fig. 5a (inset), a thin layer of *fcc*-Ni sur- rounds Ni particles in which a few *fcc*-Al atoms are trapped. The layers of amorphous Al atoms are located around Al particles and contain a few *unk*-Ni atoms. The same microstructure of MZs is observed after compression of Ni–Al polycrystalline particles (see inset in Fig. 5b). The MZ is thicker in this case, with more dissolved *unk*-Al atoms and *unk*-Ni atoms. This result indicates that internal grain

boundaries in Al particles enhance the mobility of *unk*-Al during deformation. Indeed, the number of atoms in MZs is greater (n_{MZ} = 15 at%) in the case of polycrystalline particles than in the case of monocrystalline particles (n_{MZ} =12.6 at%) (Table 4). The presence of linear defects (lines of *hcp*-atoms) was observed in Ni monocrystalline particles (Fig. 5a), and in the inner grains of polycrystalline particles (Fig. 5b). Defects are fewer in Al particles. This must be related to the ductility of Al in comparison with that of Ni.

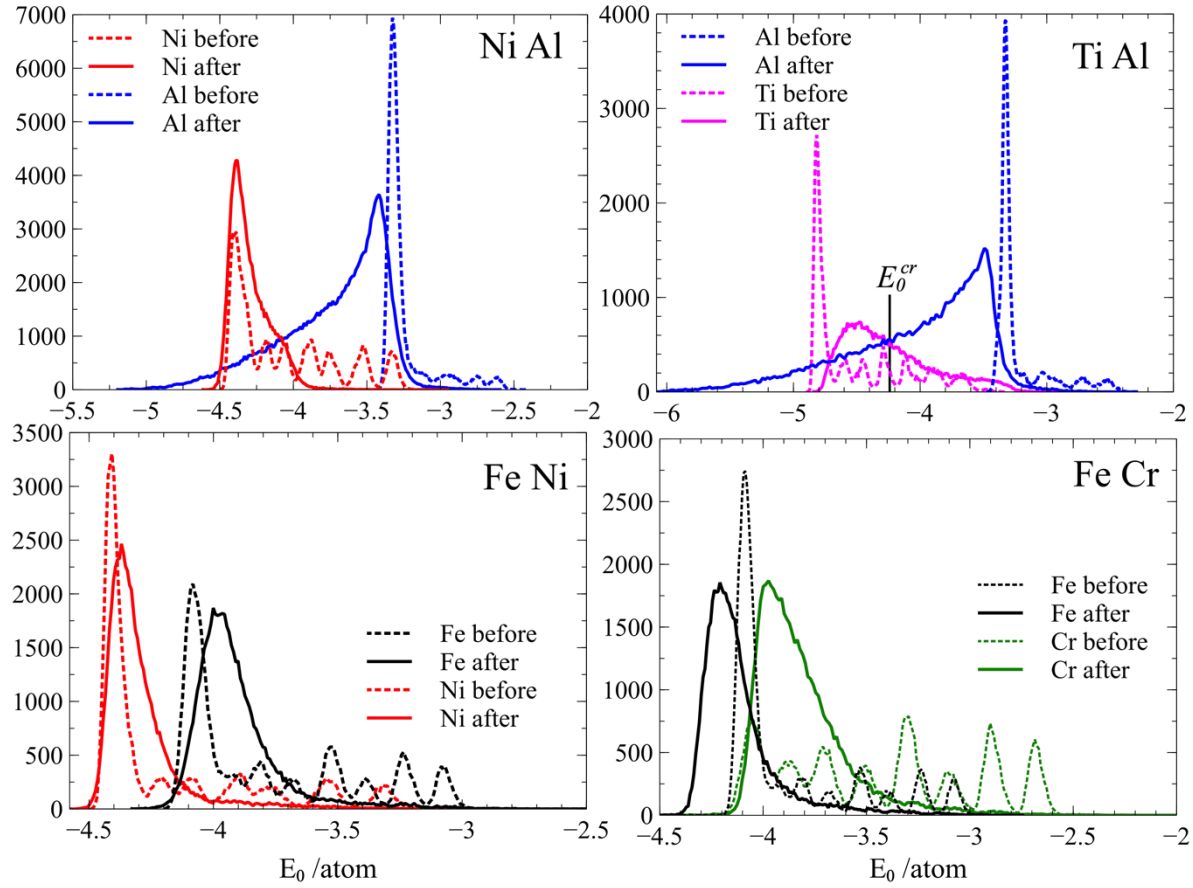

Figure 7: Histogram of potential energy per atom prior to deformation and at ϵ = 73 % in *end*-MZs.

3.2.2. Ti-Al system

The effect of deformation is noticeably different in the Ti–Al system. The layering of both elements is more pronounced. Here, the two elements have a different crystalline structure: *hcp*-Ti and *fcc*-Al, and the metallic radius of Ti is slightly larger than the metallic radius of Al: r_{metal}(Ti) = 1.47 pm and r_{metal}(Al) = 1.43 pm. The number of atoms in MZs after deformation does not exceed 7.6 at% (Table 4). The mole fraction in MZs after deformation, x_{MZ} = 45 at%, corresponds to an excess of Al compared to the value prior to deformation, x = 52 at%. Half of *end*-MZ atoms are amorphous, in equal ratios for Al and Ti. Other atoms are either *fcc* (32 at% in equal quantities for Al and Ti) or *hcp* (21 at%with an excess of Ti).

Partial RDFs keep a long-range order typical of an ordered crystalline structure (Fig. 6b). The $g_{\mathrm{TiTi}}(r)$ first peak shifts to a slightly lower value compared to the pure *hcp*-Ti first peak. The third and fourth peaks merge. The $g_{\mathrm{AlAl}}(r)$ peaks are located at positions corresponding to *fcc*-Al. These observations corroborate the existence of an *fcc* crystallographic structure in MZs after deformation. Histograms of potential energy per atom are plotted in Fig. 7b. The Al peakshifts to a lower value after deformation compared to the value prior to deformation. The Al distribution developed a long tail over a large range [-3.5 eV; -6 eV]. The opposite result is observed in the Ti histogram. There is an overlap of energies for Ti and Al atoms. The crossing value E_0^{Cr} of the two distributions corresponds to the energy value of Al atoms in direct contact with Ti atoms (or Ti with Al). This value corresponds to the situation where half of the nearest neighbors of Al(Ti) are Ti(Al) atoms. Aluminum (Titanium) atoms with E_0 lower (higher) than E_0^{Cr} are surrounded by a larger number of atoms of the other species. Figure 3b shows that a thick external shell of Ti particles contributes to CZs and MZs at the end of deformation, in comparison with the thin external shell for Ni particles in contact with Al (Fig. 3a).

Figure 5c depicts the typical microstructure of mixing zones after deformation in the case of monocrystalline particles. We noted *fcc*-arrangement of Ti and Al atoms in small hexagons in (111) orientation (highlighted in the insets). In Fig. 5d (polycrystalline particles), we observed ordered regions with *fcc*-atoms in MZs after deformation. A substantial number of Ti atoms adopt *fcc*-configuration when in contact with Al atoms. In other regions, MZs are amorphous, with dispersion of *unk*-Ti in a pool of *unk*-Al atoms. As in the case of the Ni–Al system, polycrystalline particles promote the mixing of atoms during deformation because of the increasing mobility of *unk*-atoms in internal grain boundaries.

3.2.3. Fe–Ni system

The effect of deformation was also analyzed in a system composed of monocrystalline *bcc*-Fe and *fcc*-Ni. Both elements have comparable hardness. Figure 5f shows that Fe particles keep their rounded shape and Ni particles are crushed. The CZs and MZs are mainly fed with atoms from the thin shells of Fe particles and the thicker shells of Ni particles, as shown in Fig. 3c. We observed the creation of defects in Ni particles in the form of stacking faults and localized amorphization. The number of atoms in MZs is considerably reduced (4.5 at%) compared to that of systems with Al, and the mole fraction in MZs is preserved. Amorphous atoms in MZs are in the majority (u_{MZ} = 62.5 at%), with an excess of Fe. Crystallized atoms in MZs are either *fcc*-atoms (21 at%) or *bcc*-atoms (12 at%). Only a small proportion of crystallized atoms adopt the structure of the other element. The partial RDF $g_{\mathrm{FeFe}}(r)$ partly loses the strict *bcc*-structure, while $g_{\mathrm{NiNi}}(r)$ keeps the long-range order (see Fig. 6c). The distributions of potential energy per atom developed a long tail for higher values of E_0 and their maximum shifted to the right (Fig. 7c). This result indicates a loss of stability for both elements. A typical MZ microstructure is presented in Fig. 5e. Typically, MZs are composed of *fcc*- Ni/*unk*-Fe or *bcc*-Fe/*unk*-Ni layers. A few atoms adopted the structure of the opposite element. In the case of the Fe–Ni system, deformation creates metastable mixing zones.

3.2.4. Fe-Cr system

Finally, we considered the effect of deformation in a system composed of monocrystalline *bcc*-Fe and *bcc*-Cr. A snapshot of the system after deformation is given in Fig. 5f Chromium hardness is much greater than that of iron. This may explain why Fe particles are crushed by Cr particles due to compression. The number of atoms in MZs is only 4.7 at%, with mole fraction x_{MZ} = 51 at%, almost equal to the mole fraction x = 50 at% of the global system. The majority of atoms in MZs are in *bcc*-configuration (68 at%). This observation is corroborated by the analysis of partial RDFs (Fig. 6d). Both elements in MZs keep their *bcc*-ordered configuration. Peaks correspond to nearest neighbor positions of *bcc*-Fe and *bcc*-Cr. Note that the lattice parameter of *bcc*-Cr is nearly equal to that of *bcc*-Fe. The maximum of the histogram E_0 per atom of Fe shifts slightly to the left, and that of Cr to the right (Fig. 7d). Both distributions developed along tail for higher values of E_0. Atoms in MZs are thus less stable compared to bulk atoms. As shown in Fig. 5f (inset), MZs contain layers composed of *bcc*-Fe and *bcc*-Cr or *unk*-Fe and *unk*-Cr. Only a few localized defects were created, in the form of amorphous atoms in particle cores. In the case of the Fe–Cr system, deformation gives rise to thin metastable mixing zones, with an excess of *bcc*-atoms.

3.3. Deformation and atom mobility

We noted that the number of atoms in CZs and MZs increased during compaction (Fig. 2b). Particle motion is relatively complex, and several types of impact were observed. As an example, the collision between one Ni particle and one Al particle is depicted in Fig. 8. An impact occurs when particles have a relative velocity normal to the surface where the contact takes place (Fig. 8a). At impact, the two particles were in contact, and locally Al atoms became amorphous (Fig. 8b). The Ni particle started to rotate. This induced friction between the two particles. We observed that the Ni particle caught Al *unk*-atoms that remained stuck to the particle. At the same time, the Al was crushed and lost its rounded shape (Fig. 8c). This sequence illustrates the very first steps of mechanical activation and the formation of mixing zones.

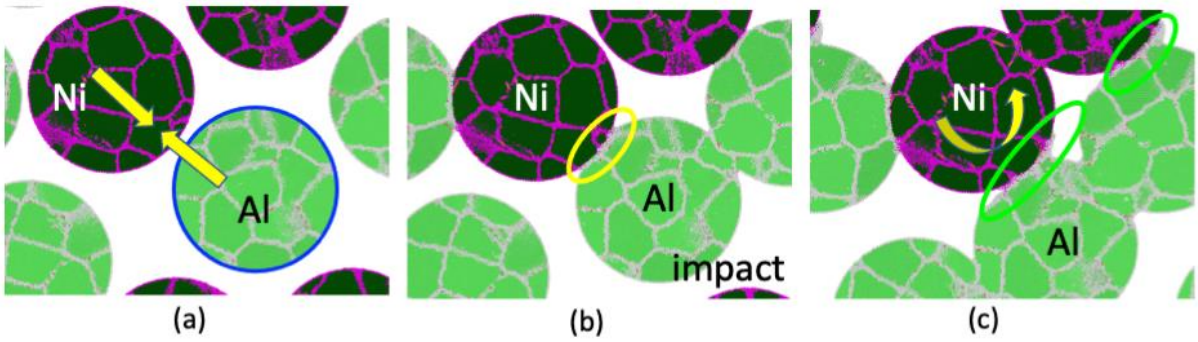

Figure 8: Ni–Al system: (a) collision between 2 particles. Arrows indicate the displacement direction. Blue circle marks the rounded shape of the Al particle prior to deformation. (b) Impact. The yellow ellipse indicates the contact zone. (c) Shearing between particles. The green ellipse indicates the contact zone. All atoms are represented with the color coding of Fig. 1.

Deformation induces a redistribution of atom positions in the system. Each particle has a distinct path during the simulation; hence, it is necessary to analyze particles one by one and to take into account the displacement of the center of mass of each particle in order to study atomic mobility. In order to follow atoms during compression, we introduced an indicator to determine how atom mobility was affected. We here consider the relative displacement of atoms with respect to the particle they belong to and define the mean square displacement associated with mechanical deformation, MSD_{deform}, as

$$MSD_{deform} = \frac{1}{N_{part}(K)} \sum_{j=1}^{N_{part}(K)} \frac{1}{N_{end-MZ}(K,j)} \sum_{i=1}^{N_{end-MZ(K,j)}} \left| r_i(t) - r_i(0) - (r_{CM_j}(t) - r_{CM_j(0))} \right|^2 \quad (2)$$

where $\epsilon = v.t$ is deformation and v the constant deformation rate, K corresponds to one of the two elements in the system (Al, Ni, Ti, Fe or Cr), $N_{part}(K)$ is the number of particles of the K element, $r_i(t)$ is the position of the i-th atom at time t, $r_{CMj}(t)$ is the center of mass position of the particle j, and $N_{end-MZ}(K, j)$ the number of atoms K in *end*-MZs of particle j. The MSD_{deform} as a function of deformation is presented in Fig. 9a. The behavior is very different for each binary system:

- In the Ni–Al system, Al is much more mobile than Ni. This could be related to the higher ductility of Al compared to Ni. In addition, the majority of Al atoms in MZs(86.3 at%) are amorphous (see Table 4), and amorphization promotes mobility. The Al mobility already starts at ϵ = 20 at% before plastic deformation. A possible mechanism is featured in Fig. 8, where amorphous Al atoms are stuck to the rotating Ni particle after impact.
- In the Ti–Al system, Al is less mobile than in the Ni–Al system. The mobility of both elements starts with plastic deformation. The interaction between Ti and Al is not strong enough to induce Al atoms to stick to Ti particles. The lower mobility of Al atoms is certainly due to the fact that half of the Al atoms in *end*-MZs are crystallized. The formation of *fcc*-seeds observed in MZs (Fig. 5d) restricts their mobility.
- In the Fe–Ni system, Fe and Ni are characterized by a similar hardness, and the number of *unk*-Ni is just slightly larger than the number of *unk*-Fe. Nevertheless, Ni atoms are more mobile than Fe atoms. The main difference between the two elements is the large number of planar defects in *fcc*-Ni particles compared to *bcc*-Fe particles (Fig. 5e). Figure 3c confirms the fact that more Ni atoms located in the core of the particles participate in MZs with increased mobility.
- In the Fe–Cr system, the hardness of Cr is greater than the hardness of Fe. This may explain the limited mobility of Cr atoms compared to Fe atoms. In addition, only 23 at% of Cr are amorphous in MZs. More *unk*-Fe atoms in MZs implies increased mobility.

The short-range order parameter Ω (Eq. (1)) as a function of deformation is depicted in Fig. 9. For all systems, we noted an acceleration of mixing during plastic deformation. Mixing efficiency correlates noticeably with atom mobility: Ω(Ni–Al) is higher at any deformation rate. Mixing is more pronounced for populated MZs:

$$n_{MZ}(\mathrm{Ni}-\mathrm{Al}) > n_{MZ}(\mathrm{Ti}-\mathrm{Al}) > n_{MZ}(\mathrm{Fe}-\mathrm{Ni}) \sim n_{MZ}(\mathrm{Fe}-\mathrm{Cr}).$$

But mixing is not directly related to the number of amorphous atoms in MZs:

$$u_{MZ}(\mathrm{Ni}-\mathrm{Al}) > u_{MZ}(\mathrm{Ti}-\mathrm{Al}) > u_{MZ}(\mathrm{Fe}-\mathrm{Ni}) > u_{MZ}(\mathrm{Fe}-\mathrm{Cr}).$$

As observed in the Ti–Al system, the formation of intermetallic seeds also leads to mixing. The analysis of the four binaries demonstrates that the effect of deformation is directly related both to mechanical properties and structural characteristics (crystallographic structure, lattice parameters, etc.) of ground elements. Solid-state solubility associated with MZs, structural transformations, and defects were actually induced by the mechanical treatment.

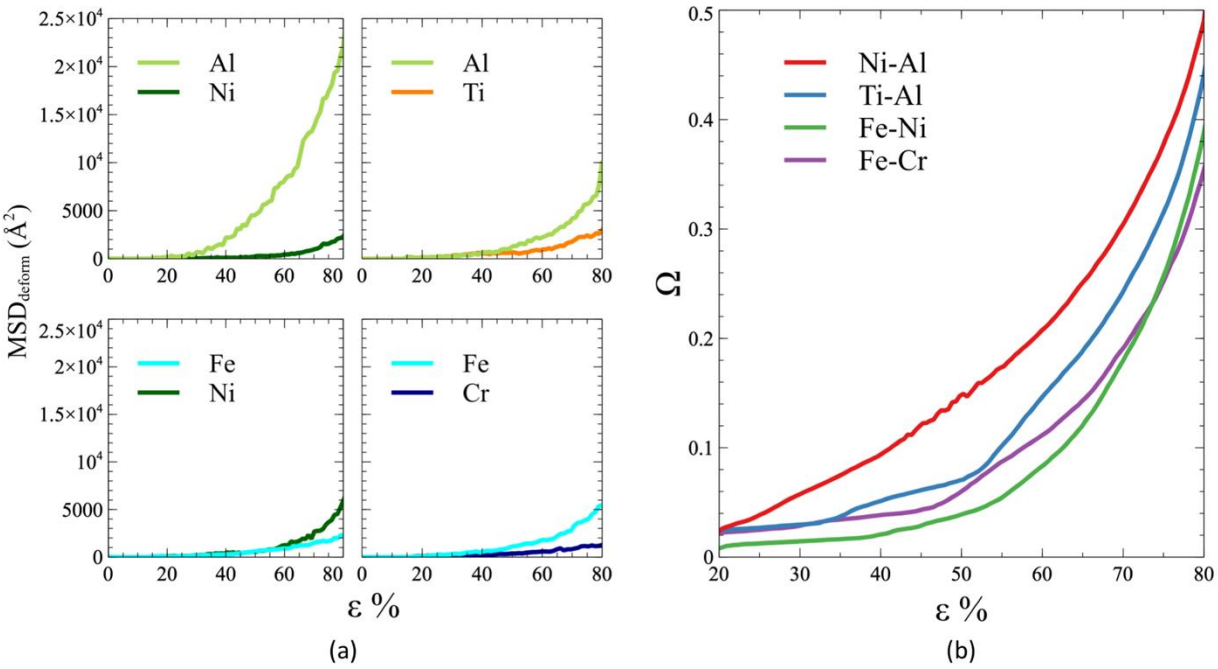

Figure 9: Evolution of the MSD$_{deform}$ (a) and mixing short-range order parameter Ω (b) among *end*-MZs during deformation for the four binary systems composed of monocrystalline particles.

4. Conclusion

In the present work, molecular dynamics simulations were used to provide in situ observations of the mechanical activation of a pulverulent mixture composed of two metallic powders. A system composed of nanometric particles of *K* and *L* (Ni–Al, Ti–Al, Fe–Ni, and Fe–Cr) was subjected to compaction and plastic deformation mimicking the action of grinding balls during mechanical treatment. The system was then studied during deformation in order to detect the effect of mechanical activation. We focused on the 3D defects created by mechanical activation, in particular mixing zones (MZs) where the two elements are in direct contact. The efficiency of mixing, the degree of amorphization, and atom mobility were quantified during deformation. Mixing zones are of special interest because they could play the role of precursor in subsequent alloying processes. We observed that the effect of deformation depends both on mechanical properties and on the structural characteristics of *K* and *L*. The main characteristics of mixing zones after deformation are summarized as follows:

- In the Ni–Al system, both elements are *fcc* but Ni is harder than Al ($H_{Ni} > H_{Al}$). Mechanical treatment produces thick and amorphous MZs with an excess of Al. The other crystallized atoms adopt the *fcc*-Ni lattice. In this case, the ductile element adheres easily to hard particles, as in a wetting process. This is corroborated by the high mobility of Al atoms that already occurs during the compaction stage. After plastic deformation is completed, *hcp* planar defects (stacking faults) are created in Ni particles.
- In the Ti–Al system, there is a considerable difference in hardness ($H_{Ti} \gg H_{Al}$), as in the Ni–Al system, but the elements have a different crystallographic structure (*hcp*-*fcc*). The consequences of mechanical treatment are very different in comparison with the Ni–Al system. Mixing zones have a limited extent, with only half of the atoms being amorphous, and a moderate excess of Al. Atom mobility is limited, and occurs during the plastic deformation stage. Crystallized atoms in MZs are *fcc*- Al, *fcc*-Ti, *hcp*-Al, or *hcp*-Ti. In other words, Al(Ti) can adopt the original Ti(Al) structure. Aluminum atoms are stabilized when they are in close vicinity to Ti atoms. This feature leads to the creation of *fcc* seeds that could play the role of nucleus in the formation of an intermetallic. After deformation, *fcc* stacking faults (2D) and *fcc* regions (3D) are created in Ti particles.
- In the Fe–Ni system, both elements have the same hardness ($H_{Fe} \sim H_{Ni}$) but a different crystallographic structure (*bcc*/*fcc*). After mechanical treatment, Ni particles are crushed by Fe particles that remain spherical. Thin mixing zones are formed with a majority of amorphous atoms and slightly more Ni *unk*-atoms. Crystallized atoms in MZs form layers of *fcc*-Ni/*unk*-Fe and *unk*- Ni/*bcc*-Fe. There is no mixing between *fcc* and *bcc* atoms. Stacking fault (*hcp*) defects are created in Ni particles after deformation is completed.
- In the Fe–Cr system, both elements are *bcc*, with a difference in hardness ($H_{Cr} \sim H_{Fe}$). Thin mixing zones with a low degree of amorphization are observed. Layers of *bcc*-Fe/*bcc*-Cr and *unk*-Fe/*unk*-Cr form the MZs. Amorphous defects are created in Fe particles.

Deformation due to mechanical activation leads to the formation of partly amorphous mixing zones. The nature and microstructure of MZs depend both on mechanical properties and on the microscopic characteristics of the pure elements.

Microscopic simulations provide an interesting tool to observe the effects of a mechanical treatment on the fabrication of nanocomposites. This work could be extended in order to take into account the activation associated with the friction of sliding interfaces. It would be interesting to estimate the efficiency of amorphization and chemical mixing, in the case where heat dissipation is taken into account. Another important issue is to understand the fragmentation process during HEBM. Alternative approach such as extended finite element method [48] could be undertaken to handle fracture and crack propagation at the mesoscopic scale.

References

[1] C. Suryanarayana, Mechanical alloying and milling, Prog. Mater. Sci. (2001) 184.

[2] P. Baláž, M. Achimovičová, M. Baláž, P. Billik, Z. Cherkezova-Zheleva, J.M. Criado, F. Delogu, E. Dutková, E. Gaffet, F.J. Gotor, R. Kumar, I. Mitov, T. Rojac, M. Senna, A. Streletskii, K. Wieczorek-Ciurowa, Hallmarks of mechanochemistry: from nanoparticles to technology, Chem. Soc. Rev. 42 (2013) 7571–7637. https://doi.org/10.1039/C3CS35468G.

[3] A.S. Rogachev, Mechanical activation of heterogeneous exothermic reactions in powder mixtures, Russ. Chem. Rev. 88 (2019) 875–900. https://doi.org/10.1070/RCR4884.

[4] S. Paris, E. Gaffet, F. Bernard, Z.A. Munir, Spark plasma synthesis from mechanically activated powders: a versatile route for producing dense nanostructured iron aluminides, Scr. Mater. 50 (2004) 691–696. https://doi.org/10.1016/j.scriptamat.2003.11.019.

[5] A. Fourmont, S. Le Gallet, O. Politano, C. Desgranges, F. Baras, Effects of planetary ball milling on AlCoCrFeNi high entropy alloys prepared by Spark Plasma Sintering: Experiments and molecular dynamics study, J. Alloys Compd. 820 (2020) 153448. https://doi.org/10.1016/j.jallcom.2019.153448.

[6] A.A. Nepapushev, D.O. Moskovskikh, V.S. Buinevich, S.G. Vadchenko, A.S. Rogachev, Production of Rounded Reactive Composite Ti/Al Powders for Selective Laser Melting by High-Energy Ball Milling, Metall. Mater. Trans. B. 50 (2019) 1241–1247. https://doi.org/10.1007/s11663-019-01553-9.

[7] Q. Nguyen, C. Huang, M. Schoenitz, K.T. Sullivan, E.L. Dreizin, Nanocomposite thermite powders with improved flowability prepared by mechanical milling, Powder Technol. 327 (2018) 368–380. https://doi.org/10.1016/j.powtec.2017.12.082.

[8] S. Beinert, G. Fragnière, C. Schilde, A. Kwade, Analysis and modelling of bead contacts in wet-operating stirred media and planetary ball mills with CFD–DEM simulations, Chem. Eng. Sci. 134 (2015) 648–662. https://doi.org/10.1016/j.ces.2015.05.063.

[9] S. Rosenkranz, S. Breitung-Faes, A. Kwade, Experimental investigations and modelling of the ball motion in planetary ball mills, Powder Technol. 212 (2011) 224–230. https://doi.org/10.1016/j.powtec.2011.05.021.

[10] C.F. Burmeister, A. Kwade, Process engineering with planetary ball mills, Chem. Soc. Rev. 42 (2013) 7660–7667. https://doi.org/10.1039/C3CS35455E.

[11] A.S. Rogachev, D.O. Moskovskikh, A.A. Nepapushev, T.A. Sviridova, S.G. Vadchenko, S.A. Rogachev, A.S. Mukasyan, Experimental investigation of milling regimes in planetary ball mill and their influence on structure and reactivity of gasless powder

exothermic mixtures, Powder Technol. 274 (2015) 44–52. https://doi.org/10.1016/j.powtec.2015.01.009.

[12] U. Hoffmann, C. Horst, E. Kunz, Reactive comminution, in: Integr. Chem. Process., K. Sundmacher, A. Keinle, A. Seidel-Morgenstern, Wiley, Hoboken, 2005: pp. 407–436.

[13] B.B. Khina, Effect of mechanical activation on SHS: Physicochemical mechanism, Int. J. Self-Propagating High-Temp. Synth. 17 (2008) 211. https://doi.org/10.3103/S1061386208040018.

[14] A.S. Mukasyan, B.B. Khina, R.V. Reeves, S.F. Son, Mechanical activation and gasless explosion: Nanostructural aspects, Chem. Eng. J. 174 (2011) 677–686. https://doi.org/10.1016/j.cej.2011.09.028.

[15] A.S. Rogachev, N.F. Shkodich, S.G. Vadchenko, F. Baras, R. Chassagnon, N.V. Sachkova, O.D. Boyarchenko, Reactivity of mechanically activated powder blends: Role of micro and nano structures, Int. J. Self-Propagating High-Temp. Synth. 22 (2013) 210–216. https://doi.org/10.3103/S1061386213040067.

[16] A.S. Rogachev, N.F. Shkodich, S.G. Vadchenko, F. Baras, D.Yu. Kovalev, S. Rouvimov, A.A. Nepapushev, A.S. Mukasyan, Influence of the high energy ball milling on structure and reactivity of the Ni+Al powder mixture, J. Alloys Compd. 577 (2013) 600–605. https://doi.org/10.1016/j.jallcom.2013.06.114.

[17] C.E. Shuck, A.S. Mukasyan, Reactive Ni/Al Nanocomposites: Structural Characteristics and Activation Energy, J. Phys. Chem. A. 121 (2017) 1175–1181. https://doi.org/10.1021/acs.jpca.6b12314.

[18] S. Odunuga, Y. Li, P. Krasnochtchekov, P. Bellon, R.S. Averback, Forced Chemical Mixing in Alloys Driven by Plastic Deformation, Phys. Rev. Lett. 95 (2005) 045901. https://doi.org/10.1103/PhysRevLett.95.045901.

[19] F. Delogu, Forced chemical mixing in model immiscible systems under plastic deformation, J. Appl. Phys. 104 (2008) 073533. https://doi.org/10.1063/1.2987476.

[20] A.C. Lund, C.A. Schuh, Molecular simulation of amorphization by mechanical alloying, Acta Mater. 52 (2004) 2123–2132. https://doi.org/10.1016/j.actamat.2004.01.004.

[21] J.E. Hammerberg, B.L. Holian, S.J. Zhou, Studies of sliding friction in compressed copper, AIP Conf. Proc. 370 (1996) 307–311. https://doi.org/10.1063/1.50796.

[22] D.A. Rigney, S. Karthikeyan, The Evolution of Tribomaterial During Sliding: A Brief Introduction, Tribol. Lett. 39 (2010) 3–7. https://doi.org/10.1007/s11249-009-9498-3.

[23] N.Q. Vo, J. Zhou, Y. Ashkenazy, D. Schwen, R.S. Averback, P. Bellon, Atomic Mixing in Metals Under Shear Deformation, JOM. 65 (2013) 382–389. https://doi.org/10.1007/s11837-012-0542-7.

[24] E.-Q. Lin, L.-S. Niu, H.-J. Shi, Z. Duan, Molecular dynamics simulation of nano-scale interfacial friction characteristic for different tribopair systems, Appl. Surf. Sci. 258 (2012) 2022–2028. https://doi.org/10.1016/j.apsusc.2011.04.117.

[25] K. Chen, L. Wang, Y. Chen, Q. Wang, Molecular dynamics simulation of microstructure evolution and heat dissipation of nanoscale friction, Int. J. Heat Mass Transf. 109 (2017) 293–301. https://doi.org/10.1016/j.ijheatmasstransfer.2017.01.105.

[26] M.J. Cherukara, T.C. Germann, E.M. Kober, A. Strachan, Shock Loading of Granular Ni/Al Composites. Part 1: Mechanics of Loading, J. Phys. Chem. C. 118 (2014) 26377–26386. https://doi.org/10.1021/jp507795w.

[27] M.J. Cherukara, T.C. Germann, E.M. Kober, A. Strachan, Shock Loading of Granular Ni/Al Composites. Part 2: Shock-Induced Chemistry, J. Phys. Chem. C. 120 (2016) 6804–6813. https://doi.org/10.1021/acs.jpcc.5b11528.

[28] K.V. Manukyan, B.A. Mason, L.J. Groven, Y.-C. Lin, M. Cherukara, S.F. Son, A. Strachan, A.S. Mukasyan, Tailored Reactivity of Ni+Al Nanocomposites: Microstructural Correlations, J. Phys. Chem. C. 116 (2012) 21027–21038. https://doi.org/10.1021/jp303407e.

[29] A. Fourmont, O. Politano, S. Le Gallet, C. Desgranges, F. Baras, Reactivity of Ni–Al nanocomposites prepared by mechanical activation: A molecular dynamics study, J. Appl. Phys. 129 (2021) 065301. https://doi.org/10.1063/5.0037397.

[30] D.R. Maurice, T.H. Courtney, The physics of mechanical alloying: A first report, Metall. Trans. A. 21 (1990) 289–303. https://doi.org/10.1007/BF02782409.

[31] S. Plimpton, Fast Parallel Algorithms for Short–Range Molecular Dynamics, J. Comput. Phys. 117 (1995) 42. https://doi.org/10.1006/jcph.1995.1039.

[32] A. Perron, S. Garruchet, O. Politano, G. Aral, V. Vignal, Oxidation of nanocrystalline aluminum by variable charge molecular dynamics, J. Phys. Chem. Solids. 71 (2010) 119–124. https://doi.org/10.1016/j.jpcs.2009.09.008.

[33] O. Politano, F. Baras, Reaction front propagation in nanocrystalline Ni/Al composites: A molecular dynamics study, J. Appl. Phys. 128 (2020) 215301. https://doi.org/10.1063/5.0028054.

[34] G.P. Purja Pun, Y. Mishin, Development of an interatomic potential for the Ni-Al system, Philos. Mag. 89 (2009) 3245–3267. https://doi.org/10.1080/14786430903258184.

[35] R.R. Zope, Y. Mishin, Interatomic potentials for atomistic simulations of the Ti-Al system, Phys. Rev. B. 68 (2003) 024102. https://doi.org/10.1103/PhysRevB.68.024102.

[36] G. Bonny, R.C. Pasianot, L. Malerba, Fe–Ni many-body potential for metallurgical applications, Model. Simul. Mater. Sci. Eng. 17 (2009) 025010. https://doi.org/10.1088/0965-0393/17/2/025010.

[37] G. Bonny, R.C. Pasianot, D. Terentyev, L. Malerba, Iron chromium potential to model high-chromium ferritic alloys, Philos. Mag. 91 (2011) 1724–1746. https://doi.org/10.1080/14786435.2010.545780.

[38] F. Delogu, G. Cocco, Numerical simulations of structural modifications at a Ni − Zr sliding interface, Phys. Rev. B. 72 (2005). https://doi.org/10.1103/PhysRevB.72.014124.

[39] P. Zhang, S.X. Li, Z.F. Zhang, General relationship between strength and hardness, Mater. Sci. Eng. A. 529 (2011) 62–73. https://doi.org/10.1016/j.msea.2011.08.061.

[40] A. Stukowski, Visualization and analysis of atomistic simulation data with OVITO–the Open Visualization Tool, Model. Simul. Mater. Sci. Eng. 18 (2009) 015012. https://doi.org/10.1088/0965-0393/18/1/015012.

[41] A. Stukowski, Structure identification methods for atomistic simulations of crystalline materials, Model. Simul. Mater. Sci. Eng. 20 (2012) 045021. https://doi.org/10.1088/0965-0393/20/4/045021.

[42] A. Stukowski, Dislocation analysis tool for atomistic simulations, in: Handb. Mater. Model., ed. by W. Andreoni, S. Yip, Springer, Cham, 2018.

[43] O. Politano, A. Fourmont, S.L. Gallet, F. Baras, A.A. Nepapushev, A.S. Sedegov, S.G. Vadchenko, A.S. Rogachev, Mechanical activation of metallic powders in planetary ball

mills: multi-scale modeling and experimental observation, IOP Conf. Ser. Mater. Sci. Eng. 558 (2019) 012034. https://doi.org/10.1088/1757-899X/558/1/012034.

[44] A.C. Lund, C.A. Schuh, Topological and chemical arrangement of binary alloys during severe deformation, J. Appl. Phys. 95 (2004) 4815–4822. https://doi.org/10.1063/1.1691481.

[45] R. Banerjee, R. Ahuja, H.L. Fraser, Dimensionally Induced Structural transformations in Titanium-Aluminum Multilayers, Phys. Rev. Lett. 76 (1996) 3778–3781. https://doi.org/10.1103/PhysRevLett.76.3778.

[46] S.K. Maurya, J.F. Nie, A. Alankar, Atomistic analyses of HCP-FCC transformation and reorientation of Ti in Al-Ti multilayers, Comput. Mater. Sci. 192 (2021) 110329. https://doi.org/10.1016/j.commatsci.2021.110329.

[47] Q. Bizot, O. Politano, A.A. Nepapushev, S.G. Vadchenko, A.S. Rogachev, F. Baras, Reactivity of the Ti–Al system: Experimental study and molecular dynamics simulations, J. Appl. Phys. 127 (2020) 145304. https://doi.org/10.1063/5.0004550.

[48] K.M. Hamdia, T. Rabczuk, Key Parameters for Fracture Toughness of Particle/Polymer Nanocomposites; Sensitivity Analysis via XFEM Modeling Approach, in: M. Abdel Wahab (Ed.), Proc. 7th Int. Conf. Fract. Fatigue Wear, Springer, Singapore, 2019: pp. 41–51. https://doi.org/10.1007/978-981-13-0411-8_4.

Chapter III: Reactivity of Ni–Al nanocomposites prepared by mechanical activation: A molecular dynamics study

1. Introduction

Milling several compounds in order to mix them is a very old and common technique. However, high energy milling is relatively new to the domain of metallurgy [1]. Despite its widespread use today, the high energy ball milling of metallic powders is not completely understood, especially in terms of the evolution of the microstructure at atomic scale during the milling or even the description of ball movement [2]. In the area of Self-Propagating High Temperature Synthesis (SHS), high energy ball milling is a well-known elaboration process. First, two compounds are milled together and then the milled powders are heated at a low temperature (up to 900 K). When the ignition temperature is reached, the reaction starts and self-propagates. It has been observed that milling two powders leads to high reactivity and solid-state reactions, which translate into a lower ignition temperature and a faster reaction [3-5]. In this situation, the amount of the liquid phase is reduced, and the reaction occurs at a moderate temperature as compared to other SHS processes such as SHS in nanolaminates. One of the more widely studied systems is the Ni-Al system which forms the intermetallic $Ni_{50}Al_{50}$ compound with an ordered *B2* structure. To explain this high reactivity, Rogachev *et al.* studied milled powders of Ni+Al by means of High-Resolution Transmission Electron Microscopy (HRTEM) and suggested 6 activating factors [6]:

(i) decreasing apparent activation energy by the magnitude of the energy stored in reactants during MA;
(ii) increasing atomic mobility due to high concentration of the grain boundaries anddefects created by plastic deformation;
(iii) formation of non-equilibrium meta-stable phases;
(iv) increase in the contact (interfacial) surface area between reactants;
(v) formation of freshly formed reactive surfaces; and
(vi) nano-scale mixing of the reagents.

These factors are nearly impossible to thoroughly study experimentally because of the time and space scales. Despite the recent success of innovative experiments investigating milling regimes in planetary ball mills [7], today's technologies do not make in-situ microscopic observations possible. Thus, microscopic simulations such as Molecular Dynamics (MD) could provide a useful tool to describe both milling and SHS processes. The milling mechanism has been modelized in several ways in the literature. The sliding of metallic blocks and the subsequent friction leading to mixing has been studied by several research groups [8-10].

They have observed mixing at the atomic scale in an amorphous zone and have noted that the mixing resulted from ballistic diffusion rather than classic thermal diffusion. These teams also observed the formation of structural defects resulting from this friction. Chen *et al.* studied the sliding of blocks of Ni and Al. They have reported that the mixing layer is mainly formed in the softer Al material [11,12]. Odunuga *et al.* and Delogu *et al.* evaluated another kind of simulation using cyclic deformations that mimic milling [13,14]. They studied forced chemical mixing driven by plastic deformation and observed that the mixing resulted from dislocation gliding and that it was similar to the mixing of a substance subject to a turbulent flow. The reactivity of these simulated systems is to analyze because two main, interdependent aspects have to be considered: the creation of structural defects and the induced chemical mixing. Adding to the complexity of analysis is the fact that the importance of one aspect could overtake that of the other due to issues of scale.

Microscopic simulation of the reactivity of a milled system is a challenging undertaking because of the co-occurrence of many factors. Preliminary attempts to examine the reactivity of activated systems have been carried out in specific cases.
Cherukara *et al.*, Manukyan *et al.* and Xiong *et al.* studied the shock between powder particles and the subsequent reactivity [15-18]. Here, the rise in temperature is a consequence of the impact, contrary to the case of a classic SHS process. This is a one stepprocess: shock-induced chemistry. The authors demonstrated that in this case, compression is associated with the sharp rise in temperature and that the subsequent reaction isdominated by interdiffusion. They also showed that porosities play a major role by acting as hot spots during the deformation [17]. Witbeck *et al.* have evaluated the effects of lattice defects and grain boundaries [19,20]. This work corresponds to an exploration of activating factor (ii). The authors observed that point defects greatly increased the reactionspeed in SHS propagation, whereas grain boundaries acted as heterogeneous nucleationsites in the formation of the intermetallic compound *B2*-NiAl which further inhibited Ni diffusion. This study was performed in the context of nanolaminates where temperature increased tremendously (up to 2200K); indeed, temperature is the key factor in the reaction. However, these findings are not necessarily relevant to the case of milled systems, in which temperature and the resulting diffusion are not likely to be the main factors. Crone *et al.* and Cherukara *et al.* have indirectly studied activating factors (iv) and (v): the effect of surfaces [21,22]. They have reported that the misfit strain decreased the activation energy of the reaction. They also observed that voids and porosity led to a slower mechanism compared to the case in which the two elements were in direct contact. The Weihs group has indirectly studied (vi) in the case of temperature driven mixing [23-25]. They noted that a pre-mixing step hindered diffusion and that a nano-scale gradient suppressed the homogeneous nucleation of *B2*-NiAl. They also observed that *B2*-NiAl readily nucleates and grows at the interface between an amorphous pre-mixed region and an *fcc*-Ni block. Kuhn *et al.* and Ovrutsky *et al.* have studied nucleation in an $Ni_{50}Al_{50}$ undercooled amorphous zone [26,27]. They analyzed the crystallization resulting from decreasing temperature. They observed that nucleation occurred in two steps: segregation of the Ni and Al into an amorphous but ordered structure, and, then, crystallization into the *B2* compound. They observed that *B2*-NiAl homogeneous nucleation began at 900 K. Examining the case of a bilayer configuration, Baras *et al.* have reported that the crystallization of *B2*-NiAl resulted from a liquid phase [28,29].

A systematic study of the effect of mixing (vi) in the framework of milled systems is still lacking. Indeed, two main parameters significantly differ from those which apply to studies on laminate systems: first, the temperature range is significantly lower and secondly, the reaction mainly occurs in solid-state. In addition, the microstructure of such systems includes more defects in the form of large amorphous zones generated during the milling process. It is nearly impossible to take into account all the significant parameters to model a real-world milled Ni/Al reactive materials at once. In the present work, we focused on the effect of pre-mixing in an amorphous system and on the resulting crystallization of *B2*-NiAl at low temperatures (below the melting temperature of Al). Indeed, a careful examination on the current literature on the topic led us to believethat this viewing angle was of primary importance [30]. This study modelized a two-step process in which the reactants are first milled and then heated, as is usually the case insuch experiments.

2. Simulation details

To describe the Ni-Al system, we employed the classic Molecular Dynamics (MD) approach using the Embedded-Atom Method (EAM) potential developed by Purja Punand Mishin [31]. This interatomic potential has been fitted to reproduce a large set of physical quantities determined experimentally or by ab-initio calculations. It therefore accurately describes the main physical properties of the pure elements (i.e. Ni and Al) as well as selected intermetallic compounds, namely *B2*-NiAl and $L1_2$-Ni_3Al. Despite its good transferability, this potential necessarily deals with a simplified system containing a limited number of phases as compared to a real Ni-Al system. Table 1 reports the melting temperature, cohesive energies and lattice parameters computed using this potential [32]. The MD simulations were conducted using the Large-scale Atomic/Molecular Massively Parallel Simulator (LAMMPS) open-source software [33] and the atomic visualizations were effected via the Open Visualization Tool (OVITO) [34].

	Thermodynamic properties		Structural properties	
Phase	T_m (K)	T_m exp. (K)	Cohesive energy (eV)	Lattice parameter (nm)
Ni	1710	1728	-4.45	0.352
Al	1055	933	-3.36	0.405
B2-NiAl	1675	1850	-4.51	0.283
$L1_2$-Ni_3Al	1755	1720	-4.63	0.353

Table 1: Physical properties of pure elements and intermetallics calculated using Purja Pun and Mishin [31]. For more details, see Turlo *et al.* [32]

Following on from our previous work [28], we considered a layered Ni-Al-Ni system with the following characteristics. The reference system is made up of one layer of Al of 35 atomic planes in between two Ni layers of 36 atomic planes each along the z-direction (Fig. 1a). Both pure metals are in *fcc* configuration and the interface orientation is (001). The typical size of the simulation box is $Lx = Ly \sim 14$ nm and $Lz = 20$ nm. The system is submitted to periodic

boundary conditions in all directions. The initial distance δ between the Ni- and Al-atomic planes at the interface is 2.5 Å. The system is made up of 305 214 atoms (n(Ni) = 231 276 and n(Al) = 73 938). The inner layer is defined as the layer of Al plus 3 atomic planes of Ni interfaces on each side. The width in the x and y directions of the inner layer is chosen to be smaller than that of the outer Ni layers (Lx(inner) < Lx(outer) and Ly(inner) < Ly(outer)). The thickness of the inner layer is 8.3 nm. This specific geometry including a narrower inner layer allows us to avoid artificial constraints due to the application of periodicity on both inner and outer layers during the construction of the system and its subsequent evolution. Each system is then denoted as 'REFxxK' where xx K refers to the temperature of the simulation (see Table 2).

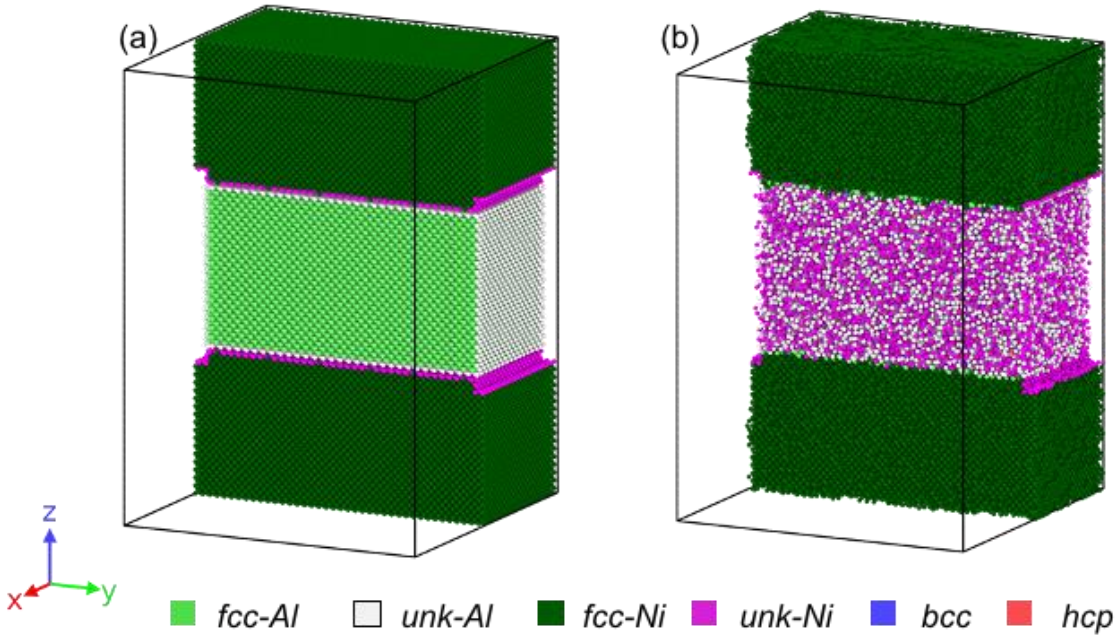

Figure 1: Geometry of the system. (a) Reference system. (b) Mixing layer. Dark green = *fcc*-Ni, light green = *fcc*-Al, pink = *unk*-Ni, and white =*unk*-Al, where *unk* stands for unknown atoms.

After high energy ball milling of Ni-Al powders, one can observe around the remaining Ni grains (the toughest element) a mixed layer composed of highly crushed Al with a certain quantity of Ni.

In order to mimic this mixing layer resulting from mechanical activation, a microstructure consisting of an amorphous layer placed in between two Ni layers was designed. The *fcc*-Ni / *fcc*-Al / *fcc*-Ni system was heated to above the melting temperature of Al and Ni (2000 K) in the isothermal-isobaric ensemble (NPT) over a very short time, namely 10 ps. This heating step resulted in the complete melting of the Al layer but an incomplete melting of the Ni. The sample was then cooled to room temperature (300 K) over 10 ps. The inner Al layer became amorphous while the outer layer remained crystallized at the end of this rapid heating-cooling treatment. The *mixing layer* is defined as a layer of 7.8 nm in thickness along the z-direction in the middle of the system. The mixing layer is just slightly narrower than the inner layer. A random substitution of the atoms in the mixing layer according to their type was then carried out in order to fix the Ni concentration (ranging from 10 to 60 at. %). The energy of the system was

then minimized by means of a conjugate gradient procedure. The goal of the above procedure was to create a representative model microstructure acting as a starting configuration for the reactivity simulation. It does not reflect any sequence of physical phenomena and only the resulting bilayer configuration with a pre-mixed zone is of interest. Each system is denoted 'MLXX%*xx*K' where the mixing layer consists of XX at. % of Ni and xx K is the temperature of the simulation (see Table 2). The system contains 305 013 atoms with n(ML) = 85 220 in the mixing layer. For example, the mixing layer in the ML20% system contains 17 036 Ni atoms. In order to ensure that most of the mixing layer was truly amorphous at 300 K, we chose to consider the pair correlation function $g(r)$ of the mixing layer as our main criterion. The $g(r)$ functions of the inner layers of our different systems are displayed in Fig. 2. The pair correlation function of the mixing layer created in this way is similar to that of a liq-Al system (i.e. melted Al) generated by heating *fcc*-Al at 2000 K over a long period: 3 ns. Hence, the amorphous character of the mixing layer is indeed mimicked by means of this rapid heating-cooling treatment. Note that the substitution ratio does not modify the degree of amorphisation. The configuration of the initial system with a mixing layer is depicted in Fig. 1b. In order to study the reactivity of such systems, both REF and MLXX% systems were studied at various temperatures in the isothermal-isobaric ensemble (NPT) in the range of 600 K-1200 K around the bulk melting temperature of aluminum.

Generic name	Ni at. %[a]	Temperature (K)	Name
REF (reference system)	0	600	REF600K
		800	REF800K
		900	REF900K
		1200	REF1200K
ML (Mixing layer)	20	900	ML20%900K
	20	1200	ML20%1200K
ML (Mixing layer)	30	900	ML30%900K
	30	1200	ML30%1200K
ML (Mixing layer)	40	900	ML40%900K
	40	1200	ML40%1200K
ML (Mixing layer)	50	600	ML50%600K
	50	800	ML50%800K
	50	900	ML50%900K
	50	1200	ML50%1200K
ML (Mixing layer)	60	1200	ML60%1200K

Table 2: Set of simulated systems.

[a]In the mixing layer.

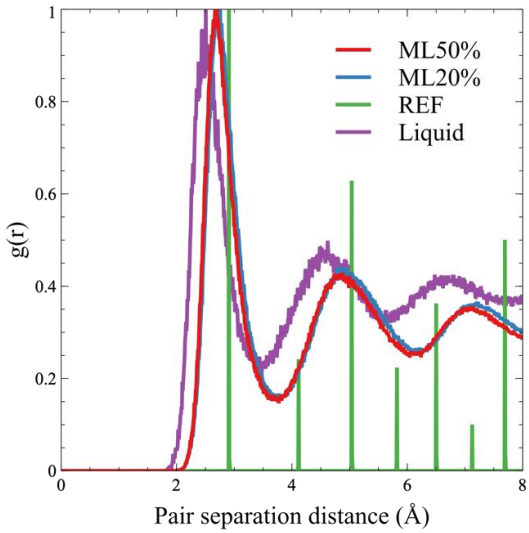

Figure 2: Pair correlation function g(r) of the initial configurations after the procedure, normalized on the first peak. g(r) in the case of pure liquid Ni+Al has been added for the sake of information.

Several indicators allow us to follow the evolution of the system at the microscopic level. If we calculate the local lattice structure according to the common neighbor analysis, we obtain the local configuration around a given atom. It is possible to distinguish between different configurations: *bcc* (1), *fcc* (2), *hcp*, and unknown (0). Each atom is thus labeled by the color of the species and by its local lattice structure. The potential energy per atom, which is very sensitive to the local environment of a given atom, was also evaluated. In addition, global indicators were followed during the evolution of thesystem: the atomic percentage of Ni atoms in the inner or mixing layer; the amount of *bcc*-atoms in at.% out of the maximum that could be formed

$$\Xi = 100 \times \frac{n(bcc)}{2 \times n(Al)} \quad (1)$$

where $n(bcc)$ and $n(\mathrm{Al})$ are the numbers of *B2*- and Al-atoms in the mixing layer (*B2* atoms form a *bcc* lattice if we do not make the distinction between atomic species). If all Al-atoms are *bcc*, Ξ is close to 100 % and the phase is pure *B2*-NiAl. Ξ makes the comparison between several stoichiometries possible. A cluster analysis was developed in order to analyze the nucleation and growth of the intermetallic phase during evolution of the system. A cluster of atoms is defined as a set of neighboring *bcc* atoms. If the cluster is made up of at least 20 atoms, the cluster is counted as a nucleus.

3. Results and discussion

In a bilayered system Ni-Al-Ni, the typical evolution at an elevated temperature consists of several stages: the melting of aluminum, the progressive dissolution of Ni-atoms into the liquid layer and, eventually, the formation of *B2*-NiAl at interfaces. The corresponding scheme of reaction reads as follows:

$$\mathrm{Ni(s) + Al(l) \rightarrow Ni(s) + AlNi_x(l) \rightarrow Ni(s) + AlNi_{x'}(l) + NiAl(s)} \quad (2)$$

This mechanism is named *mosaic dissolution-precipitation* [35]. After saturation of the Al- melt by Ni-atoms, crystallites of the intermetallic products (NiAl) nucleate at the solid-liquid interface and grow along this interface. The microstructure consists of rounded NiAl grains separated by liquid gaps. Further growth of NiAl crystallites occurs due to diffusion through liquid gaps and precipitation at the intermetallic-liquid interface.

Fig. 3 tracks the evolution of amorphous- and *fcc*-atoms in the reference system at 1200 K (REF1200K), above the melting temperature of Al. The rapid increase in the number of amorphous atoms and decrease in *fcc*-atoms corresponds to the melting of the inner layer. This melting step occurs in less than 0.2 ns. From 0.2 to 2 ns, the number of *fcc*-atoms slowly decreases while the number of amorphous atoms increases. This corresponds to the progressive dissolution of Ni into liquid Al. At 2 ns, the number of amorphous atoms reaches a maximum and *B2*-NiAl starts to form (formation of *B2*- NiAl is followed by Ξ). A plateau is reached at about 8 ns. More than half of the Al-atoms remain in the liquid state.
Next, we considered a system with a premixed layer that mimics an activated Ni/Alsystem after milling. The mixing layer contains 50 at.% of Ni and the bilayer is heatedat 1200 K. The behavior of the ML50% system is actually very different from that of the REF1200K. There is

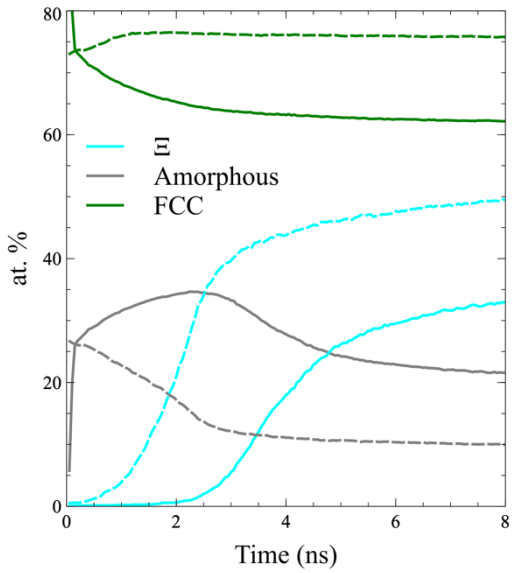

Figure 3: Evolution of the structure type as a function of time at 1200 K. Dashed lines correspond to the ML50%1200K system and solid lines to the REF1200K system.

no delay in the formation of *B2*-NiAl and the ratio Ξ reaches a higher value close to 50%. The decrease in *unk*-atoms (amorphous) is concomitant with the formation of *B2*-NiAl. As amorphous Al- and Ni-atoms are present in the mixing layer from the start, the reorganization of atoms takes place from the very beginning. No prior melting was required. Note that the number of *fcc*-atoms increased slightly at the start of the phase transformation before reaching a plateau. We observed that the number of *fcc*-atoms is higher in the ML50% system as depicted in Fig. 9.

The main differences observed are certainly due to the fact that the melting and dissolution steps have already been performed in ML50%. However, it has been noted that a mixing layer hinders diffusion [23]. Indeed, according to Fick's Law, the concentration gradient decreases and diffusion slows down. In addition, diffusion of Ni atoms in a Nickel amorphous zone is known to be faster than in a Nickel crystalline zone, as it was reported by Manukyan *et al.* for instance [36]; in this case, the use of amorphous Ni as reactant was proved to be more efficient than crystalline Ni.

In order to evaluate the effect of melting/dissolution as compared to diffusion in *B2*- formation, we studied the diffusion of Ni-atoms in both systems. Figure 4a depicts the evolution of the Ni concentration (at.%) in the mixing layer and the evolution of the *B2* phase in the ML50% and REF systems. Ni concentrations were calculated in the whole mixing layer (solid lines) and in the 1 nm slice just above or below the interface (dashed lines) in order to evaluate the dissolution of Ni coming from the two *fcc*-Ni blocks. We also considered the ML20% system at 1200 K, where the inner layer is not saturated in Ni. The evolution of Ni-concentration can be correlated with the appearance of *B2*-nuclei as shown in Fig. 4b.
In ML50%, the Ni concentration does not evolve much since the inner layer is closeto saturation in Ni [37]. There is nevertheless some limited diffusion at the interface. The only phenomenon which occurs is the ordering in *B2*. Nucleation proceeds very quickly until 0.5 ns at which point the seeds coalesce. In the end, there is one main grain of 34000 atoms. In a perfect *B2* structure, the grain corresponds to a total volume of 410 nm^3. Assuming the grain is a sphere, it has a radius of 4.6 nm.
In ML20%, the Ni concentration in the 1nm slice close to the interface undergoes asharp increase until 0.5 ns, then continues to increase. The Ni concentration in the entiremixing layer increases more slowly and reaches a plateau value of approximately 35% at 3.5 ns. The inflexion point in the evolution of Ξ in ML20% corresponds to the plateauin Ni concentration. The formation of *B2*-NiAl seems to begin efficiently when the Ni concentration in the whole layer reaches a steady value. From 0.5 to 2 ns, Ni-atoms migrated from interfaces to the 'center' of the mixing layer and *B2* seeds appeared. After 1.5 ns, nucleation takes place with an increasing number of nuclei (Fig. 4b). After 3 ns, the number of nuclei decreased but some grains grew towards the 'center' of the mixing layer. At 8 ns, a limited number of rounded grains clung to the interfaces (Fig. 4c). In ML20%, phase formation proceeds through heterogeneous nucleation: no grains formed spontaneously in the bulk of the mixing layer.
The behavior of the REF sample is similar to that observed in ML20%, except that the Ni concentration reaches its steady value slightly later and this value is lower. Nucleation of *B2*-

NiAl grains is shifted to 2 ns. In addition, fewer but larger grains are formed (biggest nucleus r = 3.2 nm). Small grains merged with larger ones, as there is some coalescence.
At high temperature (1200 K), the REF system and the ML system with a low Ni concentration exhibit similar behavior: dissolution of Ni close to the interface, heterogeneous nucleation, further dissolution of Ni to the 'center', growth. But in the case ofthe premixed layer, the formation of *B2* occurs sooner and the system is more reactive.

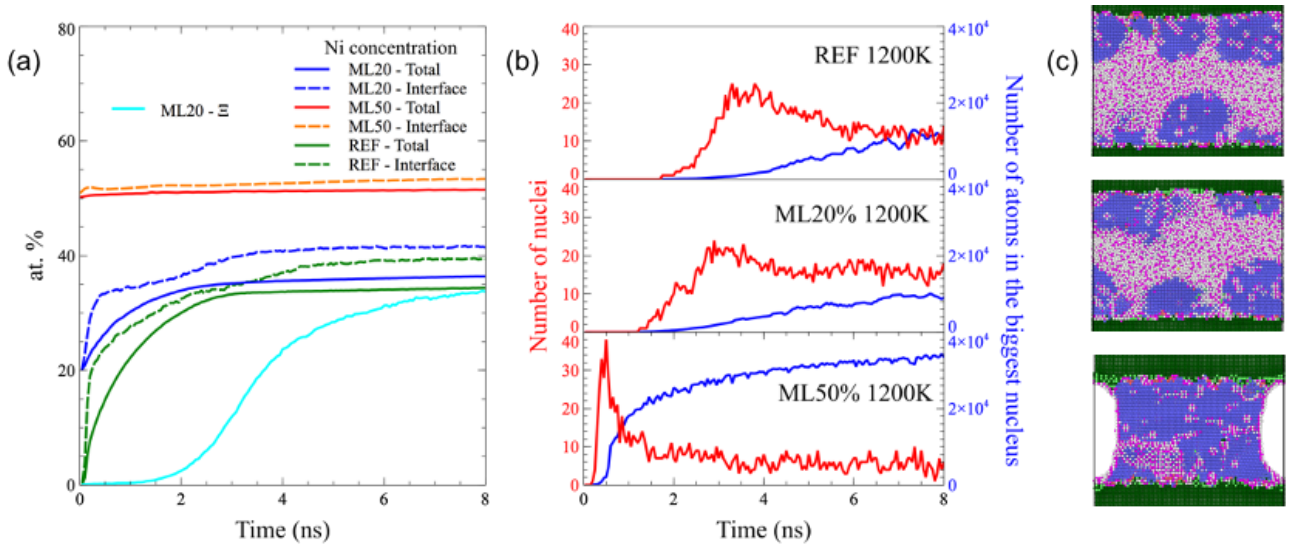

Figure 4: (a) Evolution of the Ni concentration in the mixing layer (solid lines), Ni concentration in a 1 nm slice just above or below the interface (dashed lines) and % of B2 formed Ξ in ML20%. (b) Evolution of the number of B2 nuclei (red) and the size of the biggest nucleus (number of atoms) (blue) as a function of time. (c) Snapshot of the mixing layer for REF (top), ML20% (middle), and ML50% (bottom) at 8 ns.

Figure. 5 shows the diffusion paths during the 8 ns simulation of the Ni coming from the *fcc*-block. In the case of the REF and the ML20% systems, the grain boundaries act as channels to bring Ni atoms into the middle of the inner layer. As a result, the 50-50 stoichiometry is reached and *B2*-NiAl continues to grow towards the middle. In the case of ML50%, there is almost no diffusion from the Ni blocks to the middle of the layer, confirming the results presented in Fig. 4a.

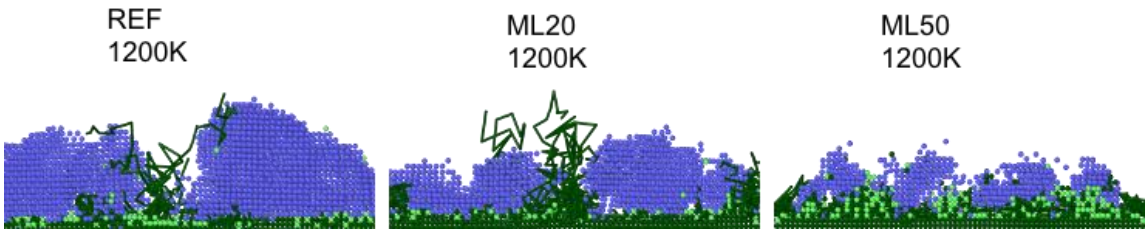

Figure 5: Snapshots of the atoms at 5 ns for REF and ML20 and at 0.3 ns for ML50. The trajectories of some Ni atoms from the *fcc* block calculated over the 8 ns simulation are also displayed. Dark green = *fcc*-Ni, light green = *fcc*-Al, and blue = *bcc*.

We next investigated the influence of Ni content in the mixing layer on the mechanism of *B2*-NiAl formation. Figure. 6a presents the evolution of *B2*-NiAl in the different systems from 10% to 60%. The inflexion point corresponds to a characteristic time associated with ignition. Higher Ni concentrations in the mixing layer lead to a shift in the start of nucleation. In addition, the final amount of *B2*-NiAl is larger in higher concentrations. This observation holds until 50%. For concentrations of Ni equal to 60% and higher, the *fcc* solid solution forms more rapidly at the interface and slows down the formation of *B2*-NiAl. The Al cohesive energy/atom E_0(Al) depends on the structure to which it belongs:
$E_0(fcc\text{−Al})$ = -3.36 eV for pure Al and $E_0(bcc\text{−Al})$ = -4.51 eV (see Table 1) for Al in *B2*-NiAl. Before mixing, the cohesive energy $E_0(unk\text{−Al})$ of amorphous Al atoms in the mixing layer was computed and its distribution plotted in Fig.6b (REF *unk* in the figure). This value is not significantly different from the value for *fcc*-atoms but we note a slight shift to the right. After random substitution of Al atoms by Ni atoms, the potential energy/atom was computed for the different substitution rates (from 10% to 60%). The corresponding distributions are plotted in Fig. 6b. There is an almost linear shift in the potential energy of Al atoms as substitution ratios increase. The potential energy/atom moves closer and closer to the reference *B2* value. The change in E_0(Al) from the initial structure to the final structure is equal to -0.57 eV in the REF case (from *fcc*-Al to *B2*-NiAl). It reaches -0.24 eV in the ML50% system (from *unk*-Al to *B2*-NiAl), i.e. a 42% decrease. Note that the potential energy of Al atoms does not evolve significantly with temperature. For instance, Fig. 6b is nearly identical at 1200 K and at 900 K. This change in E_0(Al) facilitates the phase transformation in *B2*-NiAl. But the decrease in E_0(Al) is certainly not the only factor responsible for the high reactivityobserved in premixed systems. As evidence of this, the ML60% system does not form more *B2* than the others.

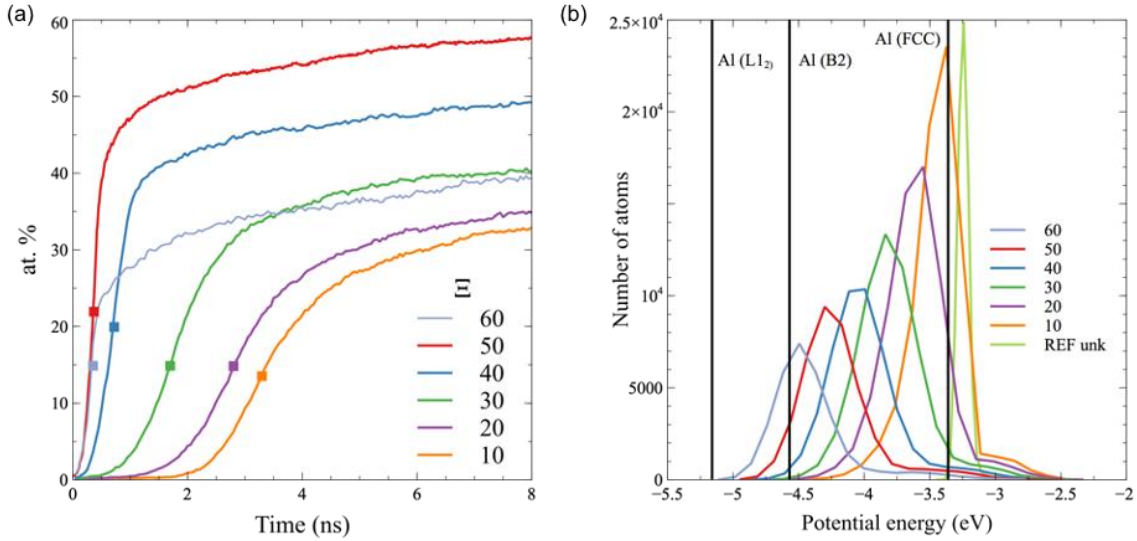

Figure 6: (a) Evolution of at. % of formed *B2*-NiAl at various Ni concentrations in the mixing layer. (b) Evolution of the initial potential energy of the Al atoms at various Ni concentrations in the mixing layer. The three black vertical lines correspond to the potential energies of the reference structures.

As stated above, the purpose of this work was to evaluate the formation of *B2*-NiAl at low temperatures to mimic the ignition of milled Ni-Al which usually occurs experimentally at around 750 K [6]. The temperatures chosen for our simulations are higher in order to obtain results within an acceptable computing time.

First, the actual Al melting temperature in the particular geometry was roughly estimated. Figure. 7a gives the number of *unk*-Al as a function of time in the reference system at different temperatures. At 800 K, most Al-atoms remain *fcc*. At 900 K, after 4 ns, all the aluminum has melted. In this geometry, the effective Al melting temperature seems to be in the range of [800 K – 900 K], much lower than the bulk melting temperature of 1055 K (see Table 1). However, simply meeting the criterion of a melted inner layer is not enough to ensure the formation of *B2*-NiAl. Indeed, the REF systems at 900 K up to 1100 K do not exhibit the formation of *B2*-NiAl (see Fig. 7b).
The evolution of the Ξ factor is plotted in Fig. 7c at different operating temperaturesin the case of ML50%. In this pre-mixed system, *B2*-NiAl is formed even at 800 K, below the effective melting temperature. The $(Al+Ni)_{solid}$ is in an amorphous or supercooled state. Hence, for a high Ni concentration in the mixing layer, this configuration already exhibits solid state reaction at 800 K. Formation of *B2*-NiAl becomes more significant at 900 K.

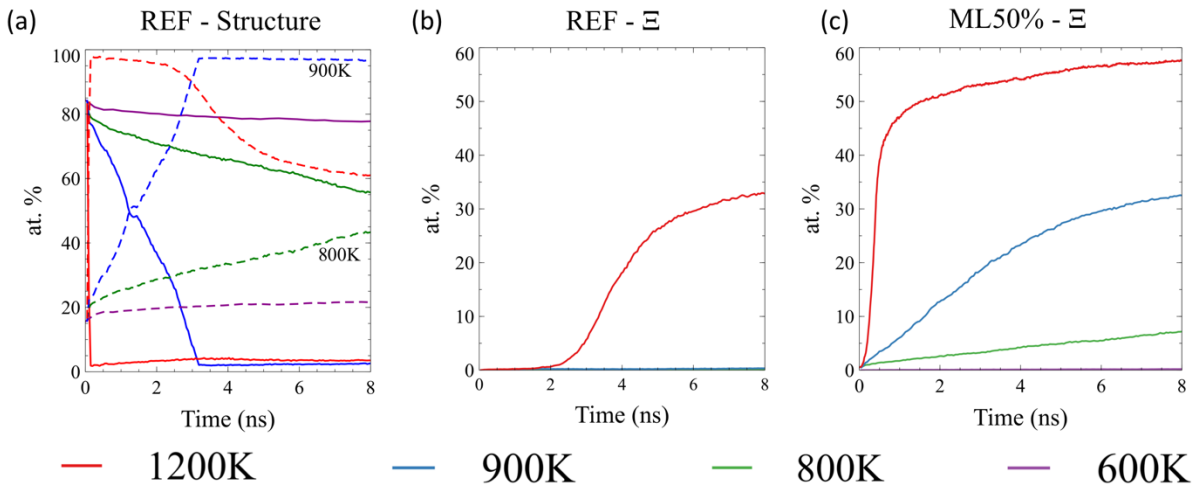

Figure 7: (a) Evolution of the % of *fcc*-Al atoms (solid lines) and amorphous Al atoms (dashed lines) in the REF system at different temperatures. Evolution of the at. % of formed B2-NiAl as a function of time at different temperatures: (b) REF system and (c) ML50%.

It is important to compare the mechanism of *B2*-NiAl formation at low (800 K and 900 K) and high temperatures (1200 K) at the different rates of premixing from 20% up to 50%. Figure. 8 shows representative snapshots of the ML20% and ML50% systems at different times during *B2*-NiAl formation. In ML20%, the seeds nucleate at the interface. The nuclei grow due to precipitation of the Ni and Al atoms present in the inner layer. In the very beginning, some grains may coalesce while others grow, retaining their initial orientation. For an interface oriented normal to the [001] direction, the intermetallic *B2*-NiAl phase appears plane by plane.

The atomic arrangement is characteristic of the (110) orientation in NiAl. In each plane, only four orientations in (110) planes were observed, due to the specific orientation relationships between *bcc*- and *fcc*-phases[29]. Thus, small disoriented grains separated by grain boundaries were observed. The situation is radically different in the ML50% system at 900 K and 800 K. Seeds appear in the middle of the layer, far from interfaces. This is the signature of a homogeneous nucleation. In addition, the typical profile depicted in Fig. 8 shows that the inner layer remains compact and concave in a solid amorphous state. Wetting of the Ni substrate is observed, but its impact remains limited since the layer is already amorphous. This means that the homogeneous nucleation occurs as a solid reaction. The behavior is similar at 800 K and 900 K, except for the fact that *B2* is formed more rapidly at 900 K. These findings indicate the possibility of *B2*-NiAl formation at temperatures below the melting point of aluminum and could explain the enhanced reactivity of milled systems.

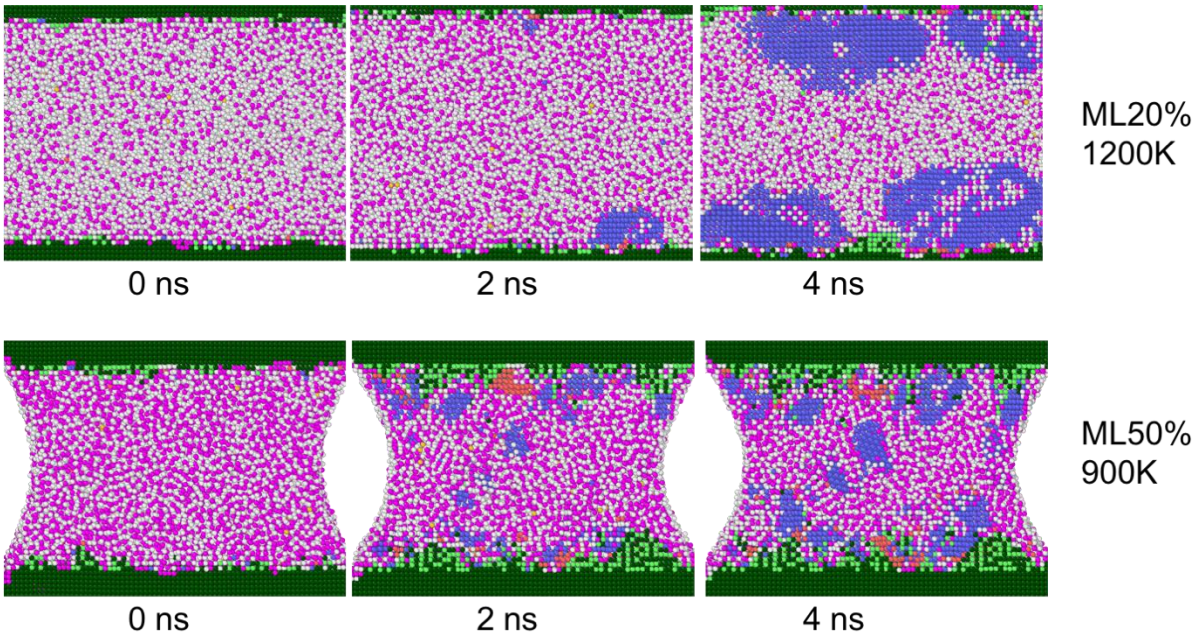

Figure 8: Pictures of ML20 at 1200 K (top) and ML50 at 900 K (bottom).

Experimentally, the intermetallic $L1_2$-Ni_3Al phase is sometimes observed in this kind of study. In our simulation work, it does not seem to be the case. Fig. 9 shows the atoms in the *fcc* configuration according to adaptative-CNA and the local chemical order according to the Polyhedral Template Matching [38] at 8 ns. It depicts the state of the *fcc* solid solution. Table 3 displays the potential energy of Al atoms in this configuration as well as the Ni concentration in this phase. These two elements of data point to the conclusion that the intermetallic $L1_0$-NiAl or $L1_2$-Ni_3Al phases are not yet fully formed but that its formation seems underway. Indeed, in contrast to what have been reported by Turlo *et al.*for the Fe-Ni system [39], the amount of ordered *fcc* phase does not exceed 0.2 % in our systems. The relative short simulation time (8 ns) could explain why only a disordered *fcc* solid solution could form. The lattice parameter of this solid solution is relatively close to that of pure *fcc*-Ni; we may therefore assume that the solid solution plays the same role as pure Ni with respect to *B2*-NiAl heterogeneous nucleation.

System	ML50%900K	ML50%1200K	ML60%1200K	$L1_2$-Ni_3Al
Al potential energy (eV)	-4.43	-4.57	-4.62	-5.16
Ni at. %	50	55	62	75

Table 3: Data on the *fcc* solid solution formed in different simulations.

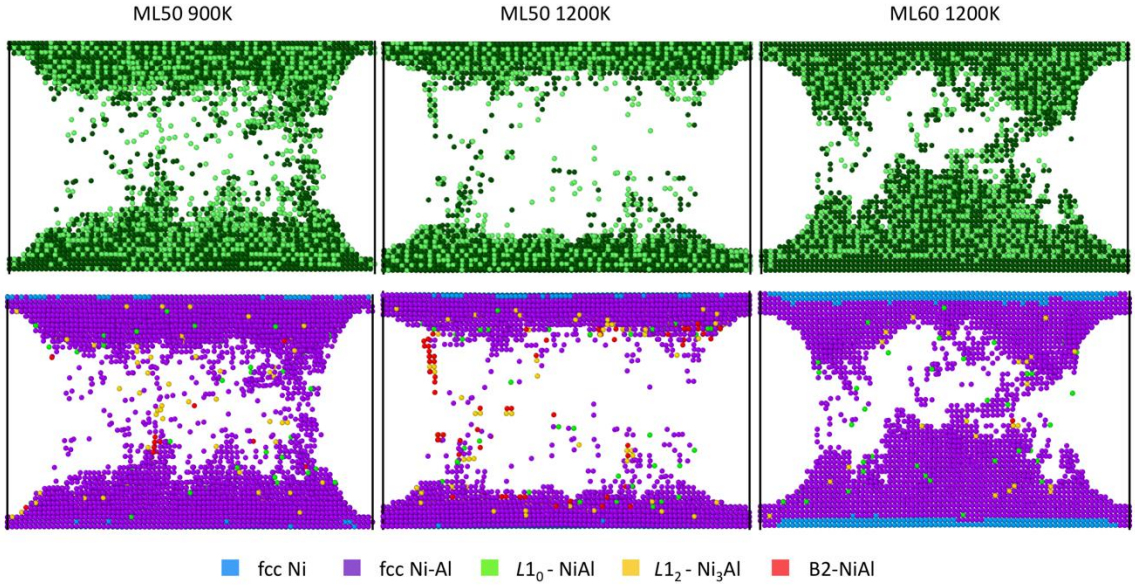

Figure 9: Snapshots of the atoms in the *fcc* configuration in the inner layer for ML50% at 900 K and 1200 K and ML60% at 1200 K. Snapshots correspond to the state of the system at 8 ns. (Top) Dark green atoms are *fcc*-Ni atoms and light green atoms are *fcc*-Al atoms calculated with adaptative-CNA. (Bottom) Local chemical order calculated with polyhedral template matching.

The observation of homogeneous nucleation in a mixing layer at 900 K leads to other questions. Is homogeneous nucleation caused solely by the 50% pre-mixed layer? Would another premixing stoichiometry also lead to homogeneous nucleation? These questions are of great interest since an experimental milled system could be modelized as the sum of several zones, each with a different stoichiometry. Three compositions prone to homogeneous nucleation at 900 K were more closely studied: ML30%, ML40% and ML50%.

Figure. 10a shows the evolution of Ξ as a function of time in the three systems. We noted an unexpected finding: the formation of *B2* in the case of the ML40% systemis faster and more plentiful than in the two other cases. Figure 10b, in which we note a high nucleation rate, confirms this observation. Grain size then increases due to coalescence and precipitation. This behavior is quite similar to that observed in the 1200 K cases.
ML50% at 900 K exhibits a different behavior. This system shows a slower but steadynucleation rate. Grain size does not increase much, as revealed in the global evolution.At the end, there are approximately 40 nuclei and the largest grain does not exceed thesize of 2000 atoms (r = 1.8 nm).

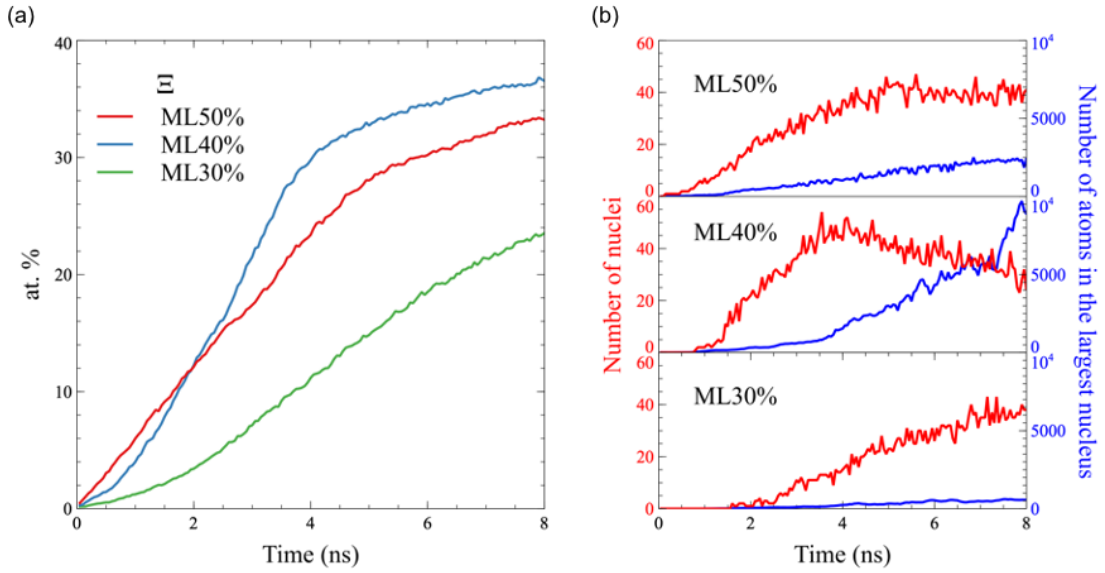

Figure 10: (a) Evolution of the at. % of *B2*-NiAl at low temperature (900 K). (b) Evolution of the number of *B2* nuclei (red) and size of the biggest nucleus (number of atoms) (blue) over time.

In order to investigate the differences between behavior in ML50% and ML40%, representative grains in each system were followed over the course of their formation. For selected systems, a significant time was chosen. This time corresponds to the complete formation of nuclei of reasonable size. From that time, all the *BCC* atoms in a selected nucleus are then selected. This observation is represented in Fig. 11. The nuclei are labeled 'HON' if they form by homogeneous nucleation and 'HEN' if formed by heterogeneous nucleation. The data presented in Fig. 11 result from the tracking of several nuclei. The mean square displacement of selected atoms as a function of time is reported in Fig. 11a. No difference was noted between Ni and Al atoms. Two types of behavior were observed: (1) A strong and linear increase until 1.5ns followed by a plateau. This behavior is shared by HON40 and HEN30 grains. It reflects high mobility in the system. (2) A slight increase corresponding to very low mobility. This kind of evolution is shared by HEN40 and HON50. The ML40% system was thus foundto present both mechanisms of nucleation. Although mobility is hindered close to the interface, this is precisely where heterogeneous nucleation takes place. When mobility is high far from the interface, homogeneous nucleation develops spontaneously. Figure. 11b illustrates the rearrangement of atoms during homogeneous nucleation in HON40: randomly distributed atoms diffuse and explore a large domain for 1.5ns before the rapid crystallization of the *B2*-NiAl phase. The situation is radically different in HON50, as shown in Figure. 11c. From the start, a fifth of the atoms form a seed of *bcc*-atoms that barely evolves up to 1.2ns. At that time, some new atoms adhere to the seed and then the rest of atoms abruptly become *bcc*. Crystallization begins sooner in the ML50% system, but since mobility is hindered, the atoms truly rearrange into a crystalline structure only after 1ns.

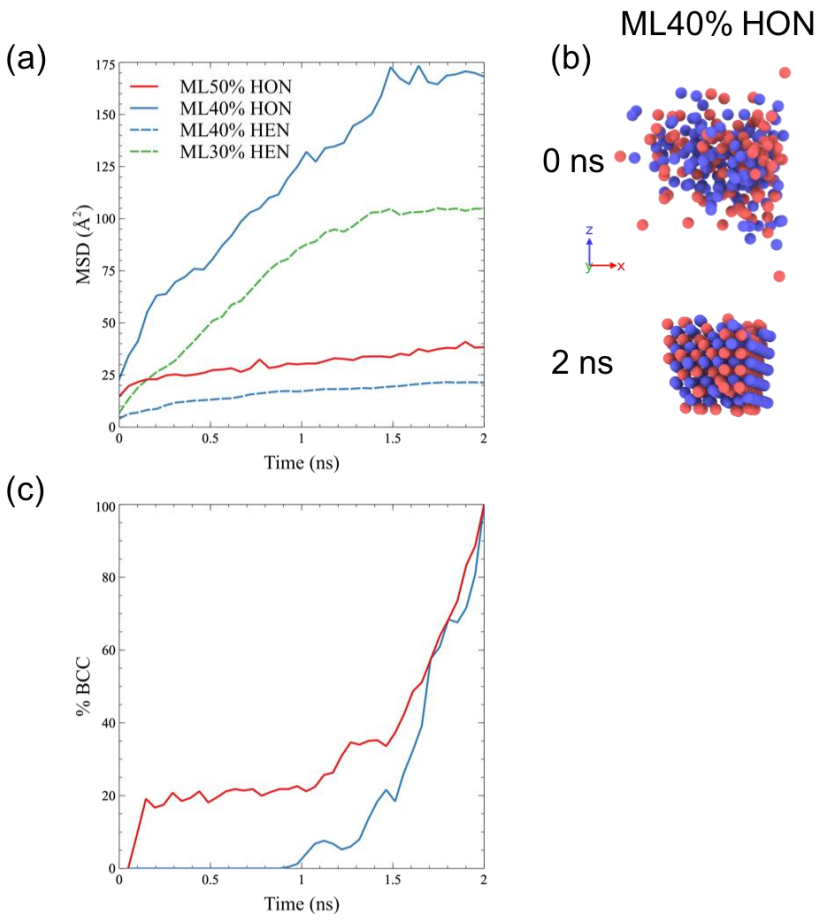

Figure 11: Analysis of the homogeneous (HON) and heterogeneous (HEN) nuclei in ML30%, ML40%, and ML50%. (a) Evolution of the MSD in different groups of selected atoms. (b) Snapshots of a HON 40 at the beginning (the amorphous state) and at the end of the observation (fully crystallized in the *B2* configuration). (c) Evolution of the percentage of *bcc* among the selected atoms.

Homogeneous nucleation was observed in mixing layers at 900 K and 800 K. The 50% pre-mixed layer promotes the required conditions for such a nucleation as the stoichiometry is satisfied locally. But nuclei were also detected for pre-mixed layers less rich in Ni (ML30% and ML 40%) (see Fig. 10a). These nuclei progressively grew and the amount in NiAl reached nearly 30 at.% of the inner layer. Different premixing stoichiometries thus lead to homogeneous nucleation provided than the operating temperature is less than the melting temperature of Al. Homogeneous nucleation here occurred in an amorphous solid solution. This can be considered as the counterpart of a strong undercooling. Because an experimental milled system could be modelized as the sum of several zones, each with a different stoichiometry, we may expect homogeneous nucleation of NiAl at low temperatures and heterogeneous nucleation at higher temperatures.

Fig. 12 depicts the evolution of the diffusion coefficient of Ni at 900 K according to concentration. The maximum is reached at around 30% and the diffusion at 40% is 1.3 times higher than at 50%, according to these calculations. There are indeed different mechanisms at work in the ML40% and ML50% systems. The higher mobility in ML40% is due to the lower

Ni concentration. The high reactivity of activated systems results from a compromise between diffusion and previously effected mixing.

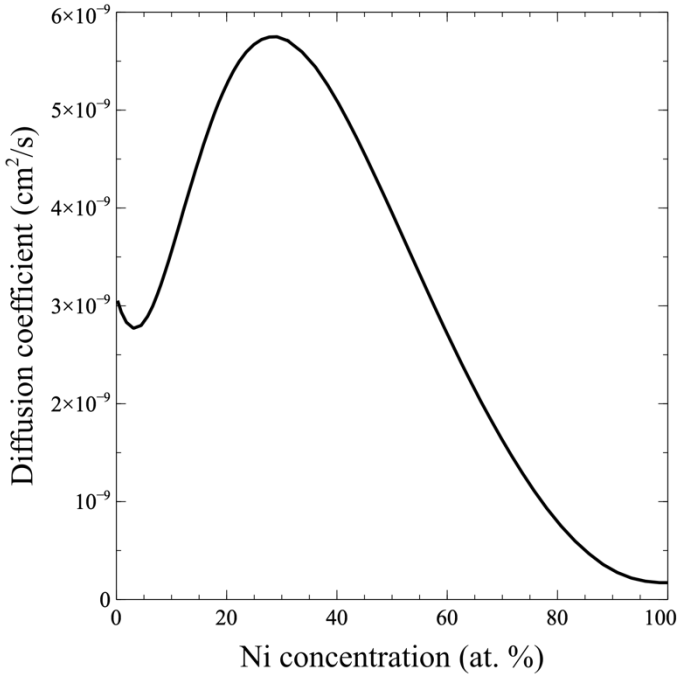

Figure 12: Evolution of the diffusion coefficient of Ni in amorphous Al at 900 K according to Ni concentration. Calculated with ThermoCalc and Dictra using the MOBHEA1 database.

4. Conclusion

The bilayer configuration with a pre-mixed zone is indeed characterized by high reactivity. Here, reactivity was evaluated by measuring the amount of *B2*-NiAl formed during homogeneous heating. In this pre-mixed configuration, two steps usually performed over time by temperature effect are already achieved in the initial configuration. The melting and amorphization of Al and the diffusion of Ni are already accomplished. Conversely, diffusion is slower because of the pre-mixing. Taking into account the two conflicting phenomena, we nonetheless note that the pre-mixed configuration results in higher reactivity compared to the reference bilayer configuration. At the microscopic scale, it has been observed that pre-mixing decreases the cohesive energy / atom by as much as 40% for the pre-mixing with 50% Nickel. At low temperatures below the melting temperature of Al, homogeneous and heterogeneous nucleation occur in concentrated pre-mixing zones. The presence of both kinds of nucleation leads to faster formation of higher amounts of *B2*-NiAl, whereas in systems where only heterogeneous nucleation occurs, the formation is slower. It is interesting to note that the equimolar stoichiometry 50% Al-50% Ni is not associated with the best reactivity at low temperature. The mobility of atoms indeed seems to be the predominant factor in the onset of reaction. A slightly less concentrated system (ML40%) is a better compromise to ensure higher reactivity.

In addition, in cases in which the system is not pre-mixed, the Ni/Al interfaces are rapidly saturated and the formation of *B2* slows down the interdiffusion of Ni. The intermetallics formed at the interfaces seem to channel the Ni diffusion through grain boundaries. Thus, the formation at the center of the inner layer is possible but inhibited.

In conclusion, our simulations demonstrate that the nano-scale mixing of the reagents (factor (vi) as suggested by Rogachev *et al.*) is indeed an activating factor. Experimentally, the two main conclusions drawn in this work could still stand. At low temperature,pre-mixing does not seem to slow down the diffusion of the Ni atoms in an amorphousAl region. In addition, the homogeneous nucleation resulting from the peculiar milled microstructure would accelerate the general reaction of *B2*-NiAl formation. Interestingly enough, similar results were obtained in the case of irradiated films where a Ni/Alamorphous interlayer was generated and found to be improving the general reaction [40].

There remain several parameters which could be added to the simulation to better mimic the milled system. In addition to the nano-scale mixing (vi), the role of defects created by plastic deformation (ii) could be investigated. Point defects and grain boundaries might enhance the general diffusivity of the system, whereas dislocations could act as nucleation sites [41]. Nanoscale porosity could also change the process dynamics and nucleation features [17]. The combined consequences of all these aspects milling need, however, to be thoroughly studied.

References

[1] J.S. Benjamin, Dispersion strengthened superalloys by mechanical alloying, Metall. Trans. (1970) 9.
[2] C. Suryanarayana, Mechanical alloying and milling, Prog. Mater. Sci. (2001) 184.
[3] E. Gaffet, F. Bernard, Mechanical alloying in the SHS research, Int. J. SHS. 10 (2) (2001) 109–132.
[4] F. Maglia, U. Anselmi-Tamburini, C. Deidda, F. Delogu, G. Cocco, Z.A. Munir, Role of mechanical activation in SHS synthesis of TiC, J. Mater. Sci. 39 (2004) 5227–5230. https://doi.org/10.1023/B:JMSC.0000039215.28545.2f.
[5] J.D.E. White, R.V. Reeves, S.F. Son, A.S. Mukasyan, Thermal Explosion in Al−Ni System: Influence of Mechanical Activation, J. Phys. Chem. A. 113 (2009) 13541–13547. https://doi.org/10.1021/jp905175c.
[6] A.S. Rogachev, N.F. Shkodich, S.G. Vadchenko, F. Baras, D.Yu. Kovalev, S. Rouvimov, A.A. Nepapushev, A.S. Mukasyan, Influence of the high energy ball milling on structure and reactivity of the Ni+Al powder mixture, J. Alloys Compd. 577 (2013) 600–605. https://doi.org/10.1016/j.jallcom.2013.06.114.
[7] A.S. Rogachev, D.O. Moskovskikh, A.A. Nepapushev, T.A. Sviridova, S.G. Vadchenko, S.A. Rogachev, A.S. Mukasyan, Experimental investigation of milling regimes in planetary ball mill and their influence on structure and reactivity of gasless powder exothermic

mixtures, Powder Technol. 274 (2015) 44–52. https://doi.org/10.1016/j.powtec.2015.01.009.

[8] F. Delogu, G. Cocco, Molecular dynamics investigation on the role of sliding interfaces and friction in the formation of amorphous phases, Phys. Rev. B. 71 (2005) 144108. https://doi.org/10.1103/PhysRevB.71.144108.

[9] H.-J. Kim, S. Karthikeyan, D. Rigney, A simulation study of the mixing, atomic flow and velocity profiles of crystalline materials during sliding, Wear. 267 (2009) 1130–1136. https://doi.org/10.1016/j.wear.2009.01.030.

[10] B. Li, P.C. Clapp, J.A. Rifkin, X.M. Zhang, Molecular dynamics calculation of heat dissipation during sliding friction, Int. J. Heat Mass Transf. 46 (2003) 37–43. https://doi.org/10.1016/S0017-9310(02)00258-2.

[11] K. Chen, L. Wang, Y. Chen, Q. Wang, Molecular dynamics simulation of interfaces and microstructure evolution during high-speed sliding, Numer. Heat Transf. Part Appl. 72 (2017) 519–535. https://doi.org/10.1080/10407782.2017.1386513.

[12] K. Chen, L. Wang, Y. Chen, Q. Wang, Molecular dynamics simulation of microstructure evolution and heat dissipation of nanoscale friction, Int. J. Heat Mass Transf. 109 (2017) 293–301. https://doi.org/10.1016/j.ijheatmasstransfer.2017.01.105.

[13] S. Odunuga, Y. Li, P. Krasnochtchekov, P. Bellon, R.S. Averback, Forced Chemical Mixing in Alloys Driven by Plastic Deformation, Phys. Rev. Lett. 95 (2005) 045901. https://doi.org/10.1103/PhysRevLett.95.045901.

[14] F. Delogu, Forced chemical mixing in model immiscible systems under plastic deformation, J. Appl. Phys. 104 (2008) 073533. https://doi.org/10.1063/1.2987476.

[15] M.J. Cherukara, T.C. Germann, E.M. Kober, A. Strachan, Shock Loading of Granular Ni/Al Composites. Part 1: Mechanics of Loading, J. Phys. Chem. C. 118 (2014) 26377–26386. https://doi.org/10.1021/jp507795w.

[16] M.J. Cherukara, T.C. Germann, E.M. Kober, A. Strachan, Shock Loading of Granular Ni/Al Composites. Part 2: Shock-Induced Chemistry, J. Phys. Chem. C. 120 (2016) 6804–6813. https://doi.org/10.1021/acs.jpcc.5b11528.

[17] K.V. Manukyan, B.A. Mason, L.J. Groven, Y.-C. Lin, M. Cherukara, S.F. Son, A. Strachan, A.S. Mukasyan, Tailored Reactivity of Ni+Al Nanocomposites: Microstructural Correlations, J. Phys. Chem. C. 116 (2012) 21027–21038. https://doi.org/10.1021/jp303407e.

[18] Y. Xiong, S. Xiao, H. Deng, W. Zhu, W. Hu, Investigation of the shock-induced chemical reaction (SICR) in Ni + Al nanoparticle mixtures, Phys. Chem. Chem. Phys. 19 (2017) 17607–17617. https://doi.org/10.1039/C7CP03176A.

[19] B. Witbeck, J. Sink, D.E. Spearot, Influence of vacancy defect concentration on the combustion of reactive Ni/Al nanolaminates, J. Appl. Phys. 124 (2018) 045105. https://doi.org/10.1063/1.5035091.

[20] B. Witbeck, D.E. Spearot, Grain size effects on Ni/Al nanolaminate combustion, J. Mater. Res. 34 (2019) 2229–2238. https://doi.org/10.1557/jmr.2019.53.

[21] J.C. Crone, J. Knap, P.W. Chung, B.M. Rice, Role of microstructure in initiation of Ni–Al reactive multilayers, Appl. Phys. Lett. 98 (2011) 141910. https://doi.org/10.1063/1.3575576.

[22] M.J. Cherukara, K.G. Vishnu, A. Strachan, Role of nanostructure on reaction and transport in Ni/Al intermolecular reactive composites, Phys. Rev. B. 86 (2012) 075470. https://doi.org/10.1103/PhysRevB.86.075470.

[23] A.J. Gavens, D. Van Heerden, A.B. Mann, M.E. Reiss, T.P. Weihs, Effect of intermixing on self-propagating exothermic reactions in Al/Ni nanolaminate foils, J. Appl. Phys. 87 (2000) 1255–1263. https://doi.org/10.1063/1.372005.

[24] M.L. Falk, T.P. Weihs, Suppression of homogeneous crystal nucleation of the NiAl intermetallic by a composition gradient: A molecular dynamics study, J. Chem. Phys. 146 (2017) 184501. https://doi.org/10.1063/1.4982821.

[25] P. Yi, M.L. Falk, T.P. Weihs, Intermetallic formation at deeply supercooled Ni/Al multilayer interfaces: A molecular dynamics study, J. Appl. Phys. 124 (2018) 165303. https://doi.org/10.1063/1.5048911.

[26] P. Kuhn, J. Horbach, Molecular dynamics simulation of crystal growth in Al 50 Ni 50 : The generation of defects, Phys. Rev. B. 87 (2013). https://doi.org/10.1103/PhysRevB.87.014105.

[27] A. Ovrutsky, A. Prokhoda, Particularities of nucleation and growth of the B2-phase: Results of simulations for the Al50Ni50 alloy, Comput. Mater. Sci. 79 (2013) 193–200. https://doi.org/10.1016/j.commatsci.2013.05.045.

[28] F. Baras, O. Politano, Molecular dynamics simulations of nanometric metallic multilayers: Reactivity of the Ni-Al system, Phys. Rev. B. 84 (2011). https://doi.org/10.1103/PhysRevB.84.024113.

[29] F. Baras, O. Politano, Epitaxial growth of the intermetallic compound NiAl on low-index Ni surfaces in Ni/Al reactive multilayer nanofoils, Acta Mater. 148 (2018) 133–146. https://doi.org/10.1016/j.actamat.2018.01.035.

[30] A.S. Rogachev, Mechanical activation of heterogeneous exothermic reactions in powder mixtures, Russ. Chem. Rev. 88 (2019) 875–900. https://doi.org/10.1070/RCR4884.

[31] G.P. Purja Pun, Y. Mishin, Development of an interatomic potential for the Ni-Al system, Philos. Mag. 89 (2009) 3245–3267. https://doi.org/10.1080/14786430903258184.

[32] V. Turlo, F. Baras, O. Politano, Comparative study of embedded-atom methods applied to the reactivity in the Ni–Al system, Model. Simul. Mater. Sci. Eng. 25 (2017) 064002. https://doi.org/10.1088/1361-651X/aa6cfa.

[33] S. Plimpton, Fast Parallel Algorithms for Short–Range Molecular Dynamics, J. Comput. Phys. 117 (1995) 42. https://doi.org/10.1006/jcph.1995.1039.

[34] A. Stukowski, Visualization and analysis of atomistic simulation data with OVITO–the Open Visualization Tool, Model. Simul. Mater. Sci. Eng. 18 (2009) 015012. https://doi.org/10.1088/0965-0393/18/1/015012.

[35] A.S. Rogachev, S.G. Vadchenko, F. Baras, O. Politano, S. Rouvimov, N.V. Sachkova, M.D. Grapes, T.P. Weihs, A.S. Mukasyan, Combustion in reactive multilayer Ni/Al nanofoils: Experiments and molecular dynamic simulation, Combust. Flame. 166 (2016) 158–169. https://doi.org/10.1016/j.combustflame.2016.01.014.

[36] K.V. Manukyan, C.E. Shuck, M.J. Cherukara, S. Rouvimov, D.Y. Kovalev, A. Strachan, A.S. Mukasyan, Exothermic Self-Sustained Waves with Amorphous Nickel, J. Phys. Chem. C. 120 (2016) 5827–5838. https://doi.org/10.1021/acs.jpcc.6b00752.

[37] V. Turlo, O. Politano, F. Baras, Dissolution process at solid/liquid interface in nanometric metallic multilayers: Molecular dynamics simulations versus diffusion modeling, Acta Mater. 99 (2015) 363–372. https://doi.org/10.1016/j.actamat.2015.07.076.

[38] P.M. Larsen, S. Schmidt, J. Schiøtz, Robust structural identification via polyhedral template matching, Model. Simul. Mater. Sci. Eng. 24 (2016) 055007. https://doi.org/10.1088/0965-0393/24/5/055007.

[39] V. Turlo, T.J. Rupert, Linear Complexions: Metastable Phase Formation and Coexistence at Dislocations, Phys. Rev. Lett. 122 (2019) 126102. https://doi.org/10.1103/PhysRevLett.122.126102.

[40] K.V. Manukyan, W. Tan, R.J. deBoer, E.J. Stech, A. Aprahamian, M. Wiescher, S. Rouvimov, K.R. Overdeep, C.E. Shuck, T.P. Weihs, A.S. Mukasyan, Irradiation-Enhanced Reactivity of Multilayer Al/Ni Nanomaterials, ACS Appl. Mater. Interfaces. 7 (2015) 11272–11279. https://doi.org/10.1021/acsami.5b01415.

[41] V. Turlo, T.J. Rupert, Dislocation-assisted linear complexion formation driven by segregation, Scr. Mater. 154 (2018) 25–29. https://doi.org/10.1016/j.scriptamat.2018.05.014.

Chapter IV: Effects of planetary ball milling on AlCoCrFeNi high entropy alloys prepared by Spark Plasma Sintering: Experiments and molecular dynamics study

1. Introduction

High entropy alloys (HEA) contain five or more principal elements with each elemental concentration set between 5 at% and 35 at% [1]. They offer a wide range of properties and are a very promising field of study [2]. The AlCoCrFeNi composition has attracted much attention in recent years because it can easily be compared to common materials composed of similar elements (e.g., steels or M-Cr-Al alloys). These multi-component alloys are typically produced by arc-melting. When elaborated by means of this process, AlCoCrFeNi alloys exhibit a disordered BCC Cr-Fe rich phase and an ordered BCC Al-Ni rich phase [3–7]. Interesting mechanical properties [8] and encouraging oxidation resistance [9] have been reported. However, this type of elaboration, including a solidification step, may lead to the formation of dendrites and a deterioration of mechanical properties.

Other processes, such as Powder Metallurgy, have been studied and appear advantageous as compared to the common arc-melting process [10]. Indeed, a solid-state route enables industrial manufacturing and results in nanocrystalline materials with enhanced properties. Powder Metallurgy combines high-energy ball milling (HEBM) and consolidation processes such as Spark Plasma Sintering (SPS). High-energy ball milling has been extensively studied and is a rather versatile technique [11] that may induce either the mechanical activation of the green mixture or the complete transformation of the powder reactants. This latter process is usually referred to as Mechanical Alloying (MA), mechanosynthesis or mechanochemical synthesis. Most of the work on the elaboration of HEAs by powder metallurgy concerns the use of MA with a complete chemical reaction. In this case, the total consumption of the initial constituents can be verified, for instance, with XRD by noting the disappearance of elemental peaks. The synthesized powder is then consolidated by means of an appropriate technique. Concerning the AlCoCrFeNi alloys, the various investigations in the literature mainly concern MA. Ji *et al.* reported the formation of a BCC phase and an FCC phase with the combination of Mechanical Alloying (in a high-energy ball mill) and Spark Plasma Sintering [12], whereas Mohanty *et al.* found a more complex microstructure with precipitates of a tetragonal phase [13]. Yang *et al.* started from a glassy precursor in the MA+SPS route and obtained a microstructure similar to those obtained by arc-melting: an ordered BCC phase dispersed in a disordered BCC matrix [14]. Zhang *et al.* synthesized HEA using SPS only, starting from elemental powders without

any HEBM step and reported the formation of a FCC phase and a duplex BCC structure [15]. Several investigations concern MA only. For instance, Vaidya *et al.* studied the influence of the sequential addition of elements during milling in Mechanical Alloying [16].

Very few variations have been explored. Colombini *et al.* considered the combination of simple mechanical activation of the green mixture followed by the microwave or field-assisted powder metallurgy route, but concluded that these techniques were not sufficiently efficient in attaining chemical homogeneity [17]. In the present work, we evaluate the use of mechanical activation (i.e., incomplete Mechanical Alloying) followed by a reactive sintering step. The mechanical activation enhances particle reactivity by creating defects and by increasing the number of interfaces between reactants [18–21]. The SPS treatment becomes crucial in producing HEA with the effective synthesis of activated powders. In addition, the versatility of HEBM provides new control parameters in order to achieve unexpected characteristics associated with the consolidation process, such as the non-equilibrium state. This specific elaboration route was found to lead to a unique HEA microstructure. Special attention was paid to the crystalline state of agglomerates after milling. In order to reach a better understanding of the milling results, molecular dynamics simulations (MD) were carried out, producing valuable information at the atomic scale and helping to interpret experimental diffractogramms. In addition, thermodynamic calculations provide an interesting counterpart to the experimental results.

2. Materials and methods

2.1. Experimental setup

Elemental powders of Al, Co, Cr, Fe and Ni of high purity (all > 99.2 wt%, Alfa Aesar) were first blended with a TURBULA® mixer (WAB Turbula T2F) for 24 hours. Particle sizes were smaller than 45 μm for Al, 2 μm for Co, 75 μm for Cr, 10 μm for Fe and 15 μm for Ni. Given that Chromium is the hardest material and has the largest particle size, a pre-milling of Cr powder was also undertaken to reduce its median for the volume distribution (D_v50) to 17 μm before blending it with the other elemental powders. The pre-milling of Cr was performed in a high-energy ball mill (Fritsch Pulverisette 4). The pre-milling conditions were 250 rpm for the rotating speed of the sun wheel, 250 rpm for the relative speed of the grinding vial and 28h duration with 2h pauses every 7h. Pauses prevent the powder from agglomerating into large particles.

The blended powders in equimolar proportions were then processed by high-energy ball milling (Fritsch Pulverisette 4) with two sorts of duration used: 28h processing without pausing and 28h processing with 2h pauses every 7h. Hardened steel grinding bowls and balls of 15 mm diameter were used. The ratio between the weight of the balls and the powders was set at 7:1. The ratio $K= \omega/\Omega$ between the rotating speed of the sun wheel Ω and the relative speed of the grinding vial ω was set at 0.2 (milling M1) and 1 (milling M2). These relatively low ratios were

chosen in order to reach mechanical activation and not mechanical alloying. The different milling conditions are summarized in Table 1.
The powders were subsequently consolidated by means of Spark Plasma Sintering (FCT Systeme GmbH HPD 10) at 80 MPa in a 10 mm inner-diameter graphite die. The milled powders obtained with initial Cr were sintered at 1000 °C whereas the milled powders obtained with pre-milled Cr were sintered at 1100 °C. Two temperatures have been investigated because one aim of this work was to obtain the most interesting material in terms of microstructure. Indeed, two factors have been arbitrary chosen: the density of the sintered sample and the absence of weakening secondary phases. Increasing the temperature can improve the density and hinder the formation of secondary unwanted phases (for instance the tetragonal Cr-rich sigma phase is known to be stable at 1000°C but not at 1100°C [9]). These two temperatures are quite high compared to sintering temperatures for Mechanically Alloyed powders. Indeed, diffusion may need to be favored for the alloying to occur completely during the reactive sintering. The same heating rate of 50 °C/min was used in both cases. No dwell time was applied in order to avoid grain growth and to preserve the nanostructure of the material. Sintering was carried out in a vacuum. Grinding bowls and SPS dies were filled in a glove box under argon atmosphere in order to avoid possible oxygen contamination. The sintered samples were 5 mm thick discs with a radius of 1 cm. The sintering conditions are reported in Table 1.

The powder size distribution was measured by laser granulometry (Malvern 2000). The powders and the sintered samples were analyzed using X-Ray Diffraction with Cu Kα radiation (XRD, Siemens D5000), scanning electron microscopy and electron backscatter diffraction (SEM and EBSD, JEOL JSM 7600F), inductively coupled plasma atomic emission spectrometry (ICP-AES, Thermo Electron iCAP 7400) and X-Ray Fluorescence (XRF, Brucker S8 Tiger). The upper surfaces of the sintered samples were observed after polishing. The density of all the sintered samples was determined via hydro-static weighing using Archimede's method. Relative density is the ratio between the sample density and the theoretical density, as determined by the mixing law (6978 kg/m^3). Hardness was measured using Vickers indenters (ZwickRoell ZHVμ) with a load of 100g and a 10s dwell time. Certain hardness markers were precisely observed using SEM to ensure the accuracy of the hardness measurement.

Cr Powder	Milling				Batch	Sintering			
	Mode	Ω (rpm)	ω (rpm)	Duration (hours)		T (°C)	Heating rate (°C/min)	Dwell time	P (MPa)
initial	M1	250	-50	28	M1-CR-L	1000	50	-	80
				4x7	M1-CR				
pre-milled					M1-cr	1100			
initial	M2	250	-250	28	M2-CR-L	1000			
				4x7	M2-CR				
pre-milled					M2-cr	1100			

Table 1: Milling and sintering conditions. Milling M1 refers to K=0.2 and milling M2 to K=1. Batch conditions are denoted Mi-j where i corresponds to the milling mode (i=1 or 2), j corresponds to the characteristics of the Cr powder (j=CR is for the large 75 µm powder and j=cr for the pre-milled powder). Milling duration was usually 4x7h milling with 2h pauses. A long milling duration (28h) without pauses is specified by "L" for long duration.

2.2. Modeling approach

In order to better understand the milling process and shed some light on the experimental results, especially XRD, molecular dynamics (MD) simulations were carried out using the LAMMPS code [22]. The main goal of these simulations was to evaluate the evolution of the lattice parameter for different structures during the formation of solid solutions by mechanical alloying. Interatomic interactions are described by an Embedded Atom potential (EAM) developed by Zhou for several pure metals, especially for Al, Co Fe, Ni [23] and by Lin *et al.* for Cr [24]. The cross-potential for multi-component systems is obtained by the weighted averages of elemental components [25]. The mechanical properties of a wide range of metallic elements are correctly described, including the pure metals of interest here. Two types of simulation were performed. The first type aims at mimicking the chemical mixing induced by plastic deformation [26]. The second one creates a random solid solution of different elements.

In the first type of simulation, a polycrystalline structure is generated for different, nearly equimolar ternary alloys. The structure contains 18 grains of average diameter equal to 40 Å created by using Voronoi tessellation [27]. Each grain is initially composed of one of the pure elements. The total number of atoms and the compositions are summarized in Table 2. The combinations of 3 elements proposed are justified by the XRD results presented further in this work (paragraph 3.1). An energy minimization was first carried out under periodic boundary conditions to allow atoms located at grain boundaries to rearrange. A thermalization step was then performed: at 100K for 50 ps in the NVT ensemble and a second run at the same temperature and zero pressure for 50 ps in NPT ensemble. As underlined in [18], the temperature was chosen below ambient temperature to avoid any thermally activated diffusion.

Afterwards, 100 cyclical compressions along the 3 directions of the simulation box were applied in the NPT ensemble. One compression cycle lasted 150 ps and consisted of 3 successive deformations of 50 ps along X, Y and Z. To perform the deformation along the considered direction (e.g. X), the box size was rescaled 500 times (i.e. every 0.1 ps) to gradually reach a final strain of 25% after 50 ps. After each rescaling, the atomic positions were remapped into the new box in the appropriate manner. The two other dimensions of the box (e.g. Y and Z) were allowed to move independently (i.e., anisotropic NPT) in order to maintain zero pressure along these directions. After 50 ps, the same procedure was repeated along Y and Z to complete a full compression cycle. In all, the total simulation run lasted 15 ns (i.e., 100 cycles x 3 directions x 50 ps). The atomic positions were relaxed before measuring relevant indicators. It was verified that this minimization only reduced the noise on the indicators but did not change the atomic configuration obtained by the deformation procedure. These simulations aimed to describe the mixing driven by plastic deformation (PDM) that occurs during milling.

For the second type of simulation, an initial bcc-Fe or -Cr (or fcc-Ni) structure with the appropriate lattice parameter was constructed. Then, Al and Co atoms were randomly substituted. The simulation box (anisotropic volume change) and the atomic positions were then relaxed and relevant indicators measured. In this case, the mixing is due to a random substitution (RSM) procedure.

The final microstructure was analyzed using relevant indicators:
• The crystal structure was assessed by means of adaptive CNA (common neighbor analysis by Stukowski *et al.* [28]), which compares the local coordination of all atoms to perfect crystalline structures (*bcc*, *fcc*, *hcp*, *ico*) and assigns them the structure which best fits. The specificity of the *adaptative* CNA is that it determines a local cut off radius for each atom. It is particularly useful in the case of a simulation exhibiting different structures and consisting of several elements.
• The lattice parameters were calculated using well defined peaks in the Radial Distribution Function. This function was averaged over all atoms of the simulation box.
• The chemical mixing was monitored by the Micro-Chemical Inhomogeneity parameter (MCI), ζ, which is useful to characterize a mixture with N types of atoms (particularly when N > 2) [29]. The average number of neighbors around an atom of type i, Z_i, is the sum of the average number of i-j nearest neighbors Z_{ij}

$$Z_i = \sum_j Z_{ij} \quad (1)$$

Next, the ratio of similar and dissimilar nearest neighbors is introduced:

$$p_{ii} = {Z_{ii}}/{Z_i} \quad (2)$$

$$p_{ij} = {Z_{ij}}/{Z_i} \quad (3)$$

and a local parameter is defined

$$\zeta_i = p_{ii} - \frac{1}{N-1}\sum_j p_{ij} \quad (4)$$

whose summation gives the MCI parameter

$$\zeta = \sum_i \zeta_i . c_i \quad (5)$$

For an equimolar mixture, ζ ranges from 1 (perfectly segregated) to 0 (randomly mixed = the average local composition being the same as the global one). In the case of a non-equimolar mixture, the ideal value of the mixed state can be calculated.

System	Al (at. %)	Co (at. %)	Ni/Fe/Cr (at. %)	Number of atoms
AlCoNi	24.7	37.2	38.1	64693
AlCoFe	25.4	38.3	36.2	62800
AlCoCr	25.4	38.3	36.2	62800

Table 2: Characteristics of the simulated systems.

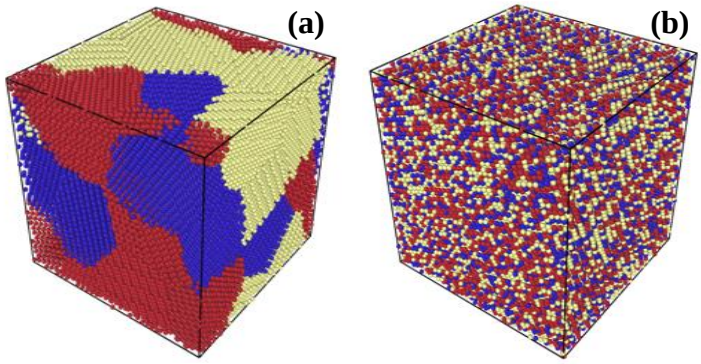

Figure 1: (a) Initial polycrystalline system with 18 grains of average diameter 40Å and (b) final microstructure after mixing driven by plastic deformation simulation. The system shown is Al-Co-Fe (Al in red, Co in blue and Fe in yellow).

3. Results and discussion

3.1. Milling

Cross sections of representative agglomerates of each milling mode are displayed in Fig. 2. After milling M1, the agglomerates exhibit a granular microstructure composed of almost pure elemental particles. Each contrast corresponds to an almost pure element; the black area is Al. After milling M2, it becomes nearly impossible to precisely identify each elemental zone. The microstructure becomes lamellar in most agglomerates. The characteristic dimension of these lamellar zones is less than 100 nm. As indicated by the several remaining contrasts in Back Scattering Electron (BSE) mode, complete Mechanical Alloying has not been achieved, we are still at the stage of mechanical activation.

The compositions of the milled powders (M1-CR-L and M2-CR-L) were characterized by ICP and compared to that of a blended powder (Table 3). There is no evidence of contamination by Fe from the grinding media or of any loss of elements that could have preferentially adhered to the vials during the milling step. The analysis shows an increase in chromium, probably due to the poor chemical homogeneity of the M1-milled powder.

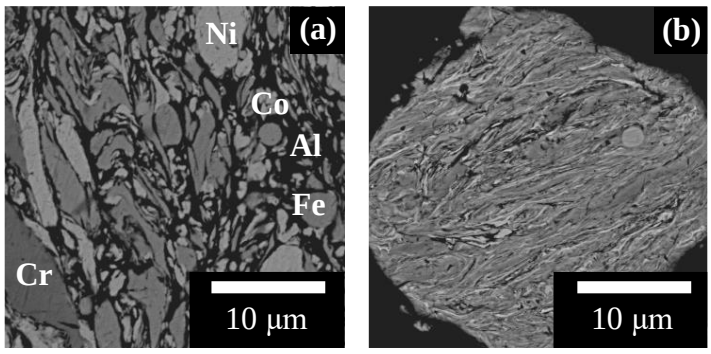

Figure 2: SEM images (BSE mode) of cross sections of (a) M1-CR-L and (b) M2-CR-L powders.

at. %	Al	Co	Cr	Fe	Ni
blended powder	19.5	19.2	21.4	19.7	20.2
M1-CR-L	17.5	17.8	30.3	17.7	16.7
M2-CR-L	19.6	19.9	21.2	19.8	19.5

Table 3: ICP results on blended and milled powders.

X-Ray Diffraction patterns of the powders are shown in Fig. 3-a. For the blended powder, all elemental peaks are identified. However, an XRD quantitative analysis (Rietveld analysis) shows that chromium is underestimated. This observation can likely be attributed to the peculiar crystalline state with nanosized crystallites and a possible texture within particles, already existing in the commercial Cr powder. Indeed, the Rietveld analysis indicates that the average crystallites size is 76 nm and that the standard relative intensity between peaks is not respected.

After milling, the intensity of the Al and Co peaks decreased compared to the other phases. There is a strong decrease in the case of the M1 milling, whereas it is a complete disappearance in the other case. In both cases, there might be a slight amorphous halo. There are no significant shifts in the other peak positions. The lattice parameter of the Ni/FCC phase remains around 3.525 Å and those of the Fe and Cr/BCC phases around 2.87 Å. However, the FCC peaks become asymmetrical after M2 milling (Fig. 3-b). At this level of analysis, the size of the chromium particle (commercial or pre-milled) and defects density (in the initial powder or introduced by the pre-milling) do not significantly affect the milling mechanism.

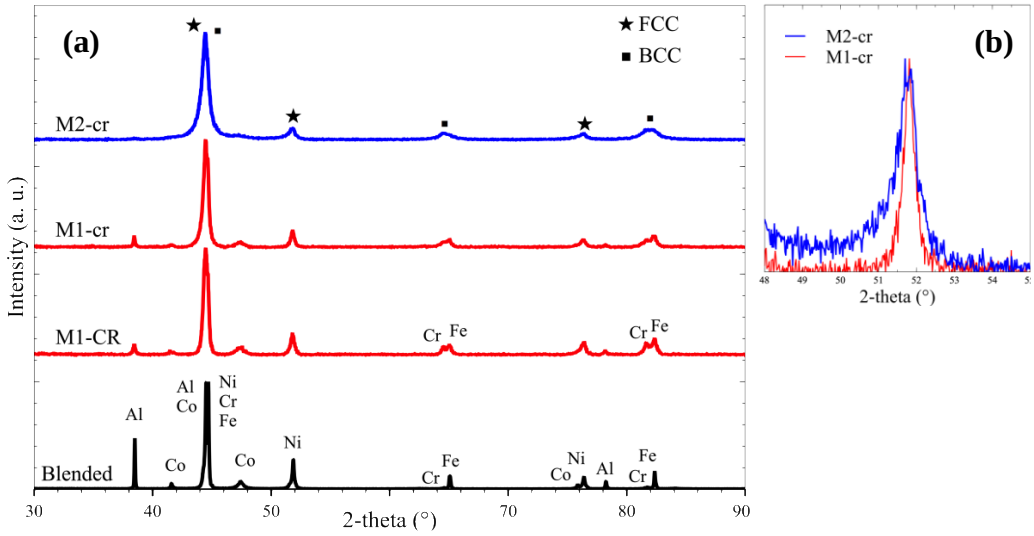

Figure 3: (a) X-ray diffraction patterns of milled powders (M1-CR, M1-cr, M2-cr and blended powders). The intensities are normalized on the main BCC peak. (b) Close up view of the normalized (200) peak of the FCC to show the asymmetry.

At this point, it is difficult to claim that solid solutions are forming during the milling. Indeed, the disappearance of the Co and especially the Al peaks associated with the non-evolution of the lattice parameters are two clues pointing to two different conclusions. The Al atomic radius (143 pm) is larger than the others (~125 pm on average [30]). Because of the larger size of Al atoms, Vegard's law predicts that substituting Al and Co atoms into Ni, Fe and/or Cr matrices would cause an increase in the lattice parameter. Since we observed both the disappearance of Al and Co peaks in XRD patterns and the persistence of two phases, we studied the case of 3-element systems: Al-Co-Ni for the FCC-phase and Al-Co-Fe and/or Al-Co-Cr for the BCC-phase. Vegard's law gives a lattice parameter of 3.66 Å for a 3-element FCC-system of composition $Al_{24.7}Co_{37.2}Ni_{38.1}$ and 2.98 Å for a 3-element BCC-system of composition $Al_{25.4}Co_{38.3}Fe_{36.2}$ or $Al_{25.4}Co_{38.3}Cr_{36.2}$, as compared to 3.52 Å for pure Ni, 2.87 Å for pure Fe, and 2.88 Å for pure Cr.

The experimental evolution of the lattice parameter during the milling was undertaken by means of MD simulations. Indeed, simulation of solid solution formation, even with a small number of atoms and short time scale, gives valuable trends which can be directly compared to experimental macroscopic data. The exact composition of each system is of lesser importance since the main question here is binary: Does the lattice parameter really increase with substitution in these cases, as Vegard's law indicates? The MD results are summarized in Table 4. Note that the PDM procedure was carried out for the AlCoCr system; however, it did not form a solid solution but rather a bcc-Cr and an amorphous phase. Indeed, Cr is known to be imperfectly fitted by an EAM and its properties are poorly reproduced in MD [31]. In addition, high Cr hardness might prevent Al and Co substitution into its structure.

System	Type of MD simulations	Lattice Parameter	% FCC or BCC	MCI parameter (Ideal mixing)
AlCoNi	PDM	3.646	55	0.05 (0.02)
	RSM	3.633	100	-0.01 (0.02)
AlCoFe	PDM	2.877	73	0.02 (0.01)
	RSM	2.895	100	-0.01 (0.01)
AlCoCr	RSM	2.884	100	-0.01 (0.01)

Table 4: Measured indicators (lattice parameters in Å, at. % of crystal structure and Microchemical Inhomogeneity) obtained by Molecular Dynamics simulations following the PDM or RSM procedures.

First, the values of the MCI parameter ζ (eq. (5)) indicate that in both kinds of simulation, local mixing is achieved (the initial ζ -values for non-mixed polycrystalline systems are ~0.9). Thus there are no major segregations in the final systems: the solid solutions have indeed been formed. Secondly, the amounts of FCC and BCC in the final system after the PDM simulation show that the main part of the system is indeed crystallized (the remaining part being amorphous). The most interesting values of the MD simulations are the lattice parameters. For the FCC $Al_{24.7}Co_{37.2}Ni_{38.1}$ system, the lattice parameter increases significantly from the pure Ni to the solid solution (+3.5%). However, for the BCC structures, there is only a small increase in the case of the simulation (1%). The evolution of the BCC lattice parameter seems not to obey Vegard's law.

It can be concluded that, in our case, an FCC solid solution is only beginning to form since the experimental FCC lattice parameter is not really increasing but the peaks are becoming asymmetrical (Fig. 3b). The Al and Co atoms may have already partly substituted for the Fe and/or Cr atoms in the BCC structure since the lattice parameter does not seem to evolve much with the substitution ratio. Similar observations have been reported in the literature. After a milling step more powerful than the one used in this work, Mohanty *et al.* observed a lattice parameter of 3.56 ± 0.02 Å (3.52 Å for pure Ni) for the FCC-phase and 2.89 ± 0.05 Å (2.87 Å / 2.88 Å) for the BBC-phase [13]. Ji *et al.* observed a BCC lattice parameter of 2.88 Å after a milling step powerful enough to reach complete Mechanical Alloying [12]. A small portion of the milled powder may also be constituted by an amorphous phase; indeed, Portnoi *et al.*

reported the formation of an amorphous phase after 2h milling only for the AlCoCrFeNiTi alloy [32].

The milled powders were also analyzed by particle size analysis (laser granulometry). The results are displayed in Table 5. Particle size distribution is influenced by the milling conditions. The M2 milling results in smaller agglomerates. D_v50 is 4.8 times smaller than those obtained with M1 milling. Introducing pauses leads to thinner particles in M1 and M2. D_v50 is 2.3 times lower than that obtained without pauses. It may be argued that a higher temperature is reached over a longer duration without pauses. Aluminum particles particularly could act as a binder in conditions of higher temperature. Chromium pre-milling does not affect either the D_v50 or the agglomerates size distribution of the final 5-element batches. Hence, chromium pre-milling solely impacts the microstructure of the agglomerates.

Batch	D_v10 (µm)	D_v50 (µm)	D_v90 (µm)
M1-CR-L	130	389	625
M1-CR	49	166	533
M1-cr	39	159	528
M2-cr	11	33	98

Table 5: Particle size distribution of the milled powders.

At this stage, it appears that milling conditions affect milled powders in terms of their morphology, their microstructure and the arrangement at the microscopic scale. In order to quantify the milling efficiency, we adopted a very common, although questionable, point of view based on kinematic models [21,22]. Burgio's model gives the shock energy and power as a function of milling parameters (see Table 6) [33]. According to this approach, collision power is the key factor impacting the final crystallinity and milling progress [34]. Millings M1 and M2 used in this work are lower in energy that those commonly found in the literature, which often lead to total disappearance of the FCC phase during the milling step [12,35]. This estimation suggests that neither of our two milling modes do actually achieve complete Mechanical Alloying. Although these simple kinematic models are very popular, different works based on direct visualization of ball motion in the vials [36] and discrete element methods [37] demonstrate their limitations in accurately describing milling regimes, especially in terms of the relative influence of collision events over friction.

Routes	mJ/hit/g	mW/hit/g	E_{tot} (kJ/g)	K ratio	Centrifugal acceleration
M1	3	47	5	-0.20	9 g
M2	8	109	11	-1	
Moravcik [35] for $AlCoCrFeNiTi_{0.5}$	16	221	19	-1.82	4 g
Mohanty [13]	12	130	12	-2	9 g

Table 6: Calculated quantities (energy by hit and by ball, power (W) by hit and by ball, total energy of the milling by ball) using Burgio's model. Note that these quantities are normalized 'by ball' in order to compare several millings with different numbers of balls.

3.2. Sintering

The different samples presented in Table 1 were sintered using SPS. XRD diffraction patterns are depicted in Fig. 4 for M1-CR-L and M2-CR-L at 1000ºC (commercial Cr with low energetic milling M1 and higher energetic milling M2 of 28h duration) and M1-cr and M2-cr at 1100ºC (pre-milled Cr low energetic milling M1 and higher energetic milling M2 of 4x7h duration with pauses). This characterization allows us to follow the modifications due to sintering as compared to milling (see Fig. 3).

The main observations are as follows:

- An ordered BCC phase (B2) is formed. Cieslak *et al.* claim that XRD characterization does not offer the opportunity to prove the existence of a single B2 phase or an ordered B2 and a disordered A2 phase [38]. However, by considering either one BCC phase (B2) or two BCC phases (B2+A2), the Rietveld analysis presents a better goodness of fit for the first hypothesis of a single B2 phase.
- The FCC peaks clearly shift to lower angles: the FCC phase is not pure Ni at all. For the M1-cr and M2-cr samples, the lattice parameters were calculated using a Rietveld analysis. The FCC lattice parameter is found to be 3.595 Å in both samples. Here, the FCC lattice parameters of M1-cr and M2-cr have increased, meaning that the FCC solid solution was formed during sintering.
- The small peaks around the two main peaks correspond to a tetragonal sigma phase. The sigma phase has often been observed by other researchers, both in powder metallurgy [13] and casting [5]. The sigma phase is present at 1000 °C when the elemental powders are M2-milled. There remain only traces of this phase at 1100 °C for M1-milled powders. Here, the presence of the sigma phase depends on the combination of the milling conditions, the sintering temperature and Cr particles size.

Besides phase characterization, the Rietveld analysis provides interesting information about the structure of the sintered samples. The M1-cr and M2-cr samples, sintered at 1100 °C, are nanostructured:

- M1-cr: BCC phase crystallites size 85 nm, FCC phase crystallites size 140 nm;
- M2-cr: BCC 125 nm, FCC 100 nm.

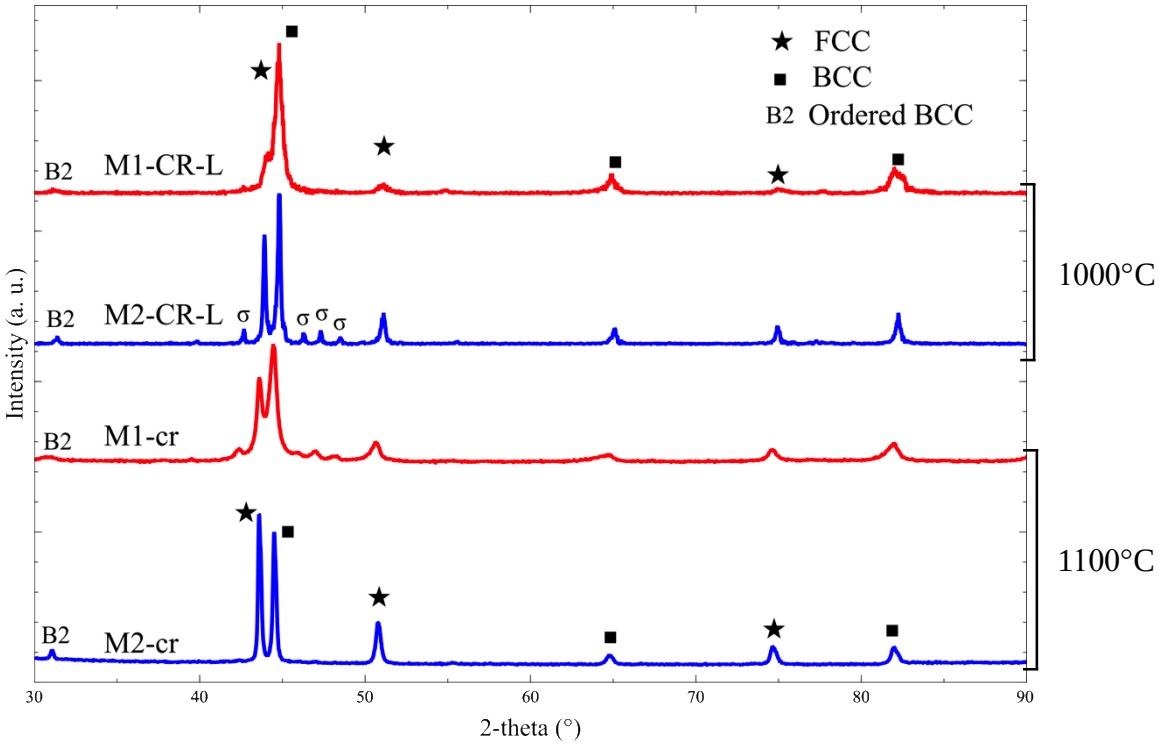

Figure 4: X-ray diffraction patterns of M1-CR-L, M2-CR-L (sintered at 1000°C) M1-cr, M2-cr (sintered at 1100°C) samples. The intensities are normalized on the main BCC peak.

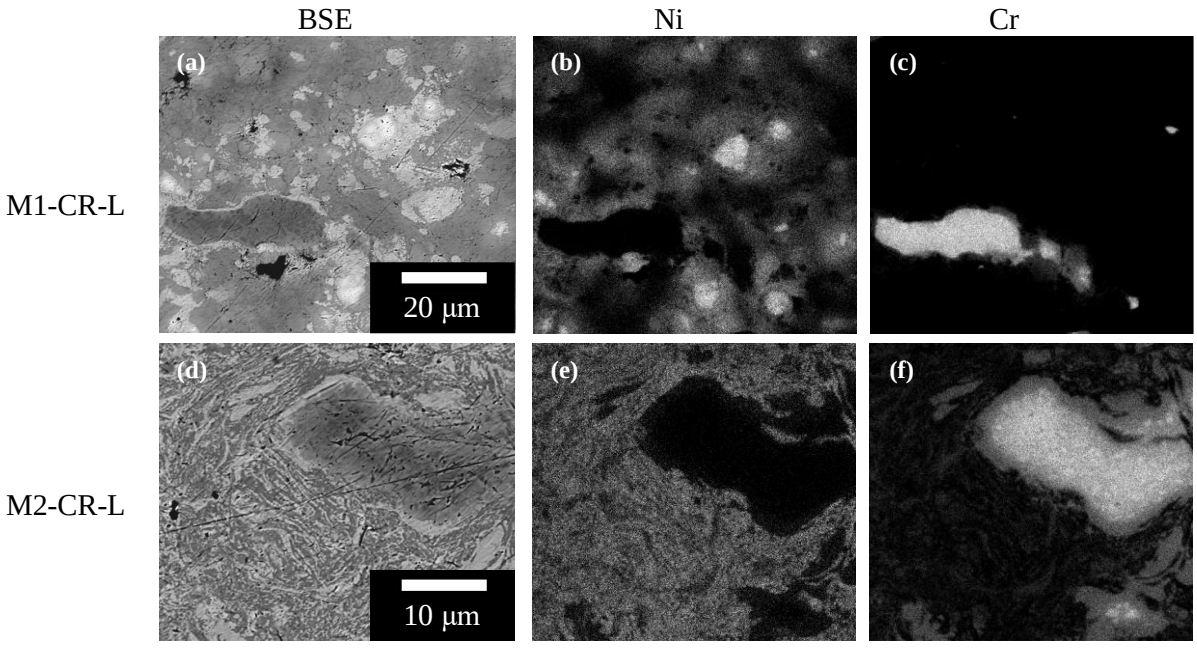

Figure 5: SEM image (BSE mode) (a), Ni distribution (b) and Cr distribution (c) of the samples M1-CR-L sintered at 1000°C. SEM image (BSE mode) (d), Ni distribution (e) and Cr distribution (f) of the samples M2-CR-L sintered at 1000°C.

The microstructure of sintered samples was investigated by means of usual SEM characterization. Figure 5 shows the SEM images of samples sintered at 1000 ºC with commercial chromium. It is evident that milling conditions affect the microstructure. An energetic milling favors a lamellar structure (Fig. 5a and Fig. 5d). Let us note that the M1-sample microstructure remains heterogeneous (Fig. 5a) as compared to agglomerates (Fig. 2a). In this case, sintering does not drastically modify the distribution of elements observed after the milling step. EDX cartography demonstrates that elemental distribution is far from being homogenous (Fig. 5b 5c 5e 5f). Highly concentrated Ni zones are still present in the M1-sample, whereas Ni is rather well mixed in the M2 sample. For both millings, initial chromium grains remain practically intact and Cr barely diffuses into the rest of the sample.

As shown in Fig. 6, sintering results in a better chemical homogeneity, when the temperature is increased to 1100 °C and chromium is pre-milled. M1-samples consist mainly of two phases and chromium particles (Fig. 6a). There are also black dots around the grains: these have not yet been precisely analyzed, but they must be carbides and/or oxides (mainly Cr_xC_y [39] and Al_2O_3 [35]). EDX mapping confirms this hypothesis. It also suggests the presence of chromium oxides (see Supplementary Material, Fig. A1). The microstructure of M2-samples is still lamellar and exhibits two to three contrasts in the BSE mode.

Finally, the modification of two parameters (temperature and chromium initial size) leads to a more interesting material. Indeed, compared to M1-samples sintered at 1000 ºC, the distribution of the two main phases is much thinner in the M2-samples sintered at 1100ºC. Hence, M2-cr parameters genuinely lead to unique and interesting HEAs.

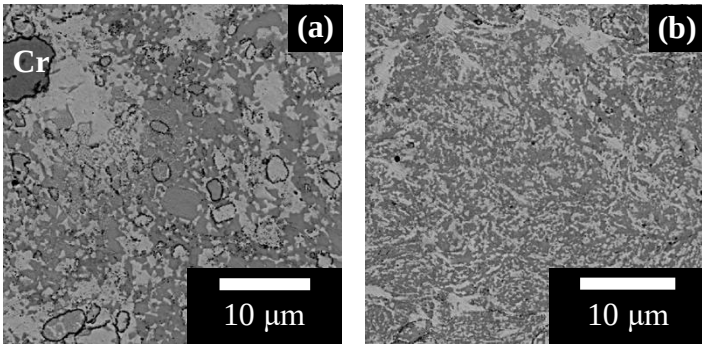

Figure 6: SEM images (BSE mode) of microstructure of M1-cr sintered at 1100 °C (a) and M2-cr samples sintered at 1100 °C (b).

Table 7: Compositions (in at.%) of the different phases measured from EDX.

Samples	SEM Contrast	Al	Co	Cr	Fe	Ni
M1-cr	Light-grey phase	9.6	23	23.7	25.7	18
	Medium-grey phase	25	19	13	17	26
M2-cr	Light-grey phase	8	25	25.7	25.7	15.6
	Medium-grey phase	27.5	17.5	16	15	24

The composition associated with each observed BSE phase was determined by EDX analysis (see Table 7):

- The light-grey contrast corresponds to an Al-Ni poor and Fe-Cr-Co rich composition.
- The medium-grey contrast corresponds to an Al-Ni rich and Fe-Cr-Co poor composition.

The σ phase ($\simeq Co_{0.25}Cr_{0.5}Fe_{0.25}$) detected by XRD in the M2-CR-L sample sintered at 1000 ºC may possibly surround the chromium particles as shown in Fig. 5f. It is more difficult to precisely locate the σ phase in the M1-cr sample with pre-milled chromium.

The EBSD phase map and the corresponding SEM image are shown in Fig. 7. Comparison between the two pictures demonstrates that the Al-Ni rich phase corresponds to the BCC phase observed in the diffraction patterns and the Fe-Cr-Co rich phase corresponds to the FCC phase. By combining the results of the Rietveld analysis, EBSD and SEM pictures, the volume fraction of each phase can be estimated. It is close to 50-50% and never exceeds 60% locally in the M2 milling samples. For M1 milling, the BCC phase constitutes over 75% of the sintered sample.

In addition, XR Fluorescence results indicate that the composition of the whole M2-cr sintered sample is very close to equimolar.

The CALPHAD approach was used in order to determine the FCC/BCC ratio at thermodynamic equilibrium. The phase volume fraction and corresponding composition are presented in Fig. 8a in the equimolar case $Al_xCoCrFeNi$ (x=1). According to our calculations, based on the database TCNI9 [40] (Thermo-Calc [41]), only 2 BCC phases should form at the target temperatures (1000°C or 1100°C). That is precisely observed in as-cast HEAs [3–7]. The BCC phase consists of an ordered and a disordered phase. In the case of the solid route used in this work, an FCC phase was also formed during elaboration. It does not seem that the presence of

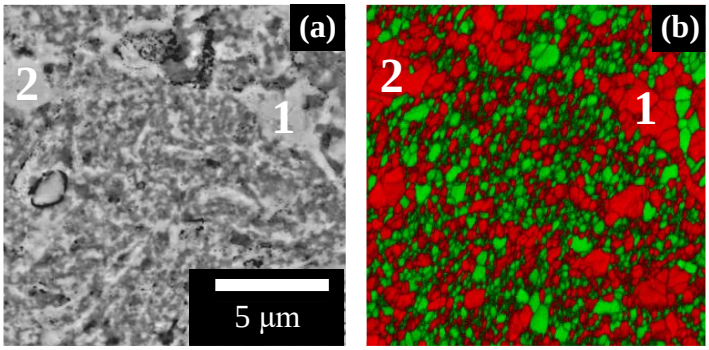

Figure 7: (a) SEM image (BSE) and (b) EBSD phase map of the M2-milled, 1100°C sintered sample (green corresponding to BCC and red to FCC).

the FCC phase is due to the initial state of the milled agglomerates exhibiting the coexistence of FCC and BCC phases. Indeed, other groups report the formation of FCC and BCC phases by sintering from only BCC agglomerates [12].

Calculating with a slightly lower Al content, corresponding to $Al_xCoCrFeNi$ (x=0.75) composition, gives the coexistence of a disordered FCC phase, $Al_6Co_{21}Cr_{29}Fe_{25}Ni_{17}$, and an ordered BCC phase (Fig. 8b). The sigma phase is not expected in the range of processing temperatures. Although the agreement between thermodynamic calculations and experimental observations is encouraging, a quantitative discrepancy persists. Different assumptions may be formulated:

- The chosen composition AlxCoCrFeNi is at the border of two domains (Figs. 8a, 8b, 8c) and a slight shift in Al composition may induce different phase equilibriums.
- In our experiments, equilibrium has not been reached because of the solid-state fabrication. Indeed, powder metallurgy routes are known to produce metastable materials, especially with HEBM [42]. The effect of a heat treatment on the samples would be interesting way to detect the persistence of an FCC phase at higher temperatures.
- Chemical homogeneity is not reached locally: the fact that some areas are depleted of Al and reach an equilibrium corresponding to Fig. 8b could explain the presence of FCC. In addition, a slight decrease in Cr content could also lead to the formation of FCC (Fig. 8d).
- Finally, the database we use could be improved, especially since the $Al_1CoCrFeNi$ composition seems to be at the border of two domains. Indeed, other researchers come to different conclusions using different databases [43,44]. However, results similar to ours have been reported by Butler *et al.* [9].

We here report the material properties of the samples we fabricated. Relative density is 91.1% for M1-CR-L sample and 98% for M2-CR-L. The M1-CR-L sample exhibits a hardness of 525 HV and the M2-CR-L sample of 670 HV. Relative density is 97.5% for the M1-cr sample and 96% for M2-cr. The sample sintered from the M1-activated powder exhibits a hardness of 530 HV and that from the M2-milled powder exhibits hardness of 610 HV. These values are consistent with the results from the literature. HEAs elaborated by the solid-state route are harder than arc-melted HEAs. For instance, an AlCoCrFeNi cast-alloy of 500 HV was reported here [5] whereas the hardness of the same sintered alloy was found to attain 625 HV [12]. Compared to cast alloys, increased hardness is mainly due to impurities resulting from the process (precipitation hardening, especially for hard ceramic precipitates) and limited grain size (grain boundary hardening) [35,45]. The M2-CR-L sample exhibits the highest hardness because of its highest content of sigma phase. Indeed, the sigma phase is known to increase hardness of similar alloys [5,13].

It was not possible to measure the hardness of each phase separately with the micro-hardness instrument we used. However, the difference in hardness between the M1 and M2 samples may be due to different FCC/BCC distribution. Indeed, the Fe-Cr-Co rich FCC phase is more abundant in the M2 sample and could be harder than the Al-Ni rich BCC phase.

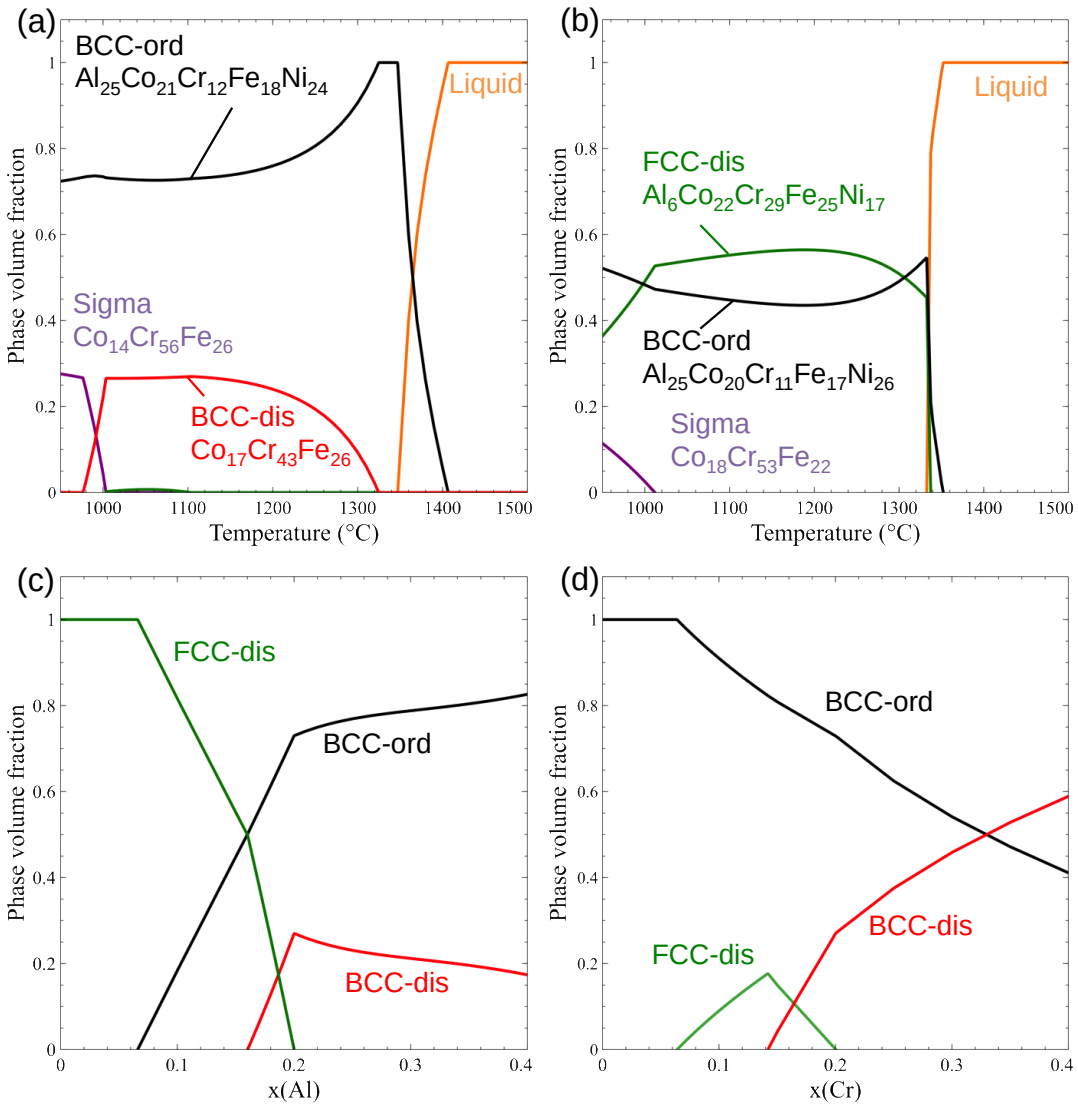

Figure 8: Phase volume fraction as a function of Temperature together with composition. x(Al)=0.2 $Al_1CoCrFeNi$ (a) and x(Al)=0.15 $Al_{0.75}CoCrFeNi$ (b). Phase volume fraction as a function of Al content (c) and Cr content (d) at sintering temperature (1100°C). Thermo-Calc with TCNI9.

4. Conclusion

In this work, we tested the versatility of powder metallurgy routes, especially by studying the combination of mechanical activation and reactive sintering. “Medium” energy ball milling of 5 elemental powders produced agglomerates of enhanced reactivity. Their microstructure depended on the milling conditions. The typical lamellar structure, observed in the K=1 case, consists of closely imbricated elements. Complementary experimental characterization and numerical study of milled powders enabled us to accurately depict their crystalline state as precursors of solid solutions. Given the right parameters, the SPS process produced a nanostructured sample (M2-cr) with two multicomponent solid solutions (BCC+FCC) homogenously distributed.
Our work, based on the reactive sintering of activated agglomerates, proves that a complete Mechanical Alloying is not necessary to elaborate High Entropy Alloys. We have demonstrated that this new way of producing HEAs leads to a unique microstructure. This kind of dual microstructure could have remarkable properties, especially mechanical ones [46]. For high temperature applications, the stability of this microstructure needs to be evaluated by long duration heat treatments. This study could also be valuably extended to other compositions and other metallic elements.

We have not yet identified, however, the nanosized precipitates formed during the process. They could be oxides (due to the impurities of the initial powders) or carbides (due to the use of graphite dies for SPS). Future work will thus need to determine the nature of these precipitates and find a way to hinder their formation.
It would also be interesting to correctly predict the amount of each phase via Calphad, either by using an improved database or by precisely understanding the reasons for the observed discrepancies. This improvement will enable us to tailor the mechanical properties of the high entropy alloys prepared by reactive sintering and to investigate other HEAs.

Finally, the milling and sintering steps can be further optimized to control the formation of unwanted phases (σ) and impurities as well as to shorten the duration of the process.

References

[1] J.-W. Yeh, S.-K. Chen, S.-J. Lin, J.-Y. Gan, T.-S. Chin, T.-T. Shun, C.-H. Tsau, S.-Y. Chang, Nanostructured High-Entropy Alloys with Multiple Principal Elements: Novel Alloy Design Concepts and Outcomes, Adv. Eng. Mater. 6 (2004) 299–303. https://doi.org/10.1002/adem.200300567.

[2] D.B. Miracle, O.N. Senkov, A critical review of high entropy alloys and related concepts, Acta Mater. 122 (2017) 448–511. https://doi.org/10.1016/j.actamat.2016.08.081.

[3] S. Uporov, V. Bykov, S. Pryanichnikov, A. Shubin, N. Uporova, Effect of synthesis route on structure and properties of AlCoCrFeNi high-entropy alloy, Intermetallics. 83 (2017) 1–8. https://doi.org/10.1016/j.intermet.2016.12.003.

[4] M. Ren, B. Li, H. Fu, Formation condition of solid solution type high-entropy alloy, Trans. Nonferrous Met. Soc. China. 23 (2013) 991–995. https://doi.org/10.1016/S1003-6326(13)62557-1.

[5] A. Munitz, S. Salhov, S. Hayun, N. Frage, Heat treatment impacts the micro-structure and mechanical properties of AlCoCrFeNi high entropy alloy, J. Alloys Compd. 683 (2016) 221–230. https://doi.org/10.1016/j.jallcom.2016.05.034.

[6] A. Manzoni, H. Daoud, R. Völkl, U. Glatzel, N. Wanderka, Phase separation in equiatomic AlCoCrFeNi high-entropy alloy, Ultramicroscopy. 132 (2013) 212–215. https://doi.org/10.1016/j.ultramic.2012.12.015.

[7] K.R. Lim, K.S. Lee, J.S. Lee, J.Y. Kim, H.J. Chang, Y.S. Na, Dual-phase high-entropy alloys for high-temperature structural applications, J. Alloys Compd. 728 (2017) 1235–1238. https://doi.org/10.1016/j.jallcom.2017.09.089.

[8] Y.P. Wang, B.S. Li, M.X. Ren, C. Yang, H.Z. Fu, Microstructure and compressive properties of AlCrFeCoNi high entropy alloy, Mater. Sci. Eng. A. 491 (2008) 154–158. https://doi.org/10.1016/j.msea.2008.01.064.

[9] T.M. Butler, M.L. Weaver, Oxidation behavior of arc melted AlCoCrFeNi multi-component high-entropy alloys, J. Alloys Compd. 674 (2016) 229–244. https://doi.org/10.1016/j.jallcom.2016.02.257.

[10] S. Varalakshmi, M. Kamaraj, B.S. Murty, Synthesis and characterization of nanocrystalline AlFeTiCrZnCu high entropy solid solution by mechanical alloying, J. Alloys Compd. 460 (2008) 253–257. https://doi.org/10.1016/j.jallcom.2007.05.104.

[11] C. Suryanarayana, Mechanical alloying and milling, Prog. Mater. Sci. 46 (2001) 1–184. https://doi.org/10.1016/S0079-6425(99)00010-9.

[12] W. Ji, Z. Fu, W. Wang, H. Wang, J. Zhang, Y. Wang, F. Zhang, Mechanical alloying synthesis and spark plasma sintering consolidation of CoCrFeNiAl high-entropy alloy, J. Alloys Compd. 589 (2014) 61–66. https://doi.org/10.1016/j.jallcom.2013.11.146.

[13] S. Mohanty, T.N. Maity, S. Mukhopadhyay, S. Sarkar, N.P. Gurao, S. Bhowmick, K. Biswas, Powder metallurgical processing of equiatomic AlCoCrFeNi high entropy alloy: Microstructure and mechanical properties, Mater. Sci. Eng. A. 679 (2017) 299–313. https://doi.org/10.1016/j.msea.2016.09.062.

[14] C. Yang, J. Lin, J. Zeng, Shenggua. Qu, X. Li, W. Zhang, D. Zhang, High-Strength AlCrFeCoNi High Entropy Alloys Fabricated by Using Metallic Glass Powder as Precursor., Adv. Eng. Mater. 18 (2016) 348–353. https://doi.org/10.1002/adem.201500339.

[15] A. Zhang, J. Han, J. Meng, B. Su, P. Li, Rapid preparation of AlCoCrFeNi high entropy alloy by spark plasma sintering from elemental powder mixture, Mater. Lett. 181 (2016) 82–85. https://doi.org/10.1016/j.matlet.2016.06.014.

[16] M. Vaidya, A. Prasad, A. Parakh, B.S. Murty, Influence of sequence of elemental addition on phase evolution in nanocrystalline AlCoCrFeNi: Novel approach to alloy synthesis using mechanical alloying, Mater. Des. 126 (2017) 37–46. https://doi.org/10.1016/j.matdes.2017.04.027.

[17] E. Colombini, R. Rosa, L. Trombi, M. Zadra, A. Casagrande, P. Veronesi, High entropy alloys obtained by field assisted powder metallurgy route: SPS and microwave heating,

Mater. Chem. Phys. 210 (2018) 78–86. https://doi.org/10.1016/j.matchemphys.2017.06.065.

[18] E. Gaffet, F. Bernard, J.-C. Niepce, F. Charlot, C. Gras, G. Le Caër, J.-L. Guichard, P. Delcroix, A. Mocellin, O. Tillement, Some recent developments in mechanical activation and mechanosynthesis, J. Mater. Chem. 9 (1999) 305–314. https://doi.org/10.1039/a804645j.

[19] V.V. Boldyrev, Mechanochemistry and mechanical activation of solids, Russ. Chem. Rev. 75 (2006) 177–189. https://doi.org/10.1070/RC2006v075n03ABEH001205.

[20] M. Kiani, T. Ebadzadeh, Effect of mechanical activation and microwave sintering on crystallization and mechanical strength of cordierite nanograins, Ceram. Int. 41 (2015) 2342–2347. https://doi.org/10.1016/j.ceramint.2014.10.044.

[21] P. Tsokov, V. Blaskov, D. Klissurski, I. Tsolovski, Effect of mechanical activation on the synthesis of α-Fe2O3-Cr2O3 solid solutions, J. Mater. Sci. 28 (1993) 184–188. https://doi.org/10.1007/BF00349050.

[17] S. Plimpton, Fast Parallel Algorithms for Short–Range Molecular Dynamics, J. Comput. Phys. 117 (1995) 42. doi:10.1006/jcph.1995.1039. http://lammps.sandia.gov.

[23] X.W. Zhou, R.A. Johnson, H.N.G. Wadley, Misfit-energy-increasing dislocations in vapor-deposited CoFe/NiFe multilayers, Phys. Rev. B. 69 (2004). https://doi.org/10.1103/PhysRevB.69.144113.

[24] Z. Lin, R.A. Johnson, L.V. Zhigilei, Computational study of the generation of crystal defects in a bcc metal target irradiated by short laser pulses, Phys. Rev. B. 77 (2008). https://doi.org/10.1103/PhysRevB.77.214108.

[25] R.A. Johnson, Alloy models with the embedded-atom method, Phys. Rev. B. 39 (1989) 12554–12559. https://doi.org/10.1103/PhysRevB.39.12554.

[26] S. Odunuga, Y. Li, P. Krasnochtchekov, P. Bellon, R.S. Averback, Forced Chemical Mixing in Alloys Driven by Plastic Deformation, Phys. Rev. Lett. 95 (2005). https://doi.org/10.1103/PhysRevLett.95.045901.

[27] A. Perron, S. Garruchet, O. Politano, G. Aral, V. Vignal, Oxidation of nanocrystalline aluminum by variable charge molecular dynamics, J. Phys. Chem. Solids. 71 (2010) 119–124. https://doi.org/10.1016/j.jpcs.2009.09.008.

[28] A. Stukowski, Structure identification methods for atomistic simulations of crystalline materials, Model. Simul. Mater. Sci. Eng. 20 (2012) 045021. https://doi.org/10.1088/0965-0393/20/4/045021.

[29] J.H. Li, L.T. Kong, B.X. Liu, Proposed Definition of Microchemical Inhomogeneity and Application To Characterize Some Selected Miscible/Immiscible Binary Metal Systems, J. Phys. Chem. B. 108 (2004) 16071–16076. https://doi.org/10.1021/jp047897x.

[30] A.F. Wells, Structural Inorganic Chemistry, 5th ed., Clarendon Press, Oxford, 1984.

[31] J. Wallenius, P. Olsson, C. Lagerstedt, N. Sandberg, R. Chakarova, V. Pontikis, Modeling of chromium precipitation in Fe-Cr alloys, Phys. Rev. B. 69 (2004). https://doi.org/10.1103/PhysRevB.69.094103.

[32] V.K. Portnoi, A.V. Leonov, S.E. Filippova, A.N. Streletskii, A.I. Logacheva, Mechanochemical synthesis and heating-induced transformations of a high-entropy Cr-Fe-Co-Ni-Al-Ti alloy, Inorg. Mater. 50 (2014) 1202–1211. https://doi.org/10.1134/S0020168514120188.

[33] N. Burgio, A. Iasonna, M. Magini, S. Martelli, F. Padella, Mechanical alloying of the Fe−Zr system. Correlation between input energy and end products, Il Nuovo Cimento D. 13 (1991) 459–476. https://doi.org/10.1007/BF02452130.

[34] M. Abdellaoui, E. Gaffet, The physics of mechanical alloying in a planetary ball mill: Mathematical treatment, Acta Metall. Mater. 43 (1995) 1087–1098. https://doi.org/10.1016/0956-7151(95)92625-7.

[35] I. Moravcik, J. Cizek, P. Gavendova, S. Sheikh, S. Guo, I. Dlouhy, Effect of heat treatment on microstructure and mechanical properties of spark plasma sintered AlCoCrFeNiTi0.5 high entropy alloy, Mater. Lett. 174 (2016) 53–56. https://doi.org/10.1016/j.matlet.2016.03.077.

[36] A.S. Rogachev, D.O. Moskovskikh, A.A. Nepapushev, T.A. Sviridova, S.G. Vadchenko, S.A. Rogachev, A.S. Mukasyan, Experimental investigation of milling regimes in planetary ball mill and their influence on structure and reactivity of gasless powder exothermic mixtures, Powder Technol. 274 (2015) 44–52. https://doi.org/10.1016/j.powtec.2015.01.009.

[37] S. Rosenkranz, S. Breitung-Faes, A. Kwade, Experimental investigations and modelling of the ball motion in planetary ball mills, Powder Technol. 212 (2011) 224–230. https://doi.org/10.1016/j.powtec.2011.05.021.

[38] J. Cieslak, J. Tobola, K. Berent, M. Marciszko, Phase composition of AlxFeNiCrCo high entropy alloys prepared by sintering and arc-melting methods, J. Alloys Compd. 740 (2018) 264–272. https://doi.org/10.1016/j.jallcom.2017.12.333.

[39] S.-H. Joo, H. Kato, M.J. Jang, J. Moon, E.B. Kim, S.-J. Hong, H.S. Kim, Structure and properties of ultrafine-grained CoCrFeMnNi high-entropy alloys produced by mechanical alloying and spark plasma sintering, J. Alloys Compd. 698 (2017) 591–604. https://doi.org/10.1016/j.jallcom.2016.12.010.

[36] TCNI9: Thermo-Calc Ni-base alloys database, version 9.0. Developed and provided by Thermo-Calc Software AB (2019), https://www.thermocalc.com/media/83726/TCNI9_extended_info.pdf

[41] J.-O. Andersson, T. Helander, L. Höglund, P. Shi, B. Sundman, Thermo-Calc & DICTRA, computational tools for materials science, Calphad. 26 (2002) 273–312. https://doi.org/10.1016/S0364-5916(02)00037-8.

[42] C.C. Koch, O.B. Cavin, C.G. McKamey, J.O. Scarbrough, Preparation of "'amorphous"' $Ni_{60}Nb_{40}$ by mechanical alloying, Appl. Phys. Lett. 43 (1983) 1017–1019. https://doi.org/10.1063/1.94213.

[43] C. Zhang, F. Zhang, H. Diao, M.C. Gao, Z. Tang, J.D. Poplawsky, P.K. Liaw, Understanding phase stability of Al-Co-Cr-Fe-Ni high entropy alloys, Mater. Des. 109 (2016) 425–433. https://doi.org/10.1016/j.matdes.2016.07.073.

[44] A. Manzoni, S. Singh, H. Daoud, R. Popp, R. Völkl, U. Glatzel, N. Wanderka, On the Path to Optimizing the Al-Co-Cr-Cu-Fe-Ni-Ti High Entropy Alloy Family for High Temperature Applications, Entropy. 18 (2016) 104. https://doi.org/10.3390/e18040104.

[45] C. Shang, E. Axinte, J. Sun, X. Li, P. Li, J. Du, P. Qiao, Y. Wang, CoCrFeNi(W 1−x Mo x) high-entropy alloy coatings with excellent mechanical properties and corrosion resistance prepared by mechanical alloying and hot pressing sintering, Mater. Des. 117 (2017) 193–202. https://doi.org/10.1016/j.matdes.2016.12.076.

[46] S. Gangireddy, B. Gwalani, V. Soni, R. Banerjee, R.S. Mishra, Contrasting mechanical behavior in precipitation hardenable AlXCoCrFeNi high entropy alloy microstructures: Single phase FCC vs. dual phase FCC-BCC, Mater. Sci. Eng. A. 739 (2019) 158–166. https://doi.org/10.1016/j.msea.2018.10.021.

Chapter V: Effects of mechanical activation on chemical homogeneity and contamination level in dual-phase AlCoCrFeNi high entropy alloy

1. Introduction

High Entropy Alloys have attracted much attention since the pioneer articles by Yeh et al. [1] and Cantor et al. [2]. Materials scientists quickly realized the potential revolution inherent in the initial concept and generalized it to a broader topic: Complex Concentrated Alloys (CCA), alloys with no obvious base element [3].

One of the top five most studied compositions is AlCoCrFeNi. Indeed, Al often represents the promise of light weight and high temperature oxidation resistance [4], two very important properties. However, for sintered and cast alloys, the $Al_xCoCrFeNi$ composition is characterized by a large diversity of microstructures: these range from ordered Body Centered Cubic (BCC) precipitates (B2) in a disordered BCC matrix for x=1 [5] to a single BCC or a single Face Centered Cubic (FCC) phase depending on the Al content [6,7]. In fact, the elaboration process plays an important role in microstructure formation. Indeed, the disordered BCC+B2 microstructure is commonly observed in AlCoCrFeNi alloys prepared by arc-melting while other phases may appear as a result of powder metallurgy. Ji *et al.* observed the combination of B2 and disordered FCC phases [8] whereas other researchers reported much more complex microstructures containing disordered FCC, ordered FCC ($L1_2$) and tetragonal sigma phases [9–11].

One of the main challenges in HEA development is to understand the relation between the elaboration method and the resulting microstructure/properties. Only a small fraction of HEAs are synthesized by solid state processing, although HEAs elaborated this way often exhibit better homogeneity in their microstructures compared to those elaborated using the classical arc melting method [12]. Powder metallurgy has proven to be an alternative way to produce nanostructured HEA with promising properties [13–16]. However, most of the literature on powder metallurgy synthesis of HEAs reports the use of High Energy Ball Milling in order to reach complete Mechanical Alloying (MA). One of the main difficulties in this regard is the compromise between required time and milling power. This route often leads to contamination. Contamination during milling usually arises either via the Process Control Agent (PCA) [17–20] which is used to prevent cold welding and oxidation, or by the grinding media such as WC or Fe [21,22]. Contamination does not necessarily lead to a weakening of desired properties. It remains of the highest importance to precisely control the amounts of minor elements (C, O or N) during the elaboration process.

Addressing this issue in their review, Vaidya et al. identified several challenges in the development of HEAs processed by powder metallurgy [23]. They highlighted the importance of producing a contamination-free alloy in order to thoroughly understand the key features of nanostructured HEAs, that is, without taking into account the role of minor elements. They also suggested that understanding the discrepancies between Calphad predictions and experimental results was one of the next steps in improving the production of HEAs by powder metallurgy. In fact, two main factors may induce such discrepancies: the out of equilibrium process associated with powder metallurgy and contamination by minor elements. A study evaluating the relative contribution of each factor would be truly valuable.

In the present work, Medium Energy Ball Milling was used in order to reach mechanical activation. The corresponding milling power and time alleviates the main drawbacks of solid state processing such as contamination by minor elements. The mechanical activation enhances particle reactivity by creating defects and by increasing the number of interfaces between reactants [24]. However, a solid solution is not formed during milling. This manner of elaborating alloys shifts the critical step to the sintering, which can be easier to handle. Preliminary studies on mechanical activation have confirmed the potential interest of this production method of High Entropy Alloys. A first reserve, however, is that one might expect to obtain a final inhomogeneous stage as a result, arguing that the sintering of inhomogeneous agglomerates will lead to poor chemical distribution in the sintered alloy. Colombini *et al.* tried to perform short mechanical activation of the AlCoCrFeNi composition [25]. As-sintered samples exhibited complex microstructures. Only an annealing of 50h led to the formation of a single FCC phase and even here some chemical segregation remained. Emphasizing that the presence of carbides in HEAs influences their plasticity, John *et al.* studied the elaboration of $Al_{0.3}$CoCrFeNi by mechanical activation and SPS [26]. They reported the formation of a major FCC phase with carbides and alumina precipitates. They demonstrated that mechanical activation efficiently decreased the amount of carbides and claimed that carbon came mainly from the toluene, used as a PCA. They suggested that dry milling could be one of the ways to improve the process. Concerning the formation of oxides during powder metallurgy processes, Kang *et al.* argued that most oxygen contamination occurred during the milling. They determined a minimum milling time limiting the contamination of the $Al_{0.1}$CrNbVMo composition [27]. The sintered sample exhibited a major BCC phase with some alumina inclusions. They reported outstanding mechanical properties, such as high yield strength, as compared to as-cast similar refractory alloys.
In our previous work, we studied the influence of planetary ball milling on the synthesis of AlCoCrFeNi [28]. We demonstrated that long mechanical alloying was not mandatory in the elaboration of sintered alloys with high entropy solid solutions. In the present work, we used APT in order to provide valuable information on the distribution of all alloying elements, their spatial correlation and the nature of the nano-impurities which are not discernible or identifiable by more classical methods of characterization. New Calphad calculations were performed in order to take into account the nature of the precipitates in the global composition. These calculations shed light on the various factors that induce discrepancies between thermodynamic and experimental results.

2. Materials and methods

Elemental powders of Al, Co, Cr, Fe and Ni of high purity (all > 99.2 wt%, Alfa Aesar) were first blended with a TURBULA® mixer (WAB Turbula T2F) for 24 hours.
The blended powders were then processed by planetary ball milling (Fritsch Pulverisette 4) for 28h with 2h pauses every 7h. Pauses prevent the powder from adhering to the vial wall. The ratio between the weight of the balls and the powders was set at 7:1. The milling speed was set to 250 rpm for the disk and the relative speed of the vials was 250 rpm. No process control agent was used to prevent any supplementary contamination.
The powders were subsequently consolidated by means of Spark Plasma Sintering (SPS, FCT Systeme GmbH HPD 10) at 80 MPa in a 10 mm inner-diameter graphite die. A target temperature of 1100°C and a heating rate of 50°C/min were used. No dwell time was applied in order to preserve the nanostructure of the material. Sintering was carried out in a vacuum. Grinding bowls and SPS dies were filled under argon atmosphere in order to avoid possible oxygen contamination.
The powders and the sintered samples (upper surfaces after polishing) were analyzed using X-Ray Diffraction with Cu Kα radiation (XRD, Siemens D5000), scanning electron microscopy (SEM, JEOL JSM 7600F). Oxygen and Nitrogen were determined by the inert gas fusion method using LECO TC-136 and LECO TC-436AR oxygen/nitrogen analyzer. The carbon content was determined by LECO CS-744 carbon sulfur analyzer. Both kinds of chemical analyses were performed on powders and sintered samples.
X-ray Photoelectron Spectrometry (XPS) analyses were performed using a PHI 5000 Versaprobe apparatus with monochromatic Al Kα1 X-Ray source.
In addition, Atom Probe Tomography (APT) was performed on sintered samples. APT specimens were prepared via the lift-out technique using a dual-beam FIB-SEM [29]. The micro-tips were prepared by means of the annular milling method to obtain an end radius of ~100 nm. The APT analyses were carried out in a LEAP 3000X-HR instrument using the electrical pulsing mode (100 kHz). The detection rate was kept at 0.002 event/pulse by progressively increasing the applied voltage. The specimen temperature and the fraction of pulsing were set to 80 K and 20% of applied voltage respectively.

3. Results and discussion

As we reported in a previous study, the milling parameters used in this work do not achieve complete Mechanical Alloying. The peculiar state of the milled powders is the specificity of the mechanical activation process. Comprehensive characterization of the powder is reported elsewhere [28].

3.1.Mechanical activation of Al-Co-Cr-Fe-Ni powders

Figure 1a depicts the diffractograms of the powder before and after milling. The FCC Al and HCP Co peaks completely disappear. Two sets of peaks remain observable: one corresponding to a Body Centered Cubic structure, lattice parameter: 2.87 Å and the other corresponding to a Face Centered Cubic structure, lattice parameter: 3.53 Å. Contrary to results from more energetic milling of Al-Co-Cr-Fe-Ni powders [8], asymmetric FCC peaks are still observed after 28h of milling in our case. The dissymmetry indicates that there is a gradient of concentration of other elements (especially Al which has a larger metallic radius than the others) in the FCC Ni-based matrix. Simply put, we can infer from the XRD that two intermediate solid solutions are formed but that complete Mechanical Alloying is not attained.
Figure 1b shows the SEM image of the cross section of the milled powder. The agglomerates are in an intermediate state between composite and Mechanically Alloyed. Indeed, the lamellae are very thin (~100 nm) and are not perfectly pure, judging from the asymmetric peaks of the XRD.
Because of this peculiar starting state of the agglomerates, the sintering step is described as "reactive sintering". Homogeneous high entropy solid solutions will actually be formed during sintering.

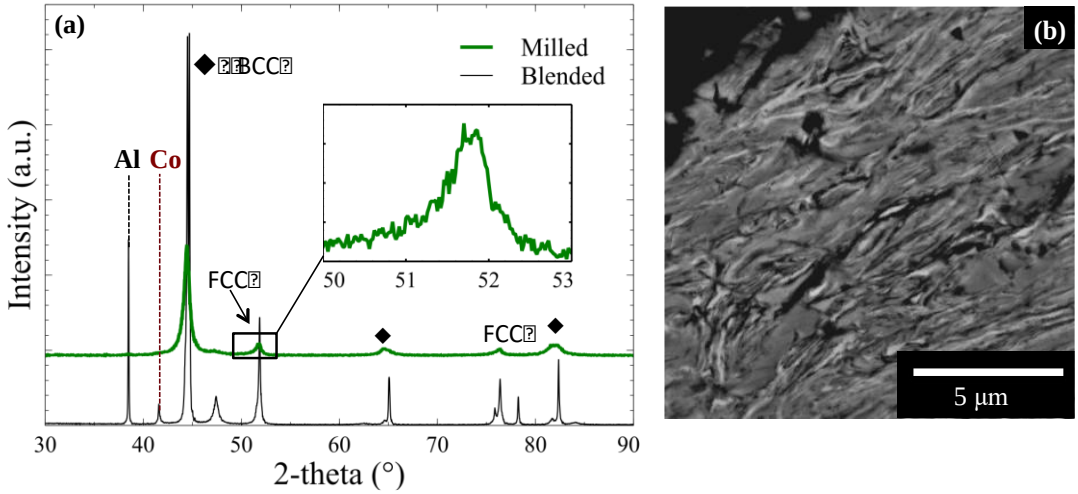

Figure 1 : (a) Diffractograms of blended and milled AlCoCrFeNi powders. The inset is a close-up view of the asymmetric (200) FCC peak. (b) BSE SEM cross-section of AlCoCrFeNi milled agglomerates.

Figure 2a reveals the presence of three or four phases after sintering. The peak at 32° 2θ indicates the formation of an ordered B2 phase. At this point, we do not know if the entire BCC phase is partly or fully ordered. There are very slight traces of a sigma phase (2θ = 42.4°), a finding previously observed in other studies concerning HEA composition with Cr [30]. The lattice parameter of the FCC phase after sintering is 3.60 Å and the peaks are no longer asymmetric. This observation suggests that there are two actual high entropy solid solutions, one FCC and one BCC (disordered and/or B2). Rietveld analysis indicates that the average crystallite size is approximately 100 nm for the two main phases and is not measurable for the sigma phase.

Figure 2b depicts the unique microstructure obtained by reactive sintering. Indeed, after Mechanical Alloying followed by SPS densification, the microstructure is usually uniform [10]. Here, the microstructure is lamellar and very thin. The average width of a region is approximately 500 nm. Two main contrasts are observed. EDX, EBSD and XRD analyses reveal that the bright one corresponds to a Fe-Cr-Co rich FCC phase and the dark one corresponds to an Al-Ni rich BCC phase. The volume ratio is estimated through our different characterization techniques to be around 50-50 %. The compositions of these phases, obtained by averaging ten points, are listed in table 1. The sigma (σ) phase, in addition to being in trace form as mentioned above, seems to have a very close BSE contrast to that of the BCC phase. We therefore did not manage to precisely evaluate the composition of sigma by means of EDX. The presence of black precipitates is also noticeable. It is not possible to precisely identify them by means of SEM EDX since their size never exceeds 10 nm. They could be principally carbides (as commonly seen in Spark Plasma Sintered samples [31]) or
oxides originating elsewhere [17]. EDX mapping was used but was not wholly conclusive on this point.

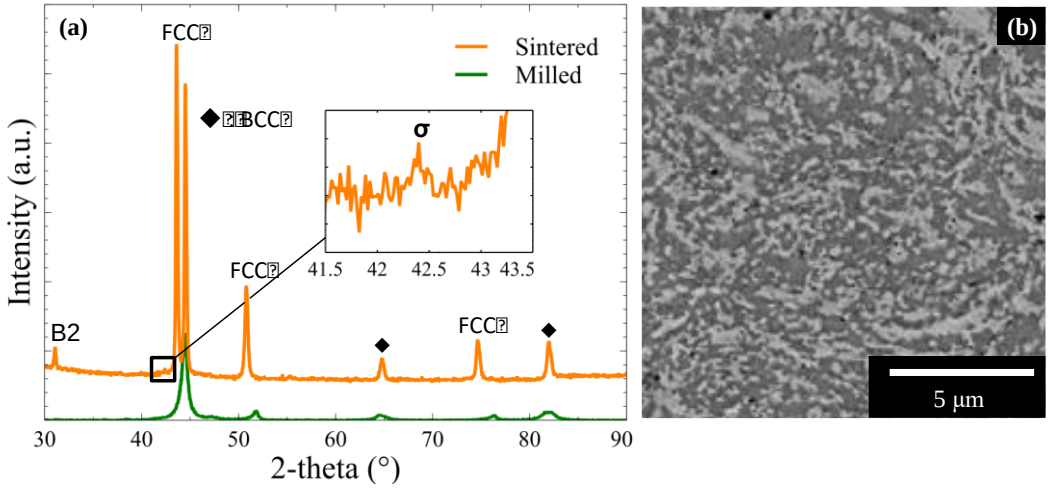

Figure 2: (a) Diffractograms of milled and sintered AlCoCrFeNi. The inset is a close-up view of the (112) σ peak. (b) BSE SEM picture of AlCoCrFeNi sintered alloy.

It should be noted that an EDX point radius is larger than the characteristic width of a lamella. At this point, we can observe the trend, but each point measures a small portion of the other phase as well.

Phase	Al	Co	Cr	Fe	Ni
FCC	8 ± 1	25 ± 4	26 ± 2	26 ± 2	16 ± 2
BCC	27 ± 1	17 ± 1	16 ± 3	15 ± 2	24 ± 3

Table 1: Average composition (at. %) of main phases measured by SEM EDX.

3.2. Atom Probe Tomography investigation

In order to more accurately address this question and shed some light on the microstructure at the atomic scale, Atom Probe Tomography was carried out.

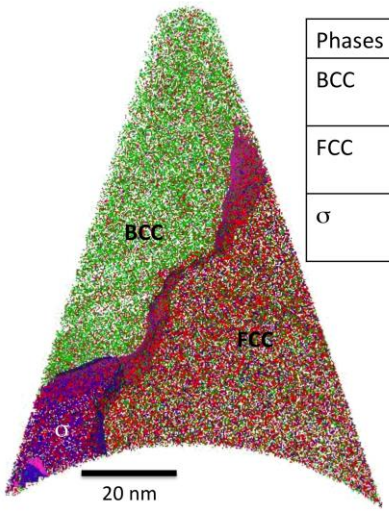

Phases	Al	Co	Cr	Fe	Ni
BCC	37.0 ± 2	17.1 ± 1	3.4 ± 0.3	11.0 ± 0.4	31.4 ± 0.7
FCC	7.4 ± 0.5	23.6 ± 0.6	27.6 ± 1	28.7 ± 0.6	12.7 ± 1
σ	4.0 ± 0.4	11.2 ± 0.7	63 ± 2	18.9 ± 0.4	2.6 ± 0.6

Figure 3 : APT reconstruction of the sintered AlCoCrFeNi alloy. Measured compositions (at. %) of each phase with the standard deviations calculated from 3 volumes observed by means of APT. Three contrasts are observed in the chemical distribution.

Figure 3 shows the 3D reconstruction of one of the three analyzed volumes (70 nm * 68 nm * 91 nm). The total chemical composition of this volume is very close to equimolar. Two iso-concentration surfaces of 12 at. % Al and 40 at. % Cr reveal the interfaces between the three phases. Their compositions are summarized alongside the standard deviations in Fig. 3. The precise composition of the FCC phase is close to that measured using SEM EDX, whereas the precise composition of the BCC phase is very different. For example, the Aluminum content is measured at up to 37 at. % instead of 27.5 at. % as measured by means of SEM. The main reason for this discrepancy seems to be the Al-Ni rich BCC and the Cr rich sigma phases sharing the same BSE contrast, leading to an EDX composition averaged over the two phases.
In addition, the standard deviations calculated from the composition of each phase from the three analyzed volumes indicate that each phase is very homogeneous from one region to another. The volume ratio between (sigma+BCC)/FCC in this volume is close to 50-50 %, corresponding to what has been observed at the microscopic scale.

A proximity histogram calculated from the BCC/FCC interface of Fig. 3 is shown in Fig. 4a. There is almost no sign of segregation at the interfaces between the different phases, even though the starting agglomerates are not fully alloyed. Indeed, Figure 1 indicated that the milled powder was far from chemically homogeneous. We could reasonably have expected that this lack of homogeneity would impact the final sintered sample, but this is not the case. These phases are very homogenous and there is no strong fluctuation of Fe or Cr, contrary to what was observed by Manzoni *et al.* by means of APT for the same as-cast alloy composition [32].

The sigma/BCC and sigma/FCC interfaces are tortuous; hence it is not possible to calculate proper proxigrams. A simple profile concentration through the sigma/BCC interface of the volume presented is depicted in Fig. 4b. This concentration profile reveals one of the very few examples of elemental segregation; in this case, the Fe surplus is higher at the interface (up to 12 at. %). This segregation may be linked to the ongoing formation/dissolution of the sigma phase.

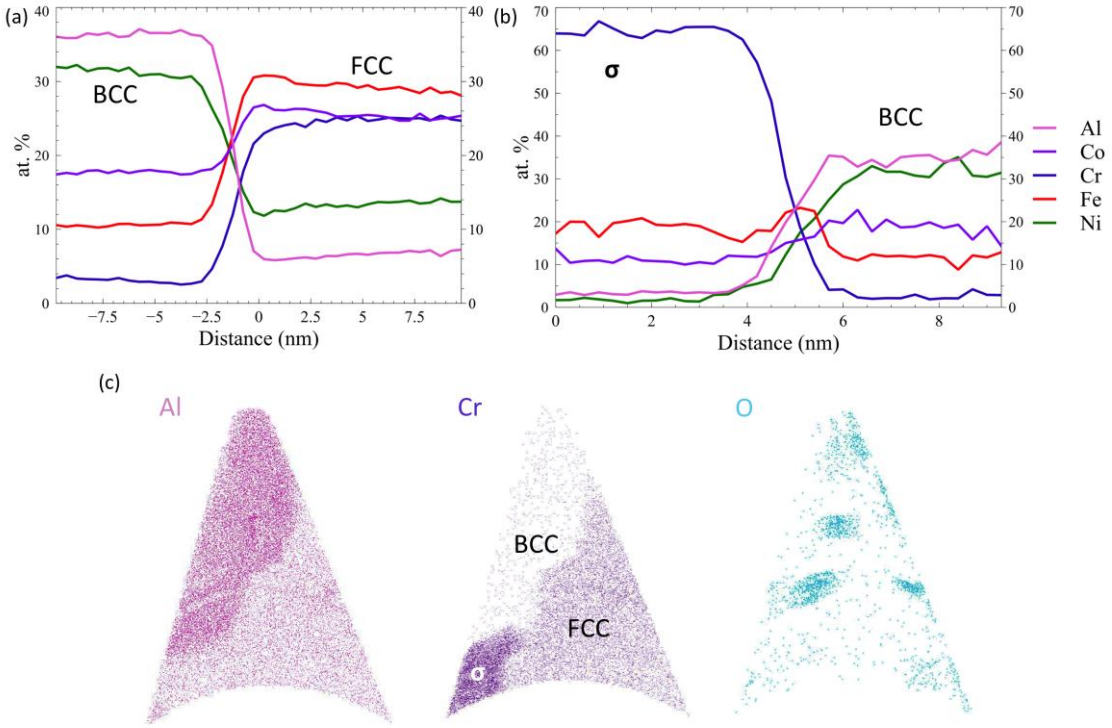

Figure 4: (a) Proximity histogram calculated from the BCC/FCC interface of the sintered AlCoCrFeNi alloy. (b) Concentration profile through one sigma/BCC interface in the sintered AlCoCrFeNi alloy. (c) Elemental mapping of the sintered AlCoCrFeNi alloy obtained by means of APT.

Figure 4c shows the elemental mapping of the volume, confirming the presence of a homogenous Al-Ni rich phase, a Fe-Cr-Co phase and a Cr rich phase. There are several oxygen rich clusters. Hence, the black precipitates seen in the SEM can be identified thanks to the APT. They turn out to be oxides. No traces of carbides were observed, in contrast to what Pohan *et al.* [33] reported in their analysis of $Al_{0.3}CoCrFeNiMn$ by means of APT. The content of C measured by APT was less than 0.01 at. % and carbon atoms seem to be in solid solution. Al_2O_3 and Cr_2O_3 are located at the interfaces of the three phases but not only. At this point, it is difficult to surmise their origin. All synthesis steps were carried out under controlled atmosphere, yet, according to the APT, the amount of oxygen is estimated at 0.5 at. %.

3.3.Oxygen contamination

Oxygen contamination may arise at three stages [34]:

- in the commercial powders themselves;
- during milling (especially since our milling takes 28h);
- during sintering due to the high reactivity of the mechanically activated agglomerate surfaces since the agglomerates have not reached the stable alloyed state.

In order to study the contamination by Oxygen during the process, precise O quantifications were carried out using the Inert Gas Fusion Technique at different stages (Table 2).

	Blended Powder	Milled Powder	Sintered sample
(wt. %)	0.6 ± 0.1	0.6 ± 0.4	0.5 ± 0.4

Table 2: Oxygen concentrations and standard deviations calculated from 4 measurements of the different samples measured by the Inert Gas Fusion Technique.

The oxygen content in the initial blended powder is already quite high as compared to industrial alloys. Here, the oxygen comes from thin passivated layers in the case of Al and Cr [35,36] and from less stable layers in the case of Co, Ni and Fe [37,38]. The standard deviation indicates that there may remain some regions richer in certain elements and particularly O-rich, despite the fact that the powders were blended for 2h. By comparison, the oxygen content in the milled powder does not increase, but the standard deviation is very high, nearly attaining the actual average value. It seems unlikely that the actual value would be lower than the initial concentration for blended powder. Hence, the real value should be close to 0.6 %. The standard deviation does thus not reflect a measurement error but rather an increased heterogeneity in oxygen distribution. The milling seems to induce a redistribution of oxygen atoms inside the agglomerates. It appears that the sintering stage does not alter this heterogeneity. At this point, these results suggest that most of the contamination originates in the initial powders and that the sintering step does not play a role in the oxygen contamination process.

In order to further investigate oxygen contamination, XPS analyses were carried out on powders originating from batches similar to the batches used for the oxygen quantification (Fig. 5). The XPS data analysis is challenging, due to the interference of the Auger transitions which overlap with 2p peaks of the main elements in the alloy [39]. Despite this issue, the spectra quantification shows that the AlCoCrFeNi milled powder surface exhibits mainly Al_2O_3. Figure 5 in fact displays the Al2p XPS window for a commercial Al powder and the AlCoCrFeNi milled powder. For this XPS measurement, the AlCoCrFeNi milled powder was handled in a protective atmosphere until the very moment of measurement. Consequently, the amount of powder measured is smaller than in the previous analysis and the spectrum exhibits more noise.

The commercial Al powder analyzed (bottom) corresponds to the one used in this work. The Al powder was stored for at least 30 days in air before analysis. We are confident that the storage of such powder is of minor importance for characterization purposes, since pure Al is highly reactive and rapidly forms a stable passivation layer (this layer is formed as soon as the powder is manufactured [40]). The finding shows that there is indeed a stable layer of oxide which does not exceed the 5 nm depth typical of XPS analysis. The spectrum of the AlCoCrFeNi milled powder, used for the sintered sample analyzed by APT, is displayed in Fig. 5, top. The spectrum reveals that the surface is mainly Al_2O_3 but that 14.7% of the aluminum is still metallic. This spectrum is very similar to that of pure Al and would indicate that a thin Al_2O_3 passivated layer is also formed in the case of milled AlCoCrFeNi. The oxygen content corresponding to the presence of this thin oxide layer is significantly lower than the global oxygen level measured by the inert gas fusion technique. We can therefore conclude that most of the oxygen is inside the agglomerates, far from the surface measured by XPS.

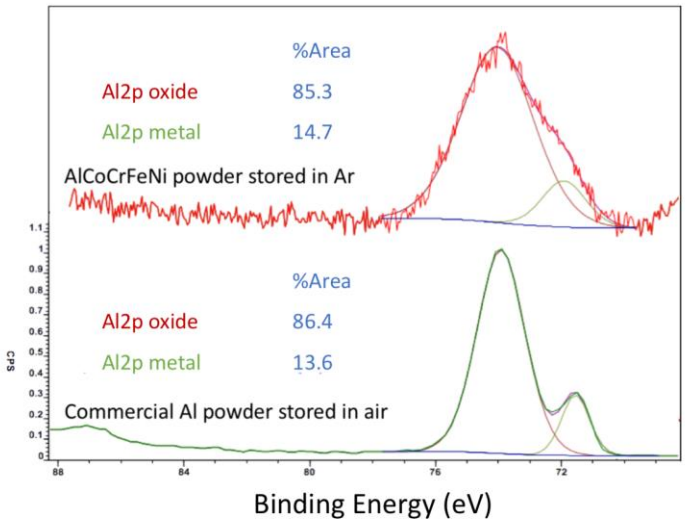

Figure 5 : XPS spectra of the Al2p window and corresponding quantification for the HEA powder stored in Ar (top) and commercial Al powder stored in air (bottom).

APT analyses show that only Al_2O_3 and Cr_2O_3 are present in the sintered HEA. Yet, initially, the powders which contain the most oxygen are those of iron, nickel and cobalt. In addition, the oxygen content measured in the sintered HEA cannot result solely from the passivating layers of chromium and aluminum at the surface. We may thus infer that the oxides of iron, cobalt and nickel have probably disappeared in favor of the formation of more Al_2O_3 and Cr_2O_3. According to the Ellingham diagram, aluminum and chromium are able to reduce the oxides of nickel, cobalt and iron in the whole range of temperatures studied. Moreover, the reduction is effective when the metals are in contact with the oxides, which is facilitated by the nanoscale distribution of the phases in the agglomerates and the cracking of the passivating layers (Al_2O_3) due to the creep of the underlying metal (Al).

The oxygen, carbon and nitrogen concentrations were measured together on a bulk sintered sample and the values are reported as follows: 0.8 at. % O, 0.4 at. % C and 0.1 at. % N. The

oxygen content is quite high for this kind of structural alloy (especially compared to classic superalloy ingot) but not excessively high for alloys elaborated by powder metallurgy [41].
Contrary to what has previously been reported in the literature concerning HEA Spark Plasma Sintered samples [41–43], carbon contamination is of lesser magnitude than the oxygen contamination (as indeed the APT results suggested). In addition to the lack of PCA in the present study, this finding could be attributed to the greater amount of oxides, itself resulting from the presence of highly reactive elements. Indeed, during sintering, chromium carbide formation may be expected; however, more stable chromium oxides have likely already formed. In addition, the nano-oxides may slow down carbon diffusion by blocking diffusion paths such as grain boundaries. Hence, the initial oxygen contamination could serve to inhibit a potential carbon contamination occurring during sintering. Finally, if we consider that the whole of the oxygen measured is in the form of oxides, we note that there is approximately 0.5 wt. % of oxides, far from enough to be observable by XRD (especially if the oxides are in two distinctive structures, Cr_2O_3 and Al_2O_3, as the APT result revealed).

The CALPHAD approach was used to gain insight into the kind of microstructure the alloy might have regarding its oxygen content. The phase volume fraction in $AlCoCrFeNiO_{0.008}$ was calculated with the TCNI9 database (Thermo-Calc) and is presented in Fig. 6a. The composition was chosen according to the oxygen analyzer results, namely 0.8 at. % of oxygen. At 1100 °C, the sintering temperature, the microstructure is expected to be 58 vol. % $Al_{28}Co_{20}Cr_8Fe_{17}Ni_{27}$ BCC-B2, 30 vol. % $Al_6Co_{19}Cr_{43}Fe_{25}Ni_8$ disordered BCC, 10 vol. % $Al_6Co_{23}Cr_{30}Fe_{26}Ni_{15}$ FCC and 2 vol. % Al_2O_3. According to our calculations, the sigma phase, which has the exact same composition as the disordered BCC, disappears at 1003°C to be replaced by this latter. Our calculations do not predict a chromium oxide phase except in extreme cases of Cr rich and Al poor composition.

Several discrepancies between thermodynamic simulations and our sample still exist, even when the oxygen content is taken into account. These discrepancies have been identified: the formation of the sigma phase even at 1100°C, the formation of a greater amount of FCC and the stoichiometry of each phase. These discrepancies between experimental results and thermodynamic calculations also point to new hypotheses which could shed some light on experimental observations.
First, according to the calculations, the sigma phase is not stable above 1003°C yet this phase was observed in the three volumes analyzed by APT. The sigma phase could form during the cooling; however, the cooling rate is high (around 400 °C.min^{-1}) in the sigma stability domain (544-1003°C). This hypothesis hence seems unlikely. In addition, according to Bracq *et al.* [44], this phase seems difficult to predict with the current databases.
Secondly, the experimental volume ratio of the FCC phase is around 50% as compared to 10% in the calculations. This discrepancy may be partially explained by the extensive presence of Al and Cr oxides. We have calculated the phase evolution according to oxygen content at 1100°C (Fig. 6b). It appears that increasing oxygen content indeed leads to the formation of a greater amount of FCC and this hypothesis seems adequate. Indeed, as shown in Fig. 6c, aluminum mainly leaves the Ni-Al rich B2 phase without modifying the B2 phase composition to form Al_2O_3 (see Fig. 6d). The significant heterogeneity of the milled powder revealed by

oxygen quantification could also cause the formation of a greater amount of FCC. It is interesting to note that the TCNI9 database predicts a greater amount FCC than the TCHEA3 database (see [28] for instance). The main difference between the two databases is that the TCHEA3 database was mainly developed for equimolar and near equimolar solid solutions.
Finally, the experimental composition of the B2 phase is richer in Al and Ni than the calculated one. Significant trends are observed: Ni-Al on the B2 side and Cr-Fe on the FCC side. The actual presence of the sigma phase at 1100°C, depleting the B2 phase of Cr, could accentuate the increase in Al content in the B2 phase.

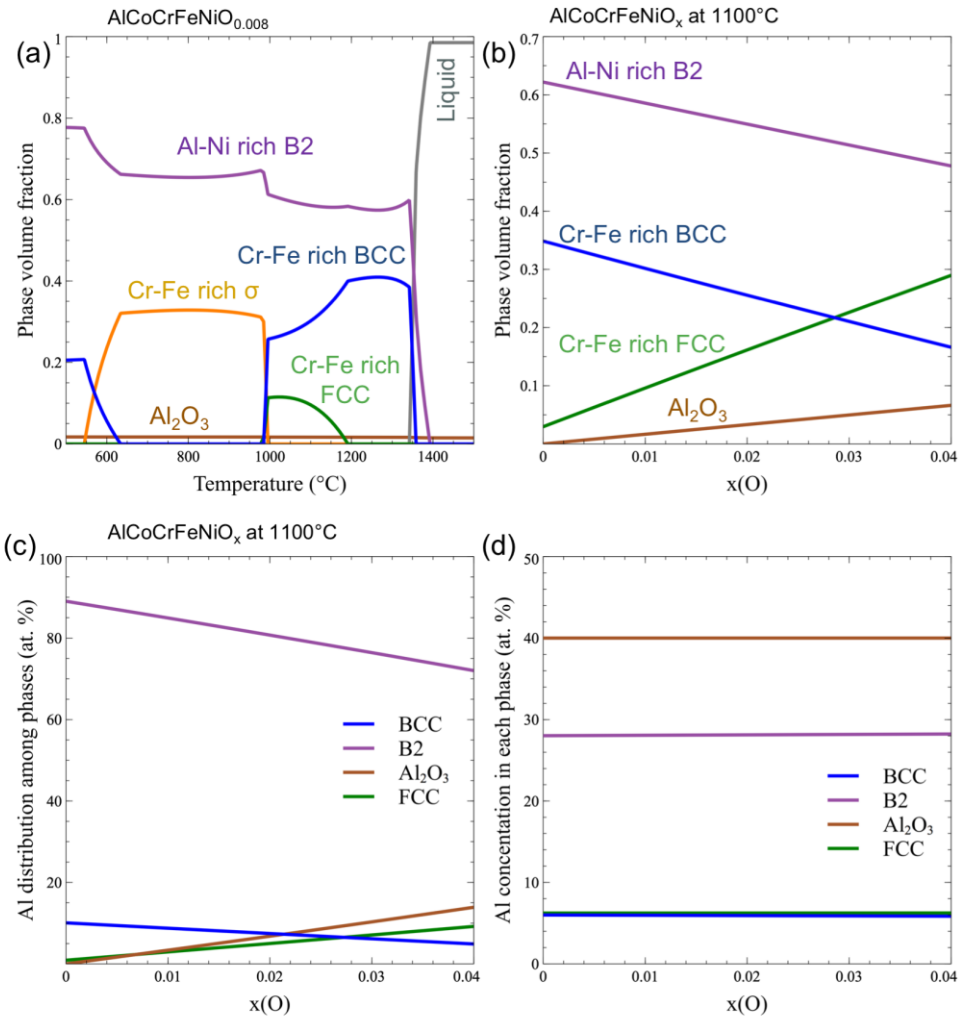

Figure 6: (a) Phase volume fraction as a function of temperature. (b) Phase volume fraction as a function of O content. (c) Al distribution among phases as a function of O content. (d) Al concentration in each phase as a function of O content. Thermo-Calc with TCNI9.

Concerning the influence of these oxides on the mechanical properties of this sample, Orowan strengthening is a well-known way to improve mechanical properties. Oxide Dispersed Strengthened Steels (ODS) are the combination of a ductile metallic matrix and hard oxide inclusions, often Yttria, and are a perfect example of this idea. In the field of HEAs produced by powder metallurgy, several works have reported studies of ODS HEAs elaborated by Powder Metallurgy [45–48]. For instance, Prasad *et al.* added alumina to a FeNiCoCrAlMn matrix and noted that this addition had no effect on the phase formation during sintering. They

also demonstrated that the hardness and thermal stability of the alloy were enhanced by these inclusions [49]. Gwalani *et al.* analyzed the microstructure of sintered $Al_{0.3}CoCrFeMnNi$ reinforced by Y_2O_3 by means of APT. The nanoscale characterization revealed that Y-Al-O complex oxides formed during the sintering [50,51]. Recently, several works have reported the advantages of producing alloys reinforced by the formation of native oxides, i.e., oxides formed from the oxygen present during the process or in the starting materials. In the field of additive manufacturing, Qiu showed that selective laser melting of a Fe-Ni alloy with a high oxygen level led to the formation of nano-oxide and to a combination of high strength and ductility [52]. A similar method was applied by Chen *et al.* to the CoCrFeNiMn high entropy alloy and was revealed to be promising [53]. In the powder metallurgy field, Moravcik *et al.* elaborated $Co_{1.5}CrFeNi_{1.5}Ti_{0.5}$ by means of Mechanical Alloying and SPS. The formation of nano-sized TiO particles was achieved without any supplementary oxygen addition. The nano-sized oxides and coherent Ni_3Ti precipitates in the FCC matrix led to a good combination of strength and ductility [54]. In most of these works, hard particles are used to strengthen a matrix known for its ductility. In the present work, Al and Cr oxides are found in a peculiar microstructure of closely interlinked BCC and FCC phases. It is reasonable to suggest that this ODS dual phase alloy is still somewhat ductile, but this hypothesis would require further confirmation. Conversely, the key features of mechanical activation on the synthesis of high entropy alloys and the origin of oxygen have here been closely analyzed. These findings could be valuable in the case of alloys with simpler microstructures such as $Al_{0.3}CoCrFeNi$, known to exhibit one single FCC phase.

4. Conclusion

In this work, we have evaluated the combination of mechanical activation and reactive sintering as an alternative to Mechanical Alloying and sintering for the AlCoCrFeNi High Entropy Alloy. Medium energy ball milling of the five elemental powders led to highly reactive agglomerates. After Spark Plasma Sintering, the distinctive lamellar structure primarily consists of two closely imbricated FCC and BCC phases with nano-oxides.

Atom Probe Tomography of the sample confirmed the satisfactory chemical homogeneity of these two main phases. There is no significant elemental segregation due to the peculiar state of the milled agglomerates. The sample elaborated by reactive sintering exhibits excellent chemical homogeneity, even at the nanoscale. However, APT and elemental analyzer also highlighted a high oxide content. In addition, the carbon content was found to be of lesser magnitude as compared to similar alloys milled with PCA. Dry milling seems to be an efficient way to reduce carbon contamination without promoting the formation of oxides. Indeed, combined oxygen quantification and XPS results demonstrated that most of the oxygen came from the commercial powders.

The CALPHAD calculations showed that, by depleting the main phases of Al and Cr, the presence of oxides could alter the phase composition and stability. As almost no work precisely reports the amount of unwanted, minor elements such as C, O or N, this could explain the large number of different microstructures reported in the HEA literature concerning AlCoCrFeNi.

References

[1] J.-W. Yeh, S.-K. Chen, S.-J. Lin, J.-Y. Gan, T.-S. Chin, T.-T. Shun, C.-H. Tsau, S.-Y. Chang, Nanostructured High-Entropy Alloys with Multiple Principal Elements: Novel Alloy Design Concepts and Outcomes, Adv. Eng. Mater. 6 (2004) 299–303. https://doi.org/10.1002/adem.200300567.

[2] B. Cantor, I.T.H. Chang, P. Knight, A.J.B. Vincent, Microstructural development in equiatomic multicomponent alloys, Mater. Sci. Eng. A. 375–377 (2004) 213–218. https://doi.org/10.1016/j.msea.2003.10.257.

[3] D.B. Miracle, O.N. Senkov, A critical review of high entropy alloys and related concepts, Acta Mater. 122 (2017) 448–511. https://doi.org/10.1016/j.actamat.2016.08.081.

[4] T.M. Butler, M.L. Weaver, Oxidation behavior of arc melted AlCoCrFeNi multi-component high-entropy alloys, J. Alloys Compd. 674 (2016) 229–244. https://doi.org/10.1016/j.jallcom.2016.02.257.

[5] M. Ren, B. Li, H. Fu, Formation condition of solid solution type high-entropy alloy, Trans. Nonferrous Met. Soc. China. 23 (2013) 991–995. https://doi.org/10.1016/S1003-6326(13)62557-1.

[6] W.-R. Wang, W.-L. Wang, S.-C. Wang, Y.-C. Tsai, C.-H. Lai, J.-W. Yeh, Effects of Al addition on the microstructure and mechanical property of AlxCoCrFeNi high-entropy alloys, Intermetallics. 26 (2012) 44–51. https://doi.org/10.1016/j.intermet.2012.03.005.

[7] M.M. Garlapati, M. Vaidya, A. Karati, S. Mishra, R. Bhattacharya, B.S. Murty, Influence of Al content on thermal stability of nanocrystalline AlxCoCrFeNi high entropy alloys at

low and intermediate temperatures, Adv. Powder Technol. 31 (2020) 1985–1993. https://doi.org/10.1016/j.apt.2020.02.032.

[8] W. Ji, Z. Fu, W. Wang, H. Wang, J. Zhang, Y. Wang, F. Zhang, Mechanical alloying synthesis and spark plasma sintering consolidation of CoCrFeNiAl high-entropy alloy, J. Alloys Compd. 589 (2014) 61–66. https://doi.org/10.1016/j.jallcom.2013.11.146.

[9] S. Mohanty, T.N. Maity, S. Mukhopadhyay, S. Sarkar, N.P. Gurao, S. Bhowmick, K. Biswas, Powder metallurgical processing of equiatomic AlCoCrFeNi high entropy alloy: Microstructure and mechanical properties, Mater. Sci. Eng. A. 679 (2017) 299–313. https://doi.org/10.1016/j.msea.2016.09.062.

[10] A.S. Rogachev, N.A. Kochetov, A.V. Panteleeva, K.V. Kuskov, D.Y. Kovalev, A.S. Shchukin, S.G. Vadchenko, Y.B. Scheck, High-Energy Ball Milling and Spark Plasma Sintering of the CoCrFeNiAl High-Entropy Alloy, Metals. 10 (2020) 1489. https://doi.org/10.3390/met10111489.

[11] V. Shivam, Alloying behaviour, thermal stability and phase evolution in quinary AlCoCrFeNi high entropy alloy, Adv. Powder Technol. (2018) 10.

[12] J. Cieslak, J. Tobola, K. Berent, M. Marciszko, Phase composition of Al x FeNiCrCo high entropy alloys prepared by sintering and arc-melting methods, J. Alloys Compd. 740 (2018) 264–272. https://doi.org/10.1016/j.jallcom.2017.12.333.

[13] S. Varalakshmi, M. Kamaraj, B.S. Murty, Processing and properties of nanocrystalline CuNiCoZnAlTi high entropy alloys by mechanical alloying, Mater. Sci. Eng. A. 527 (2010) 1027–1030. https://doi.org/10.1016/j.msea.2009.09.019.

[14] M. Murali, S.P. Kumaresh Babu, J. Majhi, A. Vallimanalan, R. Mahendran, Processing and characterisation of nano crystalline AlCoCrCuFeTi $_x$ high-entropy alloy, Powder Metall. 61 (2018) 139–148. https://doi.org/10.1080/00325899.2018.1438230.

[15] J.M. Torralba, P. Alvaredo, A. García-Junceda, High-entropy alloys fabricated via powder metallurgy. A critical review, Powder Metall. 62 (2019) 84–114. https://doi.org/10.1080/00325899.2019.1584454.

[16] J.M. Torralba, P. Alvaredo, A. García-Junceda, Powder metallurgy and high-entropy alloys: update on new opportunities, Powder Metall. 63 (2020) 227–236. https://doi.org/10.1080/00325899.2020.1807713.

[17] I. Moravcik, J. Cizek, P. Gavendova, S. Sheikh, S. Guo, I. Dlouhy, Effect of heat treatment on microstructure and mechanical properties of spark plasma sintered AlCoCrFeNiTi0.5 high entropy alloy, Mater. Lett. 174 (2016) 53–56. https://doi.org/10.1016/j.matlet.2016.03.077.

[18] A. Nouri, C. Wen, Surfactants in Mechanical Alloying/Milling: A Catch-22 Situation, Crit. Rev. Solid State Mater. Sci. 39 (2014) 81–108. https://doi.org/10.1080/10408436.2013.808985.

[19] S. Praveen, A. Anupam, R. Tilak, R.S. Kottada, Phase evolution and thermal stability of AlCoCrFe high entropy alloy with carbon as unsolicited addition from milling media, Mater. Chem. Phys. 210 (2018) 57–61. https://doi.org/10.1016/j.matchemphys.2017.10.040.

[20] S.G. Sarwat, Contamination in wet-ball milling, Powder Metall. 60 (2017) 267–272. https://doi.org/10.1080/00325899.2017.1280647.

[21] M. Vaidya, A. Prasad, A. Parakh, B.S. Murty, Influence of sequence of elemental addition on phase evolution in nanocrystalline AlCoCrFeNi: Novel approach to alloy synthesis using mechanical alloying, Mater. Des. 126 (2017) 37–46. https://doi.org/10.1016/j.matdes.2017.04.027.

[22] C. Suryanarayana, Mechanical alloying and milling, Prog. Mater. Sci. 46 (2001) 1–184. https://doi.org/10.1016/S0079-6425(99)00010-9.

[23] M. Vaidya, G.M. Muralikrishna, B.S. Murty, High-entropy alloys by mechanical alloying: A review, J. Mater. Res. 34 (2019) 664–686. https://doi.org/10.1557/jmr.2019.37.

[24] E. Gaffet, F. Bernard, J.-C. Niepce, F. Charlot, C. Gras, G. Le Caër, J.-L. Guichard, P. Delcroix, A. Mocellin, O. Tillement, Some recent developments in mechanical activation and mechanosynthesis, J. Mater. Chem. 9 (1999) 305–314. https://doi.org/10.1039/a804645j.

[25] E. Colombini, R. Rosa, L. Trombi, M. Zadra, A. Casagrande, P. Veronesi, High entropy alloys obtained by field assisted powder metallurgy route: SPS and microwave heating, Mater. Chem. Phys. 210 (2018) 78–86. https://doi.org/10.1016/j.matchemphys.2017.06.065.

[26] R. John, A. Karati, M.M. Garlapati, M. Vaidya, R. Bhattacharya, D. Fabijanic, B.S. Murty, Influence of mechanically activated annealing on phase evolution in Al0.3CoCrFeNi high-entropy alloy, J. Mater. Sci. 54 (2019) 14588–14598. https://doi.org/10.1007/s10853-019-03917-7.

[27] B. Kang, J. Lee, H.J. Ryu, S.H. Hong, Microstructure, mechanical property and Hall-Petch relationship of a light-weight refractory Al0.1CrNbVMo high entropy alloy fabricated by powder metallurgical process, J. Alloys Compd. 767 (2018) 1012–1021. https://doi.org/10.1016/j.jallcom.2018.07.145.

[28] A. Fourmont, S. Le Gallet, O. Politano, C. Desgranges, F. Baras, Effects of planetary ball milling on AlCoCrFeNi high entropy alloys prepared by Spark Plasma Sintering: Experiments and molecular dynamics study, J. Alloys Compd. (2019) 153448. https://doi.org/10.1016/j.jallcom.2019.153448.

[29] E. Kewes, F. Dahlem, S. Bec, N. Estime, K. Hoummada, J. Grollemund, J.-L. Loubet, Multi-scale chemical characterization of a ground metallurgical-grade silicon powder, Powder Technol. 270 (2015) 98–103. https://doi.org/10.1016/j.powtec.2014.08.025.

[30] M.-H. Tsai, K.-Y. Tsai, C.-W. Tsai, C. Lee, C.-C. Juan, J.-W. Yeh, Criterion for Sigma Phase Formation in Cr- and V-Containing High-Entropy Alloys, Mater. Res. Lett. 1 (2013) 207–212. https://doi.org/10.1080/21663831.2013.831382.

[31] S.-H. Joo, H. Kato, M.J. Jang, J. Moon, E.B. Kim, S.-J. Hong, H.S. Kim, Structure and properties of ultrafine-grained CoCrFeMnNi high-entropy alloys produced by mechanical alloying and spark plasma sintering, J. Alloys Compd. 698 (2017) 591–604. https://doi.org/10.1016/j.jallcom.2016.12.010.

[32] A. Manzoni, H. Daoud, R. Völkl, U. Glatzel, N. Wanderka, Phase separation in equiatomic AlCoCrFeNi high-entropy alloy, Ultramicroscopy. 132 (2013) 212–215. https://doi.org/10.1016/j.ultramic.2012.12.015.

[33] R.M. Pohan, Microstructures and mechanical properties of mechanically alloyed and spark plasma sintered Al0.3CoCrFeMnNi high entropy alloy, Mater. Chem. Phys. (2018) 9.

[34] L. He, E. Ma, Nanophase metallic alloys consolidated from powders prepared by mechanical alloying, Mater. Sci. Eng. A. 204 (1995) 240–245. https://doi.org/10.1016/0921-5093(95)09968-9.

[35] S. Hasani, M. Panjepour, M. Shamanian, The Oxidation Mechanism of Pure Aluminum Powder Particles, Oxid. Met. 78 (2012) 179–195. https://doi.org/10.1007/s11085-012-9299-1.

[36] J. Sun, M.L. Pantoya, S.L. Simon, Dependence of size and size distribution on reactivity of aluminum nanoparticles in reactions with oxygen and MoO3, Thermochim. Acta. 444 (2006) 117–127. https://doi.org/10.1016/j.tca.2006.03.001.

[37] M. Cohen, THE FORMATION AND PROPERTIES OF PASSIVE FILMS ON IRON, Can. J. Chem. 37 (1959) 286–291. https://doi.org/10.1139/v59-037.

[38] D.W. Rice, P.B.P. Phipps, R. Tremoureux, Atmospheric Corrosion of Cobalt, J. Electrochem. Soc. 126 (1979) 1459–1466. https://doi.org/10.1149/1.2129307.

[39] L. Wang, D. Mercier, S. Zanna, A. Seyeux, M. Laurent-Brocq, L. Perrière, I. Guillot, P. Marcus, Study of the surface oxides and corrosion behaviour of an equiatomic CoCrFeMnNi high entropy alloy by XPS and ToF-SIMS, Corros. Sci. 167 (2020) 108507. https://doi.org/10.1016/j.corsci.2020.108507.

[40] E. Hryha, R. Shvab, M. Bram, M. Bitzer, L. Nyborg, Surface chemical state of Ti powders and its alloys: Effect of storage conditions and alloy composition, Appl. Surf. Sci. 388 (2016) 294–303. https://doi.org/10.1016/j.apsusc.2016.01.046.

[41] I. Moravcik, A. Kubicek, L. Moravcikova-Gouvea, O. Adam, V. Kana, V. Pouchly, A. Zadera, I. Dlouhy, The Origins of High-Entropy Alloy Contamination Induced by Mechanical Alloying and Sintering, Metals. 10 (2020) 1186. https://doi.org/10.3390/met10091186.

[42] R.M. Pohan, B. Gwalani, J. Lee, T. Alam, J.Y. Hwang, H.J. Ryu, R. Banerjee, S.H. Hong, Microstructures and mechanical properties of mechanically alloyed and spark plasma sintered Al0.3CoCrFeMnNi high entropy alloy, Mater. Chem. Phys. 210 (2018) 62–70. https://doi.org/10.1016/j.matchemphys.2017.09.013.

[43] M. Li, Y. Guo, H. Wang, J. Shan, Y. Chang, Microstructures and mechanical properties of oxide dispersion strengthened CoCrFeNi high-entropy alloy produced by mechanical alloying and spark plasma sintering, Intermetallics. 123 (2020) 106819. https://doi.org/10.1016/j.intermet.2020.106819.

[44] G. Bracq, M. Laurent-Brocq, L. Perrière, R. Pirès, J.-M. Joubert, I. Guillot, The fcc solid solution stability in the Co-Cr-Fe-Mn-Ni multi-component system, Acta Mater. 128 (2017) 327–336. https://doi.org/10.1016/j.actamat.2017.02.017.

[45] H. Hadraba, Z. Chlup, A. Dlouhy, F. Dobes, P. Roupcova, M. Vilemova, J. Matejicek, Oxide dispersion strengthened CoCrFeNiMn high-entropy alloy, Mater. Sci. Eng. A. 689 (2017) 252–256. https://doi.org/10.1016/j.msea.2017.02.068.

[46] C.-L. Chen, Suprianto, Effects of nano-dispersoids on synthesis and characterization of low Cr-containing CoNiFeMnCr high entropy alloy by mechanical alloying, Intermetallics. 113 (2019) 106570. https://doi.org/10.1016/j.intermet.2019.106570.

[47] S. Yang, Y. Zhang, X. Yan, H. Zhou, J. Pi, D. Zhu, Deformation twins and interface characteristics of nano-Al2O3 reinforced Al0.4FeCrCo1.5NiTi0.3 high entropy alloy

composites, Mater. Chem. Phys. 210 (2018) 240–244. https://doi.org/10.1016/j.matchemphys.2017.11.037.

[48] Y. Song, S. Nam, Y. Kwon, K. Cho, K.-A. Lee, H. Choi, Effect of multiple oxides on the mechanical properties of CoCrFeMnNi high-entropy alloy matrix composites, Powder Metall. 0 (2021) 1–7. https://doi.org/10.1080/00325899.2021.1892988.

[49] H. Prasad, S. Singh, B.B. Panigrahi, Mechanical activated synthesis of alumina dispersed FeNiCoCrAlMn high entropy alloy, J. Alloys Compd. 692 (2017) 720–726. https://doi.org/10.1016/j.jallcom.2016.09.080.

[50] B. Gwalani, R.M. Pohan, J. Lee, B. Lee, R. Banerjee, H.J. Ryu, S.H. Hong, High-entropy alloy strengthened by in situ formation of entropy-stabilized nano-dispersoids, Sci. Rep. 8 (2018) 14085. https://doi.org/10.1038/s41598-018-32552-6.

[51] B. Gwalani, R.M. Pohan, O.A. Waseem, T. Alam, S.H. Hong, H.J. Ryu, R. Banerjee, Strengthening of Al0.3CoCrFeMnNi-based ODS high entropy alloys with incremental changes in the concentration of Y2O3, Scr. Mater. 162 (2019) 477–481. https://doi.org/10.1016/j.scriptamat.2018.12.021.

[52] C. Qiu, A new approach to synthesise high strength nano-oxide dispersion strengthened alloys, J. Alloys Compd. 790 (2019) 1023–1033. https://doi.org/10.1016/j.jallcom.2019.03.221.

[53] P. Chen, C. Yang, S. Li, M.M. Attallah, M. Yan, In-situ alloyed, oxide-dispersion-strengthened CoCrFeMnNi high entropy alloy fabricated via laser powder bed fusion, Mater. Des. 194 (2020) 108966. https://doi.org/10.1016/j.matdes.2020.108966.

[54] I. Moravcik, L. Gouvea, V. Hornik, Z. Kovacova, M. Kitzmantel, E. Neubauer, I. Dlouhy, Synergic strengthening by oxide and coherent precipitate dispersions in high-entropy alloy prepared by powder metallurgy, Scr. Mater. 157 (2018) 24–29. https://doi.org/10.1016/j.scriptamat.2018.07.034.

Chapter VI: Thermal stability of Medium and High Entropy Alloys of 3d-transition metals

1. Introduction

Since their discovery by Yeh and Cantor [1,2], HEAs have become a major research topic in material science. HEAs are characterized by outstanding properties including corrosion resistance, limited diffusion, increased plasticity at low temperatures, and other special mechanical and magnetic properties that depend on structure and composition. Nonetheless, their usage for technological purposes remains limited [3]. Prior to their future exploitation, a fundamental study of their stability is a required step. The stability of materials is of primary importance per se; indeed, reliable stability opens up new perspectives for applications including coatings, interconnects (fuel cell) [4], and heat engine components [5].

Typically, HEAs are characterized by a single-phase disordered solid solution. We may wonder if the absence of short- and long-range chemical order is maintained whatever the conditions. Is limited diffusion in a distorted crystal lattice the guarantee of this stability? What happens in the presence of defects or nanostructures that are inevitably formed during the elaboration process? One way to study the stability of a material is to submit it to annealing at high temperatures and look for possible structural transformations.

Thermal stability in cast and mechanically synthesized HEAs is debatable because experimental data are incomplete. Among the main high-entropy families, the family composed of 3d-transition metals is the most thoroughly studied. The CoCrFeNi single-phase alloy with an FCC crystal structure was characterized as stable at 1173 K for 600 h [6], but the phase decomposition occurred at 1073 K for 800 h [7]. As-cast $Al_xCoCrFeNi$ alloys commonly consist of FCC dendrites and a BCC interdendritic phase, depending on the Al content: only the FCC phase was obtained for x = 0-0.3, an FCC+BCC mixture for x = 0.5-0.8, and BCC alone for x = 0.9-3.0 [8,9]. At temperatures above 873 K, the as-cast equiatomic AlCoCrFeNi BCC phase transforms into FCC, with simultaneous precipitation of B2 and σ phase inclusions [10]. A mechanically synthesized AlCoCrFeNi BCC phase transformed into a partially disordered B2 phase after 1 h annealing at 1073 K [11,12]. Experimental data concerning phase transformations in MnCoCrFeNi, CuCoCrFeNi and other HEAs have been reported in several reviews [13-15]. For instance, it has been shown that two similar FCC structures co-existed in an annealed milled MnCoCrFeNi [16]; short-term annealing led to the release of Cr and Mn from the matrix, which shrunk and formed a second metastable FCC solid solution.
Equimolar TiCoCrFeNi is less often studied than the other compositions of the considered family. One would expect a very complex microstructure with several intermetallic phases due

to Ti. However, TiCoCrFeNi after laser cladding was reported to exhibit one main FCC phase and two secondary Simple Cubic (SC) and Laves phases [17]. In addition, the confrontation of experimental results with powerful modeling tools such as the Calphad method has proven useful. In their work, Zhang and Gao demonstrated that configurational entropy alone does not grant the stability of high-entropy alloys; thus, quantities such as phase enthalpy (whose calculation is made possible by Calphad) are of great interest in evaluating the stability of alloys in regard to chemical and temperature variations [18,19]. The chemical stability of the FCC solid solution in the MnCoCrFeNi system was thoroughly assessed and demonstrated to be very well described by a database such as TCHEA1, although an accurate secondary phase prediction was perfectible [20]. Thanks to this combined experimental and thermodynamic approach, conclusive results have been obtained by Rao et *al*. [21]. They were able to efficiently identify nano-scale precipitates predicted by thermodynamic calculations and to confirm the role of Al in the phase formation in $Al_xCoCrFeNi$ alloys.

In this work, we considered the family of HEAs composed of 3d-transition metals: CoFeNiXZ where X=Cr and Z=Al,Ti. This family has been extensively studied since the discovery of the Cantor MnCoCrFeNi HEA. Starting from the system CoFeNi that forms the core of the alloy family, we considered the quaternary CoCrFeNi and finally quinary systems. We focused on HEAs produced by mechanical alloying. This production method has rapidly developed over the last decade [22,23]. Here, the alloying is carried out by means of high-energy planetary ball milling (HEBM) of powder mixtures composed of elemental metallic powders. The alloyed powders were characterized with High Temperature X-ray Diffraction (HT-XRD) and room temperature XRD after annealing in order to estimate their stability.

We also carried out the thermodynamic description of ternary, quaternary and quinary systems using the Calphad approach. In this way, we were able to interpret the experimental results as compared to expected equilibrium phases and to evaluate the specificities of the alloying process followed by annealing.

2. Materials and methods

Elemental powders of Al, Ti, Cu, Co, Cr, Fe and Ni of purity greater than 98 wt% and of various particle sizes (all < 160 µm) were mixed in equimolar proportions and mechanically alloyed in high-energy planetary ball mills. Table 1 summarizes the structure and the lattice parameter of the metallic element used in this work. A water-cooling mill "Activator-2S" (Novosibirsk, Russia) with stainless-steel cylindrical jars and balls (7 mm in diameter) was used for most of the systems studied in this work. In these cases, the jars were evacuated and then filled with Ar gas at 4 bar. The HEBM was run at a rotating speed of the sun wheel and the grinding drums at 694 and 1388 rpm, respectively. TiCoCrFeNi was obtained using the "AGO-2" (Novosibirsk, Russia) water-cooling planetary mill with steel balls (9 mm in diameter) in air atmosphere, at a rotating speed of 912 rpm (for the mill) that corresponded to 2220 rpm for the jars. The second milling device was used in order to prove that presence of oxygen in a milling jar does not prevent formation of single-phase multicomponent alloys. The ball/powder weight ratio was 20:1 in all experiments. The milling time was systematically 90 minutes, or 120 minutes for the CuCoCrFeNi system.

The X-ray diffraction analysis of powders was performed with a DRON-3M diffractometer (Russia). Both Cu-K_α radiation (wavelength $\lambda = 0.15419$ nm) and Fe-K_α radiation ($\lambda = 0.19374$ nm) were used in order to obtain complementary data. Indeed, the Fe-K_α ensures a better angle resolution. High-temperature XRD measurements were made in a vacuum at 10^{-3} Pa, within the temperature range 298-1273 K using an ARL'XTRA diffractometer with the high- temperature accessory HTK2000 "Anton Paar" (Switzerland). The selected annealing temperatures were 873 K, 1073 K and 1273 K. For the accurate measurement of lattice parameters at room temperature (before and after annealing), crystalline silicon powder (NIST SRM 640b) admixed to the analyzing powder samples was used as inner marker (standard). The lattice parameters were determined with accuracy better than 0.002%. The SEM and EDS analyses were carried out using a Zeiss Ultra Plus field-emission scanning electron microscope (Carl Zeiss, Germany), equipped with an INCA Energy 350 XT energy dispersive spectrometer (Oxford Instruments, UK).

Element	Structure	Lattice parameter (Å)
Al	FCC	4.05
Co	HCP	2.51 / 4.07
Cr	BCC	2.88
Cu	FCC	3.61
Fe	BCC	2.87
Ni	FCC	3.52
Ti	HCP	2.95 / 4.68

Table 1: Structure and lattice parameter of the metallic element used in this work.

Thermodynamic calculations were performed using Thermo-Calc® software based on the Calphad methodology with the TCHEA3 database. Phase fractions and phase composition as a function of temperature were calculated for the different systems. The lattice parameter of the cubic solid solution was estimated in the cases of ternary and quaternary systems.

3. Results

3.1.CoFeNi and CoCrFeNi

Three metals of the iron group, Co, Fe, and Ni constitute a ternary core of the 3d-transition metal family of HEAs. These metals have similar atomic radii, but different crystal structures.

Figures 1 and 2 display the dependence of the equilibrium phase composition (expressed in volume ratio) on temperature in the case of the ternary CoFeNi and quaternary CoCrFeNi. In order to get a quick estimation of the composition of each phase, we also provide the distribution of elements in the different phases. The calculation was here performed in the case of equimolar systems. For the ternary CoFeNi, the main characteristics are as follows:

- Below 925 K, the system is composed of one ordered BCC phase and one disordered FCC phase. Nickel is the principal element in the FCC phase. The BCC ordered phase contains mainly Co and Fe elements.
- Above 925 K, a single FCC disordered phase is observed.
- The melting temperature is 1734 K.

In conclusion, the ternary CoFeNi may be considered as an HEA with only 3 elements.

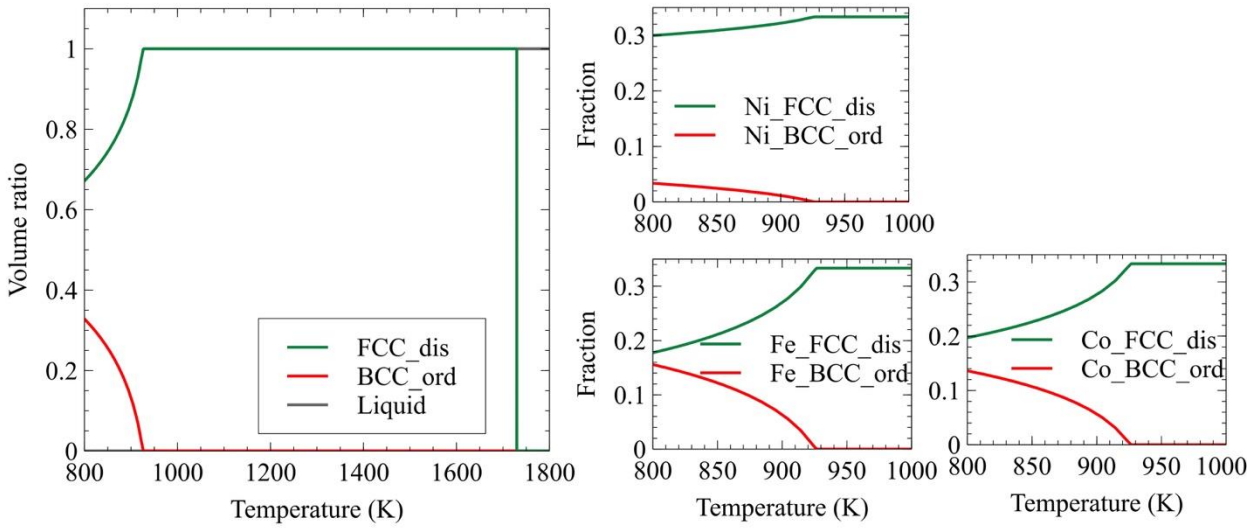

Figure 1: Phase fractions (volume fraction) in the CoFeNi system and element distributions in the different phases.

This typical behavior can be examined in light of the behavior of pure elements and binary phase diagrams. Nickel possesses an FCC structure from room temperature to its melting point.

Although Co(Fe) has an HCP(BCC) structure at room temperature, Co(Fe) undergoes a phase transformation to FCC above 695 K (1184 K). The binary phase diagrams show that a single FCC solid solution Co+Ni or Fe+Ni can be obtained in a wide range of temperatures for any ratio between the elements. On the other hand, Co and Fe form a BCC solid solution below 1173 K if the mole fraction in Fe is greater than 0.2 or an FCC solid solution at a lower content in Fe. It is therefore not surprising that a single disordered FCC solid solution is observed at high temperatures.

Adding the element Cr to obtain the quaternary system CoCrFeNi leads to the following observations:

- Above 928 K, the system is composed of a single FCC disordered phase corresponding to the HEA.
- At lower temperatures [800 K- 928 K], three phases coexist: a BCC-ordered phase with Co and Fe, a σ phase with a majority of Cr and the disordered FCC solid solution.
- The melting temperature is 1720 K.

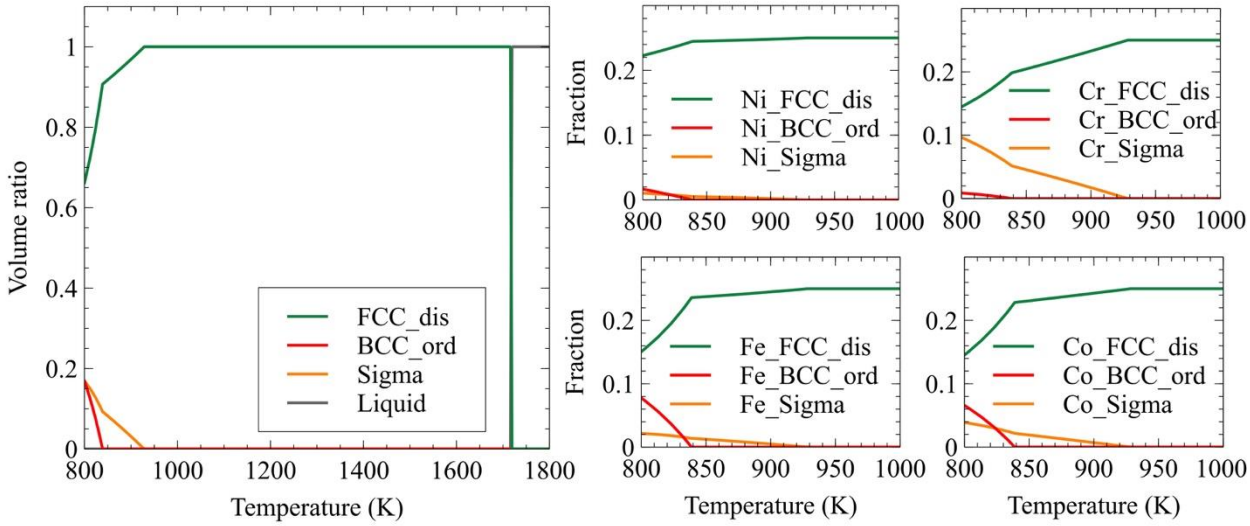

Figure 2: Phase fractions (volume percent) as a function of temperature in the equimolar CoCrFeNi system and element distributions in the different phases.

Ternary and quaternary systems are characterized by the same melting temperatures. In equilibrium conditions, a single FCC solid solution is formed in a temperature range close to the melting temperature. For lower temperatures, the equilibrium corresponds to a mixture of different phases.

Fig. 3 displays the XRD patterns of CoFeNi and CoCrFeNi after 90 min of high-energy ball milling (HEBM). At the end of the process, Co, Fe and Cr peaks have disappeared. There remain only two peaks corresponding to an FCC structure. The broadening of these two peaks is easily noticeable; this broadening signifies that the powder most likely contains a high concentration of lattice defects and nanosized crystallites. Indeed, a crystalline size (coherent-scattering regions) was roughly estimated as 15 nm for CoFeNi and 21 nm for CoCrFeNi after HEBM. In addition, there is a strong shift on the FCC peaks; for instance, for CoFeNi, the (200)

FCC peak jumps from 66.7° 2θ (corresponding to the pure Ni lattice parameter a_0=3.520Å) to 65.6° 2θ. The lattice parameters of the FCC phase after 90 min of HEBM are estimated to be 3.57Å for CoFeNi and 3.58Å for CoCrFeNi. Hence, there is a strong lattice parameter increase associated with the formation of an FCC solid solution. The calculated lattice parameters are summarized in Table 2.

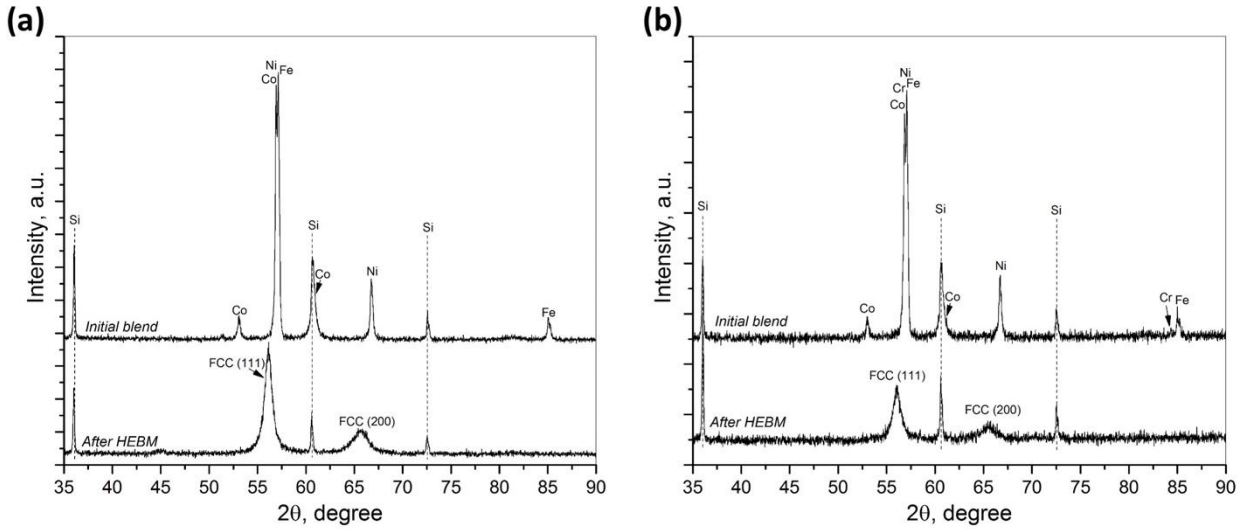

Figure 3: XRD patterns of the initial powder blend Co+Fe+Ni and mechanically alloyed CoFeNi (a) and Co+Cr+Fe+Ni and mechanically alloyed CoCrFeNi (b) after 90 min of high energy ball milling (Fe-K_a radiation). A powder of Si was added to the XRD samples in order to obtain reference peaks.

System (alloy)	Initial, at room temperature	Lattice parameter after annealing and cooling down to room temperature		
		873K	1073K	1273K
CoFeNi	3.571(2)	3.5711(2)	3.5621(3)	3.5620(3)
CoCrFeNi	3.575(4)	3.5706(2)	3.5748(1)	3.5752(3)

Table 2: Calculated lattice parameter (Å) of the CoFeNi and CoCrFeNi milled powders before and after annealing at different temperatures. The number in parentheses is the estimated standard deviation. For instance, 3.571(2) means 3.571 ± 0.002.

SEM images of milled powder cross sections are shown in Fig. 4. The lack of contrast demonstrates that only one chemically uniform phase remains after milling. EDS microanalysis reveals that the global composition is still equimolar in CoFeNi and CoCrFeNi. There is no preferential adherence to the milling apparatus by any one element in particular. From XRD measurements and SEM analyses, we can conclude that the mixtures of the individual powders Co+Fe+Ni and Co+Cr+Fe+Ni have completely transformed into the single-phase alloys CoFeNi and CoCrFeNi.

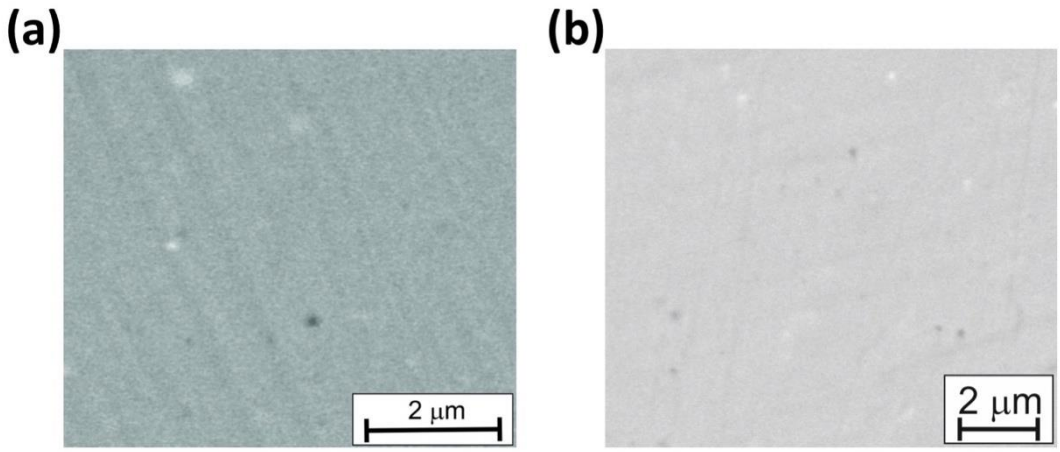

Figure 4: SEM images of the CoFeNi (a) and CoCrFeNi (b) alloys after 90 min of HEBM. Image in backscattered electrons.

The CoFeNi and CoCrFeNi milled powders were annealed at 873 K, 1073 K and 1273 K over 5.1 h. The XRD patterns at room temperature after annealing are presented in Fig. 5.

Two minor peaks at 41.5° 2θ and 50.25° 2θ probably correspond to iron-chromium oxide $(Fe,Cr)_2O_3$ (card PDF 000-34-0412). Although the samples were heated in a vacuum during the high-temperature XRD analysis, some residual oxygen results in surface oxidation of the powder particles. There is no sign of any other phase formation during annealing, although we could have expected the formation of a σ phase in the case of the CoCrFeNi alloy. The direct comparison of thermodynamic calculation to experimental results thus leads to the conclusion that the HEBM process selects the HT phase: the FCC disordered solid solution. However, there is a slight decrease in lattice parameter with temperature in the case of CoFeNi whereas there is a slight increase in the case of CoCrFeNi (see Table 2). Note that this does not correspond to thermal expansion since these XRD measurements are performed at room temperature. Rogachev et al. suggested that the decrease could be due to the relaxation of the crystal structure [16]. The increase in lattice parameter after annealing of the milled powder seems to be related to Cr. It may suggest that some Cr-rich regions remained after milling, and that annealing led to a second chemical homogenization associated with a lattice parameter increase. Indeed, Cr has the highest melting temperature among the 4 considered elements and is known to be the last element to dissolve during milling. It could also be due to the formation of the Fe,Cr oxides during annealing which would lower the actual concentrations of these elements in the alloy. A third hypothesis is linked to the fact that the (111) FCC peak shifts to the left whereas the (200) peak seems to remain stationary. This could be the sign of a weak, thermally induced martensitic transformation; indeed Rogachev *et al.* suggested that this kind of transformation could occur in the AlCoCrFeNi alloy under similar constraints [24].

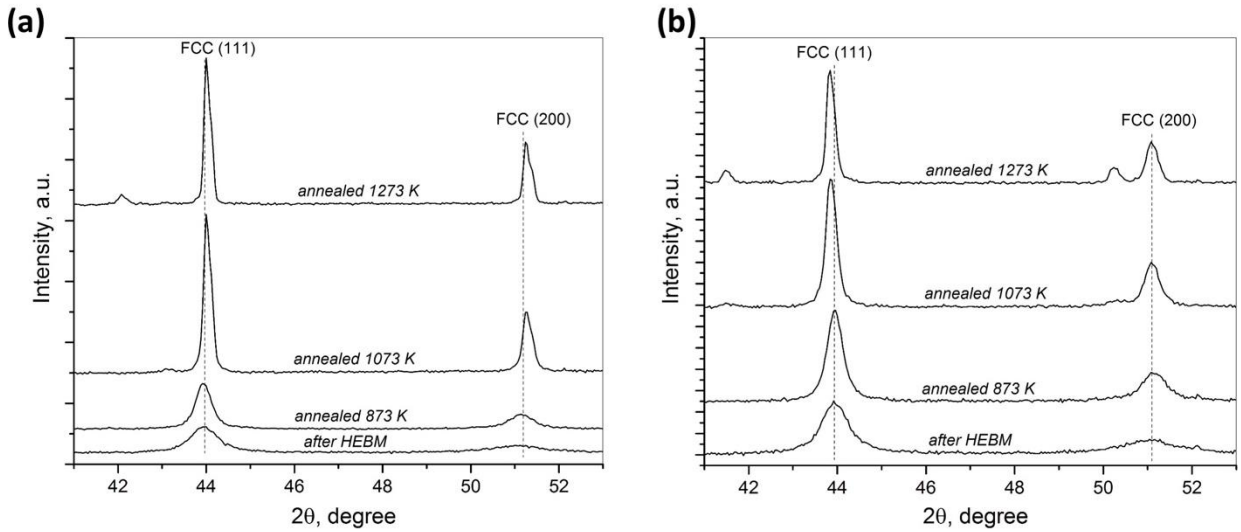

Figure 5: Room temperature XRD patterns of the CoFeNi (a) and CoCrFeNi (b) alloys after HEBM and after annealing at different temperatures over 5.1 h (Cu-K_α radiation).

In addition, the width of the peaks narrows. This narrowing means that lattice defects are relaxing and that grain size is increasing. After annealing at 1273 K, the sizes of coherent-scattering regions increase to 1340 nm and 680 nm for CoFeNi and CoCrFeNi, respectively.

The lattice parameter was estimated by XRD at annealing temperatures during the heat treatment for the ternary and quaternary (see Fig. 6). These experimental results have been compared to those obtained via two different theoretical approaches. The first estimation was directly calculated using Thermo-Calc. The second estimation relies on the well-known Vegard's law. Vegard's law is the empirical rule that the lattice parameter of a solid solution of two constituents is approximately equal to a rule of mixtures of the two constituent lattice parameters at the same temperature. If generalized to a ternary equimolar system:

$$a_0(\text{CoFeNi}) = \frac{1}{3}\left(a_0(\text{Co}) + a_0(\text{Fe}) + a_0(\text{Ni})\right) \quad (1)$$

provided that all elements have the same crystallographic structure. Here, we used Thermo-Calc to obtain a_0(FCC-Ni,T), a_0(FCC-Co,T), and a_0(FCC-Fe,T) for pure elements. In the case of the ternary, we noted that the Vegard's value best reflects the experimental observations, while the thermodynamic approach overestimates the lattice parameter at high temperatures. In the case of the quaternary, both estimations give greater values than the observed lattice parameter. Overall, both calculation methods give results that are relatively close to experimental measurements; they have proven to be useful tools in evaluating lattice parameters at elevated temperatures.

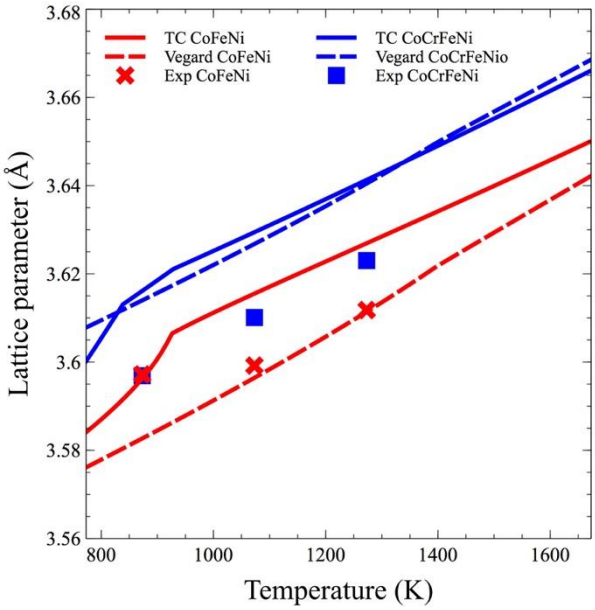

Figure 6: Lattice parameters for ternary and quaternary HEAs as a function of temperature. Only the FCC lattice has been selected. Experimental data were obtained by means of HT-XRD.

3.2.Quinary systems

The volume ratios for X-CoCrFeNi HEAs were calculated using Thermo-Calc with the database TCHEA3 over a range of temperatures [773 K-1773 K]. Despite the fact that Mn-CoCrFeNi is not considered in the present study, the phase fraction of the Cantor HEA is depicted in Fig. 7 for the sake of comparison. At low temperatures, there is coexistence between a σ phase and a disordered FCC solid solution. At 773 K, the Mn element is equally distributed in the σ phase and FCC_dis. As the temperature increases, the volume fraction of the σ phase decreases until complete disappearance at 1100 K as compared to 900 K in the quaternary

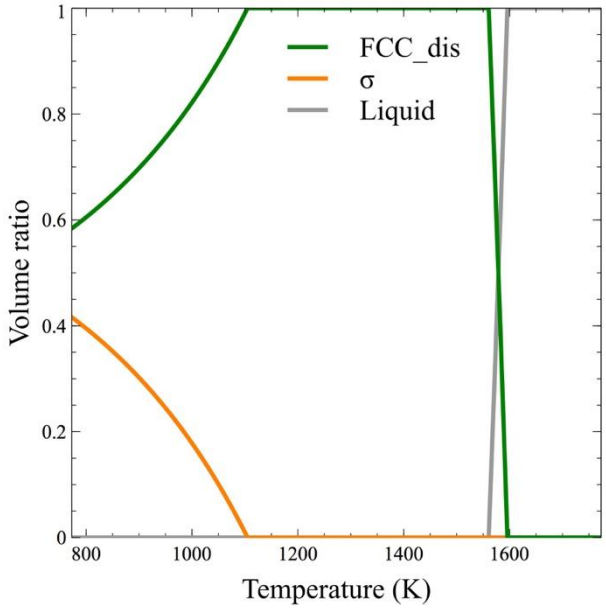

Figure 7: Volume ratios of the different phases in Mn-CoCrFeNi HEA calculated by Thermo-Calc.

CoCrFeNi. The melting temperature, 1573 K, is lower than the melting temperature of CoCrFeNi.

As shown in Fig. 8a, Al-CoCrFeNi is characterized by the presence of a BCC_ord phase over the whole temperature range [773 K-1773 K]. At 1073 K, the composition of the two coexisting phases reads:

- BCC_ord: $Al_{28}Co_{22}Fe_{17}Ni_{27}$ and
- σ: $Co_{15}Cr_{55}Fe_{26}$.

Above 1273 K, the σ phase disappears in favor of a BCC_dis phase. The chromium element is redistributed between the two BCC phases. At 1273 K, we have

- BCC_ord: $Al_{25}Co_{21}Cr_{11}Fe_{18}Ni_{25}$
- BCC_dis: $Co_{17}Cr_{45}Fe_{26}$.

Note that the composition of the BCC_dis is similar to that of the σ phase. In the equimolar case, only a very small fraction of FCC_dis is formed (0.1 % in volume). A slight variation in the composition in Al leads to a very different result with the formation of an FCC_dis phase.

High Temperature XRD (HT-XRD) results on milled Al-CoCrFeNi powder are presented in Fig. 8b. Heating was carried out in a step-like manner with isothermal stages at 873, 1073, and 1273 K. Starting from the bottom, the first pattern corresponds to room temperature XRD prior to annealing. The next three patterns correspond to XRD measurement at 873 K after 0h, 1h and 2h. The next 6 patterns follow the same logic; the final XRD pattern corresponds to room temperature measurement after annealing.

After HEBM and prior to annealing, the Al-CoCrFeNi powder alloy seems to exhibit a single BCC phase, similarly to what was reported by Ji et al. with a far less powerful milling [25]. However, a mixture of FCC+BCC has also been reported in several studies on the elaboration process of Al-CoCrFeNi by powder metallurgy [26,27]. In addition to the influence of the mechanical alloying on the phase constitution of the alloys, initial elemental particle sizes could play a major role in determining the final crystalline structure after HEBM. It is worth noting that the only peak remaining after HEBM is very broad. This peak may actually correspond to two peaks: the (111) FCC and (110) BCC, both situated around 44.5° 2θ; however, the (200) FCC peak is completely absent from the XRD pattern.

The HT-XRD patterns show that the single BCC phase is stable up to 1273 K. From this temperature, an FCC and an intermetallic σ phase begin to form. Then, close analysis of the 2h annealing pattern at 1273 K may suggest that there is a partial dissolution of σ in the FCC phase. After cooling, three phases remain: FCC, BCC and σ. The agreement between experimental and calculation results is not excellent but leads to several remarks. Indeed, the calculated domain of stability of σ seems to be slightly overestimated since there is no sign of σ at 873 K and since σ begins to disappear at 1273 K although its calculated domain was [817 K-1276 K]. Obviously, one could argue that 2h is not enough to reach thermodynamic equilibrium and that the σ phase prediction is known to be perfectible [20]. However, the formation of an FCC phase is barely expected according to the database and this constitutes a major discrepancy. The formation of an FCC phase could be partially explained by a composition modification due to oxide formation [28]. Indeed, oxide formation is a well-known drawback of the powder metallurgy route and could lead to an Al depletion in the main phase.

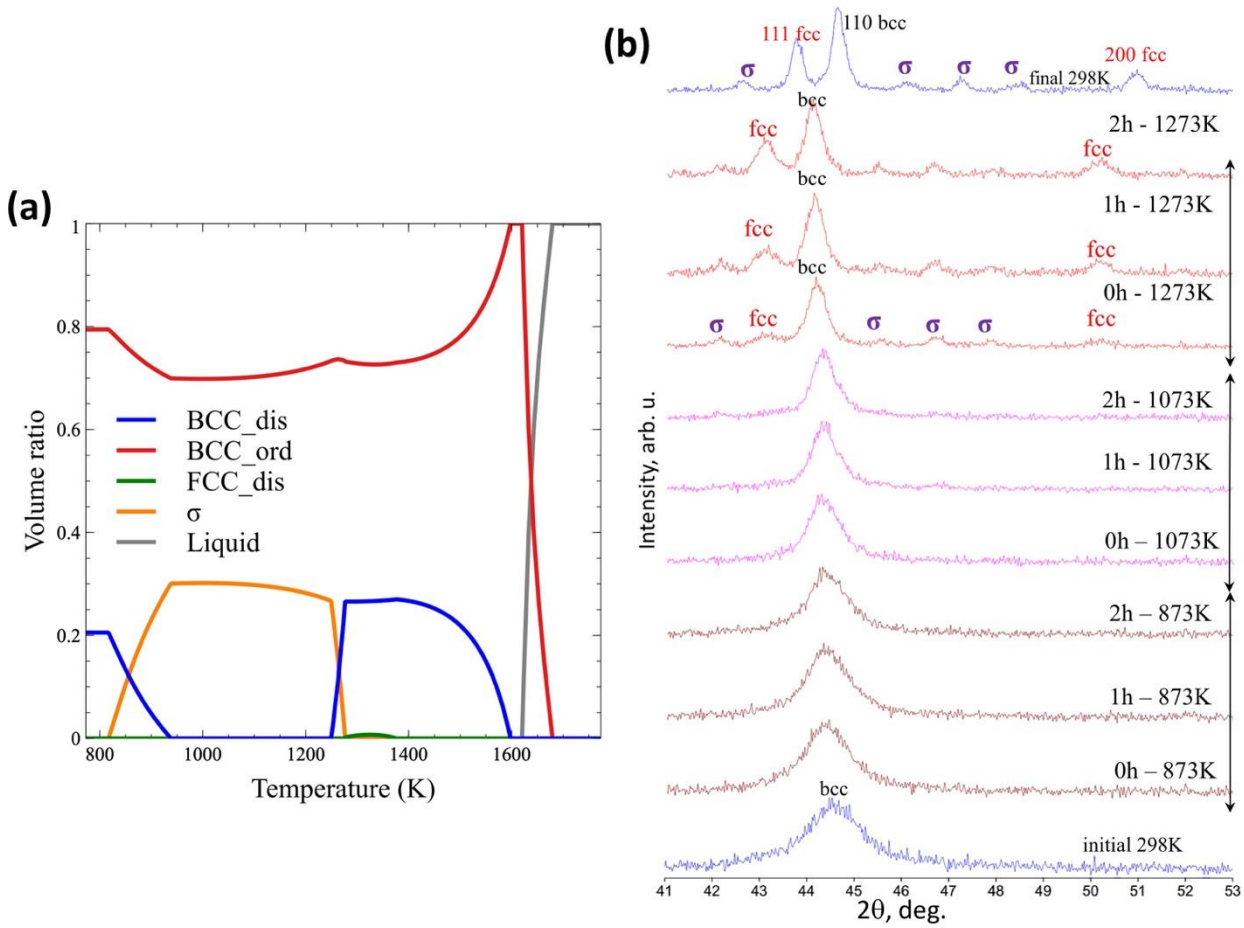

Figure 8: Volume ratios for the Al-CoCrFeNi alloy calculated using Thermo-Calc (a). High temperature XRD patterns after HEBM in Activator-2S (b).

As shown in Fig. 9a, the volume ratios for Cu-CoCrFeNi HEA were calculated using Thermo-Calc with the database TCHEA3 over a range of temperatures [773 K-1773 K]. This HEA is characterized by the coexistence of two disordered FCC solid solutions at high temperatures (T > 973 K):

- FCC_dis#1 with a majority of Cu (Cu_{89} Co_1 Fe_2 Ni_8)
- FCC_dis#2 without Cu (Cu_2 Co_{25} Cr_{25} Fe_{25} Ni_{23}).

The FCC_dis#1 phase melts prior to the appearance of the FCC_dis#2 phase. The amount of FCC_dis#1 is directly related to the fraction of Cu. The ordered BCC_ord phase and σ phase are observed at relatively low temperatures.

HT-XRD results on milled Cu-CoCrFeNi powder are presented in Fig. 9b. Measurements were carried out slightly differently than in the Al-CoCrFeNi case, the sample were heated at the selected annealing temperature over 5h and then cooled down for each temperature of interest. For the sake of comparison, the first pattern corresponds to XRD results after 1h of annealing and the second after 2h. Mechanical treatment of the five-component Cu+Co+Cr+Fe+Ni mixtures results in the formation of a single-phase FCC structure as shown in the bottom pattern.

The HT-XRD patterns reveal that a small amount of a BCC phase appears at 873 K but disappears at 1073 K and above. This BCC phase is predicted by Calphad but at a lower

temperature and could be the sign that its stability domain is shrunk by the consequences of the elaboration process (such as contamination or high concentration of lattice defects). Indeed, a high concentration of lattice defects tends to promote new phase formation. A second FCC phase, noted FCC-1, appears at 1073 K after 2h of annealing, remains at 1273 K after 1h but disappears for longer annealing times and is not visible after cooling. However, the two FCC phases could have very similar lattice parameters and appear as one XRD pattern. According to our thermodynamic calculations, a minor Cu-rich FCC is supposed to exist below 1393 K. The lattice parameter of the Cu-rich FCC phase is estimated at 3.70 Å at 1273 K by Thermo-Calc, whereas the lattice parameter of the main FCC phase is estimated at 3.64 Å. Hence, the hypothesis of two lattices of the same parameter seems unlikely.

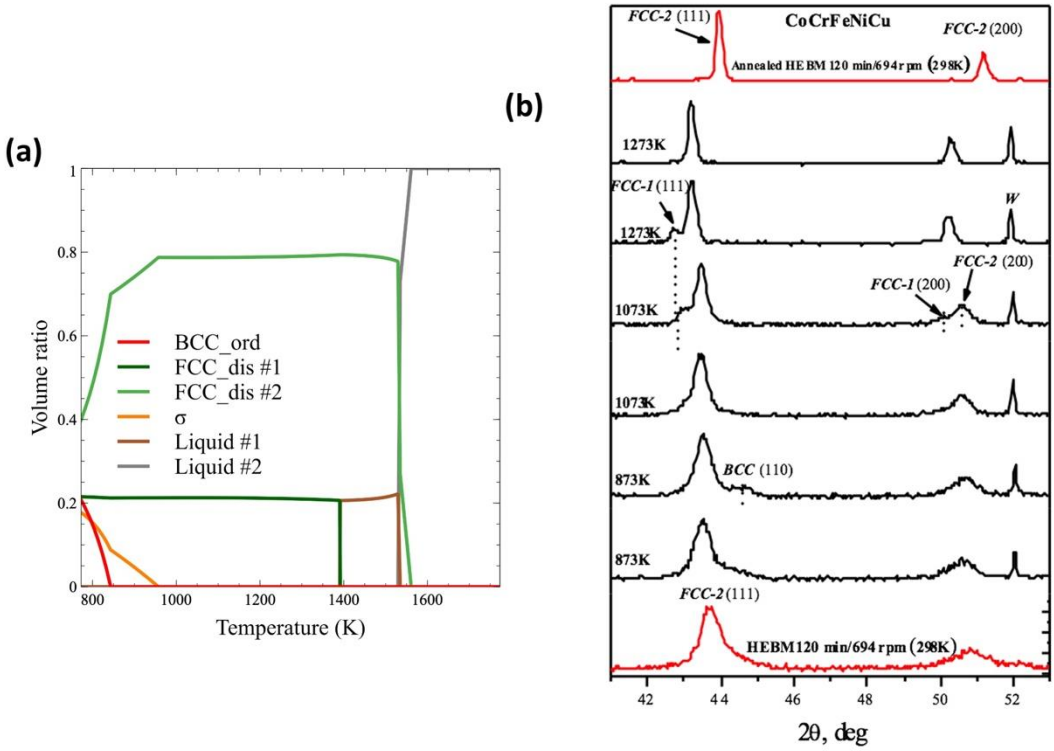

Figure 9: Volume ratios of phases for HEA Cu-CoCrFeNi calculated using Thermo-Calc (a). HT-XRD of powder after HEBM (Activator-2S, 120 min of HEBM at 694/1388 rpm) (b).

In the case of the Ti-CoCrFeNi, Calphad showed the coexistence of a disordered FCC_dis solid solution and a BCC_ord phase close to the melting temperature (see Fig. 10a). The σ phase persists upon melting. At 1273 K, the composition of the three coexisting phases reads:

- BCC_ord: $Ti_{28}\,Co_{21}\,Cr_{14}\,Fe_{16}\,Ni_{21.5}$;
- FCC_dis: $Ti_5\,Co_{20}\,Cr_{28}\,Fe_{28}\,Ni_{19}$;
- σ: $Co_{15}\,Cr_{53}\,Fe_{24}$.

Most of the Ti is in the BCC_ord phase. At low temperatures (T < 1000 K), Laves phases C14 and C15, intermetallic Ni_3Ti (D024) and the σ phase are stable. Laves phases and intermetallic Ni_3Ti rearrange at 1000 K into FCC_dis and BCC_ord. The melting of FCC_dis takes place prior to the melting of the BCC_ord. Over 40 K, the ordered BCC_ord phase coexists with the liquid phase.

HT-XRD results on milled Ti-CoCrFeNi powder are presented in Fig. 10b. Heating was carried out similarly to the previous Al-CoCrFeNi alloy, except that the XRD patterns after 0h of annealing at the selected temperature are not displayed. Mechanical treatment of the five-component Ti+Co+Cr+Fe+Ni mixtures results in the formation of a single-phase BCC structure as shown in the bottom pattern. In this case, the last remaining peak is also very broad. It could correspond to two peaks, one FCC and one BCC.

The HT-XRD patterns show that the peaks corresponding to the BCC and FCC phases at 44.5° 2θ appear clearly as two separate peaks from 873 K and above. At 873 K, the BCC phase is predominant, whereas the FCC phase becomes the main phase at 1073 and 1273 K. Note that the W peak corresponds to the measurement apparatus. In this case, there is also a noticeable peak refinement with temperature, corresponding to the increase in grain size and relaxation of the lattice defects.

The superlattice peak associated with an ordered BCC phase B2 should be close to 32° 2θ. However, the main BCC peak, (110), is already so small that the superlattice reflection would not be visible either way. The inversion between BCC and FCC phases as the main phase of the Ti-CoCrFeNi alloy as compared to calculated results is interesting; this discrepancy could be explained in a similar way to that noted in the Al-CoCrFeNi case. Indeed, Ti is known to be even more reactive with oxygen than Al and could form a significant amount of nano-oxide not discernible by XRD. However, our experimental results are coherent with laser cladded Ti-CoCrFeNi which exhibited a main FCC phase [17]. These results thus seem to point out a weakness in the TCHEA3 database.

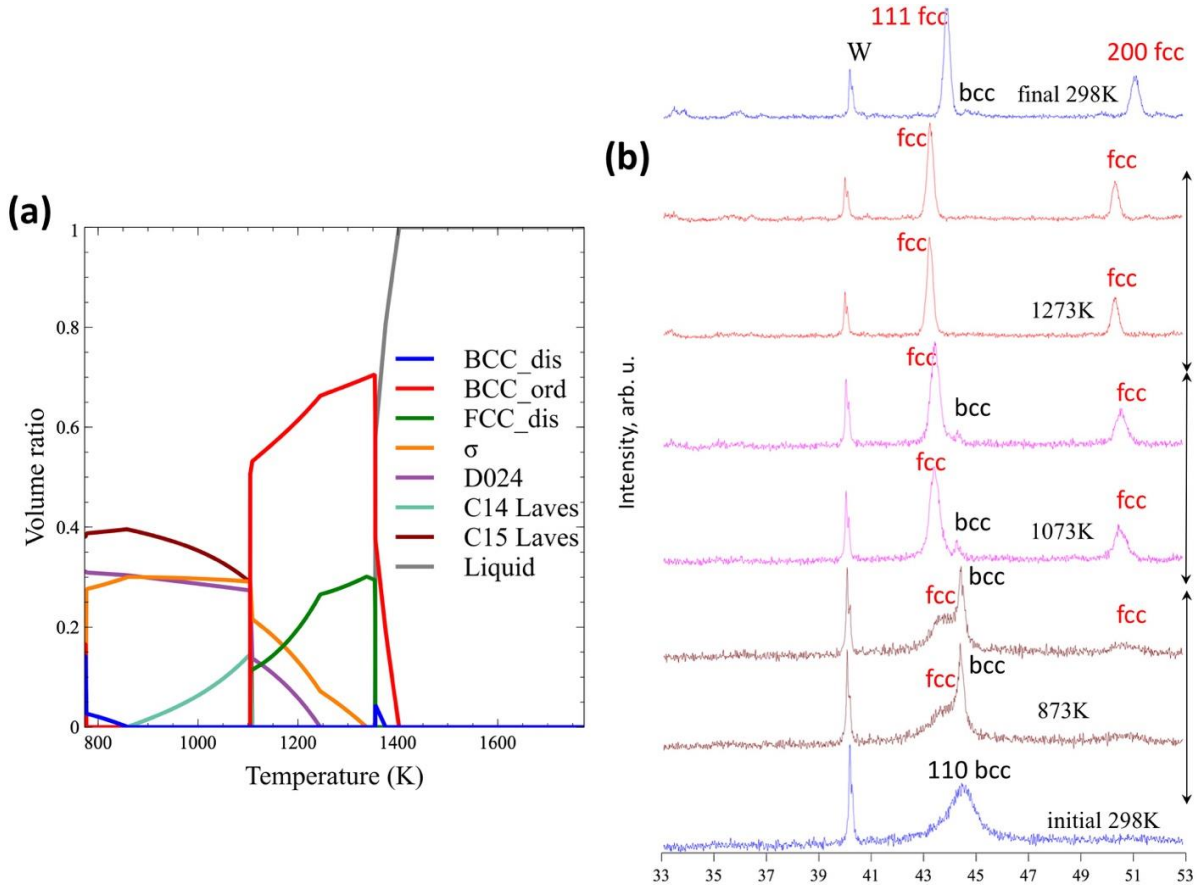

Figure 10: Volume ratios of phases for the Ti-CoCrFeNi alloy calculated using Thermo-Calc (a). High temperature XRD patterns of the powder after HEBM in AGO-2 (b).

4. Discussion

The stability of HEAs is typically associated to the relation

$$\Delta G_{\text{mix}} = \Delta H_{\text{mix}} - T\Delta S_{\text{mix}} \quad (2)$$

It is commonly accepted that the entropic term ensures the stability of the alloy at high temperatures because of the increase in configurational entropy for a large enough number of constitutive elements. This simple and elegant point of view is currently called into question, justifying the name change of HEAs to complex concentrated alloys (CCAs) [18,29]. In order to appreciate the contribution of enthalpy and entropy in HEA stability (eq. (2)), the mixing behavior in Gibbs free energy, enthalpy, and entropy is presented in Fig. 11. We compared the mixing properties at high temperature (1273 K) of the quaternary CoCrFeNi and the quinaries Al-CoCrFeNi, and Ti-CoCrFeNi for a given phase. In this analysis, the content in Cr has been varied. The diagrams depicted in Fig. 11 are pseudo-binary: there is an equal repartition of the other elements whatever the content in Cr. In our previous analysis, we have remarked that the distribution of Cr in the different phases is an important factor in the occurrence of disordered phases. In the case of the $CoCr_xFeNi$ system, we noted that the stability $\Delta G_{\text{mix}} < 0$ is ensured by eq. (2) because $\Delta H_{\text{mix}} > 0$ in almost the whole composition range.
But the Gibbs free energy of mixing ΔG_{mix} decreases monotically over the whole composition range with the increase in the number of components (4 to 5). As shown in Fig. 11b(11e), the addition of Al(Ti) radically changes the behavior of ΔH_{mix}. Achieving a more negative ΔH_{mix} implies the formation of stronger bonds among elements. This effect is very important at a low content in Cr (including the equimolar $x(\text{Cr}) = 0.2$). In the case of the equimolar Al-CoCrFeNi system, ΔH_{mix} is about -30 kJ/mol for the BCC phase and -15 kJ/mol for the FCC phase. More surprisingly, we noted a decrease in ΔS_{mix} as compared to the quaternary system and the entropic term $T\Delta S_{\text{mix}} = 4.67$ kJ/mol. The stability of the quinary HEA thus cannot be solely attributed to the entropic effect. The same conclusions can be drawn in the case of the Ti-CoCrFeNi system.

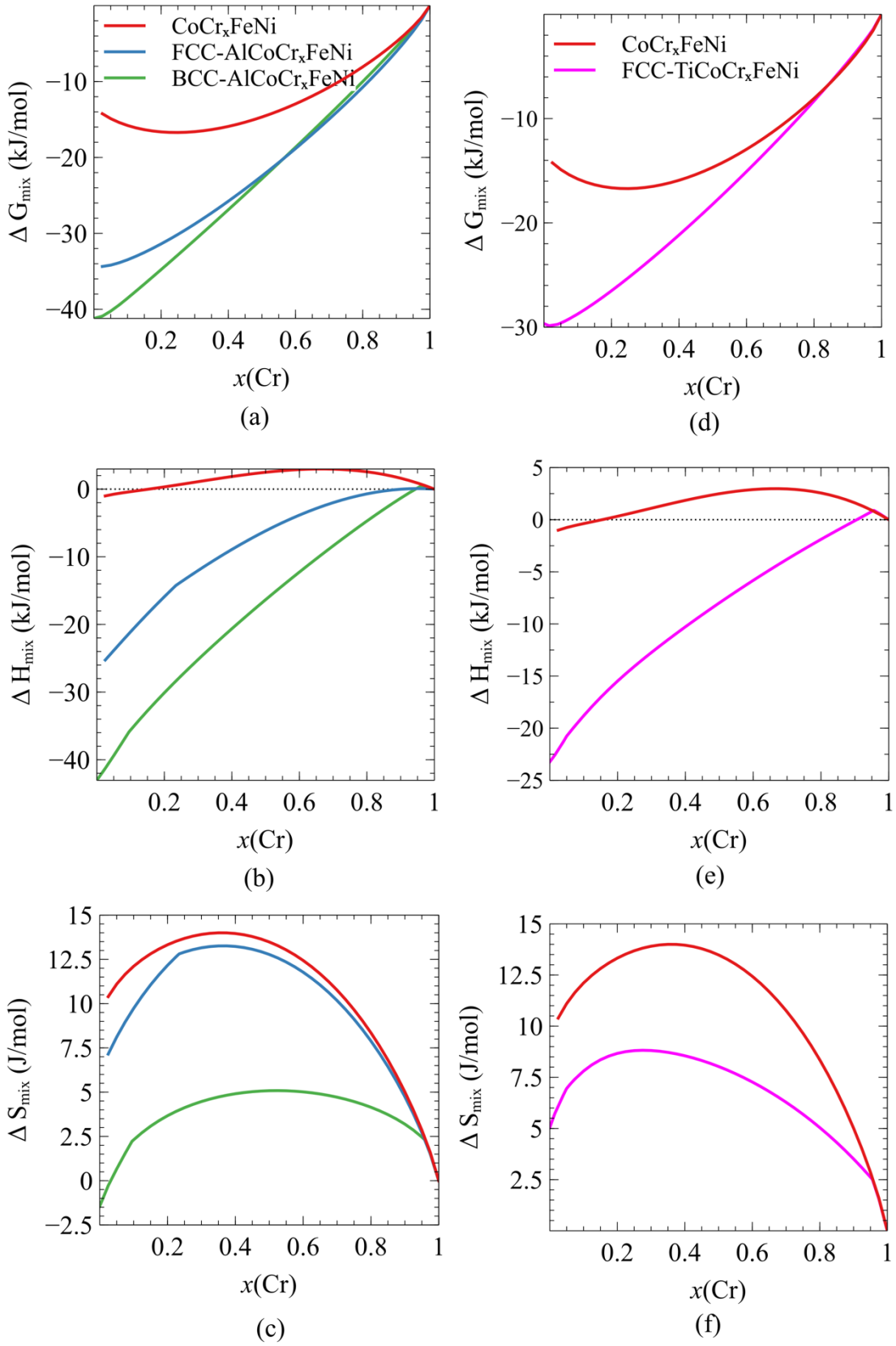

Figure 11: Calculated mixing properties of the FCC(BCC) phase at 1273 K: Gibbs free energy of mixing ΔG_{mix} , enthalpy of mixing ΔH_{mix} and entropy of mixing ΔS_{mix} as a function of Cr content for the quaternary $CoCr_xFeNi$ and quinaries Al-$CoCr_xFeNi$ (a-c) and Ti-$CoCr_xFeNi$ (d-f). The reference state is FCC(BCC) at T=1273 K. Thermo-Calc® with TCHEA3.

The ternary CoFeNi system, often named *medium-entropy alloy*, in fact satisfies the relation (2) defining the notion of high-entropy alloy despite the limited number of constituents: $\Delta H_{\text{mix}} = 32.5\ kJ/mol > 0\ ;\ -T\Delta S_{\text{mix}} = -109\ kJ/mol$ at $T = 1273\ K$.
In the present work, the ternary elaborated by HEBM is composed of a single FCC disordered phase whose lattice parameter a_0 =3.57 Å is greater than the lattice parameter of Ni (a_0 =3.52 Å). Although the three constituents have similar atomic diameters, the host FCC-Ni matrix is affected by the substitution of Ni by Co and Fe. This solid solution obtained by mechanical treatment is chemically uniform. The annealing of CoFeNi at 873 K, 1073 K, and 1273 K has no effect on the phase stability except a slight relaxation of the lattice parameter measured at room temperature ($a_0 = 3.56$ Å after the annealing at 1273 K for instance). In other words, the elaboration process selects the FCC_dis phase that remains stable upon annealing. Over the duration of annealing at 873 K, no transformation of FCC_dis to BCC_ord was observed, while this ordered phase, mainly composed of Fe and Co, is predicted in equilibrium conditions. Our hypothesis is that such discrepancies could be explained by the out of equilibrium process associated with powder metallurgy. The situation is completely different in the case of CoFeNi films prepared by reverse pulse electrodeposition with ultra-high magnetic saturation [30]. In this case, the $Co_{20}Fe_{66}Ni_{14}$ alloy is unstable for 2h annealing at 673 K with a significant reduction in magnetic saturation.

The quaternary CoCrFeNi system also fulfils relation (2). Fig. 11 demonstrates the High Entropy effect on alloy stability. The thermal stability of CoCrFeNi has recently attracted serious scrutiny in the literature. Indeed, this system can be considered as the base alloy for the class of X-CoCrFeNi HEAs where X is an element of different atomic size (Al or Ti in the present study). In a temperature range close to its melting temperature, at equilibrium, the system is characterized by a single FCC disordered phase (see Fig. 5). The thermal stability of the FCC_dis phase was investigated in systems produced by means of different techniques. In the case of HEAs prepared by arc-melting, Vaidya *et al.* did not observe any modification in structure or composition for a heat treatment in the temperature interval [1073 K-1373 K] for 96 h [31]. On the other hand, Feng He *et al.* reported that the CoCrFeNi HEA is thermally metastable at 1023 K for a long annealing of 800 h [32]. The phase decomposition is similar to the clustering of GP zones with the formation of an FCC phase with a different lattice parameter (a_0 =3.55 Å as compared to the matrix value a_0 =3.66 Å). The thermal stability is thus revealed to be very sensitive to the duration and temperature of annealing. The existence of two very similar FCC_dis phases with a slight difference in lattice parameter (0.001 Å) has also been observed in non-equimolar as-cast CoCrFeNi with no change after 3h-annealing at 1373 K [33].

In the case of HEAs synthesized by mechanical alloying followed by spark plasma sintering (SPS), the situation is quite different. S. Praveen et al. reported that elemental powders of Co, Cr, Fe, and Ni milled for 15h transformed into a major FCC_dis phase with a minor BCC_ord phase [6]. After SPS, the major FCC phase was retained and the BCC_ord phase disappeared with the formation of tiny second phase particles (carbide Cr_7C_3 and oxide Cr_2O_3). Even for a long annealing duration of 600h at 1173 K, these authors observed sluggish grain growth that did not affect the stability of the nanocrystalline HEA alloy. The same behavior has been

observed for long annealing at the lower temperature of 973 K [34]. The authors attributed the strong resistance to grain growth to the presence of carbides and oxides. In the present study, no such secondary phases were observed. Grain growth, estimated by the increase in crystallite size, is thus not inhibited by such oxides and carbides.

Nanocrystalline CoCrFeNi thin films deposited on Si/SiO_2 and c-sapphire substrates by magnetron co-sputtering have recently been investigated [35]. In addition to the FCC phase, the films contained an additional σ phase even at room temperature and in as-deposited films due to a large number of nucleation sites and accelerated kinetics as compared to bulk systems. Annealing at temperatures between 573 K and 1073 K leads to the formation of Cr oxides at the expense of the σ phase.

The powder of CoCrFeNi-HEA produced by HEBM (see Fig. 1) is characterized by a single FCC_dis solid solution of uniform chemical composition (see Fig. 2). The annealing at 873 K, 1073 K and 1273 K over 5h did not affect the stability of the disordered FCC phase, even at 873 K where thermodynamics predicts the formation of a small amount of σ phase. The only noticeable change was an increase in the lattice parameter that may be related to the complete dissolution of Cr in the solid solution upon heat treatment or to the other hypotheses raised in section 3. In conclusion, two main factors may induce discrepancies between experimental and numerical results: the metastable state attained after powder metallurgy route and contamination by minor elements. Both HEBM preparation and annealing conditions are of primary importance in the observed phase stability.

The equimolar Al-CoCrFeNi system is among the most studied HEAs after the Cantor alloy. Nevertheless, discrepancies between experimental results and thermodynamic calculations have continuously been reported. In our study, a suspicious amount of FCC phase was found as soon as the temperature reached 873 K. The hypothesis of Al oxide depleting the alloys of Al may partially explain this observation, but it is not sufficient. Indeed, we can turn to Munitz *et al.* who focused their work on the effect of heat treatment on the arc-melted Al-CoCrFeNi alloy [36]. The as-cast alloy exhibited a BCC phase (A2+B2) with an Al-Ni rich dendrite core and Co-Cr-Fe rich interdentritic regions. A σ phase and an FCC phase formed in the interdendritic regions with heat treatments between 923 K and 1248 K over 3h. The formation of Al oxide is easier to control in the case of the liquid-state process; the influence of oxygen is thus most likely negligible in this study. Yet the amount of FCC after annealing is significant; the database seems unable to predict the correct equilibrium in this case. It is interesting to note that TCNI9, a database very similar to HEA3, predicts a greater amount of FCC.

Studies of Cu-CoCrFeNi HEAs are mainly limited to thin films and coatings. An *et al*. have found that thin films were composed of FCC grains with preferential (111) orientation as compared to as-cast Cu-CoCrFeNi HEAs where two FCC phases were detected (3.58 Å and 3.61 Å): a Cu-rich phase in interdendritic regions and a Cu-poor phase in dendritic morphology [37]. The in-situ annealing in TEM of Cu-CoCrFeNi thin films prepared by magnetron sputtering has been evaluated in [38] in the temperature range [673 K-973 K] for 5 min. Up to 673 K, a single FCC phase was observed. At 823 K, the film had a two-phase structure: the

original FCC phase and a BCC phase with an epitaxial relationship. This type of transformation can be attributed to diffusionless processes. From 823 K, fast morphological and structural changes occur, controlled by volume diffusion processes with the separation of Cr-rich areas and Cu-rich ones. In the present study, the annealing of Cu-CoCrFeNi HEA produced by HEBM also revealed transient phases: a BCC phase and a second FCC phase as a function of temperature and annealing time.

Equimolar Ti-CoCrFeNi is among the least studied HEAs. Indeed, several groups evaluated the influence of Ti on the CoCrFeNi base [39-41] and they concluded that Ti often leads to complex phases such as laves and rhombohedral phases. Surprisingly enough, in our study we found only two simple phases: FCC and BCC. The main difference is related to grain size and lattice defect concentration. Indeed, milled powders are known to exhibit a loose crystalline structure and complex phases could be kinetically inhibited. Hence, long term annealing could be mandatory to reveal the actual microstructure of this alloy.
There is no consensus in the literature on the relevant duration of annealing. Indeed, annealing studies are performed over various durations. Long term annealing has been reported by several groups for a minimal annealing time of 50h or even 100h to ensure that the thermodynamic equilibrium is reached in HEAs [19,42]. Reynolds *et al*. performed high-energy synchrotron radiation X-ray diffraction measurements during in situ annealing (SR-XRD) and noted that 3h annealing was sometimes not long enough [43]. As compared to the above-mentioned studies, the annealing times of a few hours as used in the present work may seem a little short. However, conclusive remarks have been drawn in the literature reporting studies with short annealing times. Indeed, Dolique *et al*. demonstrated that HEA thin films deposited by DC magnetron sputtering were stable until a temperature just below the bulk HEA degradation temperature using HT-XRD with short time annealing [44]. Even in their SR-XRD study, Reynolds *et al*. concluded that their experimental results matched well with the Calphad predictions of the phase evolution for the B2 phase. Hence, short annealing times are an efficient way to ensure that the database and experimental results match well enough to proceed to a thorough analysis characterized by hundreds of hours annealing time.

The Calphad method, based on free energy minimization, gives the dependence of the *equilibrium* phase composition on temperature. For the compositions investigated in the present study, the disordered phase characteristic of high entropy alloys is formed in a temperature range close to the melting point, while ordered phases correspond to lower temperatures. We observed that some of these secondary phases transitorily appeared during heat treatment while others were inhibited. In order to report these observations, the kinetics of phase transformations should be taken into account with a detailed description of precipitation and diffusion mechanisms together with thermodynamic parameters (driving forces) [45].

5. Conclusion

The investigation of thermal stability in High Entropy Alloys is a vast and complex domain. On one hand, the name of these alloys has been shown to be somewhat misleading since the high entropy effect has been demystified by several research groups. On the other hand, the field of High Entropy Alloys includes a wide range of compositions and elaboration processes. In our study, we chose to start from ternary medium entropy alloys to progress to the well-known Al-CoCrFeNi and the less studied Ti-CoCrFeNi. The three studied quinary compositions are relatively simple since they are equimolar with only one element varying. The thermal stability of mechanically alloyed powders is of great interest since they embody the perfect disordered solid solution; indeed, they do not exhibit contamination such as carbon from the sintering medium or segregation occurring during solidification.

In the present study, we found that medium entropy alloys CoFeNi and CoCrFeNi were the most stable of the alloys studied. In addition, our results revealed that adding a fifth element irremediably led to the formation of secondary phases after and/or during annealing. In a further finding of relevance, even the most stable HEA, the Mn-CoCrFeNi Cantor alloy, has recently been reported to exhibit two FCC solid solutions after short time annealing [16].

The limited diffusion in a distorted crystal lattice does not seem to guarantee the thermal stability of High Entropy Alloys. Indeed, the single-phase microstructure is lost after even a short annealing time. In addition, those secondary phases were not often predicted by the Calphad method based on TCHEA3 (Thermo-Calc). It seems likely that the presence of defects related to the elaboration process led to some sort of kinetic shifting of their stability domain. However, in the case of medium entropy alloys, by confronting the thermodynamic calculations and the HT-XRD results, we observed that some phases were inhibited at relatively low temperatures. And, interestingly enough, in the case of quinary high entropy alloys, we found that complex phases such as Laves and other ordered phases could also be inhibited.

Experimental results demonstrated that phase transformations and/or precipitations of secondary phases took place in all considered equimolar HEAs. Thermodynamic calculations also showed the co-existence of two or more phases at room and moderate temperatures, which is in agreement with eq. (2) since the entropy impact decreases with decreasing temperature. At the same time, we never observed complete decay of the initial HEA phase into simple ordered compounds (intermetallics, ternary ordered alloys, etc.). High entropy FCC and BCC phases remain after annealing in all studied materials, despite the transformations. Our findings allow us to conclude that the search for stable high-temperature alloys can be continued.

References

[1] J.-W. Yeh, S.-K. Chen, S.-J. Lin, J.-Y. Gan, T.-S. Chin, T.-T. Shun, C.-H. Tsau, S.-Y. Chang, Nanostructured High-Entropy Alloys with Multiple Principal Elements: Novel Alloy Design Concepts and Outcomes, Adv. Eng. Mater. (2004) 5.

[2] B. Cantor, I.T.H. Chang, P. Knight, A.J.B. Vincent, Microstructural development in equiatomic multicomponent alloys, Mater. Sci. Eng. A. 375–377 (2004) 213–218. https://doi.org/10.1016/j.msea.2003.10.257.

[3] Y. Lu, X. Gao, L. Jiang, Z. Chen, T. Wang, J. Jie, H. Kang, Y. Zhang, S. Guo, H. Ruan, Y. Zhao, Z. Cao, T. Li, Directly cast bulk eutectic and near-eutectic high entropy alloys with balanced strength and ductility in a wide temperature range, Acta Mater. 124 (2017) 143–150. https://doi.org/10.1016/j.actamat.2016.11.016.

[4] A.-C. Yeh, Y.-M. Chen, C.-K. Liu, W.-J. Shong, Development of an advanced bond coat for solid oxide fuel cell interconnector applications, J. Power Sources. 296 (2015) 426–432. https://doi.org/10.1016/j.jpowsour.2015.07.076.

[5] J. Chen, X. Zhou, W. Wang, B. Liu, Y. Lv, W. Yang, D. Xu, Y. Liu, A review on fundamental of high entropy alloys with promising high–temperature properties, J. Alloys Compd. 760 (2018) 15–30. https://doi.org/10.1016/j.jallcom.2018.05.067.

[6] S. Praveen, J. Basu, S. Kashyap, R.S. Kottada, Exceptional resistance to grain growth in nanocrystalline CoCrFeNi high entropy alloy at high homologous temperatures, J. Alloys Compd. 662 (2016) 361–367. https://doi.org/10.1016/j.jallcom.2015.12.020.

[7] F. He, Z. Wang, Q. Wu, J. Li, J. Wang, C.T. Liu, Phase separation of metastable CoCrFeNi high entropy alloy at intermediate temperatures, Scr. Mater. 126 (2017) 15–19. https://doi.org/10.1016/j.scriptamat.2016.08.008.

[8] W.-R. Wang, W.-L. Wang, J.-W. Yeh, Phases, microstructure and mechanical properties of AlxCoCrFeNi high-entropy alloys at elevated temperatures, J. Alloys Compd. 589 (2014) 143–152. https://doi.org/10.1016/j.jallcom.2013.11.084.

[9] T.M. Butler, M.L. Weaver, Oxidation behavior of arc melted AlCoCrFeNi multi-component high-entropy alloys, J. Alloys Compd. 674 (2016) 229–244. https://doi.org/10.1016/j.jallcom.2016.02.257.

[10] L. Meshi, Y. Linden, A. Munitz, S. Salhov, M. Pinkas, Retardation of the σ phase formation in the AlCoCrFeNi multi-component alloy, Mater. Charact. 148 (2019) 171–177. https://doi.org/10.1016/j.matchar.2018.12.010.

[11] V. Shivam, J. Basu, V.K. Pandey, Y. Shadangi, N.K. Mukhopadhyay, Alloying behaviour, thermal stability and phase evolution in quinary AlCoCrFeNi high entropy alloy, Adv. Powder Technol. 29 (2018) 2221–2230. https://doi.org/10.1016/j.apt.2018.06.006.

[12] V. Shivam, Y. Shadangi, J. Basu, N.K. Mukhopadhyay, Evolution of phases, hardness and magnetic properties of AlCoCrFeNi high entropy alloy processed by mechanical alloying, J. Alloys Compd. 832 (2020) 154826. https://doi.org/10.1016/j.jallcom.2020.154826.

[13] D.B. Miracle, O.N. Senkov, A critical review of high entropy alloys and related concepts, Acta Mater. 122 (2017) 448–511. https://doi.org/10.1016/j.actamat.2016.08.081.

[14] J.-W. Yeh, Physical Metallurgy of High-Entropy Alloys, JOM. 67 (2015) 2254–2261. https://doi.org/10.1007/s11837-015-1583-5.

[15] A.S. Rogachev, Structure, Stability, and Properties of High-Entropy Alloys, Phys. Met. Metallogr. 121 (2020) 733–764. https://doi.org/10.1134/S0031918X20080098.

[16] A.S. Rogachev, S.G. Vadchenko, N.A. Kochetov, S. Rouvimov, D.Y. Kovalev, A.S. Shchukin, D.O. Moskovskikh, A.A. Nepapushev, A.S. Mukasyan, Structure and properties of equiatomic CoCrFeNiMn alloy fabricated by high-energy ball milling and

spark plasma sintering, J. Alloys Compd. 805 (2019) 1237–1245. https://doi.org/10.1016/j.jallcom.2019.07.195.

[17] S. Zhang, B. Han, M. Li, Q. Zhang, C. Hu, S. Niu, Z. Li, Y. Wang, Investigation on solid particles erosion resistance of laser cladded CoCrFeNiTi high entropy alloy coating, Intermetallics. 131 (2021) 107111. https://doi.org/10.1016/j.intermet.2021.107111.

[18] C. Zhang, M.C. Gao, CALPHAD Modeling of High-Entropy Alloys, in: M.C. Gao, J.-W. Yeh, P.K. Liaw, Y. Zhang (Eds.), High-Entropy Alloys, Springer International Publishing, Cham, 2016: pp. 399–444. https://doi.org/10.1007/978-3-319-27013-5_12.

[19] C. Zhang, F. Zhang, H. Diao, M.C. Gao, Z. Tang, J.D. Poplawsky, P.K. Liaw, Understanding phase stability of Al-Co-Cr-Fe-Ni high entropy alloys, Mater. Des. 109 (2016) 425–433. https://doi.org/10.1016/j.matdes.2016.07.073.

[20] G. Bracq, M. Laurent-Brocq, L. Perrière, R. Pirès, J.-M. Joubert, I. Guillot, The fcc solid solution stability in the Co-Cr-Fe-Mn-Ni multi-component system, Acta Mater. 128 (2017) 327–336. https://doi.org/10.1016/j.actamat.2017.02.017.

[21] J.C. Rao, H.Y. Diao, V. Ocelík, D. Vainchtein, C. Zhang, C. Kuo, Z. Tang, W. Guo, J.D. Poplawsky, Y. Zhou, P.K. Liaw, J.Th.M. De Hosson, Secondary phases in AlxCoCrFeNi high-entropy alloys: An in-situ TEM heating study and thermodynamic appraisal, Acta Mater. 131 (2017) 206–220. https://doi.org/10.1016/j.actamat.2017.03.066.

[22] J.M. Torralba, P. Alvaredo, A. García-Junceda, High-entropy alloys fabricated via powder metallurgy. A critical review, Powder Metall. 62 (2019) 84–114. https://doi.org/10.1080/00325899.2019.1584454.

[23] M. Vaidya, G.M. Muralikrishna, B.S. Murty, High-entropy alloys by mechanical alloying: A review, J. Mater. Res. 34 (2019) 664–686. https://doi.org/10.1557/jmr.2019.37.

[24] A.S. Rogachev, D.Yu. Kovalev, N.A. Kochetov, A.S. Shchukin, S.G. Vadchenko, Evolution of crystal structure in high-entropy AlCoCrFeNi alloy: An in situ high-temperature X-ray diffraction study, J. Alloys Compd. 861 (2021) 158562. https://doi.org/10.1016/j.jallcom.2020.158562.

[25] W. Ji, Z. Fu, W. Wang, H. Wang, J. Zhang, Y. Wang, F. Zhang, Mechanical alloying synthesis and spark plasma sintering consolidation of CoCrFeNiAl high-entropy alloy, J. Alloys Compd. 589 (2014) 61–66. https://doi.org/10.1016/j.jallcom.2013.11.146.

[26] A.S. Rogachev, N.A. Kochetov, A.V. Panteleeva, K.V. Kuskov, D.Y. Kovalev, A.S. Shchukin, S.G. Vadchenko, Y.B. Scheck, High-Energy Ball Milling and Spark Plasma Sintering of the CoCrFeNiAl High-Entropy Alloy, Metals. 10 (2020) 1489. https://doi.org/10.3390/met10111489.

[27] A. Fourmont, S. Le Gallet, O. Politano, C. Desgranges, F. Baras, Effects of planetary ball milling on AlCoCrFeNi high entropy alloys prepared by Spark Plasma Sintering: Experiments and molecular dynamics study, J. Alloys Compd. 820 (2020) 153448. https://doi.org/10.1016/j.jallcom.2019.153448.

[28] A. Fourmont, S. Le Gallet, K. Hoummada, M. Descoins, C. Desgranges, O. Politano, F. Baras, Dual-phase AlCoCrFeNi HEA: Reactive Spark Plasma Sintering, Atom Probe Tomography investigation and oxygen contamination, Be Publ. (2021).

[29] S. Gorsse, J.-P. Couzinié, D.B. Miracle, From high-entropy alloys to complex concentrated alloys, Comptes Rendus Phys. 19 (2018) 721–736. https://doi.org/10.1016/j.crhy.2018.09.004.

[30] I. Tabakovic, V. Venkatasamy, Preparation of metastable CoFeNi alloys with ultra-high magnetic saturation (Bs = 2.4–2.59 T) by reverse pulse electrodeposition, J. Magn. Magn. Mater. (2018) 9.

[31] M. Vaidya, K. Guruvidyathri, B.S. Murty, Phase formation and thermal stability of CoCrFeNi and CoCrFeMnNi equiatomic high entropy alloys, J. Alloys Compd. 774 (2019) 856–864. https://doi.org/10.1016/j.jallcom.2018.09.342.

[32] F. He, Z. Wang, Q. Wu, J. Li, J. Wang, C.T. Liu, Phase separation of metastable CoCrFeNi high entropy alloy at intermediate temperatures, Scr. Mater. 126 (2017) 15–19. https://doi.org/10.1016/j.scriptamat.2016.08.008.

[33] U. Dahlborg, J. Cornide, M. Calvo-Dahlborg, T.C. Hansen, A. Fitch, Z. Leong, S. Chambreland, R. Goodall, Structure of some CoCrFeNi and CoCrFeNiPd multicomponent HEA alloys by diffraction techniques, J. Alloys Compd. 681 (2016) 330–341. https://doi.org/10.1016/j.jallcom.2016.04.248.

[34] P. Sathiyamoorthi, J. Basu, S. Kashyap, P. K G, R.S. Kottada, Thermal stability and grain boundary strengthening in ultrafine-grained CoCrFeNi high entropy alloy composite, Mater. Des. 134 (2017). https://doi.org/10.1016/j.matdes.2017.08.053.

[35] M.K. Kini, S. Lee, A. Savan, B. Breitbach, Y. Addab, W. Lu, M. Ghidelli, A. Ludwig, N. Bozzolo, C. Scheu, D. Chatain, G. Dehm, Nanocrystalline equiatomic CoCrFeNi alloy thin films: Are they single phase fcc?, Surf. Coat. Technol. 410 (2021) 126945. https://doi.org/10.1016/j.surfcoat.2021.126945.

[36] A. Munitz, S. Salhov, S. Hayun, N. Frage, Heat treatment impacts the micro-structure and mechanical properties of AlCoCrFeNi high entropy alloy, J. Alloys Compd. 683 (2016) 221–230. https://doi.org/10.1016/j.jallcom.2016.05.034.

[37] Z. An, H. Jia, Y. Wu, P.D. Rack, A.D. Patchen, Y. Liu, Y. Ren, N. Li, P.K. Liaw, Solid-Solution CrCoCuFeNi High-Entropy Alloy Thin Films Synthesized by Sputter Deposition, Mater. Res. Lett. 3 (2015) 203–209. https://doi.org/10.1080/21663831.2015.1048904.

[38] M. Arfaoui, G. Radnóczi, V. Kovács Kis, Transformations in CrFeCoNiCu High Entropy Alloy Thin Films during In-Situ Annealing in TEM, Coatings. 10 (2020) 60. https://doi.org/10.3390/coatings10010060.

[39] P. Cui, Y. Ma, L. Zhang, M. Zhang, J. Fan, W. Dong, P. Yu, G. Li, R. Liu, Effect of Ti on microstructures and mechanical properties of high entropy alloys based on CoFeMnNi system, Mater. Sci. Eng. A. 737 (2018) 198–204. https://doi.org/10.1016/j.msea.2018.09.050.

[40] T.-T. Shun, L.-Y. Chang, M.-H. Shiu, Microstructures and mechanical properties of multiprincipal component CoCrFeNiTix alloys, Mater. Sci. Eng. A. 556 (2012) 170–174. https://doi.org/10.1016/j.msea.2012.06.075.

[41] T.-T. Shun, C.-Y. Hsieh, W.-J. Hung, C.-F. Lee, Age Heat Treatment of the $CoCrFeNiTi_{0.3}$ High-Entropy Alloy, Mater. Trans. 59 (2018) 730–733. https://doi.org/10.2320/matertrans.M2017418.

[42] E.J. Pickering, R. Muñoz-Moreno, H.J. Stone, N.G. Jones, Precipitation in the equiatomic high-entropy alloy CrMnFeCoNi, Scr. Mater. 113 (2016) 106–109. https://doi.org/10.1016/j.scriptamat.2015.10.025.

[43] C.R. Reynolds, Z. Herl, N.A. Ley, D. Choudhuri, J.T. Lloyd, M.L. Young, Comparing CALPHAD predictions with high energy synchrotron radiation X-ray diffraction measurements during in situ annealing of Al0.3CoCrFeNi high entropy alloy, Materialia. 12 (2020) 100784. https://doi.org/10.1016/j.mtla.2020.100784.

[44] V. Dolique, A.-L. Thomann, P. Brault, Y. Tessier, P. Gillon, Thermal stability of AlCoCrCuFeNi high entropy alloy thin films studied by in-situ XRD analysis, Surf. Coat. Technol. 204 (2010) 1989–1992. https://doi.org/10.1016/j.surfcoat.2009.12.006.

[45] S. Gorsse, F. Tancret, Current and emerging practices of CALPHAD toward the development of high entropy alloys and complex concentrated alloys, J. Mater. Res. 33 (2018) 2899–2923. https://doi.org/10.1557/jmr.2018.152.

General conclusion

In the present PhD dissertation, multi-scale modelling and experimental methodology were developed in order to investigate the mechanical milling of metallic powders.

Starting from the study of binary systems such as Ni-Al, we evaluated the influence of different parameters on the progress of the process and resulting material characteristics. We showed that linear uni-axial deformation of a simulation box filled with rounded particles could be considered as a compression of particles of powder between grinding balls, and as such could mimic the first steps of mechanical activation. This apparently simple modelling led to a complex motion of the particles, likely leading to the two mechanisms responsible for energy transfer: impact and friction. The amorphization rate, chemical mixing efficiency, and the creation of defects were thoroughly investigated in the case of 4 binary systems (Ni–Al, Ti–Al, Fe–Ni, and Fe–Cr):

- **We suggested that high amorphisation resulted from both the intrinsic characteristics of the powder and the co-milled powder properties**. In addition, amorphisation rate was potentially hindered by crystallographic structure versatility (e.g., the initially hcp-Ti in the Ti-Al system is prone to a transformation into FCC).
- We showed that the mobility of relevant groups of atoms also results from the intrinsic characteristics and is impacted by the amorphisation rate. Finally, high mobility, which could be termed “mechanical diffusion” leads to significant chemical mixing.
- We demonstrated that hexagonal compact planar defects (i.e. dislocations, twins or stacking faults) were easily created in FCC structures during plastic deformation.

In all the cases, a significant number of atoms remained crystalline, which is a feature of mechanosynthesis. More interestingly, in some cases, certain atoms adopted the crystalline structure of the other elements, thus creating a metastable mixing zone (e.g., Ni adopting a BCC structure in the case of Fe-Ni deformation). Note that the formation of a metastable phase has been suggested as an activating factor in the reactivity of metallic systems.

In both systems including Al, simulation results highlighted the crucial role of Aluminum. Indeed, because of its characteristics which differ from those of the others (electronic configuration 3p versus 3d), Al is simultaneously less hard and less refractory. Consequently, Al atoms become rapidly amorphous and exhibit high mobility.

The simulations of the first steps of mechanical activation confirmed some experimental results obtained by our Russian collaborators. In their work, they used HR-TEM to observe the microstructure of Ni-Al nanocomposites after milling. They identified regions consisting of Ni atoms trapped in an amorphous layer of Al which were in good agreement with our numerical observations.

The deformation of the simulation box leads to an indistinct combination of impact and friction, which are the two mechanisms responsible for energy transfer and microstructural transformation. Separating the influence of impact and friction on chemical mixing, amorphisation rate and defect creation involves studies that have yet to be undertaken and that deserve further investigation. Such a study would be particularly relevant since this topic is a matter of debate after the recent in-situ filming by Rogachev et al. of ball motions during High Energy Ball Milling. Indeed, until recently, the influence of impact was considered dominant as compared to friction, but the motion of balls seems to indicate otherwise.

We also evaluated the enhanced reactivity of systems after mechanical activation. The model system of interest chosen was Ni-Al, as an extensive experimental literature was produced in the framework of Self-Propagating High Temperature Synthesis for this particular system. Hence, our study focused on the low temperature reactivity of Ni-Al nanocomposites to closely mimic the experimental procedure. Combining our molecular dynamics investigation with experimental results of mechanically activated Ni-Al powders, a specific design of the reactive system was developed. Thanks to this design, we demonstrated that two phenomena occur at low temperatures (below the Al melting temperature: 580 °C) in mechanically activated 2-element systems:

- As compared to juxtaposed layers, pre-mixed layers still exhibit significant diffusion of Ni atoms in an amorphous Al region. The situation is different at higher temperatures, as other works in the laminate framework have reported.
- **This peculiar milled microstructure was found to be the seat of homogeneous nucleation. Hence, this microstructure promoted the overall B2-NiAl formation.**

At this point, given the results at low temperature, one can imagine that the nucleation of B2-NiAl is also promoted in mechanically activated 5-element systems as compared to mechanically alloyed systems. Indeed, some regions modelled by the bilayer configuration are likely to exist in mechanically activated 5-element agglomerates, whereas this seems improbable in chemically homogeneous mechanically alloyed agglomerates. Nevertheless, the framework of Self-Propagating High Temperature Synthesis is clearly different from the actual experimental considerations of this thesis. The main differences are obviously the number of elements, but also the temperature range. The temperature range difference could be explained by the fact that the formation of NiAl occurs through a highly exothermic and self-propagating reaction in contrast to the formation of the high entropy solid solutions. This feature ensures that low temperature treatments of Ni-Al reactive nanocomposites lead to dense material, whereas low temperature treatments of mechanically activated 5-element agglomerates would likely lead to porous alloys.

We demonstrated that, for SHS, nano-scale mixing alone effectively enhances the reactivity of metallic systems such as Ni−Al. Our results suggest that the methodology, and especially the bilayer configuration developed, are particularly relevant to the investigation of the behavior of such mechanically activated systems. However, for broader frameworks such as low-exothermic reactive sintering, the effect of nano-scale mixing alone on sintering enhancement is not obvious and requires a thorough analysis. *To follow up on the work performed in the*

framework of SHS, a study examining the influence of combined activating factors would be both interesting and accessible to carry out. Indeed, adding certain defects such as grain boundaries or dislocations to our developed bilayer configuration seems an adequate way to further our investigations. In a topic closer to the experimental results presented in this work, the developed configuration could be adapted to study the diffusion occurring in mechanically activated systems. Provided an adequate EAM potential is determined, 5-element systems could be designed in order to evaluate the influence of the activating factors (defects, nano-scale mixing, etc.) on the elemental diffusion, thus mimicking the sintering of mechanically activated agglomerates. The comparison of such data with data obtained by other methods such as DICTRA would be interesting.

Then, the feasibility of mechanical activation as an alternative to mechanical alloying was demonstrated for systems of five elements. After optimization of certain parameters (rotating speed, number of pauses, sintering temperature), a hard, dense, nanostructured AlCoCrFeNi high entropy alloy was synthesized by Mechanical Activation + Spark Plasma sintering. **We suggested that complete mechanical alloying is not necessary to elaborate High Entropy solid solutions and that this alternative way of producing HEAs leads to a distinctive imbricated nanostructure.**

The formation of solid solutions during milling was assessed by means of molecular dynamics simulations. Indeed, XRD results alone are not enough to precisely depict the state of the powder after milling. The FCC peaks exhibit significant asymmetry. The origin of this asymmetry is not at all obvious. We suggested that there is a wide distribution of lattice parameters resulting from a gradient of Al concentration. The simulations reported in Chapter II highlighted the major role of Al during milling, in both Ni-Al and Ti-Al systems. Indeed, Al rapidly becomes amorphous and dissolves in other matrices even before the heating step (or sintering, in this case). This simulated observation is confirmed by the disappearance of the Al peaks during milling. *Thorough TEM analysis could have helped to precisely characterize the state of crystallinity of mechanical activated agglomerates (after milling and before sintering). TEM analysis could have confirmed our hypothesis concerning Al diffusion in the FCC lattice leading to the XRD asymmetry and could have helped evaluate the amount of amorphous phase in order to better understand the diffusion and transformations occurring during sintering.*

We showed that planetary ball milling parameters affect the final microstructure after sintering and, consequently, that specific SPS parameters were required to effectively sinter mechanical activated agglomerates. Indeed, compared to results in the literature concerning powder metallurgy preparation of HEAs, the sintering temperature seems to be higher: it is often 900°C or 1000°C for 3d HEAs containing Al. In the present work, 1100°C was determined to be the most appropriate temperature. The influence of milling speed and the presence of pauses during milling were also considered:

- For reasonable sintering temperatures (below 1100°C), minimal mechanical activation was proven to be mandatory in order to synthetize high entropy alloy solid solutions with satisfactory elemental distribution.

- Introducing pauses during the milling was found to have a high impact on several critical features. Indeed, pauses both prevent powder from adhering to the milling jar and lead to thinner agglomerates. *Nevertheless, a thorough optimization of this parameter remains to be conducted.*

We also showed that the initial size of Chromium powder particles affects the final microstructure after sintering, especially the sigma formation. Chromium is both the hardest and most refractory element of the 5 metals considered. Consequently, special attention has to be paid in the case of milling systems including Cr. Pre-milling was found to be an acceptable solution. The simulation of the first steps of mechanical activation led to similar observations: the milling of the Fe-Cr system was simulated and showed that Cr was hardly impacted. Note that the influence of the size of other initial elemental particles is recorded in Appendix III. The effect of the initial size of Al, Ni and Fe on the milling progress and on the resulting powders was investigated.

In addition to decreasing contamination, one of the aims of mechanical activation is decreasing milling time. In the present work, the rotating speed is relatively low (250/-250 rpm), ensuring that mechanical alloying is not reached. *However, a more optimal solution would be a slightly faster rotating speed and a shorter milling time. Moreover, the precise criteria required to obtain the peculiar imbricated nanostructure and chemically homogeneity from mechanically activated agglomerates remains to be determined. Simply put, one can imagine that a certain thinness of layer is required for all elements to be able to diffuse homogeneously. That specific thinness could be obtained before 28h of milling.*

The evaluation of the chemical homogeneity of a bulk sample after the combination of Mechanical Activation and Spark Plasma Sintering was of great importance. Indeed, this is a main concern when mechanical activation is compared to mechanical alloying. SEM results showed that the chemical homogeneity was promising but **APT results evidenced the satisfactory distribution of elements in each phase.** The APT allowed us to more precisely quantify the phase composition and enabled a more direct comparison with Calphad results. In addition, **nanoprecipitates were formally identified as Al and Cr oxides.** These new data informed the hypothesis about the influence of Al and Cr depletion in the main phases by the oxides. To support this hypothesis, combined oxygen quantification and X-ray Photoelectron Spectrometry demonstrated that a non-negligible amount of oxygen originated from the commercial powders. As long as the process is performed under inert atmosphere, the influence of the milling, the storage and the sintering on oxygen contamination seems to be inconsequential. Finally, the Calphad calculations showed that, by depleting the main phases of Al and Cr, the presence of oxides could alter the phase composition and stability. *Compared to results reported in the literature, mechanical activation seems to lead to less carbide formation than classical mechanical alloying. This would be an interesting feature to investigate further.*

We found that the medium entropy alloys CoFeNi and CoCrFeNi were more thermally stable than 5-component HEAs. However, complete decay of the initial HEA phase into simple ordered compounds (intermetallics, ternary ordered alloys, etc.) was never observed. Hence, the concept of multi-principal elemental alloys remains relevant.

In the case of medium entropy alloys, by comparing the thermodynamic calculations and the HT-XRD results, we observed that the formation of some phases (such as the sigma phase and the ordered BCC phase) was inhibited at relatively low temperatures. It seems likely that the presence of defects related to the preparation process led to some sort of kinetic shifting of their stability domain, even though the presence of defects often leads to a decrease in the temperature at which new phases form.
Finally, a comparison between Mechanical Activation and Mechanical Alloying of the same composition with all the parameters known (in contrast to most published studies where some parameters are missing) can now be suggested. Note that the comparison is indirect since the powders used in the two cases are not identical.

- After a much more powerful milling (694 rpm versus 250 rpm), Al-Co-Cr-Fe-Ni exhibits a single BCC phase (without any asymmetry noticeable in the diffractogram) and there is only one contrast observable in SEM BSE.
- Even when starting from single BCC phase, a significant amount of FCC forms during annealing. In the case of mechanically alloyed powder, the purity of the initial elemental powders was relatively low; thus, the role of Al and Cr oxides can still partly explain this formation.
- The samples mechanically activated followed by SPS and those mechanically alloyed followed by annealing exhibited similar phases.
- Equimolar AlCoCrFeNi composition led irremediably to the formation of this phase. The formation of sigma was confirmed to start at around 1000°C and remained after annealing even when Chromium was perfectly distributed. This observation confirmed that sintering at 1100°C was an adequate solution to go beyond the stability domain of sigma in the case of mechanically activated agglomerates.

Note that a more detailed comparison between medium energy milling and very high energy milling on identical powders was performed and is presented in Appendix I. It completes the present conclusions.

The present work focused on the process and not the material. In future work, it would be interesting to evaluate the mechanical properties of such alloys. Indeed, our sintered samples exhibit several encouraging features in terms of mechanical properties: a dual-phase microstructure with a non-negligible amount of FCC for ductility, a fine distribution of oxides, two multi-principal element matrices and a nanostructuration for strengthening. Evaluating alloy ductility requires tensile tests, but such tests are not always simple to carry out on mechanically activated and Spark Plasma Sintered samples, as particular sample preparation is required. To be specific, such samples exhibit particularly high hardness and demand special cutting techniques; in addition, standardized tensile specimen preparation usually requires sintered samples much larger than those elaborated in the context of the present thesis. However, nano-hardness measurements of each phase separately could provide preliminary

information. The influence of nano-oxides and the elastic modulus could be extrapolated from such measurements. Determining the nano-hardness of each phase separately is also interesting in order to fine tune the composition to develop an alloy for a specific application.

Other properties, such as high temperature oxidation resistance, are particularly relevant to study in the case of Al, Cr rich alloys. Industrial alumina-forming nickel superalloys such as René N5 or CMSX-4 are designed to exhibit protective α-Al_2O_3 after high temperature ageing (>700°C) in an aggressive atmosphere. The first question which arises is: are Al rich High Entropy Alloys elaborated by mechanical activation and Spark Plasma Sintering comparable to such industrial alloys? A thorough study of the kinetics of degradation, adhesion of the oxide layers, nature of the phases formed and oxidation mechanisms of sintered HEAs would be both valuable and pioneering. A comparison of the behavior of our samples and that of the recently developed Alumina-forming Austenitic Stainless Steels (AFA-SS) could also be relevant. Note that an initial study of high temperature behavior in samples elaborated by the process developed in this thesis was performed and is presented in Appendix V. An assessment of $Al_xCoCrFeNi$ alloys prepared by powder metallurgy as high temperature materials is made. The influence of the Al content on the nature of the oxide layers is also investigated.

In addition, a study examining the weldability of HEAs prepared via the solid-state route was started in 2021 at the ICB Laboratory. Indeed, as high-performance materials, HEAs could be used as coating in an assembled product. Hence, it is imperative to correlate the elaboration process, the microstructure (and the thermophysical properties of the material to be welded) to the phenomenology of the laser-material interaction and then evaluate the effect of welding on the microstructure of the assembled zone.

Now that preparatory results about the progress of the process have been obtained, other multi-principal element compositions could be studied. It would be very interesting to thoroughly evaluate the influence of Al both on the milling progress and on the final microstructure. Since the combination of mechanical activation and Spark Plasma Sintering is very dependent on diffusion during sintering, systems with more refractory elements could behave very differently. It is all the more interesting to study such systems since solid-state routes are particularly relevant in cases of compositions containing elements with high melting temperatures. Note that new compositions based on 3d-transition metals were investigated and reported in Appendix IV. A short study on the effect of the Al content on the mechanically activated and Spark Plasma Sintered samples was performed. *In addition, new alloys for specific applications could also be developed by combination of Mechanical Activation and Spark Plasma Sintering. Non-equimolar AlCoCrFeNbNiTi compositions have begun to be studied at the ICB for interconnect material in ceramic fuel cells. Meticulously designed and elaborated HEAs could meet the demanding criteria for this specific application. Indeed, several constraints exist: mechanical (control of the expansion coefficient), chemical (oxidizing and reducing atmosphere) and electro-chemical (maintenance of high electronic conductivity in the conditions of use).*

Appendix I: Comparison of Mechanical Alloying and Mechanical Activation in AlCoCrFeNi High Entropy Alloy synthesis

1. Introduction

The present study focuses on the comparison between the Fritsch Pulverisette P4 (Laboratory ICB) leading to Mechanical Activation and the Activator-2S (Laboratories MISiS, Moscow and ISMAN, Chernogolovka) leading to Mechanical Alloying for the preparation of the AlCoCrFeNi composition by HEBM followed by SPS. In practice, the milled powder and sintered sample presented in Chapter V are here directly compared to similar powders obtained by a much more powerful milling.

2. Materials and methods

Three sets of powders were used: the Russian Powders (noted RP1 and RP2) and the Alfa Aesar powders (noted AA). Their characteristics are summarized in Table 1. The Russian powders are generally bigger than the AA powders. In addition, the RP1 set is characterized by a large initial Fe powder whereas the RP2 set is characterized by a large initial Ni powder.

Size (μm)	Al	Co	Cr	Fe	Ni
RP1	< 20	< 1	< 25	< 160	< 100
RP2	< 10	< 71	< 125	< 4	< 150
AA	< 30	< 8	< 20	< 5	< 15

Table 1: Summary of average sizes of initial powders. RP for Russian powders and AA for Alfa Aesar powders. Sizes estimated by SEM observations.

The milling parameters used are summarized in Table 2. The milling parameters are significantly different, as the aim here is to produce very different milled agglomerates in order to compare their subsequent behaviors. For P4, the pauses between two millings last for 2 hours whereas in the case of Activator 2S, the duration of the pause is a few minutes. The P4 milling reported in the present appendix was carried out in 80 mL jars. In the present appendix, only powders which were retrieved without solvent are compared. In both these cases, the studied milled powders were relatively easy to collect at the bottom of the milling jars.

	Speed of the sun disk (rpm)	Speed of the grinding chambers (rpm)	Ball diameters (mm)	BPR	Duration
Activator 2S	694	- 694	7 and 6	20:1	6*15 min
P4	250	- 250	15	7:1	4*7 h

Table 2: Summary of milling parameters. 6*15 means that pauses were introduced every 15 min. BPR is the ball to powder mass ratio.

In-situ High Temperature XRD measurements were performed using the parameters described in Chapter VI but with two different devices: one from the ISMAN laboratory and one from the ICB laboratory. Note that the heating ramp was set at 100°C/min in the case of the ISMAN device, whereas it was set at 60°C/min for the ICB case (the maximum here).
Thermogravimetry/Differential Scanning Calorimetry (TG/DSC) analyses were performed on different powders, using a heating rate of 20 °C.min^{-1} under argon with 2% H_2. The choice of this specific atmosphere was designed to evaluate the influence of reducing atmosphere on suppressing oxide formation during sintering.
The powders were sintered by Spark Plasma Sintering using the FCT Systeme GmbH HPD 10. The parameters used were 80 MPa, target temperature of 1100 °C and a heating rate of 50 °C/min. No dwell time was applied in order to avoid grain growth. Sintering was carried out in a vacuum.

3. Results and discussion

3.1. Powder characterization after milling

Figure 1a shows the XRD patterns of the powders milled with different parameters. After the milling of AA in the P4 mill, the powder exhibits a combination of FCC and BCC (as observed in Chapters IV and V). The FCC peaks are asymmetrical. The milling of AA in the Activator 2S also leads to a combination of FCC and BCC, but in this case the FCC peaks are no longer asymmetrical. In addition, the lattice parameter of the FCC phase increases greatly (see Table 3). The RP1 (characterized by a larger initial Fe powder size) milled in the Activator 2S leads to a single BCC phase, lattice parameter: 2.88 Å (+0.5% compared to pure Fe). The RP2 (characterized by a larger initial Ni powder size) results in a combination of FCC and BCC peaks but the FCC phase seems completely predominant. In this case too, the lattice parameter of the FCC greatly increases. In general, the XRD peaks resulting from the Activator 2S milling are much broader than those resulting from the P4 milling. This is likely to indicate a combination of smaller crystallites and a higher concentration of defects. The particle size distribution is depicted in Figure 1b. The particle size distribution seems to be influenced by several factors, even if one might have assumed that the powerful milling performed in the Activator 2S would have inevitably led to smaller agglomerates. The RP2 milled agglomerates exhibit a Dv50 twice as large as the others. In addition, the Dv50 for the two AAs are

surprisingly close. By way of explanation, we can suggest that the actual crystallography has the predominant influence. The multi-principal element FCC phase is likely more ductile than its BCC equivalent, which tends to fracture more easily and thus results in smaller agglomerates.

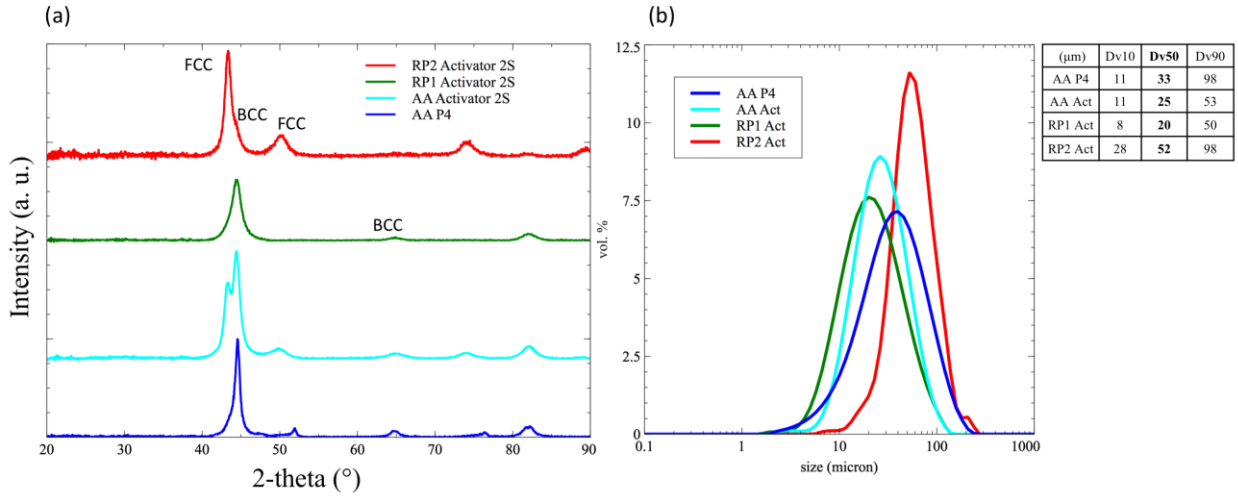

Figure 1: (a) XRD patterns of AlCoCrFeNi milled with different parameters. (b) Particle size distributions of the corresponding powders.

Table 3 summarizes the measured and evaluated lattice parameter of the FCC phase after milling. Activator 2S milling leads to a significant increase. The solid solution is actually formed during milling. Interestingly enough, the predicted value is exceeded experimentally. The FCC solid solution could have an Al content superior to 20 at. %.

Å	AA P4	AA Act	RP1 Act	RP2 Act	Vegard
a_0 FCC	3.53	3.66	-	3.64	3.63

Table 3: Measured and evaluated lattice parameters of the FCC phase after milling for different powders.

The initial powder size seems to influence the final structure resulting from milling. In addition, a stoichiometry modification could also alter the “thermo-mechanical equilibrium”. Table 4 summarizes the actual stoichiometry obtained after milling. Several EDS measurements were performed directly on the milled powder surfaces. The AA powder milled in the Activator exhibits a slight Cr deficit. The milled RP1 powder composition is significantly altered. The Fe content increases whereas the Ni content decreases. The Fe surplus likely originates in the milling media (balls and walls). There is, however, no clear explanation for the Ni loss. From a thermodynamic perspective, the final crystalline structure obtained is coherent with the stoichiometry. Indeed, Fe acts as BCC stabilizer whereas Ni is likely to acts as FCC stabilizer (see Chapter I). The results obtained for the RP2 are also coherent with the stoichiometry modification as there is a loss of Al. In this case, Al could adhere in significant amounts to the wall because of the small initial size of its powder particles (since RP2 exhibits the smallest initial particles of Al).

at. %	Al	Co	Cr	Fe	Ni
AA P4	20	20	19	20	21
AA Act	20	21	18	21	20
RP1 Act	21	19	20	24	16
RP2 Act	17	20	19	22	22

Table 4: Summary of the actual stoichiometry obtained after milling.

Considering the above results, the combined influence of several factors (such as initial powder size and stoichiometry modification) appears to determine the final crystalline state after milling. In what follows, the present work will focus on the RP1 milled in Activator 2S. Indeed, this single-phase BCC powder is the closest to the mechanically alloyed AlCoCrFeNi powder depicted in the literature (see Ji *et al.* in Chapter I for instance).

Figure 2 depicts the SEM picture (BSE mode) and the EDS mapping of the milled "AA P4" powders and the milled "RP1 Act" cross sections. The pictures of the AA show a composite, lamellar microstructure. The lamellae are approximately 100 nm thick. Five contrasts are still observable; the solid solution is not formed.
The pictures of the RP1 show very good homogeneity with a slight problem in the case of Fe. This issue has already been observed in milled powders with Activator-2S and may come from contamination by the balls and walls. EDS point analysis far from the concentrated Fe zone gives a composition of Al 20.4 at. %, Co 20.0%, Cr 20.9%, Fe 20.9% and Ni 17.9%. This last characterization of the milled powders confirms that the AA state corresponds to the mechanical activated state whereas the RP1 corresponds to a completely mechanically alloyed powder of similar composition.

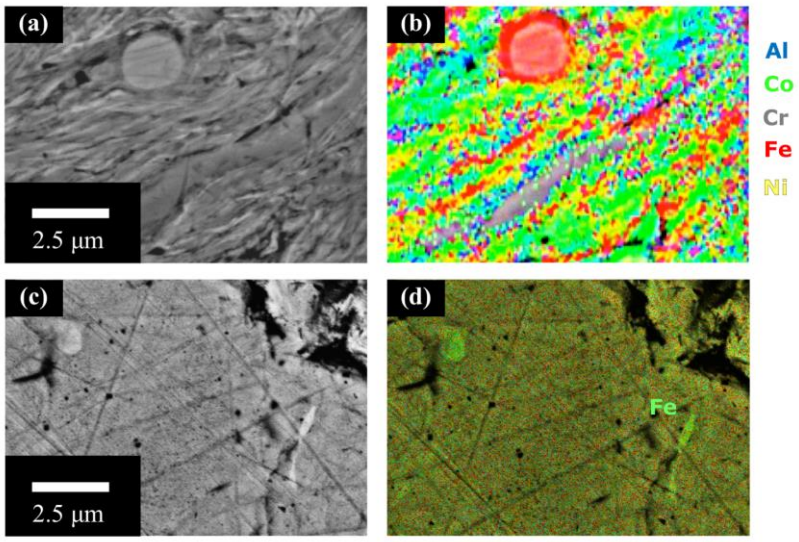

Figure 2: SEM pictures (BSE mode) and the EDX mappings of cross sections of milled powders: (a,b) AA powders after mechanical activation and (c,d) RP1 after mechanical alloying.

3.2. Powder evolution with temperature

HT-XRD results on RP1 are presented in Figure 3a. They show that the single BCC phase is stable up to 1000°C. From this temperature, an FCC and an intermetallic σ phase begin to form. Then the 2h annealing at 1000°C leads to the partial dissolution of σ into the FCC phase. After cooling, three phases remain: FCC, BCC and σ.
HT-XRD results on AA are represented in Figure 3b. Note that an FCC phase is already present before heating the sample (see Figure 1a). However, the graphite window and sensitivity inherent in the HT-XRD device prevents its correct visualization. Compared to RP1, the FCC phase and σ become apparent at much lower temperatures. In addition, σ clearly starts to dissolve at 1000°C. We can suggest that σ easily nucleates from the almost pure Cr layers observed in mechanically activated AA powder. This specific formation mechanism could lead to a specific σ stoichiometry. The resulting σ phase may be less stable at higher temperatures. The stoichiometry modification occurring during the milling might also explain this behavior. In addition, heating seems to lead to a progressive disappearance of the BCC peaks. Unfortunately, the scan window does not allow us to evaluate the formation of B2 during annealing.

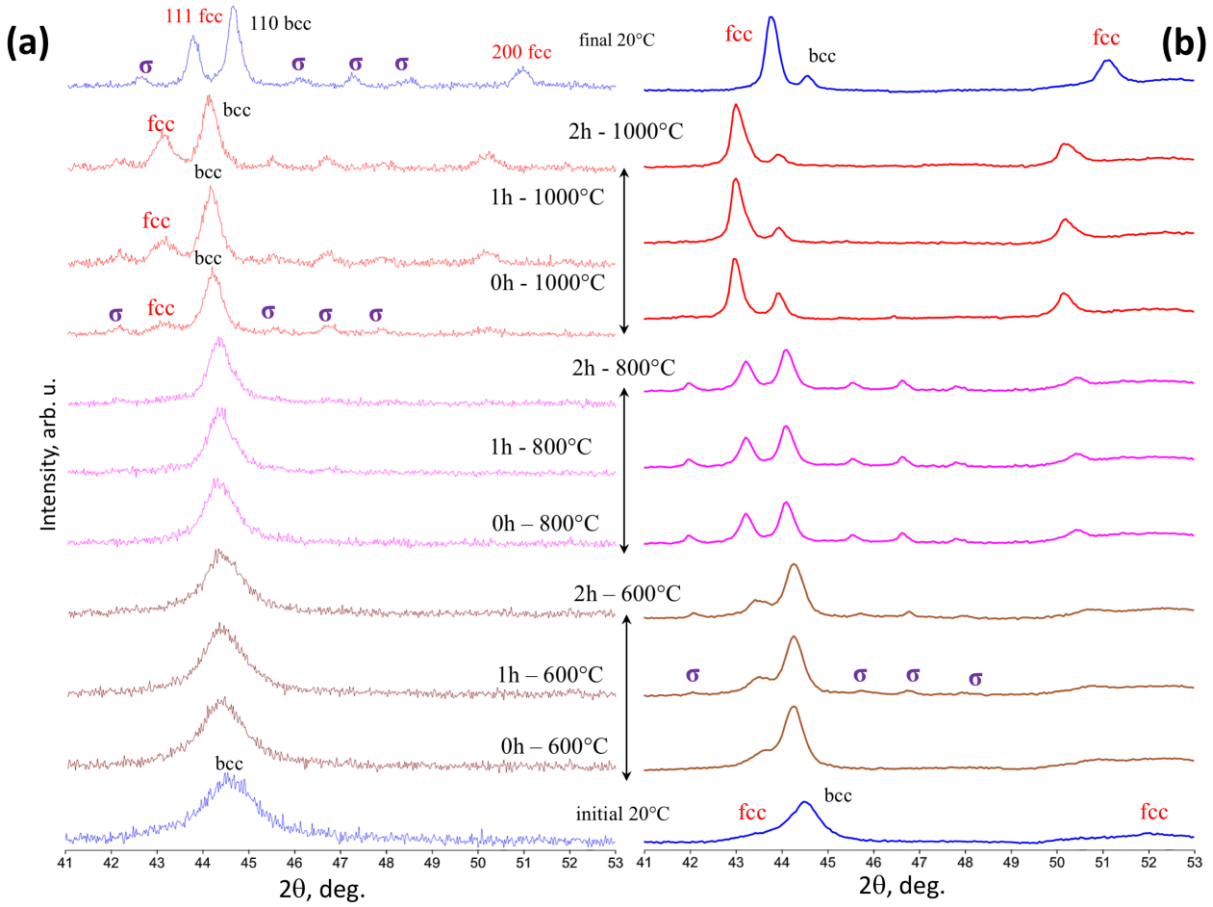

Figure 3: High temperature XRD patterns for different milled powders: (a) RP1 in Activator 2S, (b) AA in Pulverisette 4.

Figure 4 displays the shrinking curves of the two considered powders. The final sintering temperature of the RP1 is evaluated at 980°C whereas the sintering temperature of the AA

powder is close to 1070°C. This result is coherent with the characteristics of the powders since the RP1 agglomerates are smaller and have a higher concentration of defects.

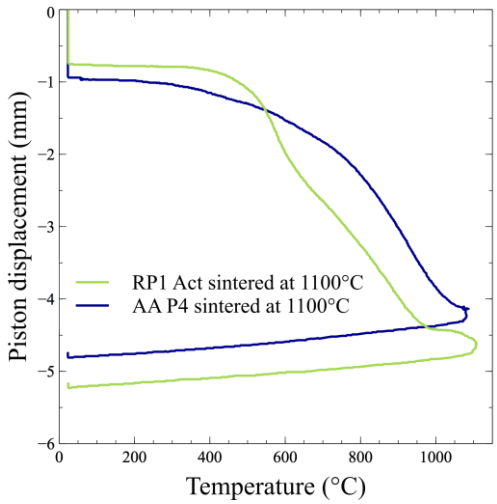

Figure 4: Shrinking curves corresponding to the two milled powders.

The XRD results of the sintered samples are presented in Figure 5. Several observations can be made:

- The RP1 powder also exhibits an FCC phase after sintering. However, the FCC/BCC ratio is not identical in the two sintered samples. In addition, as compared to annealed AA powder in HT-XRD, the amount of BCC formed seems considerably higher in the case of the sintered sample. This observation may be explained by the influence of pressure or by the additional 100°C of the SPS cycle.
- In both cases, the BCC phase seems ordered (at least partly). A cubic (100) peak reflection appears in the three diffractograms near 31° 2-theta. However, the close-up reveals that the amount of B2 is much larger in the case of mechanically activated AA agglomerates.
- The peaks of the RP1 sintered samples are much broader than those of the AA sintered sample. This finding can be explained by crystallite size, which is likely smaller in the case of the RP1 sintered samples. Rietveld analysis revealed that the crystallite size was around 100 nm in the AA sintered sample.
- Cr-rich σ is formed in a large amount for the RP1 powder, whereas there are only traces of it in the case of the AA powders.
- The formation of $Cr_{23}C_6$ is noticeable in the case of the RP1 powder. The carbon surplus could come from the Russian Fe powders whose purity is likely to be mediocre. Carbon could also come from the milling media made of steel or from the graphite die.

Chapter V demonstrated that a significant amount of Cr oxide is formed in this AA sample. This may also explain the formation of Cr-related phases in the case of the RP1 powder.

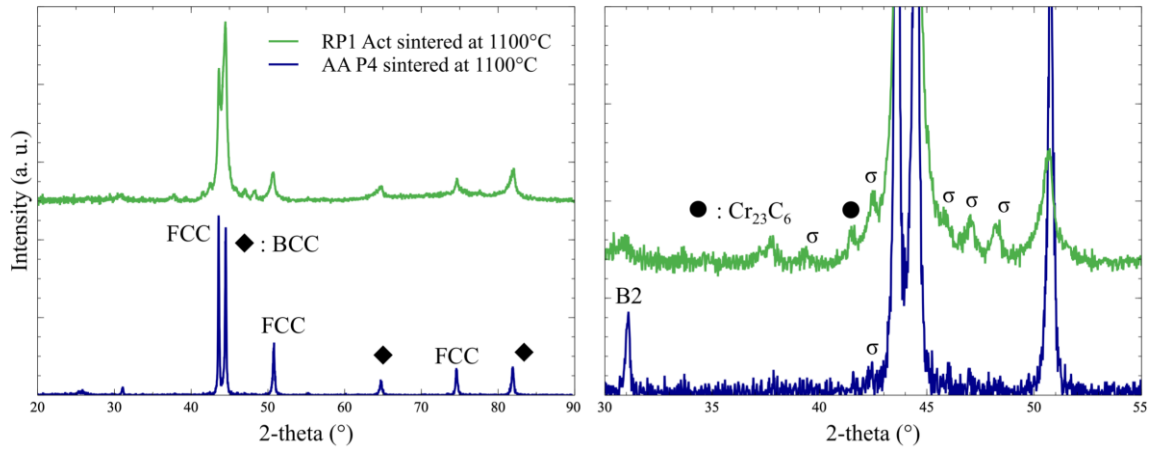

Figure 5: (Left) XRD of sintered samples. (Right) Close-up of the corresponding diffractograms.

Figure 6a depicts the microstructure of the RP sintered sample at 1100°C. It is not imbricated but rather thin. Large EDS measurements of the RP sintered samples show a general depletion in Al and Ni. The average composition of a few zones of several tens of microns is Al 18.2 at. %, Co 22.1%, Cr 19.5%, Fe 22.7% and Ni 17.5%. While Ni depletion was already observed in the milled RP1 powder, the Al depletion is intriguing. $Cr_{23}C_6$ phases (most of the black zones) reach micron-scale in the RP1 sintered sample. Two main contrasts are seen in (a). The brightest one corresponds to an Al, Ni-poor Fe-rich version of the equimolar phase. The average composition over 10 points is Al 9.3 at. %, Co 25.1%, Cr 20.1%, Fe 32.3% and Ni 13.2%. This composition trend is characteristic of the FCC phase. The surface ratio of the dark/bright zones is around 85/15 and thus agree with the XRD general relative intensity of the BCC/FCC peaks. The sigma phase, in addition to being in the form of traces, seems to have a BSE contrast which is very close to that of the BCC phase. Hence, the composition of sigma is not precisely evaluated by means of EDS.

Figure 6b shows the unique microstructure obtained with reactive sintering. The microstructure is imbricated and coarser than the microstructure of sintered RP. The average width of a region is around 200 nm. Two main contrasts are observed. EDS and EBSD analyses reveal that the bright one corresponds to a Fe-Cr rich FCC phase and the dark one corresponds to an Al-Ni rich BCC phase. The volume ratio is estimated through different characterization techniques to be approximately 50-50 %. The presence of black precipitates is also noticeable. They are mostly oxides (as identified by the APT, presented in Chapter V).

On another note, the hardness of the sintered RP sample is 753 ± 24 HV whereas it is 610 ± 43 for the sintered AA sample. This difference can be easily explained by the large amount of carbides and sigma phase in the RP1 sample, as well as by the small size of the crystallites.

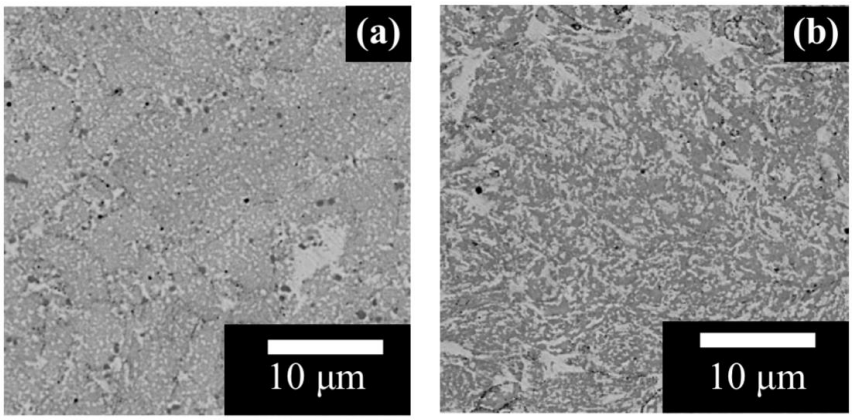

Figure 6: SEM pictures (BSE mode) of RP sintered at 1100°C (a) and AA sintered at 1100°C (b).

The DSC results are presented in Figure 7. The annealing temperatures used in the HT-XRD: 600°C, 800°C and 1000°C are also visualized. The mass change during the TG/DSC analysis is close to zero; the reducing atmosphere has no effect on the oxides of the two samples.

There are 3 peaks of interest: peak A, centered around 670°C, peak B centered around 640°C and peak C centered around 1000°C. Viewed in light of previous results, especially the HT-XRD patterns, it remains difficult to identify the phenomena corresponding to the three peaks. The wide endothermic peak A is specific to the AA powder. It could result from the melting of the non-dissolved, almost amorphous Aluminum. Note that peak A may also correspond to two peaks since an inflexion point is noticeable at 600°C. Peak B only appears in the RP1 system; hence, it could be linked to the FCC or to carbide formation. However, such explanations seem unlikely since these two phases appear at 1000°C in the HT-XRD. Hence, peak B could correspond to B2 formation. Indeed, B2-NiAl is known to form at around this temperature in the case of activated powders. Phenomena not observable in the XRD could also be responsible for this peak. Indeed, spinodal decomposition may occur during the sintering of RP1 and spinodal decomposition is often indicated by an exothermic peak. Peak C is surprisingly identical in the two powders. It could be linked to sigma since ThermoCalc calculations give the definitive dissolution of sigma at this exact temperature. However, the area of peak C is the same for AA and RP1 while the measured amount of sigma in these two samples seems very different. Several kinds of sigma could form during heating, corresponding to different nucleation mechanisms and/or different stoichiometries. Peak C might then correspond to the dissolution of one kind of sigma. DSC analyses are, in any case, a promising tool to further investigate the behavior of mechanical activated powders. The present study goal was to provide preliminary insights into the matter.

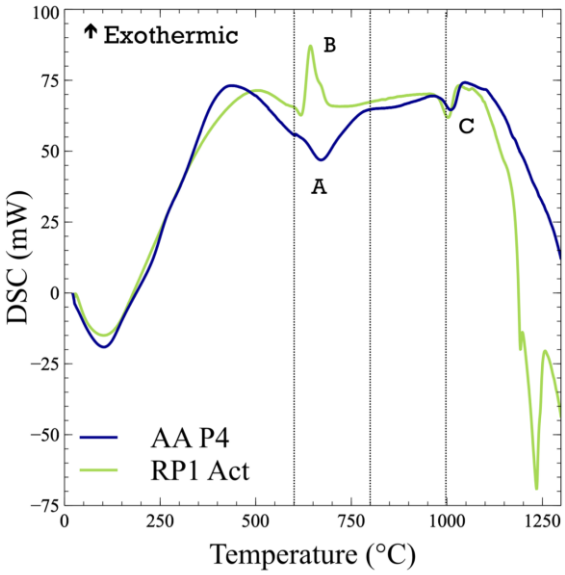

Figure 7: DSC curves of the RP1 and of the AA powders.

4. Conclusion

In the present study, we demonstrated that the crystalline structure obtained after mechanical milling depended on several factors in addition to the initial chemical composition. The initial particle size of elemental powders seemingly plays a significant role in the matter. Preliminary insights relating to the different temperature-induced behaviors of mechanically activated and mechanically alloyed powders have been presented.
In the case of mechanically activated agglomerates:

- Sigma phase formation seems to be limited at the sintering temperature,
- B2 formation seems to be promoted,
- Carbide formation might be prevented,
- The significant formation of nano-oxides has been thoroughly demonstrated; their influence has also been investigated (see Chapter V).

Unfortunately, the amount of oxygen was not evaluated in the case of mechanically alloyed powder. However, the initial purity of the various powders has to be thoroughly assessed in order to further investigate the topic.
Altogether, even if the presented comparison is not ideal, the present study confirms the relevance of mechanical activation as an alternative way to produce High Entropy Alloys.

The present study allows us to reflect critically on the results obtained in Chapter VI concerning the equimolar AlCoCrFeNi mechanically alloyed powder. It is mandatory to thoroughly evaluate the actual stoichiometry after milling. Understanding composition modification during milling, especially the lack of Ni, is essential. The quantification of the carbon and the oxygen content at each step of the process is also required to completely evaluate the thermal stability of the alloys prepared by powder metallurgy.

Appendix II: Influence of milling and sintering scale change

1. Introduction

Transitioning from a laboratory scale sample to an industrial sample is of great importance. The evaluation of each modification resulting from this transition is essential in assessing the process. In addition, certain technical milling parameters seem to be improvable in order to obtain better milling yield and more reproducible results. In the present work, both the milling jars and sintering tools were used to produce 30 mm sintered samples by SPS (from 10mm previously). The actual intent of this study was also to be able to produce larger samples in order to investigate properties such as thermal stability and oxidation behavior. Indeed, larger samples can be cut into pieces and the comparisons between samples from the same initial sintered bulk are particularly relevant.

2. Materials and methods

Both milling jars of 250 mL (F250) and 80 mL (F80) were used. They differ in one main aspect: the 250 mL jars have a similar diameter but are considerably taller (see Fig. 1).
For 80 mL jars and in the main chapters of this work, the ratio of the volume occupied by the balls over the total volume of the jar was set as indicated by the mill manufacturer (Fritsch) and corresponds to ~22%. However, the ball motion seemed hindered in some cases not reported in the present manuscript. Indeed, the height of the 80 mL jars corresponds to that of 2 or 3 stacked milling balls of 15 mm. Consequently, 10 mm balls were preferentially used instead of 15 mm balls in the case of 250 mL jars. Hence, ball movement is likely different in the two cases. Most of the milling parameters remained the same: 250/-250/7:1/no PCA. Two settings of pauses were compared: 4x7 corresponds to 4 millings of 7h separated by 2h pauses, 28x1 corresponds to 28 millings of 1h separated by 30 min pauses.
Note that the Chromium powder used in the following appendix was not described in the previous chapters. In fact, commercial powder exhibiting similar size particles as the pre-milled Cr was found to lead to identical results (XRD patterns and particle size distributions). Hence, such commercial Cr powder is used here (particle size < 45 μm).

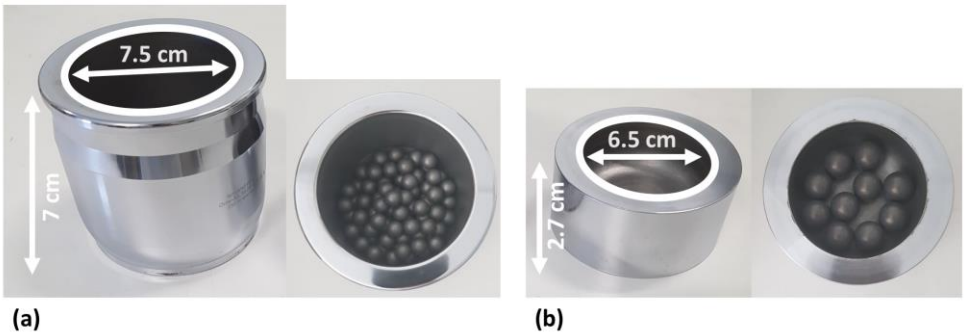

Figure 1: Top and side pictures of 250 mL (a) and 80 mL jars (b) with their dimensions (maximal inner height and inner diameter).

The sintering parameters are identical to those reported in Chapter IV:
1100°C/50°C.min^{-1}/80MPa/No holding time.
Both 10 mm inner-diameter and 30 mm inner-diameter graphite dies were used. In both of them, a hole of 1.2 mm was drilled in order to measure the temperature as close to the sample as possible by means of a thermocouple K (see [1] for instance).

3. Results and discussion

3.1. Milling

Figure 2 shows that all the powders exhibit a combination of FCC and BCC phases after milling, similar to the findings summarized in Chapter V. The lattice parameters measured from these diffractograms do not significantly differ from our previous results, i.e. they are close to elemental lattice parameters. The width of the main peak FCC (111) and BCC (110)) is greater in the case of the milling performed in the 250 mL jar. This finding is likely explained by a smaller crystallite size. The asymmetry of the (200) FCC peaks was evaluated by means of the

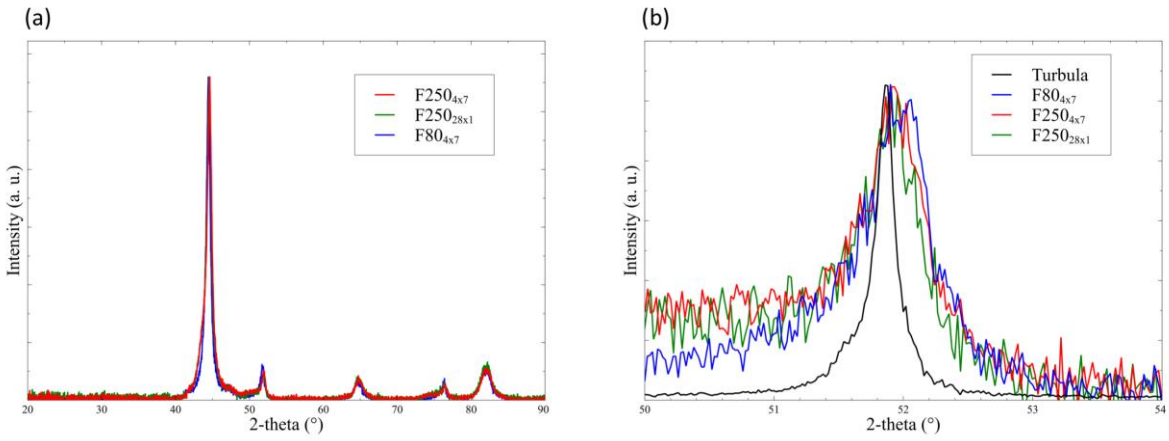

Figure 2 : (a) XRD patterns of the AlCoCrFeNi powder after complete milling cycles. (b) Close up view of the normalized (200) peak of the FCC to show asymmetry. Note that the normalization concerns intensity and position.

moment coefficient of skewness and summarized in Table 1. For the different milling parameters, the skewness is very similar for the considered peak.

Sample	Skewness
Turbula	2.2
$F80_{4x7}$	0.72
$F250_{4x7}$	0.75
$F250_{28x1}$	0.73

Table 1: Asymmetry evaluation for different milled powders.

Figures 3a and 3b summarize the data obtained by means of laser granulometry on the different milled powders. Their particle size distributions are very similar.
Figure 3d shows the cross section of the $F250_{28x1}$ powder. The picture confirmed that mechanical alloying is still not achieved: lamellae of different contrasts are still noticeable. The milling efficiency could be evaluated by the decrease in crystallite size or by the progress in chemical mixing, but it is hardly quantifiable. Hence, in the present work, there was no attempt made to precisely quantify milling efficiency. Nevertheless, we can conclude from the diffractograms and the cross section that the milling in the 250 mL jars and with 10 mm balls seems to be slightly more efficient that the previous milling but that the main features, including the asymmetry, particle size distribution and lamellar microstructure, are present in both cases.

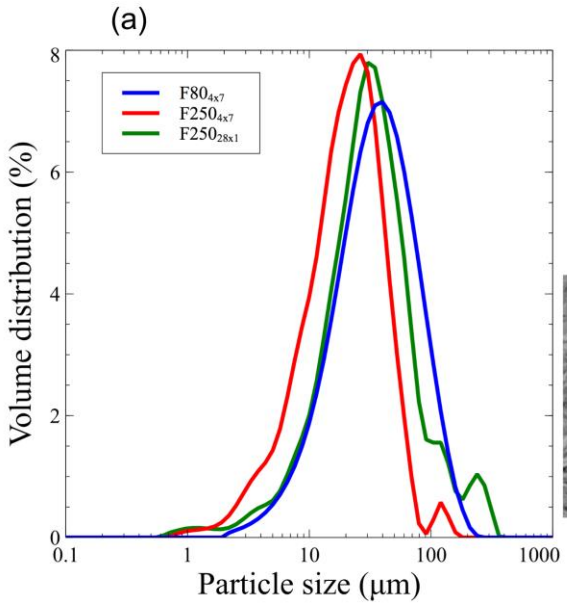

(b)

Size (µm)	$F80_{4x7}$	$F250_{4x7}$	$F250_{28x1}$
Dv10	11	6	10
Dv50	**33**	**19**	**29**
Dv90	98	40	83

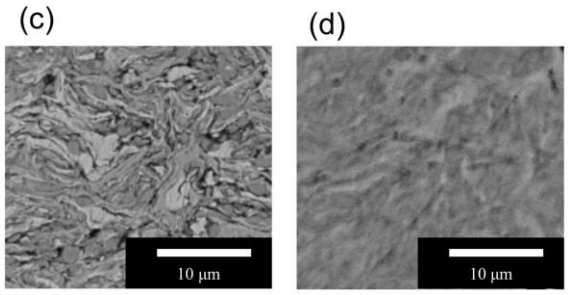

Figure 3: (a) Powder particle size distributions after different millings, (b) Summary of powder particle distribution data. (c) SEM picture (BSE) of cross section of the $F80_{4x7}$ milled powder. (d) SEM picture (BSE) of cross section of the $F250_{28x1}$ milled powder. Note that the two SEM pictures were obtained by two different SEM devices.

In fact, the main difference between $F250_{4x7}$ and $F250_{28x1}$ is the milling yield. In the case of the 4x7 parameter, nearly 60% of the powders strongly adhere to the wall of the jar (but not significantly to the balls), whereas less than 30% of the powders do so in the case of $F250_{28x1}$. This "cold-welded" layer is usually removed by a cleaning step consisting of a short milling with sand. In what follows, the present study focuses on the $F250_{28x1}$ milling since the milling yield is much better. Nonetheless, the characterization of this layer provides valuable information concerning the progress of the milling. Fig. 4 depicts a SEM (BSE) picture and an EDX profile of the layer resulting from the $F250_{4x7}$ milling. The microstructure of the layer seems to exhibit a progressive transformation: from a granular microstructure (similar to the one obtained after the M1 milling described in Chapter IV) to a lamellar microstructure. Each point of the profile is obtained by averaging the chemical composition of several regions alongside the line displayed in Fig. 4a. Al seems to preferentially adhere to the wall, whereas Ni seems to be missing from the first 400 µm. This observation highlights once again the crucial

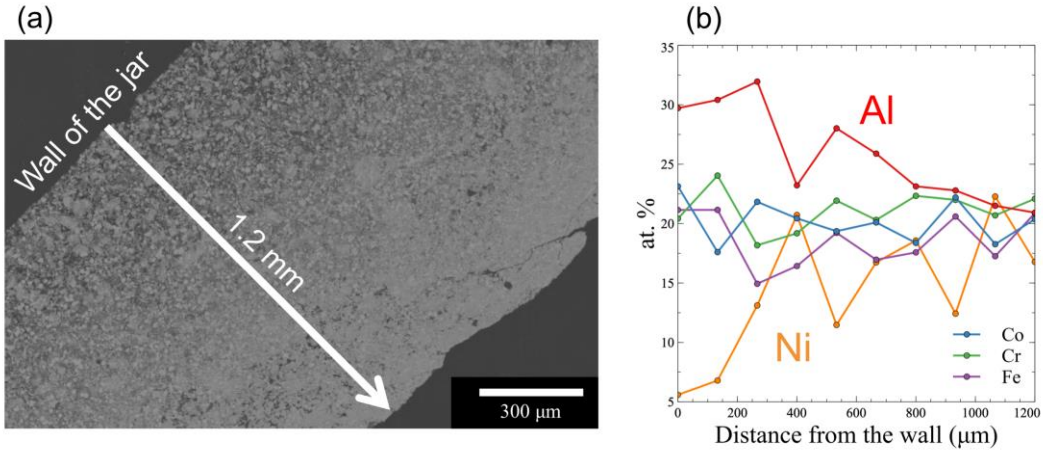

Figure 4: (a) SEM picture of a cold-welded layer resulting from the $F250_{4x7}$ milling. (b) EDX profile alongside the line displayed in the picture at left.

role of Al during milling, most likely acting as some sort of binder. Hence, in the case of significant cold-welding to the wall, special attention must be paid to the actual stoichiometry of the agglomerates after milling.

3.2. Sintering

Figure 5 depicts the shrinking curves of the various milled powders and shows the influence of the dies used. For the sake of comparison, the shrinking curves have been normalised: their initial displacement has been set to -1 mm. Their actual initial displacements are summarised in Table 2. The comparison between the two dies is not particularly relevant, but note that the powder which seems to be the most effiencetly milled is more compacted than the other. First, the influence of the milling parameters seems to be important. In the case of $F80_{4x7}$, the final sintering temperature (corresponding to the moment where the curve reaches a horizontal plateau) is harldly attained, whereas it is clearly exceeded in the case of the other sintering in D10. The density of the F80 milled sample is lower than that of the others: 6.7 versus 7.0 g/cm^3.

Despite this slight difference in density, the hardness of the samples is very similar: 610 versus 615 HV.

Secondly, the influence of the sintering die seems to be minor, the actual density of both D10 and D30 samples being close to 7.0 g/cm^3 and their sintering temperatures similar (1050 for D30 and 1070 for D10).

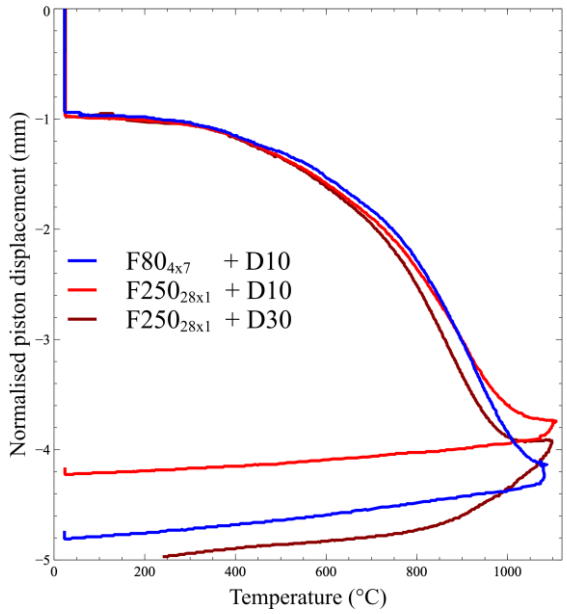

Figure 5: Shrinking curves of different milled powders and dies used. D10 corresponds to 10 mm-graphite dies.

Sample	Initial displacement (mm)
F80$_{4x7}$ + D10	-0.67
F250$_{28x1}$ + D10	-0.94
F250$_{28x1}$ + D30	-3.32

Table 2: Initial piston displacement for the different milled powders and dies used.

The XRD results of the sintered samples are displayed in Fig. 6. The phases formed are the same. However, the relative intensities are different, suggesting a different FCC/BCC ratio. The lattice parameters measured from the diffractograms are similar from one sample to the other (FCC: 3.60 Å, BCC: 2.88 Å) and similar to our previously reported results (see Chapter IV). On the other hand, the crystallite sizes, evaluated from Rietveld refinement, are very different: over 100 nm for the F80 milling versus approximately 20 nm for the F250 milling. This observation supports the suggestion of a more efficient milling with the F250 parameters.

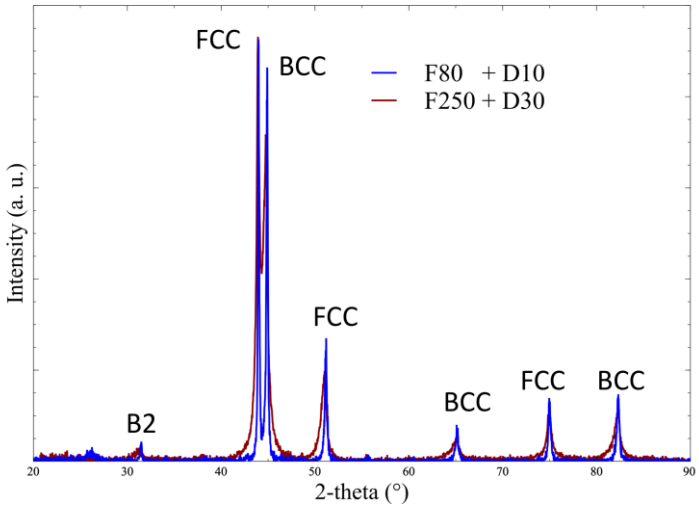

Figure 6: XRD patterns of the sintered samples resulting from different milling parameters.

SEM pictures with BSE are depicted in Fig. 7. First, EDS measurements indicated the formation of the sigma phase as some regions exhibited a composition close to the one measured in the previous chapters (IV and V). Next, the ratio BCC/FCC was measured by means of image processing. Ten distinct pictures were measured in order to evaluate this ratio. Note that the sigma phase has a contrast which is identical to that of the BCC phase, hence the measured ratio corresponds to (BCC+sigma)/FCC. The ratio is close to 50/50 in the case of F80 whereas it is close to 70/30 in the case of F250. This difference might be explained by the more efficient milling and the disappearance of local micro-heterogeneity (as suggested in Chapter IV). Note that the 70/30 ratio is closer to the ratio calculated by Thermo-Calc (almost no FCC with TCHEA1). However, at first glance, the relative intensity evolution of the XRD peaks is not coherent with the ratio obtained by image processing. This discrepancy may find an explanation in the reduced reliability of image processing in the case of such a tortuous microstructure, or in a possible effect of texture resulting from the uni-axial sintering (not investigated in the present work). Lastly, two kinds of regions are noticeable in Fig. 7b; indeed, in region A, the two phases are much more loosely imbricated than on the right. However, the B region is also not perfectly identical to the imbricated microstructure reported in the previous chapters. The

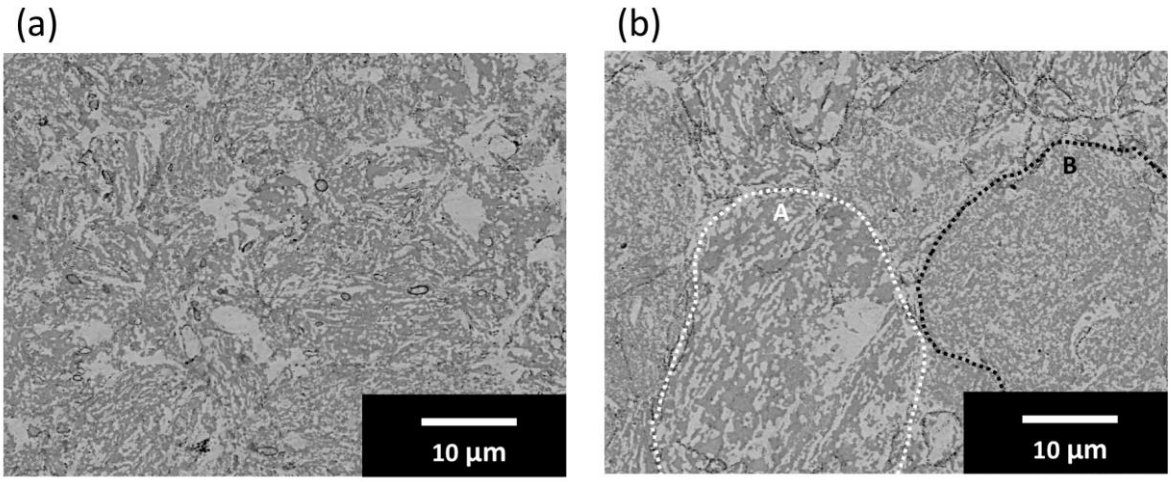

Figure 7 : BSE SEM pictures of sintered samples, $F80_{4x7}$ + D10 (a) and $F250_{28x1}$ + D30 (b). Sigma and BCC phases appear in dark grey and FCC appears in light grey.

light regions corresponding mostly to the FCC phase seem to be smaller on average. This is likely linked to the decrease in crystallite size. The microstructure depicted in Fig. 7b, and its origin in particular, are discussed in more detail in Appendix II.

4. Conclusion

To conclude, changing the considered milling parameters (milling jar and balls) has a noticeable impact on the final sample, whereas changing the size of the sintering dies has only minor consequences. Changing milling jars and milling balls and introducing more frequent pauses during milling led to a slightly more efficient milling, in particular a decrease in crystallite size. The best compromise is a large jar with small balls, probably promoting more mobility of the balls, and frequent pauses (decreasing the cold welding). Having said that, the main features of mechanical activation remained: BCC+FCC agglomerates, asymmetry and a lamellar microstructure. After sintering, the phases formed are still BCC (B2 and/or A2) + FCC + Sigma. The evaluation of the amount of oxides and carbides was not presented in the present appendix but seems to be similar to what was reported in Chapter V. Hence, only the thinness of the microstructure and the phase ratio seem to evolve as a result of the present change of scale.

References

[1] L. Minier, S. Le Gallet, Yu. Grin, F. Bernard, A comparative study of nickel and alumina sintering using spark plasma sintering (SPS), Mater. Chem. Phys. 134 (2012) 243–253. https://doi.org/10.1016/j.matchemphys.2012.02.059.

Appendix III: Influence of the initial elemental particle size on the milling progress

1. Introduction

In the results reported in the main chapters of the present work, the powders were milled for 28h. This duration was initially chosen in order to periodically draw off samples of powder and to conform to parameters found in the literature. As 7h corresponds to one workday, the duration 4x7h was initially chosen. However, in order to optimize the milling parameters, it is important to better understand the progress of this milling. For instance, the dissolution speeds of Al and Co, the steps in lamellar microstructure formation and agglomerate size evolution during milling are three topics worthy of study. In addition, the influence of the particle size of Al, Fe and Ni in the initial powder has been investigated; indeed, certain results presented in Appendix I led us to believe that this very parameter had a significant influence on the phases resulting from milling. The initial question was: Will initial particle size of the powder favor one final structure? For instance, if the Ni particle size is much larger than the others, will the phase remaining after milling be single FCC?

2. Materials and Methods

In the following appendix, the milling parameters correspond to the $F250_{28x1}$ parameters presented in the previous appendix (250/-250 rpm, 28x1h duration, 250 mL jars, commercial Chromium powder in which particle size is inferior to 45 μm). At 4h and 8h of milling, the jars were opened in a glove box in order to collect powder samples. Approximately 3-4g were collected. In order to retain the 7:1 BPR, some balls were also removed from the system. At 4h, there was almost no powder stuck on the wall or on the balls, whereas a thin layer of powder adhered to the wall at 8h. However, these intermediate quantities were never measured.
At the end of the process, the system is as depicted in Figure 1. There is a considerable amount of powder stuck to the walls, especially at the bottom of the jars. There is some “free” powder at the bottom which is easily withdrawn (noted 28h f). Most of the stuck-on powder was withdrawn “mechanically” by means of a hammer and a chisel (noted 28h s). The remaining powder was collected in laboratory air after a 30 min milling with ethanol (noted 28h w). Note that the stuck-on and wet powders do not correspond to the cold-welded layer presented in Appendix I (obtained in 4x7) but to a layer which adheres far less strongly. The stuck-on powder was then blended in a Turbula equipped with a dozen balls over 2h in order to break the large metallic chunks back down into micronic powders. As compared to the millings

presented in the previous chapters and in Appendix I, the amount of free powders was more significant. As a consequence, the distinction between free and stuck-on powders is made in the present appendix whereas these two kinds of powders were collected together and not distinguished in the previous results. Note that we realized progressively, over the course of the present study that these two kinds were, in fact, different. Hence, certain analyses and comparisons are missing.

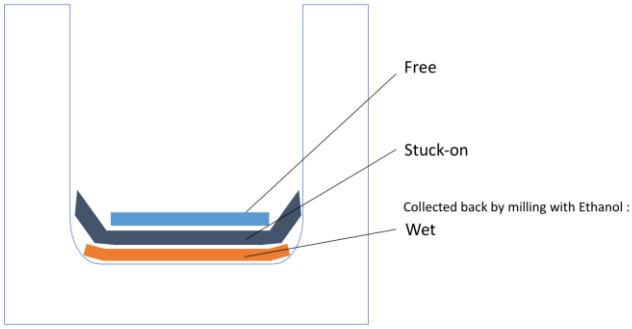

Figure 1: Schematic representation of the final state of the system after milling.

In the results reported in the present appendix, the sintering parameters are 1100°C, 50°C/min, 80 MPa, no dwell time, tools diameter 10 mm (except where otherwise stated).

3. Results

3.1. Milling progress in the case of equimolar AlCoCrFeNi

3.1.1. Milling of equimolar Al-Co-Cr-Fe-Ni

The XRD results concerning the milling progress of the equimolar AlCoCrFeNi system are presented in Fig. 2a. Similarly to what was reported in the Chapters above, the Al and Co peaks disappeared progressively. Co seems to dissolve more slowly than Al as evidenced by the fact that the Co peak around 47° 2-theta is still noticeable in the 28h s powder. Al dissolution seems to occur mainly before 4h of milling since the area of the peak had already decreased between 0h and 4h. The separate examination of free and stuck-on powders revealed that the free powder was much more mixed than the stuck-on powder. Indeed, we noted a strong shift in the FCC peak, the lattice parameter of the 28h f powder is evaluated at a0 = 3.63 Å, whereas that of the 28 g powder remains close to a0 = 3.52 Å. The widths of the peaks, the FCC peaks in particular, are very broad. Broad peaks indicate a refined microstructure of nanometric crystallites, close to an amorphous structure. One can imagine the complete disappearance of the FCC peaks if the milling had lasted longer.

Fig. 2b corresponds to the particle size distributions of the different milled powders. Starting from elemental powders smaller than 45 µm, the Dv50 of the powder milled 4h reached 157 µm, indicating a first agglomeration phenomenon. Afterward, the Dv50 decreased until reaching a limit value of 23 µm, which is identical for both free and stuck-on powders. Dn50 corresponds to Dv50 but in number instead of volume. The small value of Dn50 for the milled powders indicates that there is a significant number of sub-micronic powder particles. However, this population was not characterized by means of SEM. It could correspond to chunks of pure

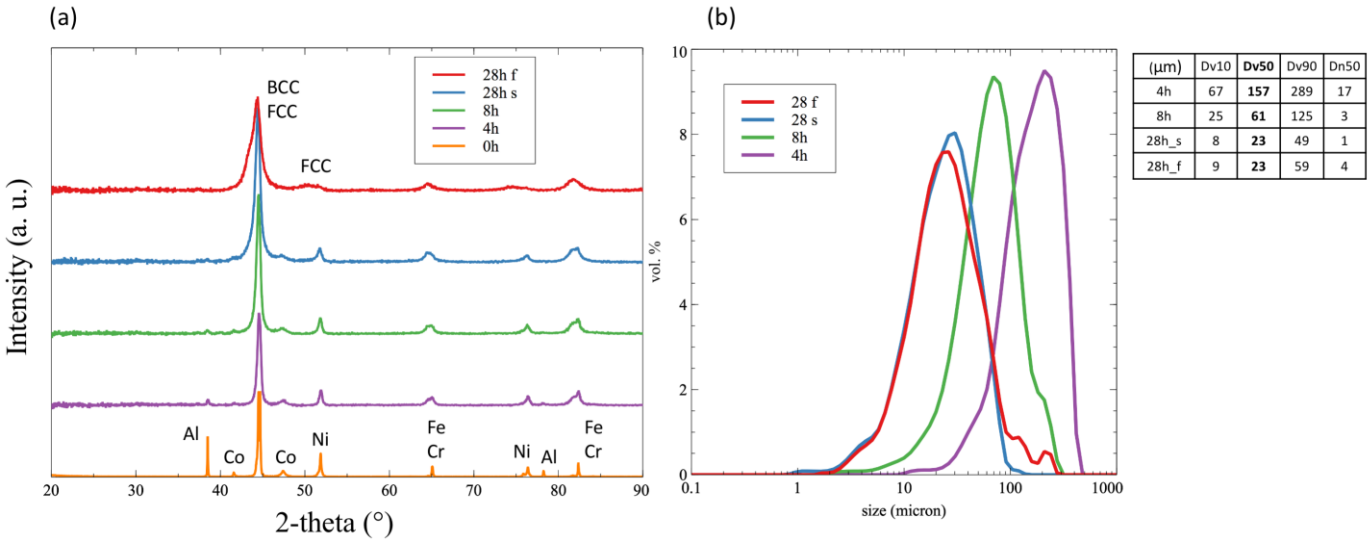

(µm)	Dv10	**Dv50**	Dv90	Dn50
4h	67	**157**	289	17
8h	25	**61**	125	3
28h_s	8	**23**	49	1
28h_f	9	**23**	59	4

Figure 2: (a) XRD patterns of milled powders. 0h corresponds to Turbula blending. (b) Particle size distributions of milled powders. f stands for free, s stands for stuck-on (see Materials and Methods of this appendix).

elements as well as agglomerates identical to micronic ones.

Fig. 3 presents the cross-sections of the different milled powders. Unfortunately, the cross section of the powder milled over 4h was not characterized. Several observations can be formulated from these results:

- 8h of milling already leads to thin lamellae.
- The chemical mixing seems to be better in the case of 28h s as compared to 8h. However, judging from the SEM pictures alone, this is not obvious. It would be interesting to quantify the progress of chemical mixing with a specific indicator such as layer size (inspired by the work of Kang *et al.* presented in the introduction to Chapter V as [27]) or a measure based on the grey level obtained by means of BSE.
- Chemical mixing is almost complete at 28h f. In fact, complete mechanical alloying seems to have been reached in this case.

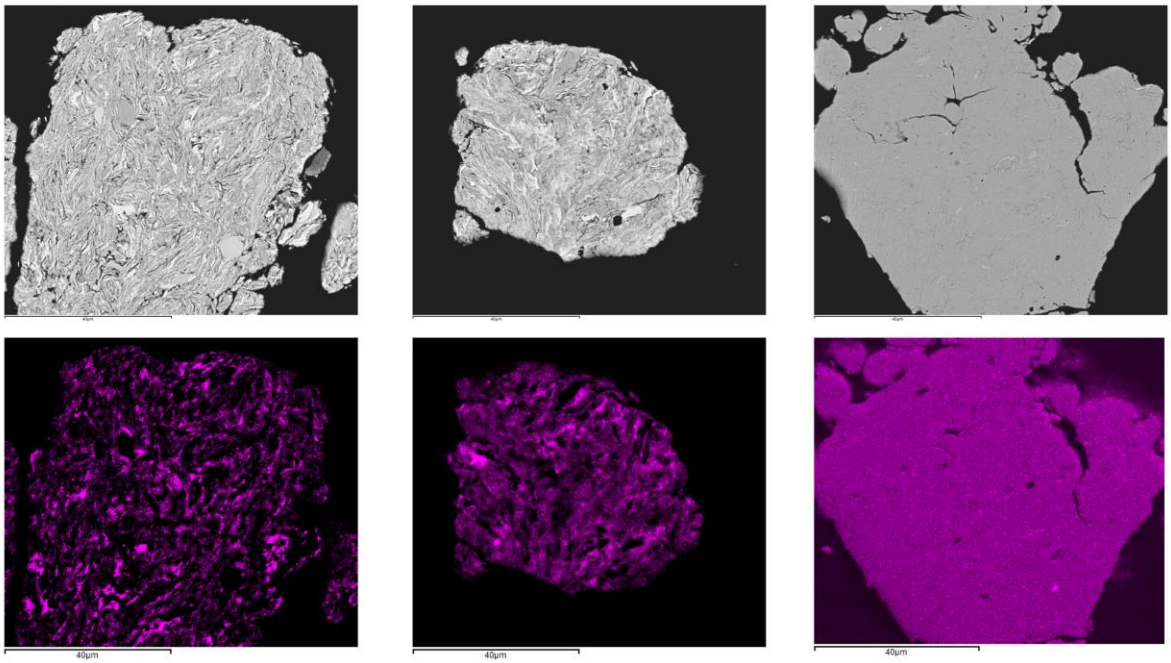

Figure 3: Cross sections of milled AlCoCrFeNi powders. From left to right: 8h, 28h s, 28h f. Corresponding elemental mappings of Aluminum.

3.1.2. Sintering of equimolar AlCoCrFeNi

Now that we have seen that powders milled in 250 mL jars exhibited inhomogeneous agglomerates (when comparing free powder and stuck-on powder); the microstructure obtained after milling and sintering can be discussed. Figure 4 shows BSE SEM pictures of the sintered sample. Three different microstructures are noticeable. A: “finely imbricated”, B: “coarsely imbricated” and C: “intergranular”.

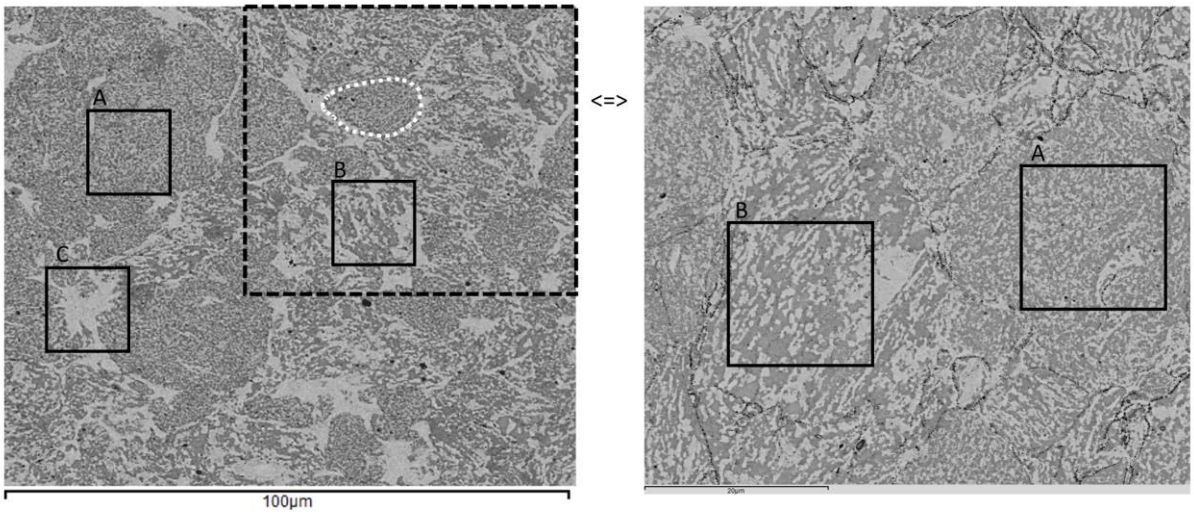

Figure 4: BSE SEM pictures of AlCoCrFeNi milled 28h s+f and then sintered at 1100°C (30 mm tools). The purpose of the dashed square is to visualize the scales used in the two pictures.

The A and B microstructures correspond to the main initial agglomerates, as shown for instance in the region circled in white. Hence, the A microstructure may result directly from the "free powder".
The B microstructure may result from the "stuck-on powder" since it is coarser than the A microstructure. However, considering the ratio of free or stuck-on powder over total powder, the amount of A should be lower and B higher. Certain preliminary observations seem to show that the B microstructure results from the formation of sigma but this suggestion would require further analyses. Indeed, most of the sigma phase identified by EDS measurements was found in the B microstructure but it is difficult to validate this hypothesis with BSE SEM since the BCC phase and the sigma phase have identical grey levels.
The global compositions of these two microstructures (A and B) are very similar; indeed, EDS measurements of several squares of approximately 5 x 5 μm indicate equimolar stoichiometry.
The C microstructure is a Cr,Fe-rich FCC phase. The C region and the white contrast inside the A and B regions may have the same composition. However, there is no proof of this assumption since the only precise characterizations of such compositions were made with Atom Probe Tomography as reported in Chapter V and these results did not distinguish the A, B and C microstructures. The C microstructure could result from the population of the smallest agglomerates observed in laser granulometry. Note that a similar microstructure was obtained by Rogachev et *al.* in a work mentioned in the introduction to Chapter V as [10]. The formation of an Fe-rich intergranular phase and a fine structure inside the grain, similar to that of microstructure A, was produced with a more powerful milling. The authors suggested that the fine structure resulted from spinodal decomposition.

3.2. Influence of initial powder size on the milling progress

The effect of Cr initial size has been studied in various ways and is reviewed in Chapter IV. Note that the powders studied in this part were never sintered. The powders used in the previous chapters are noted as X^a and the powders used in the present study are noted X^b. X^b particles sizes were larger than 45 μm.

3.2.1. The effect of Al

Al^a powder corresponds to the Alfa Aesar n°11067: average particle size 4.3 microns.
Al^b powder corresponds to the Alfa Aesar n°43022: [44:100] microns

Figure 5a shows the XRD patterns of the milled Al^bCoCrFeNi system. The results are similar to those of Al^aCoCrFeNi: a progressive disappearance of Al and Co is noticeable. The disappearance of Al peaks seems to progress at the same rhythm whatever the initial size of Al; we might suggest that most of the mixing and amorphisation of Al occurs before 4h. The "free" powder is still very well mixed. The lattice parameter of the FCC phase increases significantly. The particle size distribution depicted in Fig. 5b is similar to the distribution of the Al^aCoCrFeNi system: a first step of agglomeration followed by a decrease in size until reaching an average size of between 20 and 35 μm.

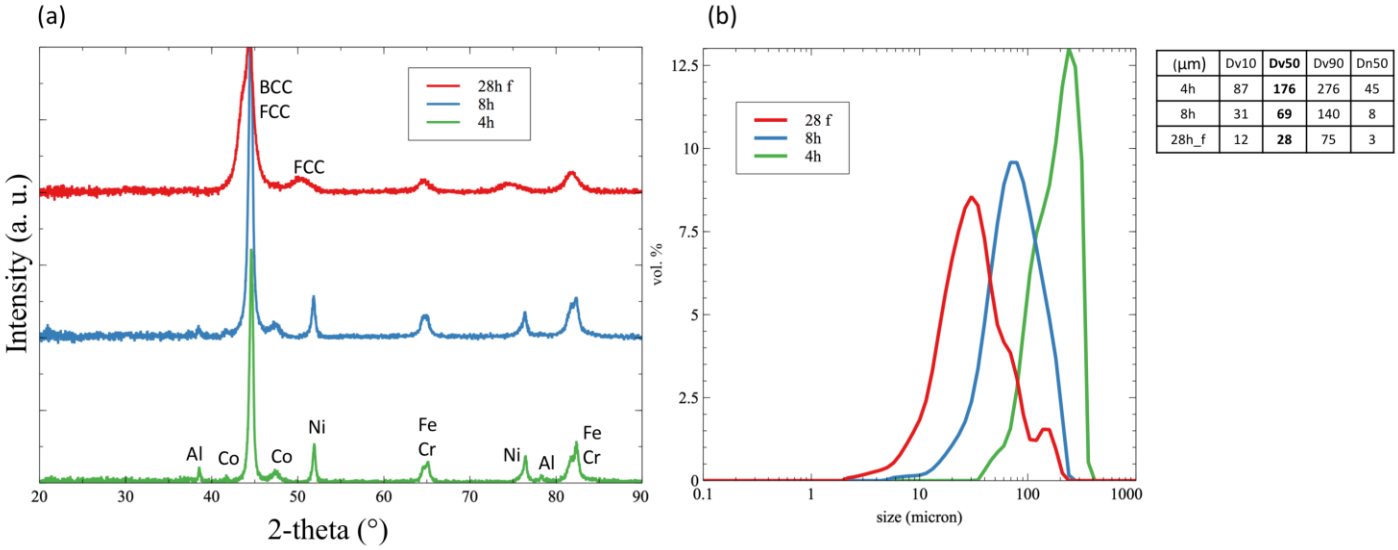

(µm)	Dv10	**Dv50**	Dv90	Dn50
4h	87	**176**	276	45
8h	31	**69**	140	8
28h_f	12	**28**	75	3

Figure 5: (a) XRD patterns of Al^{b}CoCrFeNi milled for different durations. (b) Particle size distributions of the corresponding powders.

The cross-sections and Al elemental mappings of the Al^{b}CoCrFeNi milled system are shown in Fig. 6. After 8h of milling, regions of pure Al are not observable. The progress of the mixing seems identical to that of the system with smaller initial size Al powder. The final result obtained after 28h of milling corresponds to complete mechanical alloying of the system.

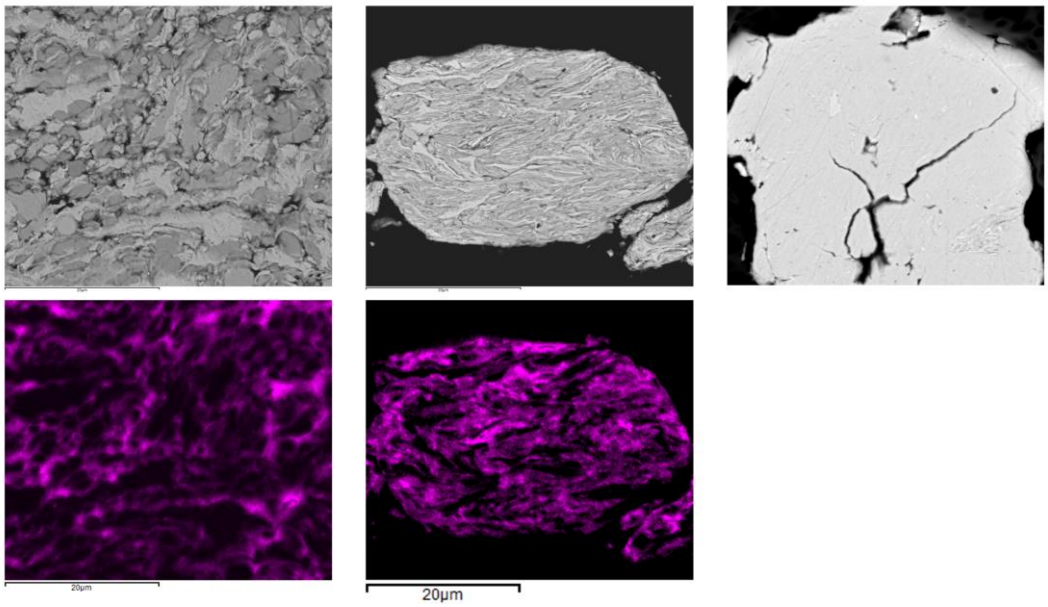

Figure 6: Cross section of milled Al^{b}CoCrFeNi powders. From left to right: 4h, 8h, 28h f. Corresponding elemental mappings of Aluminum.

3.2.2. The effect of Ni

Ni[a] powder corresponds to the Alfa Aesar n°10256 or 00663: average particle size 9 or 4 microns.
Ni[b] powder corresponds to the Alfa Aesar n°44739: [74:90] microns.

Figure 7a shows the XRD patterns of the milled AlCoCrFeNi[b] system. The results are similar to those observed in AlCoCrFeNi[a]: a progressive disappearance of Al and Co is noticeable. The Ni peaks are still extremely intense after 4h and 8h but at the end, the "free" powder remains very well mixed and exhibits a combination of FCC+BCC. The lattice parameter of the FCC phase also increases significantly. The particle size distribution depicted in Fig. 7b is similar to the distribution of the Al[a]CoCrFeNi system: a first step of agglomeration followed by a decrease in size until reaching an average size of between 20 and 35 µm.

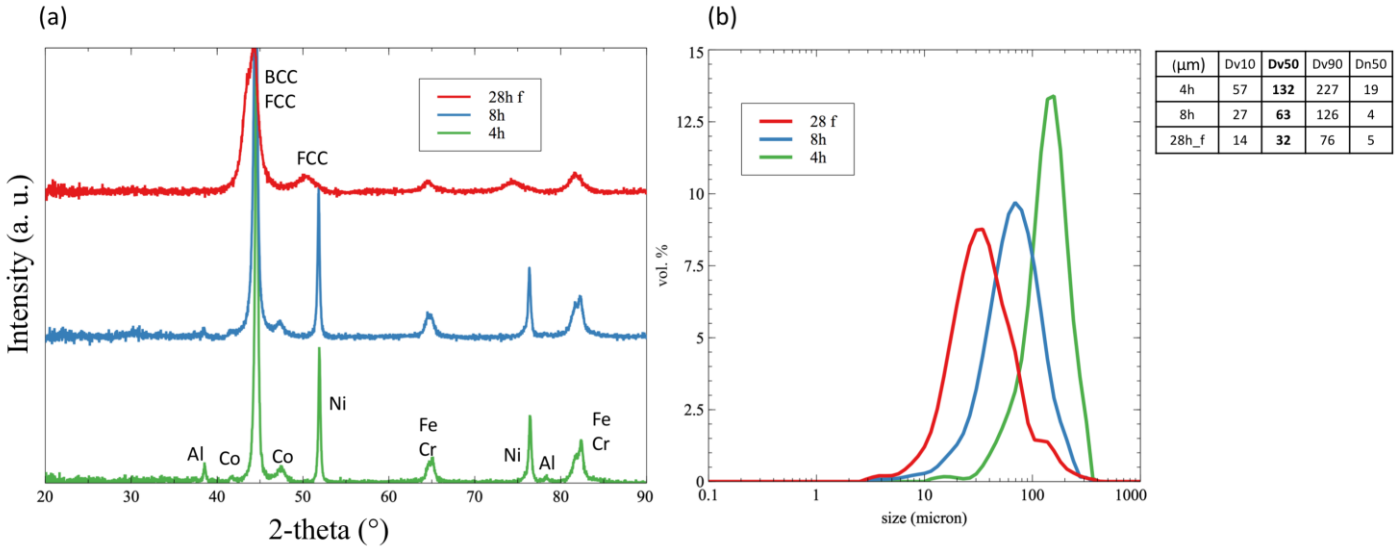

(µm)	Dv10	**Dv50**	Dv90	Dn50
4h	57	**132**	227	19
8h	27	**63**	126	4
28h_f	14	**32**	76	5

Figure 7: (a) XRD patterns of AlCoCrFeNi[b] milled for different durations. (b) Particle size distributions of the corresponding powders.

Figure 8 shows the cross section of the AlCoCrFeNi[b] system after 4h of milling. A large region of pure Ni is noticeable in the bottom right. However, the mixing progress observable in the rest of the picture is similar to what was previously observed (see Fig. 3). Hence, a larger initial size Ni powder delays the mixing of Ni but does not change the final result in the "free" powder. Introducing one element much larger than the other could be compared with the sequential milling undertaken by Vaidya *et al.* since it may be similar to mill AlCoCrFe 4h and to add Ni afterward (see ref. [62] in Chapter I).

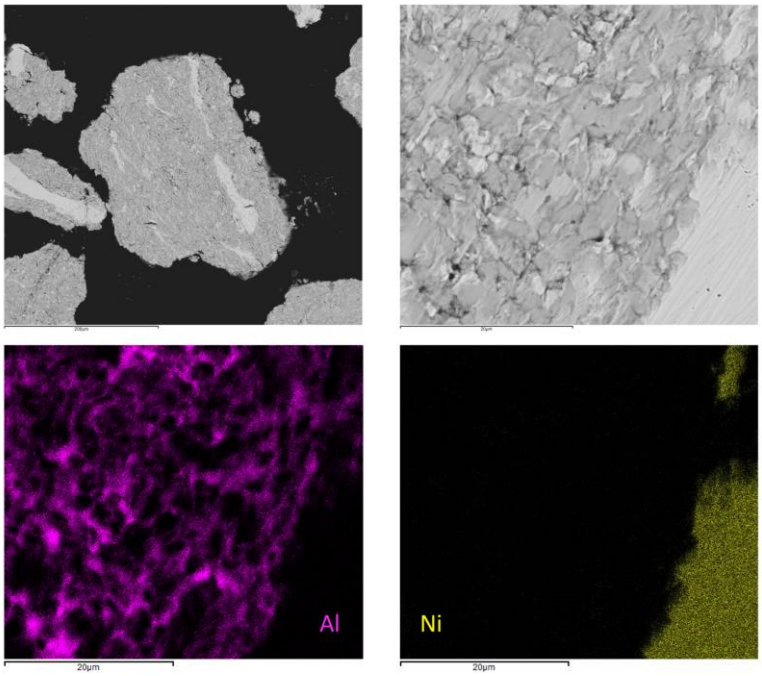

Figure 8: (top) Cross section of AlCoCrFeNi[b] milled 4h at different scales. (bottom) Elemental mapping of Al and Ni of the top right picture.

3.2.3. The effect of Fe

Fe[a] powder corresponds to the Alfa Aesar n°00170: average particle size 7 microns.
Fe[b] powder corresponds to a sieved Sigma Aldrich **FE006010**: grain size analysis gives the following measurements:

Size (µm)	Dv10	Dv50	Dv90
Before sieving	119	180	264
After sieving	92	131	181

Table 1: Particle size distribution of the Fe[b] before and after sieving.

The sieve size was 125 µm. As the Dv50 exceeds the sieve size, the powder particles are likely not purely spherical. Note that the sieving was operated in a glove box.

Figure 9a shows the XRD patterns of the milled AlCoCrFe^{b}Ni system. The results are similar to those of Al^{a}CoCrFeNi: a progressive disappearance of Al and Co is noticeable. The state of the stuck-on powder is similar to that of the milled powder observed in Fig. 2. The "free" powder is still very well mixed. The lattice parameter of the FCC phase increases significantly. The particle size distribution depicted in Fig. 9b is similar to the distribution of the Al^{a}CoCrFeNi system: a first step of agglomeration followed by a decrease in size until an average size of between 20 and 35 µm is reached. In the present case, the stuck-on and free powders exhibit slightly different agglomerate sizes, but the two sizes remain comparable.

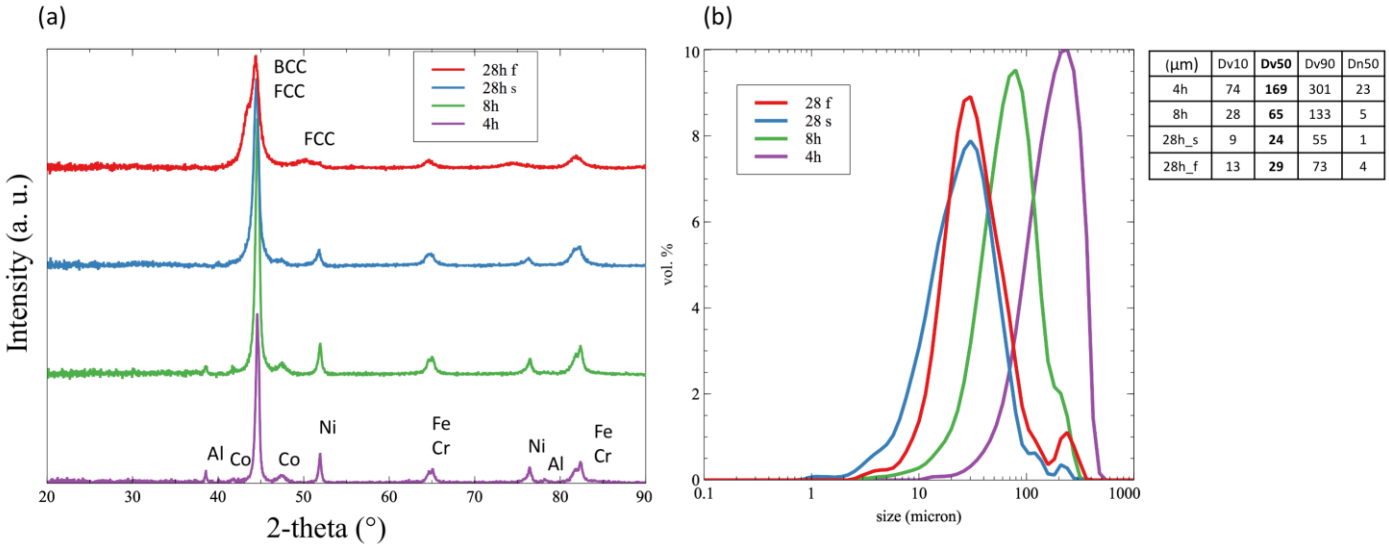

(µm)	Dv10	Dv50	Dv90	Dn50
4h	74	**169**	301	23
8h	28	**65**	133	5
28h_s	9	**24**	55	1
28h_f	13	**29**	73	4

Figure 9: (a) XRD patterns of AlCoCrFe^{b}Ni milled for different durations. (b) Particle size distributions of the corresponding powders.

The cross-sections and Al elemental mapping of the AlCoCrFe^{b}Ni stuck-on powder milled 28h are shown in Fig. 10. The mixing seems similar or slightly better than that observed in AlCoCrFe^{a}Ni.

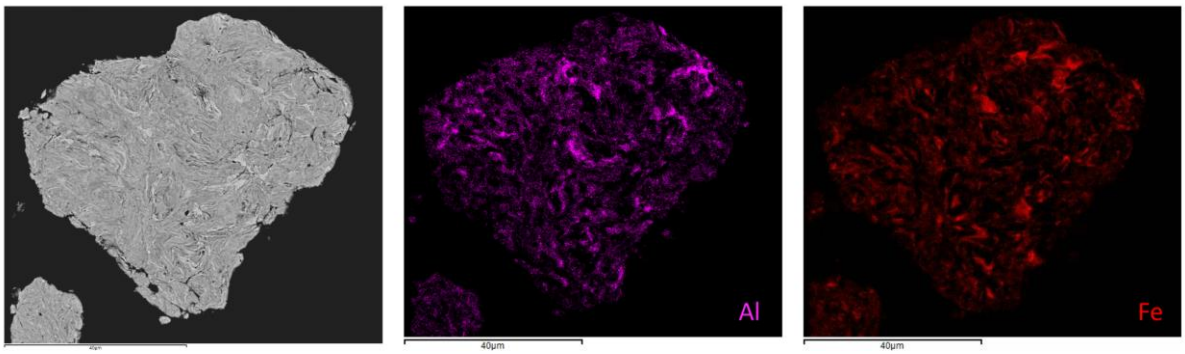

Figure 10 : Cross section and EDS mappings of milled AlCoCrFe^{b}Ni 28h s.

3.2.4. Comparison and discussion of the influence of initial particle size

Figure 11a compares the XRD patterns of the different powders at 4h and Fig. 11b compares the XRD patterns of the different powders at the end of the process (28 f). Tables 2 and 3 summarize the evolution of the main Al peak area (the peak at 37.5 2-theta) and the lattice parameter of the FCC phase respectively.

The noticeable differences are minor, and the following conclusions would require further characterizations to confirm them:

- Assuming that the XRD patterns are comparable amongst the results concerning the same composition, we can compare the "speed" at which Al is dissolved. For the Al^b and Ni^b systems, the area of the (111) Al peak is divided by two between 4h and 8h whereas it divided by approximately 1.5 for the Fe^b and 1 for the $(AlCoCrFeNi)^a$. Large initial size Al or Ni particles seem to delay the progress of the mixing.
- Identical lattice parameters are obtained in all cases. In the "free" powders, the solid solution is formed during milling.

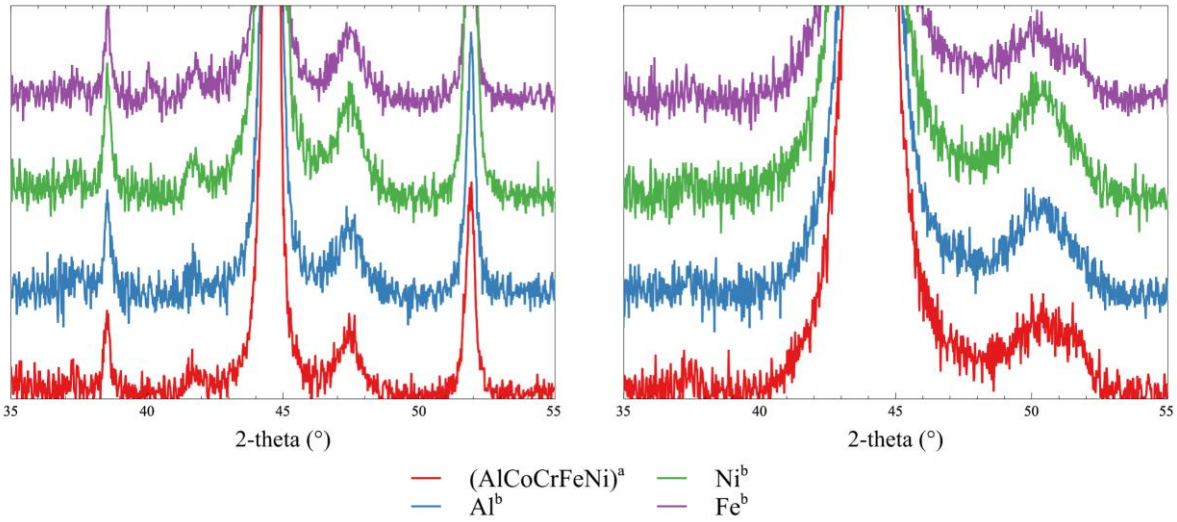

Figure 11: XRD patterns of milled AlCoCrFeNi powders for different initial elemental powder sizes. Left: 4h and right: 28h f.

Area of (111) Al peak	$(AlCoCrFeNi)^a$	Al^b	Ni^b	Fe^b
4h	0.186	0.266	0.389	0.285
8h	0.19	0.134	0.19	0.2
28h s	0.082			0.028

Table 2: Evolution of the area of the (111) Al peak with milling time and initial particle size.

	$(AlCoCrFeNi)^a$	Al^b	Ni^b	Fe^b	Vegard
a_0 FCC (Å)	3.63	3.63	3.63	3.63	3.63

Table 3: Lattice parameter of the FCC phase for the different systems considered.

Figure 12 displays the particle size distribution of the milled powders for the 4 systems considered. Considering the size distribution, the repeatability of the process is impressive, especially since mechanical milling of metallic powders is long and rather stochastic. As compared to the particle size distributions of the powders milled in the Activator 2S presented in Appendix I, the influence of the initial particle size seems almost negligible in the case of the Pulverisette 4 milling. However, the distribution of the Alfa Aesar powders milled in the Activator 2S is very close that of the Alfa Aesar powders milled in the P4 with the F25028x1 parameters.
Finally, in the present study, most of the significant changes seem to occur between the beginning and 4h. The initial size of the powder for the considered milling parameters does not seem to severely impact the final crystalline structure.

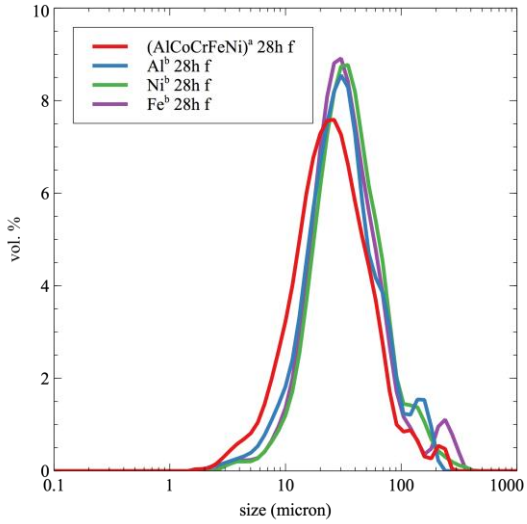

Figure 12: Particle size distribution after milling for the different initial elemental sizes.

4. Conclusion

We note powders in different states at the end of the millings performed in the present work. One such state, labeled as "free", exhibits almost complete mixing (i.e., one SEM contrast and one XRD phase). In the case of equimolar AlCoCrFeNi, this “free” powder corresponds to 12 wt. % of the initial powder and this percentage does not vary much with initial powder size.
With the considered milling parameters, the initial elemental size has a very slight influence. However, most of the noticeable differences seem to occur before 4h of milling.
This behavior is different in the case of much more powerful mills such as the Activator-2S (see Appendix I) where the initial size is the most plausible hypothesis to explain the different crystalline structures obtained after the milling of the same composition.
To conclude, the process has one major flaw: the milled powder exhibits 2 and possibly 3 different states at the end of milling. Only 10% of the powder is efficiently milled over the total duration of the milling. There are two leads to solve this problem:

- To mill for a shorter time and optimize the sintering parameters. Indeed, we demonstrated in the main chapters of the present work that Mechanical Activation was sufficient to synthetize homogeneous High Entropy Alloys after sintering.
- To optimize the milling parameters in order to prevent the powder from adhering to the wall. For instance, a limited use of a Process Control Agent can be suggested, although this will lead to a compromise between adherence and contamination.

The present study allows us to reflect critically on the results obtained in Chapters IV and V concerning milling in jars of 80 mL. The amount of stuck-on powders obviously did not equal the amount observed in the jars of 250 mL. In addition, the existence of two states of powders at the end of the milling in jars of 80 mL has not been formally observed. However, the conclusions presented in the main chapters could be altered after a meticulous examination of the as-milled powders. For instance, carefully searching for differences between the powder lying at the bottom of the jar and the powder which slightly adheres to the walls at the end of the milling could provide us with additional information.

Appendix IV: Investigation of new High Entropy Alloy compositions elaborated by Mechanical Activation and Spark Plasma Sintering

1. Introduction

The initial goal of the present study was to assess mechanical activation followed by the reactive sintering process. Indeed, contrary to the procedures reported in the previous Appendix, here the powders were sintered. Thus, the sintering progress of 3d-transition metal HEAs is also investigated. Among other objectives, one intent was to show that the sintering of powder milled 4h or 28h would lead to rather similar microstructures (and that a milling of 28h -close to true mechanical alloying- was not necessarily mandatory to obtain nanostructured and homogeneous alloys). The cases of single-phase alloys (MnCoCrFeNi and Al_7) seemed particularly relevant. In addition, the influence of Al on the progress of the process and on the resulting microstructure is investigated in order to initiate future studies concerning promising compositions for HEA applications. Note that this ambitious study was not completed, and some results are missing.

2. Materials and Methods

In the present appendix, the milling and sintering parameters are identical to those presented in Appendix III above (except where stated otherwise):

- $F250_{28x1}$ for the milling parameters,
- the sintered powders correspond to different mixes of free, stuck-on and wet powders and are specified each time,
- the sintering parameters are 1100°C, 50°C/min, 80 MPa, no dwell time, tools diameter 10 mm.

3. Results

3.1. Cantor Alloy: MnCoCrFeNi

Mn is still less hard than the others (51 HV versus 61 HV for Fe for instance) but much harder than Al.
The phase fraction of the Cantor MnCoCrFeNi alloy is depicted in Figure 1. At the sintering temperature, 1100°C, one single disordered FCC phase is expected to form.

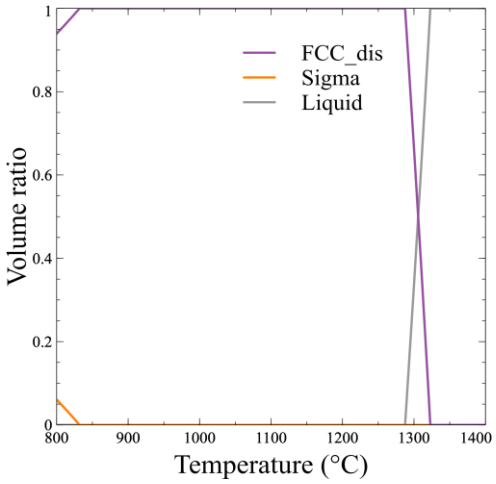

Figure 1: Volume ratios of the different phases in MnCoCrFeNi HEA calculated by Thermo-Calc

3.1.1. Milling of Mn-Co-Cr-Fe-Ni

Figure 2a illustrates the XRD patterns of the milled MnCoCrFeNi system. The progressive disappearance of Mn, Co, Cr and Fe is noticeable. The “free” powder exhibits a combination of BCC and FCC phases but one might imagine the total disappearance of the BCC phase with additional milling time. The lattice parameter of the FCC phase increases significantly (see Table 3). The particle size distribution evolution depicted in Fig. 2b is different from the evolution of the distribution in the AlCoCrFeNi system. There is no agglomeration or decrease in size. Instead, the Dv50 remains around 35 μm. In fact, the smallest and largest agglomerates progressively disappear, and the range thus decreases.

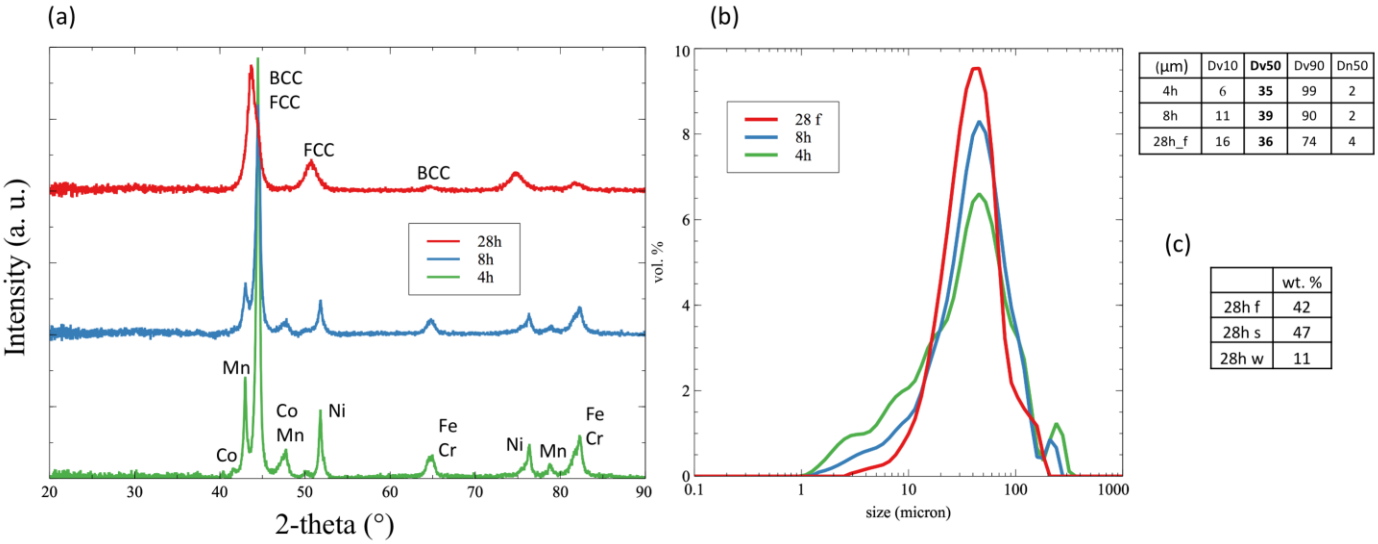

(µm)	Dv10	**Dv50**	Dv90	Dn50
4h	6	**35**	99	2
8h	11	**39**	90	2
28h_f	16	**36**	74	4

(c)

	wt. %
28h f	42
28h s	47
28h w	11

Figure 2: (a) XRD patterns of MnCoCrFeNi milled for different durations. (b) Particle size distributions of the corresponding powders. (c) Milling yield corresponding the MnCoCrFeNi composition.

The cross-sections and Mn elemental mapping of the MnCoCrFeNi milled system are shown in Fig. 3. After 4h or 8h of milling, the microstructure is composite. The mixing progress seems comparable to that of the AlCoCrFeNi system. However, the microstructure seems less lamellar. The final result in “free” powder obtained after 28h of milling corresponds to almost complete mechanical alloying of the system. Some Mn-rich dots remain.

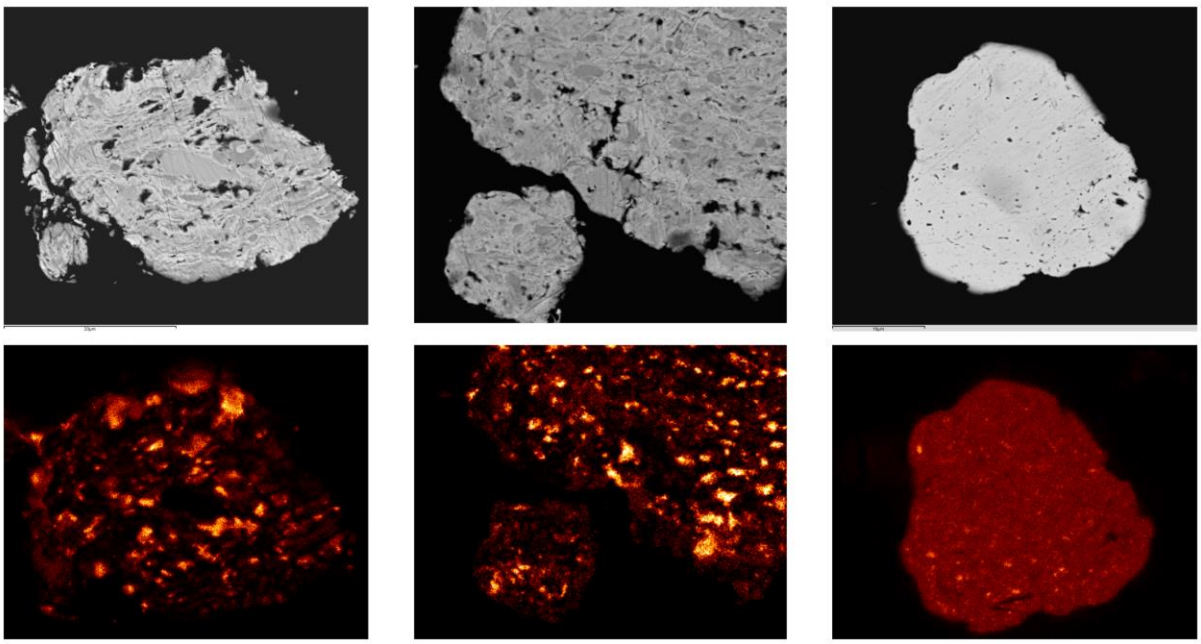

Figure 3: Cross section of milled MnCoCrFeNi powders. From left to right: 4h, 8h and 28h f. Elemental mapping of Manganese.

3.1.2. Sintering of MnCoCrFeNi

The sintering of the MnCoCrFeNi powders milled 28h f at 1100°C led to the partial melting of the sample and to the destruction of the upper piston when it was separated from the sample. The target temperature was consequently decreased to 1000°C. Interestingly enough, the 4h and 8h milled powders did not melt at 1100°C but only the 28h f powders.
Figure 4a presents the XRD patterns of the sintered MnCoCrFeNi systems. Note that 28h corresponds to the "free" powder: 28h f. The sintered samples all exhibit almost single-phase FCC. One peak at 35° 2-theta looks like an Mn_3O_4 spinel but with a larger lattice parameter. Further SEM investigations are required to help determine the identity of this phase. Interestingly enough, in all powders milled for different durations, the XRD patterns are almost identical. The shrinking curves corresponding to sintered samples are depicted in Fig. 4b. The final sintering temperatures are around 880°C for 0h of milling, 890°C for 4h, 890°C for 8h, and 980°C for 28h. Hence, the milling time seems to increase the sintering temperature. Since the Dv50 does not really vary between these powders (see Fig. 2b), the mixing progress or the lattice defect concentration would seem to be responsible for higher sintering temperature in the case of MnCoCrFeNi. This being said, the actual microstructures and chemical homogeneity remain to be investigated.

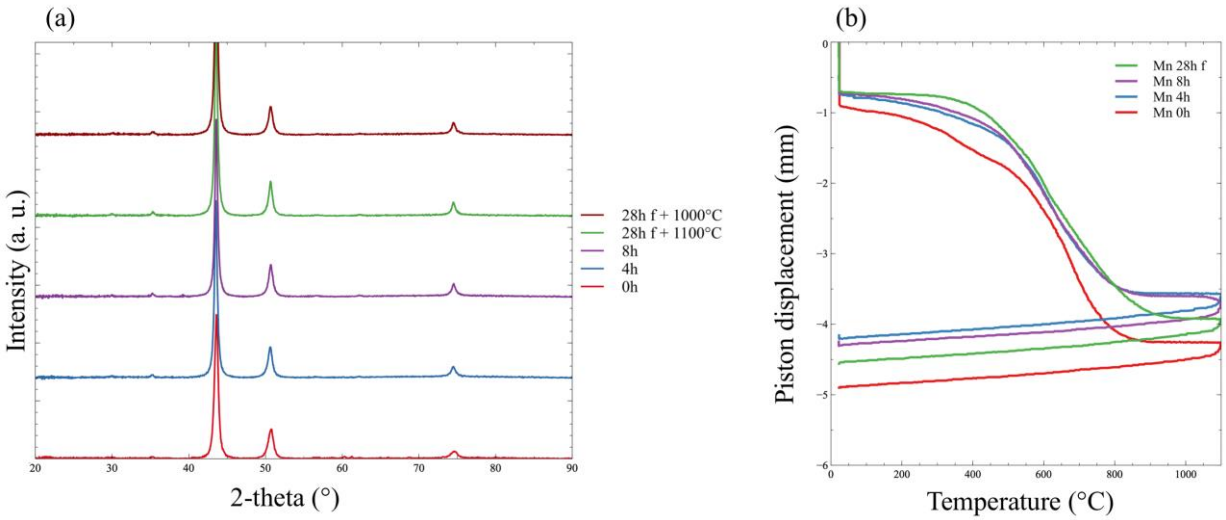

Figure 4: (a) XRD patterns of the MnCoCrFeNi powder milled for different durations sintered at 1100°C or 1000°C. (b) Shrinking curves corresponding to these samples.

Table 1 summarizes the Vickers hardness and density of the different sintered samples. Leaving aside the melted sample, hardness increases with milling time whereas density decreases. SEM investigation of each sample is required to suggest features responsible for this behavior. However, credible mechanisms of hardening would be solid solution strengthening, since the chemical homogeneity is likely enhanced with milling time, and grain boundary hardening, since crystallite size is likely decreased.

	0h + 1100°C	4h + 1100°C	8h + 1100°C	28h f + 1100°C	28h f + 1000°C
Hardness (HV)	121 ± 6	312 ± 11	366 ± 5	210 ± 4	490 ± 21
Density (g/cm^3)	7.9	7.9	7.8	7.6	7.7

Table 1: Hardness and density data for the sintered MnCoCrFeNi samples.

Figure 5 shows the only SEM analysis performed on the sintered MnCoCrFeNi samples. Three contrasts are seen on the MnCoCrFeNi alloy obtained from the "free" powder milled 28h and sintered at 1000°C. The medium and dark greys differ mainly from the O concentration. Even if these oxygen concentrations are not at all accurate, their presence may reflect some actual phenomenon (discussed in the conclusion of this appendix). The light grey seems to correspond to a Cr-poor intergrain phase. Judging from their size and shape, the medium and dark greys seem to correspond to initial agglomerates. For some reason, certain agglomerates contain more Oxygen than others. Single high entropy solid solution -one unique contrast- has not been achieved. The main reason seems to be the oxygen contamination resulting from the process. In addition, since the sample seems to be single-phase, the microstructure is no longer imbricated. The microstructure is likely a result of the sizes and shapes of the agglomerates.

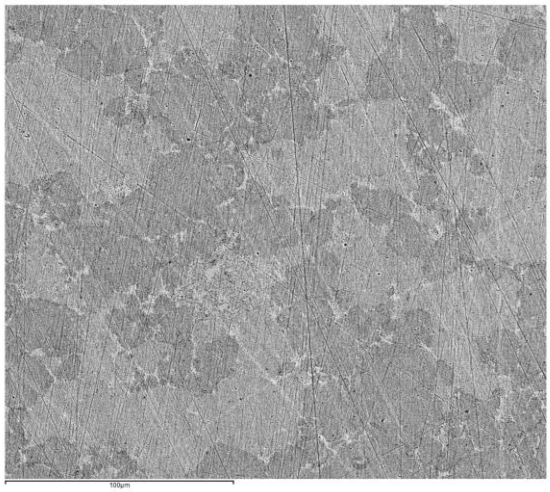

at. %	O	Mn	Co	Cr	Fe	Ni
Medium grey	6.8	18.5	18.4	18.6	19.2	18.6
Dark grey	9.1	18.2	17.9	18.1	18.7	18.0
Light grey	0	19.4	19.5	14.5	22.9	20.1

Figure 5: BSE SEM picture and EDS measurements of MnCoCrFeNi 28h f sintered at 1000°C.

3.2. $Al_7CoCrFeNi$

In the present work, the $Al_7CoCrFeNi$ notation corresponds to the $Al_{0.3}CoCrFeNi$ HEA notation (see Chapter I): 7 at. % Al, 23.25% Co, 23.25% Cr, 23.25% Fe, 23.25% Ni.
The phase fraction of the Al_7 alloy is depicted in Figure 6. At the sintering temperature, 1100°C, one ordered BCC phase and one FCC phase are expected to form. To be specific, 2 vol. % of an Al, Ni-rich B2 and 98 vol. % of an FCC co-exist. In the literature, the formation of a single disordered FCC is often reported for this composition (see ref. [18] in Chapter I for instance).

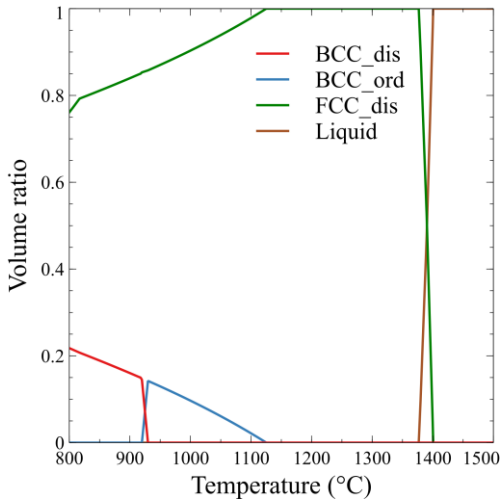

Figure 6: Volume ratios of the different phases in $Al_7CoCrFeNi$ HEA calculated by Thermo-Calc

3.2.1. Milling of Al_7-Co-Cr-Fe-Ni

Figure 7a shows the XRD patterns of the milled $Al_7CoCrFeNi$ system. Al peaks are already gone after 4h of milling. The progressive disappearance of Co is noticeable. The "free" powder exhibits a combination of BCC and FCC phases. The lattice parameter of the FCC phase increases significantly (see Table 3). The particle size distribution evolution depicted in Fig. 7b seems similar to the evolution of the distribution of the AlCoCrFeNi system. However, both the agglomeration and decrease magnitudes are much smaller in the case of $Al_7CoCrFeNi$.

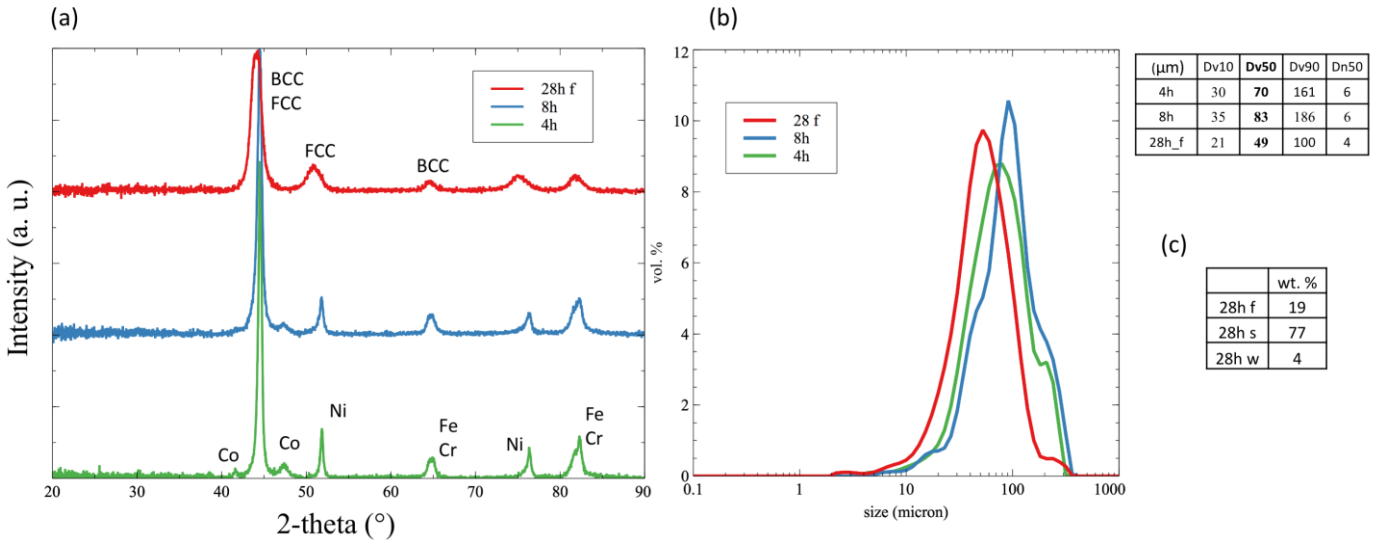

(µm)	Dv10	**Dv50**	Dv90	Dn50
4h	30	**70**	161	6
8h	35	**83**	186	6
28h_f	21	**49**	100	4

	wt. %
28h f	19
28h s	77
28h w	4

Figure 7: (a) XRD patterns of $Al_7CoCrFeNi$ milled for different durations. (b) Particle size distributions of the corresponding powders. (c) Milling yield corresponding to the $Al_7CoCrFeNi$ composition.

The cross-sections and Al elemental mappings of the $Al_7CoCrFeNi$ milled system are shown in Fig. 8. The final result obtained after 28h of milling corresponds to the mechanical alloying of the system.

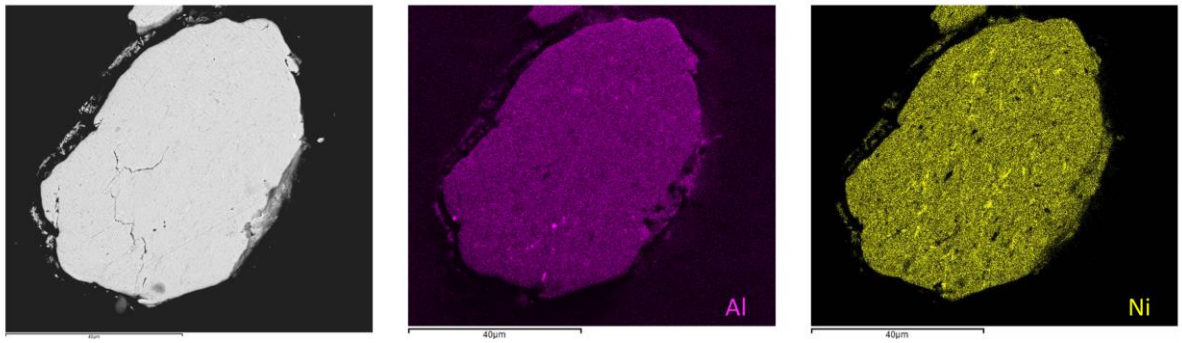

Figure 8 : Cross section of $Al_7CoCrFeNi$ milled 28h f. Elemental mappings of Al and Ni.

3.2.2. Sintering of $Al_7CoCrFeNi$

Figure 9a presents the XRD patterns of the sintered $Al_7CoCrFeNi$ samples. 28h w corresponds to the powder collected after a 30 min milling with ethanol. This kind of powder is likely similar to the "stuck-on" powder but may be contaminated by Oxygen and Carbon. The sintered samples all exhibit a single FCC phase. Interestingly, in all powders milled over different amounts of time, the XRD patterns are almost identical except for the 0h which seems less crystalline (since the peaks seem broader). The shrinking curves corresponding to sintered samples are depicted in Fig. 9b. The milling time seems to increase the final sintering temperature, from 1000°C for 0h of milling to 1100°C for 28h of milling. In the present case, the Dv50 varies between these powders although not linearly (see Fig. 7b); hence, the mixing progress seems to be responsible for higher sintering temperature in the case of $Al_7CoCrFeNi$. To confirm this, the actual microstructures and chemical homogeneity would need to be investigated. In the end, the influence of short wet milling in order to collect strongly adhered powder does not seem to lead to carbide or oxide formation noticeable on XRD.

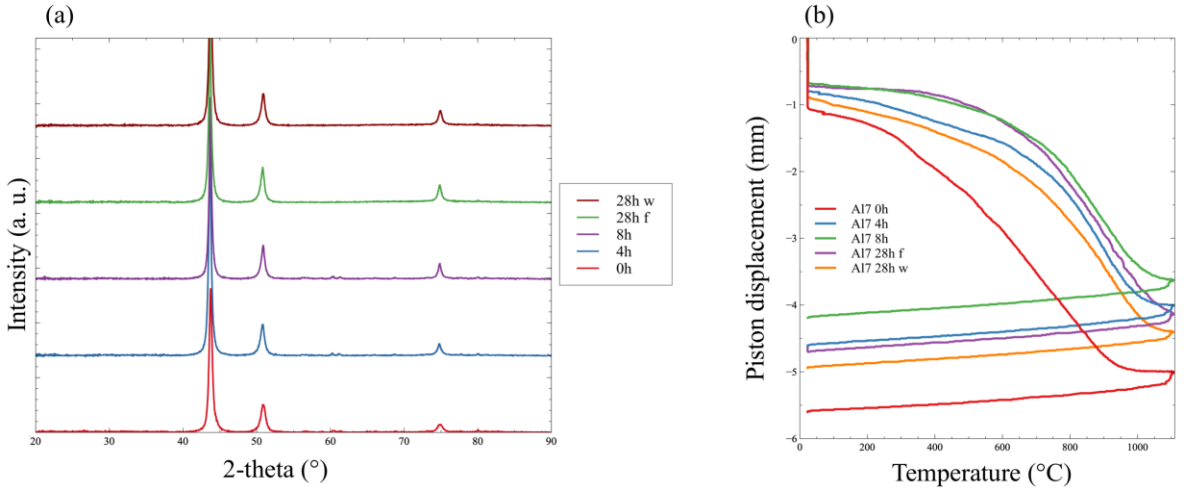

Figure 9: (a) XRD patterns of the $Al_7CoCrFeNi$ powder milled for different durations sintered at 1100°C. (b) Shrinking curves corresponding to these samples.

Figure 10 shows the only SEM analysis performed on the sintered $Al_7CoCrFeNi$ samples. Three contrasts can be seen on the $Al_7CoCrFeNi$ alloy obtained from the "wet" powder milled 28h and sintered at 1100°C. The dark grey contrast seems to correspond to initial agglomerates (see the region surrounded by the white dot). The light grey contrast seems to correspond to the "intergranular" region seen previously. The light grey contrast is less rich in Oxygen than the dark grey contrast. EDS measurements seems to indicate that black dots correspond to chromium carbides. Indeed, as compared to equimolar AlCoCrFeNi, first the Cr content goes up to 23.25 at. %; then lower Al content leads to fewer Alumina, Alumina which might hinder the carbon diffusion (a suggestion made in Chapter V). In addition, ethanol is likely to introduce some level of carbon in the milled powder. Single high entropy solid solution -one unique contrast- has not been achieved. The main reason seems to be the oxygen contamination resulting from the process. In addition, since the sample seems to be single-phase, the microstructure is no longer imbricated. The microstructure likely results from the sizes and shapes of the agglomerates.

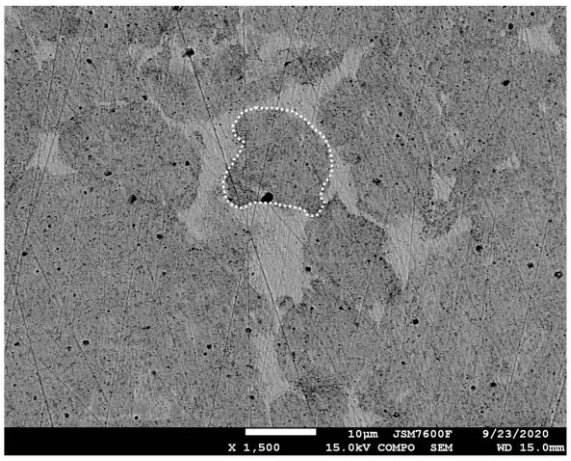

at. %	O	Al	Co	Cr	Fe	Ni
A	8.7	7.6	20.2	19.9	21.9	21.7
B	0	4.5	23.2	22.8	25.0	24.4

Figure 10: BSE SEM and EDS measurements of $Al_7CoCrFeNi$ 28h w sintered at 1100°C (30 mm tools).
Black dots correspond principally to Chromium carbides.

3.3. $Al_{30}CoCrFeNi$

In the present work, the $Al_{30}CoCrFeNi$ notation corresponds to the $Al_{1.7}CoCrFeNi$ HEA notation (see Chapter I): 30 at. % Al, 17.5% Co, 17.5% Cr, 17.5% Fe, 17.5% Ni.
The phase fraction of the Al_{30} alloy is depicted in Figure 11. At the sintering temperature, 1100°C, two ordered BCC phases are expected to form. To be specific, 24 vol. % of a Cr-rich B2 and 76 vol. % of a Fe, Co, Ni-rich B2 co-exist. In the literature, the formation of a disordered BCC and an ordered BCC are reported for this composition (see ref. [46] in Chapter I for instance).

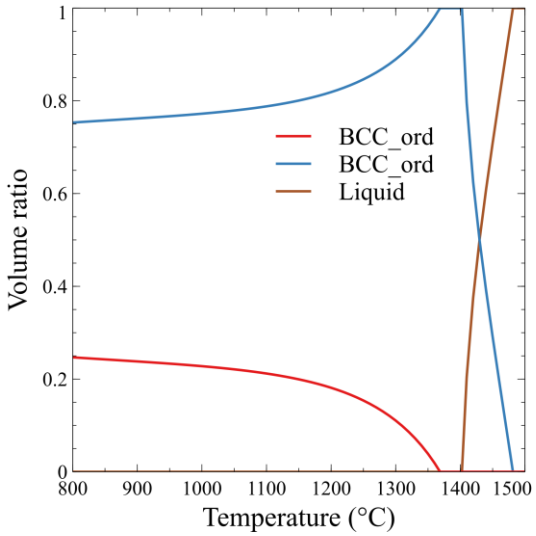

Figure 11: Volume ratios of the different phases in $Al_{30}CoCrFeNi$ HEA calculated by Thermo-Calc

3.3.1. Milling of Al_{30}-Co-Cr-Fe-Ni

Figure 12a shows the XRD patterns of the milled $Al_{30}CoCrFeNi$ system. The "free" powder exhibits a single BCC phase. The lattice parameter of the BCC phase is close to the lattice parameter of pure Fe: 2.89 Å. However, the "stuck-on" powder exhibits a combination of BCC, FCC and pure Al peaks. In addition, the FCC peaks are asymmetric. The particle size distribution of stuck-on and free powders is depicted in Fig. 12b. Interestingly enough, the Dv50 of stuck-on powder is almost divided by two as compared to the Dv50 of free powder. Unfortunately, SEM investigation of the powder cross-section is lacking; such an investigation may be valuable in explaining the difference in agglomerate size. Indeed, in the case of predominant Al composition, the role of Al as some sort of binder is likely to be different than in the case of equimolar AlCoCrFeNi.

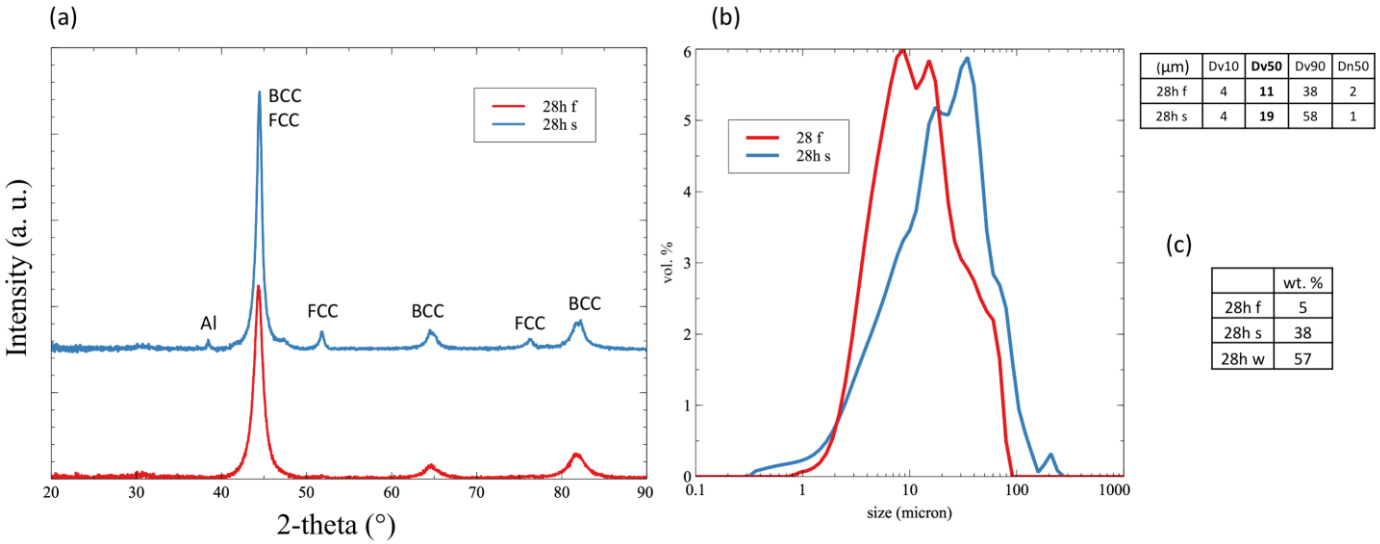

(µm)	Dv10	**Dv50**	Dv90	Dn50
28h f	4	**11**	38	2
28h s	4	**19**	58	1

(c)

	wt. %
28h f	5
28h s	38
28h w	57

Figure 12: (a) XRD patterns of $Al_{30}CoCrFeNi$ milled for different durations. (b) Particle size distributions of the corresponding powders. (c) Milling yield corresponding to the $Al_{30}CoCrFeNi$ composition.

3.3.2. Sintering of $Al_{30}CoCrFeNi$

Figure 13 shows the XRD patterns of a combination of stuck-on and wet powders sintered at 1100°C in a 30-mm die. The diffractogram exhibits only BCC peaks. Two B2 peaks at 55 and 74° 2-theta are particularly noticeable in this composition. Interestingly enough, the BCC peaks are highly asymmetrical. This feature may indicate a wide distribution of Al concentration in the BCC lattice, similarly to what was suggested in the case of the milled powder. In addition, there are no sign of carbides, oxides or sigma peaks.

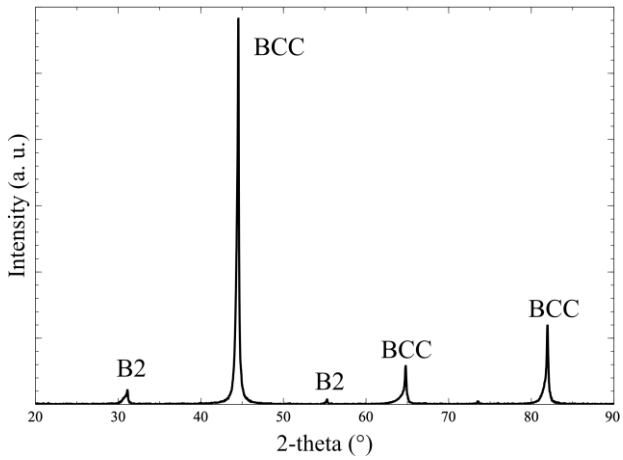

Figure 13: XRD pattern of $Al_{30}CoCrFeNi$ 28h w+s sintered at 1100°C (30 mm tools).

Figure 14 shows the only SEM analysis performed on the sintered $Al_{30}CoCrFeNi$ samples. Four contrasts can be seen in the microstructure. The contrasts “1” and “2” seem to correspond to two different kinds of initial agglomerates. For some reason, the agglomerates labeled “2” are richer in Oxygen. These agglomerates might correspond to the “wet” powder. The contrast

labeled “3” is a very rich-Cr zone and is likely to correspond to almost pure Cr BCC phase since there is absolutely no trace of a sigma phase in XRD. The contrast labeled “4” looks like an “intergranular” region but the presence of contrast “3” makes the analysis more difficult. The presence of a Cr-rich zone may indicate a less efficient milling in the case of predominant Al systems. Indeed, during milling, almost amorphous layers of Al could surround the Cr particle and hinder the chemical mixing of the elemental powders.

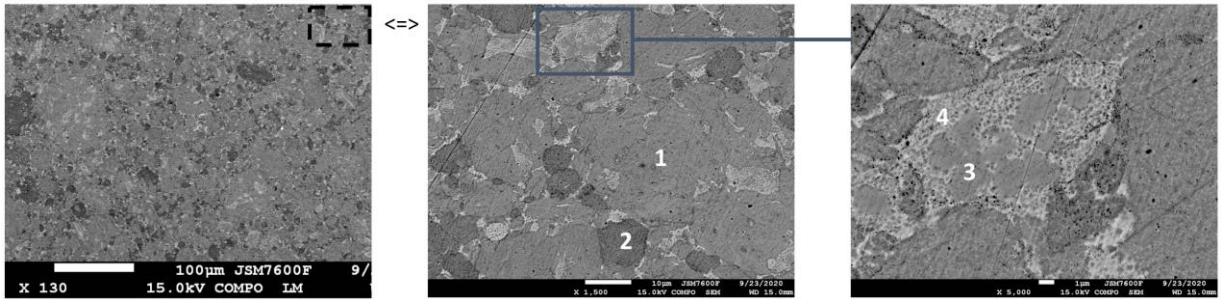

at. %	O	Al	Co	Cr	Fe	Ni
1	5.0	29.7	17.8	12.9	15.4	19.3
2	8.7	28.9	16.3	14.0	15.3	16.8
3	0	2.2	3.7	84.0	8.1	1.9
4	0	15.8	15.5	34.3	25.8	8.6

Figure 14: BSE SEM and EDS measurements of Al30CoCrFeNi 28h w+s sintered at 1100°C (30 mm tools). From left to right: different scales. The purpose of the dashed black square is to visualize the different scales (100 µm, 10 µm, 1 µm).

3.4. Comparison and discussion of the influence of the composition

Table 2 summarizes the milling yield concerning the different kinds of powder for the four compositions studied. In the $Al_xCoCrFeNi$ systems: the more Al there is, the more the powder adheres to the wall. This is particularly inconvenient in the case of the Al_{30} system where the amount of free powder is not even sufficient to sinter only this kind of powder. The free powder yield of the Mn-Co-Cr-Fe-Ni system is inferior to that of the Al_7 although the main characteristic of the corresponding agglomerates is identical: almost single FCC (see Fig. 15). However, the presence of Al irremediably leads to higher amounts of “remaining” powder.

wt. %	Mn	Al_7	Al_{20}	Al_{30}
28h f	19	42	12	5
28h s	77	47	62	38
28h w	4	11	27	57

Table 2: Milling yield corresponding to the different compositions.

Figure 15a compares the XRD patterns of the different powders at the end of the process (28 f). Several observations can be made:

- The more Al there is, the less FCC phase remains. It is interesting to note this behavior occurring even during the milling without any heating-induced diffusion.
- The less Al there is, the larger the agglomerates are.
- By comparing the particle size distribution and the milling yield, we can suggest that larger agglomerates seem to lead to greater free powder yield.

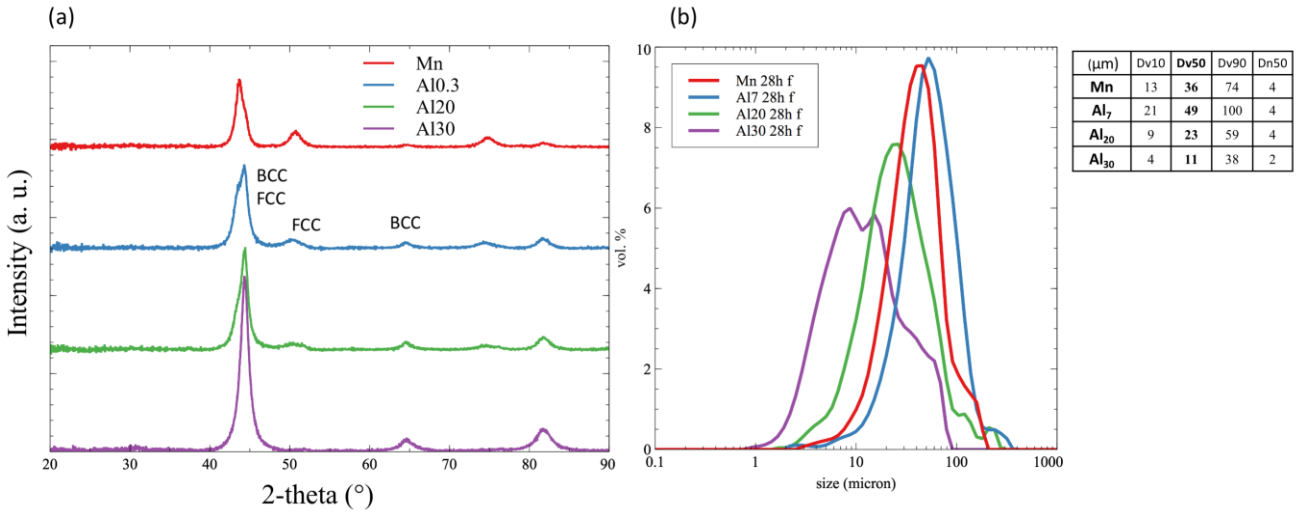

Figure 15: (a) XRD patterns of the different compositions for the 28h f powders. (b) Particle size distribution of the corresponding powders.

Table 3 summarizes the measured and predicted lattice parameters of the FCC phase after milling. The lattice parameters increase in all cases; the solid solution is formed during the milling. Vegard's prediction works well for the equimolar composition but underestimates the lattice parameter in the cases of Al_7 and Mn. However, note that Vegard's law was designed to evaluate the lattice parameter of mixtures of elements with identical structure (the FCC Fe and Mn FCC lattice parameters at room temperature are not really determined).

a_0 FCC (Å)	AlCoCrFeNi	Al_7CoCrFeNi	MnCoCrFeNi
28h f	3.63	3.59	3.60
Vegard	3.63	3.56	3.54

Table 3: Measured and predicted lattice parameters of the FCC phase after milling 28h f.

Figure 16 illustrates the shrinking curves of the blended powders (left) and milled powders (right) for the different compositions. Shrinking curves of blended powders allow us to evaluate the influence of the chemical composition whereas shrinking curves of milled powders allow us to evaluate the mixing and the influence of the chemical composition. The final sintering temperature is considerably higher for Al-containing alloys. However, the Al content does not drastically change the sintering behavior of the powders.

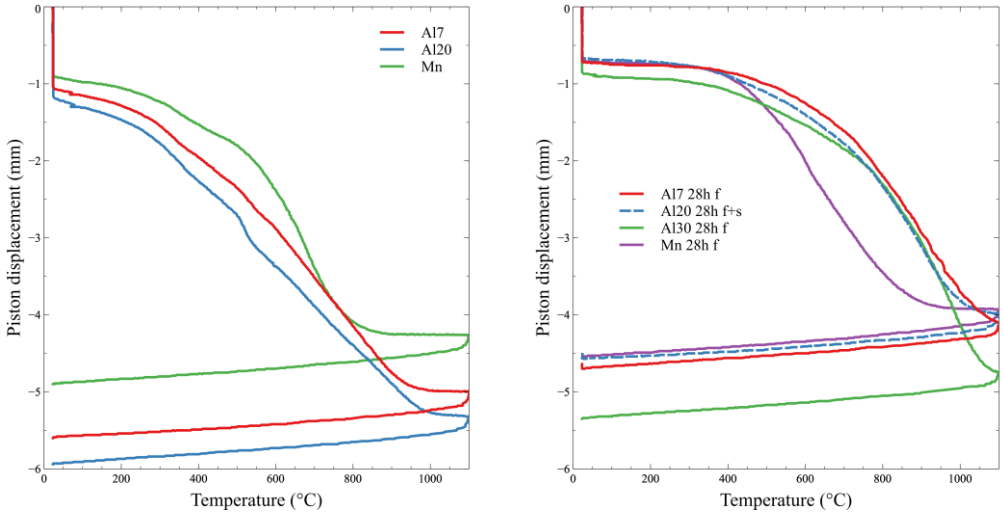

Figure 16: Shrinking curves corresponding to the different compositions. Left: 0h, right 28h f.

Figure 17 compares the XRD patterns of different sintered samples of the four compositions. The role of Al as a stabilizer of the BCC phases (ordered and disordered) is confirmed by these diffractograms.

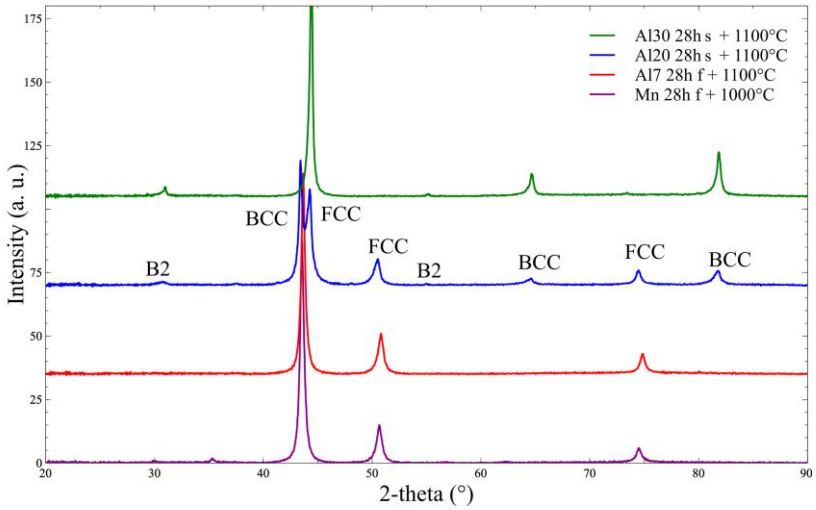

Figure 17: XRD patterns of different sintered samples.

Table 4 summarizes the Vickers hardness and density of the different sintered samples. Hardness increases with Al content whereas density decreases. The nanostructuration seems to ensure a significant hardness. In addition, the increase in hardness seems to be directly related to amount of BCC phase.

	Mn 28h f + 1000°C	Al_7 28h f + 1100°C	Al_{20} 28h s + 1100°C	Al_{30} 28h s + 1100°C
Hardness (HV)	490 ± 21	555 ± 14	615 ± 21	758 ± 21
Density (g/cm^3)	7.7	7.6	7.0	-

Table 4: Summary of hardness and density data for different sintered samples.

4. Conclusion

Al does indeed favor the BCC crystalline structure. The milling progress seems to be different for different Al concentrations. In particular, an excess of Al seems to hinder the milling efficiency.

For all considered systems, there are at least two typical microstructures linked to the process:

- Large initial agglomerates which are still very easily recognizable, even after sintering.
- "Intergranular" regions, appearing during the sintering, which are almost oxygen free.

The peculiar imbricated microstructure was found to be a specificity of the equimolar Al_{20}CoCrFeNi. The formation of two distinct phases seems mandatory to produce this kind of microstructure. Indeed, the three other compositions exhibit less complicated microstructures.

Some compositions (Mn and Al_{30}), exhibit two kinds of initial agglomerates, containing more or less Oxygen. This finding may be linked to some of the agglomerates being protected from the atmosphere by being stuck to the wall behind another layer of powder. Obviously, the contamination by Ethanol used to collect up the "wet" powder has to be taken into account, but a more thorough investigation on this topic is needed. Note that the formation of two kinds of equimolar phases, distinct only in their Oxygen content, was also observed by Rogachev *et al.* in their work mentioned in Chapter V as [10].

Interestingly enough, the mixing progress seems to shift the sintering temperature upward. However, a thorough study in which both the lattice defects and chemical mixing are quantified during the milling is required to evaluate the separate influence of the mixing progress.

Appendix V: High temperature behavior of High Entropy Alloys elaborated by mechanical activation

1. Introduction

In Chapter VI, we investigated the thermal stability of mechanically alloyed high entropy alloy powders. The focus of the following appendix is the high temperature behavior of high entropy alloys prepared by mechanical activation and SPS. In other words, both the thermal stability and the high temperature oxidation properties of sintered bulk samples are studied here. $Al_xCoCrFeNi$ high temperature behavior attracts a lot of attention since this composition is often compared to more classical alloys. Indeed, it is a common trend to compare this composition to Ni-Cr-Al alloys [1–3]. In the literature, the aim of several studies has been to determine the Al content required to form Aluminum oxides instead of Chromium oxides, following the classification of Ni-Cr-Al suggested by Giggins and Pettit in 1971 [4]. Interestingly, most of these studies are performed by means of thermal-cycling oxidation, which is different from the work undertaken here (see section 2). In addition, a specificity of the present work is to evaluate the oxidation behavior of nanostructured alloys. Although direct comparison between oxidation behavior of high entropy alloys synthesized by the liquid route and alloys synthesized by the solid route has yet to be performed, the literature shows that nanostructure may promote the formation of the stable and protective α-Al_2O_3 [5].

2. Materials and methods

Two annealing methods were used. A first evaluation of the thermal stability of the sintered samples was performed directly in the SPS chamber. The mechanically activated powder with the $J80_{4x7}$ parameters (described in Appendix 2) were first sintered at 1100°C with a heating ramp of 50°C/min under a pressure of 80 MPa. Then, in the same SPS cycle, the temperature was decreased to the annealing temperature (600°C or 900°C) and the pressure was decreased to the minimal value applicable by the SPS device (3 kN corresponding to 40 MPa). The temperature and pressure were held over 1h. Note that this annealing was performed in a low "industrial" vacuum and that the sample was continuously in contact with the graphite dies.
The second annealing method was performed in a tubular furnace in a medium vacuum whose p_{O_2} was measured at 0.2 mbar; Ti getters were disposed near the samples in order to prevent oxidation of the HEA. Two annealing temperatures, 600°C and 900°C, and two annealing durations, 1h and 50h, were studied. For both annealing methods, the first 15 µm of the surface were removed by mechanical grinding in order to eliminate the possible oxidation and carbon

diffusion occurring at the immediate surface. The crystallite size was also measured after this removal in order to estimate the size at the core of the samples.

High temperature oxidation behavior was investigated by means of continuous isothermal ageing. The ageing was performed in muffle furnaces in laboratory air. After the chosen ageing durations, 200h and 500h, the samples were retrieved from the furnace and left to cool down naturally. Two temperatures were selected, 900°C and 1100°C. Note that the furnace corresponding to the 1100°C annealing is different from the furnace corresponding the 900°C annealing. The furnace used for the 1100°C treatment is particularly known for being used for very different materials and may be a source of contamination for the HEA sample. The cross-section of the oxidized samples was prepared following a specific methodology. A thin layer of Au was first sputtered on the surface. Then, Cu was deposited by an electrolytic method. These two coatings ensure that the oxide layers are not destroyed by the later polishing step. Prior to the polishing step, the samples were embedded in electrically conductive carbon doped resin. Note that the final polishing step parameters were not optimized. A set of parameters designed for steel samples was in fact used. Both the oxide and substrate properties are very different and the polishing parameter may need to be adjusted.

The sintered samples used for the second annealing method and for the high temperature oxidation study correspond to samples milled with the $F250_{28x1}$ parameters (mix of wet and stuck-on powders) and sintered in 30 mm tools at 1100°C (see Appendix IV).

3. Results and discussion

3.1. Thermal stability

3.1.1. Calphad Prediction

Figure 1 depicts the phase volume fraction as a function of temperature for the composition evaluated by means of SEM-EDS, Oxygen and Carbon analyzers presented in Chapter V: 0.8 at. % O, 0.4 at. % C and 0.1 at. % N. This composition provides an idea of the contamination level that can be found in mechanically activated and Spark Plasma Sintered samples. The phase volume fractions of the main phases are similar to what was reported in previous chapters. At 1100°C, the sintering temperature, the Calphad approach predicts 58.8 vol. % of B2, 23.6 vol. % of disordered BCC, 14.7 % of FCC, 1.4 vol. % of Alumina and 1.5 vol. % of $C_{23}C_6$ carbides. At 600°C, the first annealing temperature, the microstructure is expected to be 69.2 vol. % of B2, 23.6 vol. % of sigma, 3.9 vol. % of disordered BCC, 1.4 vol. % of Al_2O_3 and the amount of carbides is slightly higher than at 1100°C: 1.8 vol. %. At 900°C, the annealing temperature, the microstructure is expected to be 66.9 vol. % of B2, 30.0 vol. % of sigma, 1.4 vol. % of Al_2O_3 and 1.7 vol. % of $Cr_{23}C_6$. The N concentration seems to be insufficient to form nitrides. Even for carbon concentrations lower than the C concentration found in the literature, the amount of carbides is expected to be significant at both temperatures.

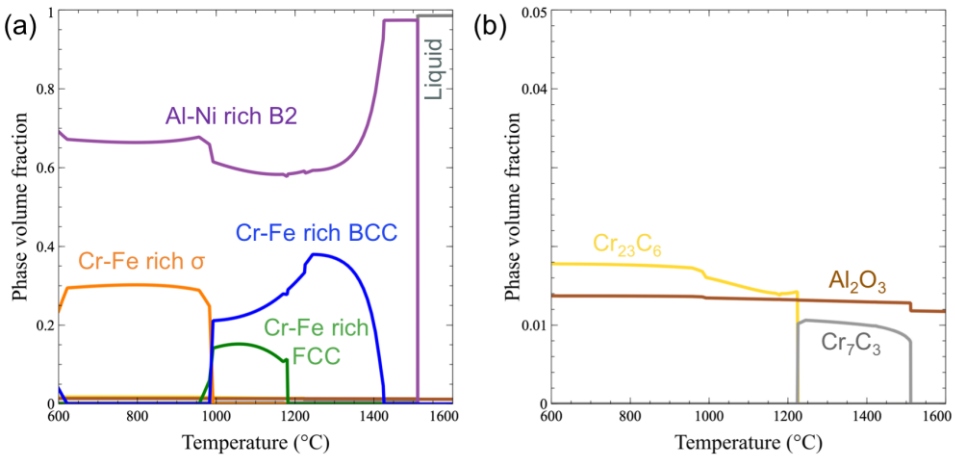

Figure 1: (a) Phase volume fraction as a function of temperature. (b) Close-up view of the figure (a) to show the oxide and carbide content. Thermo-Calc with TCNI9.

3.1.2. Thermal stability estimation by annealing in the SPS chamber

Figure 2a shows the XRD patterns of samples sintered and annealed in SPS. For the sake of comparison, XRD pattern of as-sintered sample is shown in Fig. 3a. At both 600°C and 900°C, the main phases are FCC + BCC. The FCC/BCC ratio is similar to that in as-sintered samples. The FCC phase does not seem to disappear with annealing. At 600°C, there is a significant amount of sigma phase. At 900°C, the sigma phase is replaced by Chromium carbides $Cr_{23}C_6$. Figure 2b and c show SEM-BSE pictures of the samples annealed at 900°C. The microstructure is still imbricated but some regions of sigma are visible. In addition, nanometric black dots have

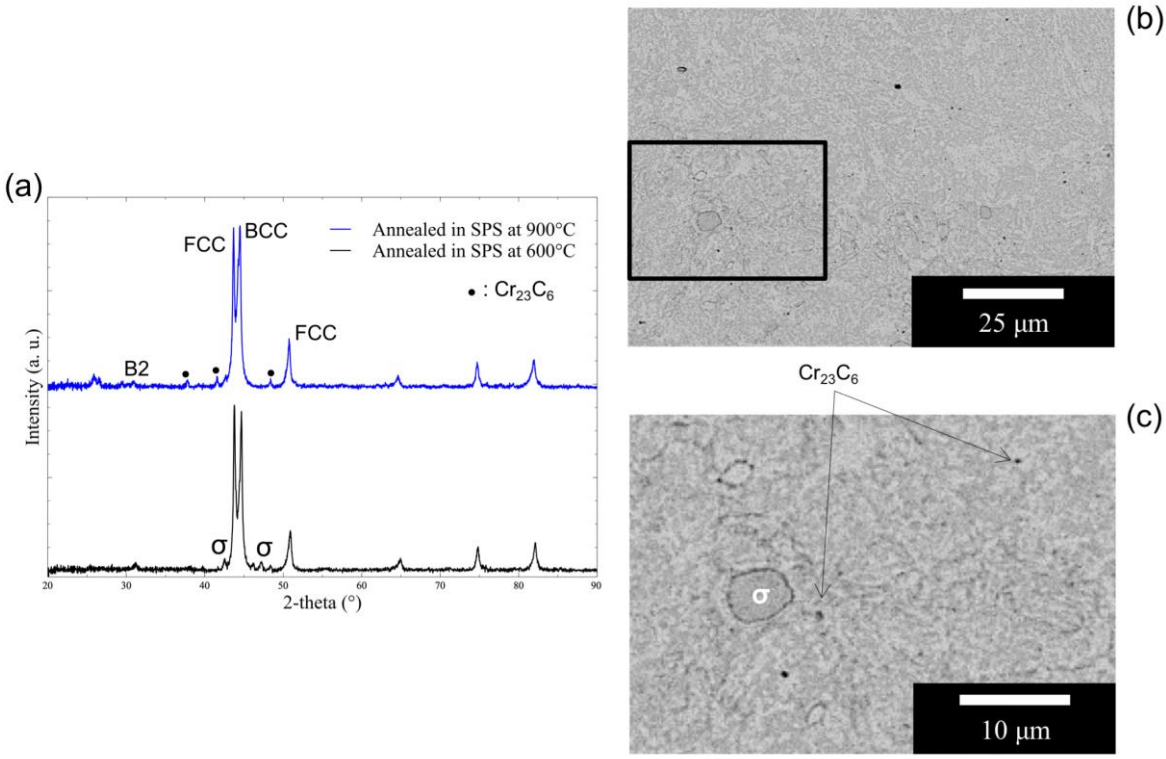

Figure 2: (a) XRD patterns of mechanically activated sintered and annealed samples for two different annealing temperatures. (b) SEM-BSE pictures of the sample annealed at 900°C.

been clearly identified as chromium carbides by means of SEM-EDS in this case. The significant formation of carbides instead of sigma in the case of the 900°C annealing may result from the carbon contamination originating in the graphite tool of the SPS. The actual C concentration after this annealing remains to be measured using, for example, the inert gas fusion method.

3.1.3. Thermal stability investigation by annealing performed in medium vacuum

3.1.3.1. 1h annealing

Figure 3 shows the XRD patterns of sintered samples after a short 1h-annealing at 600°C and 900°C. At 600°C, sigma peaks are already noticeable. At 900°C, the sigma peaks are even more noticeable. In addition, peak width does not increase. Assuming that the width results mainly from the crystallite size after annealing (since lattice defects are likely to relax during heating), the crystallite size can be estimated thanks to Scherrer's equation. In the sintered and annealed samples, the crystallite size of the FCC phase is evaluated at 20 nm. Note that the immediate surfaces of the annealed samples were removed by mechanical grinding in order to estimate the crystallite size at the core of the material. Based on the presented XRD patterns, the sigma phase formation seems to be the only modification occurring during short annealing.

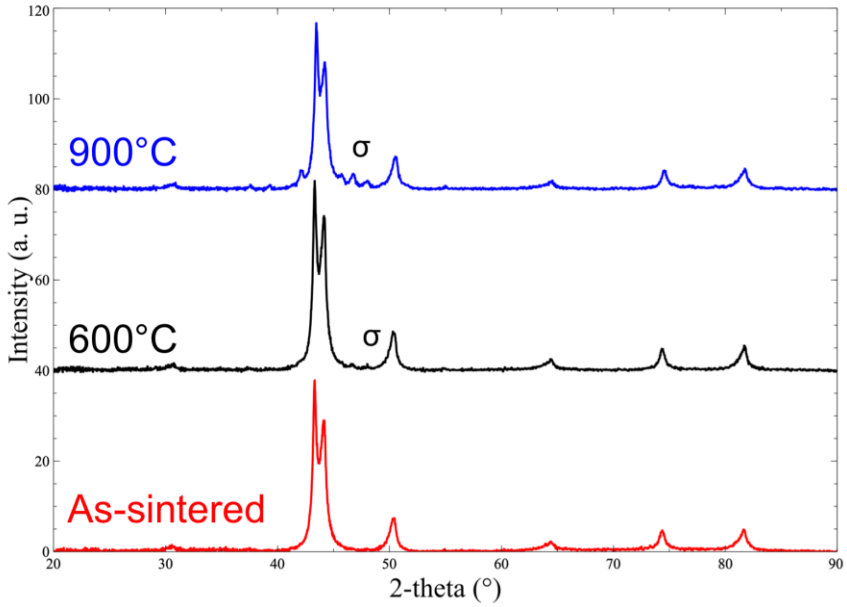

Figure 3: XRD patterns of sintered samples annealed for 1h.

Figure 4 presents the SEM-BSE pictures of the sintered and 1h-annealed samples. Qualitatively speaking, the three microstructures seem identical. The formation of sigma is still difficult to observe.

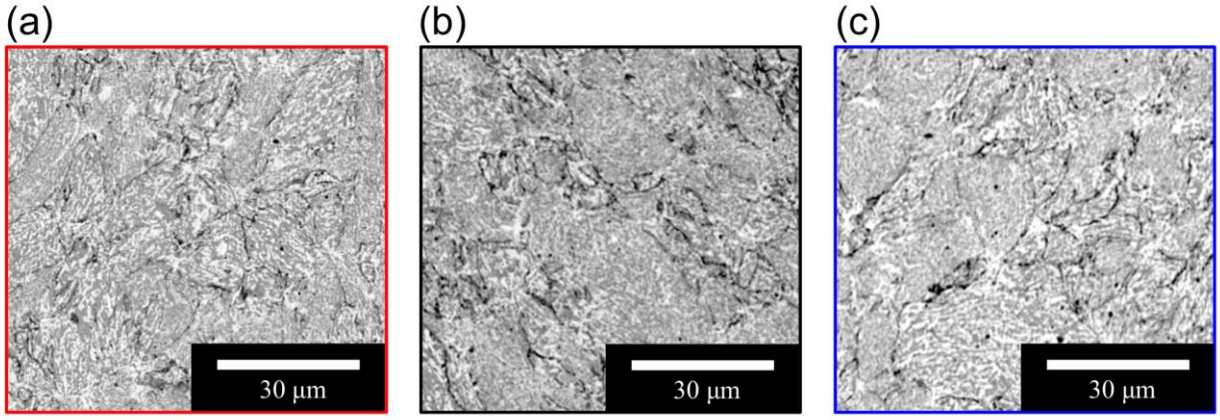

Figure 4: SEM-BSE pictures of (a) as-sintered sample, (b) sample annealed at 600°C, (c) sample annealed at 900°C.

3.1.3.2. 50h annealing

Figure 5 shows the XRD patterns of sintered samples after a longer 50h-annealing at 600°C and 900°C. Note that the XRD pattern corresponding to the 600° annealing exhibits an abnormal amount of noise. The result has therefore to be considered with caution. Indeed, the evolution of the relative intensity between the most intense FCC and BCC peaks is not consistent with the results obtained after 1h-annealing. At 600°C, sigma peaks are already noticeable. At 900°C, sigma peaks are even more noticeable. In addition, peak width does not increase. In the sintered and annealed samples, the crystallite size is evaluated at 20 nm. Based on the presented XRD patterns, the sigma phase formation seems to be the only modification occurring during longer annealing. As compared to the 1h-annealing, the ratio between the sigma peaks and the FCC peaks increases significantly.

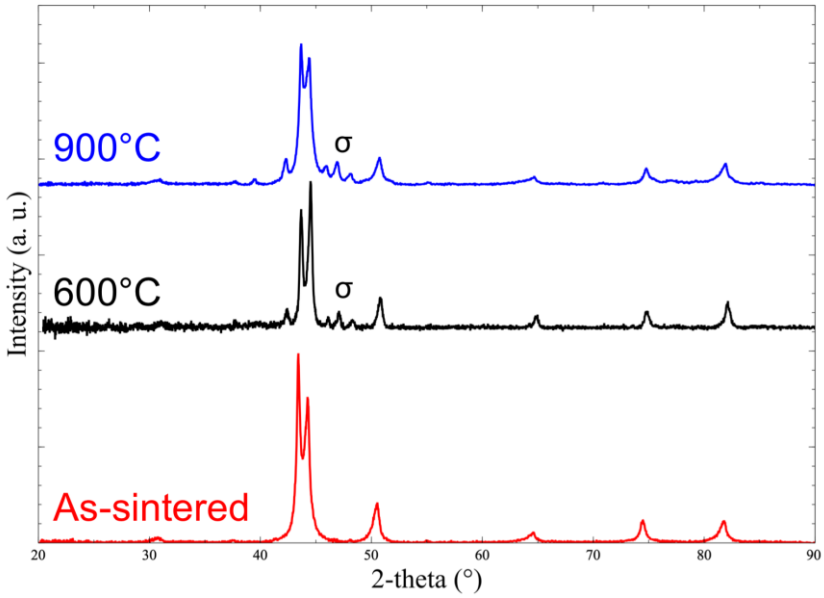

Figure 5: XRD patterns of sintered samples annealed for 50h.

Figure 6 presents the SEM-BSE pictures of the sintered and 50h-annealed samples. Qualitatively speaking, the three microstructures seem identical. The formation of sigma is still difficult to observe. Figure 5d and Figure 5e correspond to SEM pictures with better resolution and higher magnification than the others. In particular, Figure 5e allows us to observe the fine distribution of nanometric precipitates. EDS measurements confirm that the larger ones are oxides. Note that a rough estimation of the surface ratio of each contrast indicates that the lighter contrast corresponding to the FCC phase increases after 50h at 900°C. From 70/30, the (BCC+sigma)/FCC ratio changes to 65/35. However, given the tortuosity of the microstructure, such a "small" difference is difficult to accurately demonstrate by means of image processing.

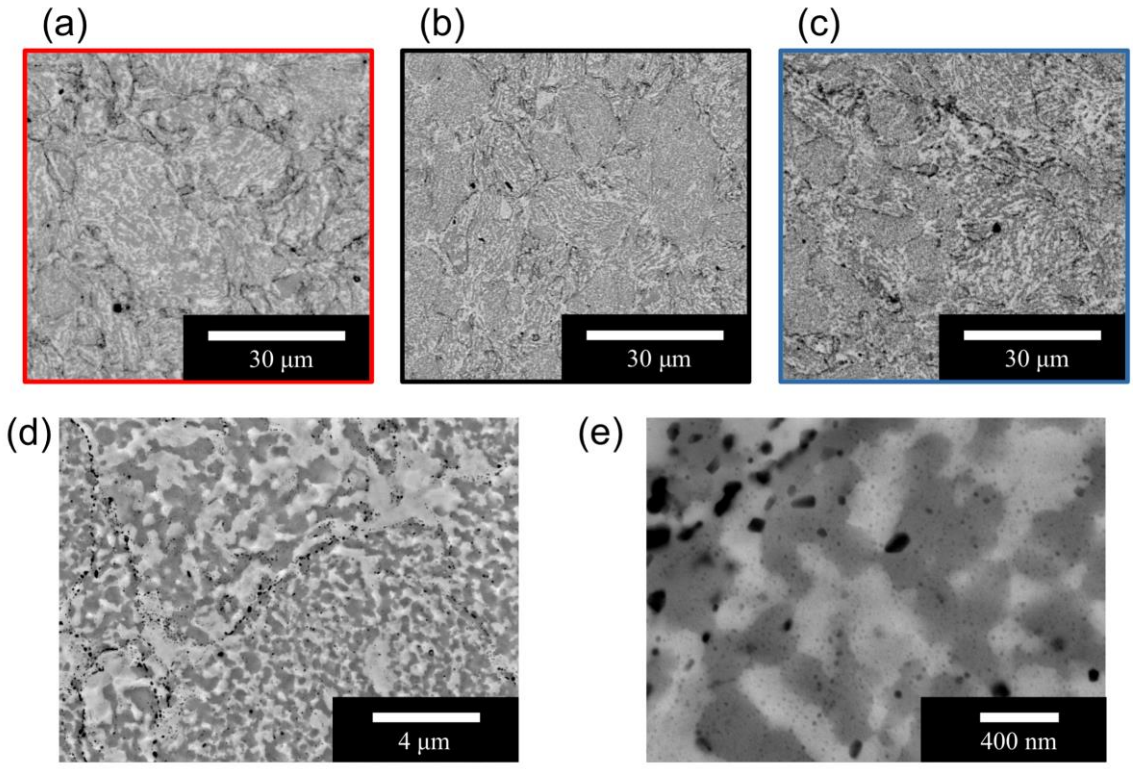

Figure 6: SEM-BSE pictures of (a) as-sintered sample, (b) sample annealed at 600°C, (c, d, e) sample annealed at 900°C.

3.2. High temperature oxidation

The following paragraphs summarize the results concerning the high temperature oxidation behavior of the three different sintered alloys presented in Appendix IV.

- "Al_7" corresponds to 7 at. % Al, 23.25% Co, 23.25% Cr, 23.25% Fe, 23.25% Ni.
- "Al_{20}" corresponds to 20 at. % Al, 20% Co, 20% Cr, 20% Fe, 20% Ni.
- "Al_{30}" corresponds to 30 at. % Al, 17.5% Co, 17.5% Cr, 17.5% Fe, 17.5% Ni.

The methods carried out to investigate this behavior are detailed in section 2 of the present Appendix.

Figure 7a summarizes the XRD patterns of the as-sintered alloys. The Al_7 alloy exhibits one single FCC phase whereas Al_{30} exhibits only BCC phases. The Al_{20} alloy exhibits a combination of FCC and BCC (with some amount of B2). Figure 7b is a schematic oxide map corresponding to the Ni-Cr-Al classification developed by Giggins and Pettit [4]. Simply put, group II preferentially forms chromium oxides whereas group III forms aluminum oxides. Note that the borders of the present map correspond to the borders for Ni-Cr-Al at 1100°C. One intent of the present study was to estimate the position of the actual border between groups II and III for $Al_xCoCrFeNi$ HEA at 900°C (represented here by the dotted line for visualization of the problematic). Note that the three dots correspond to the three compositions studied.

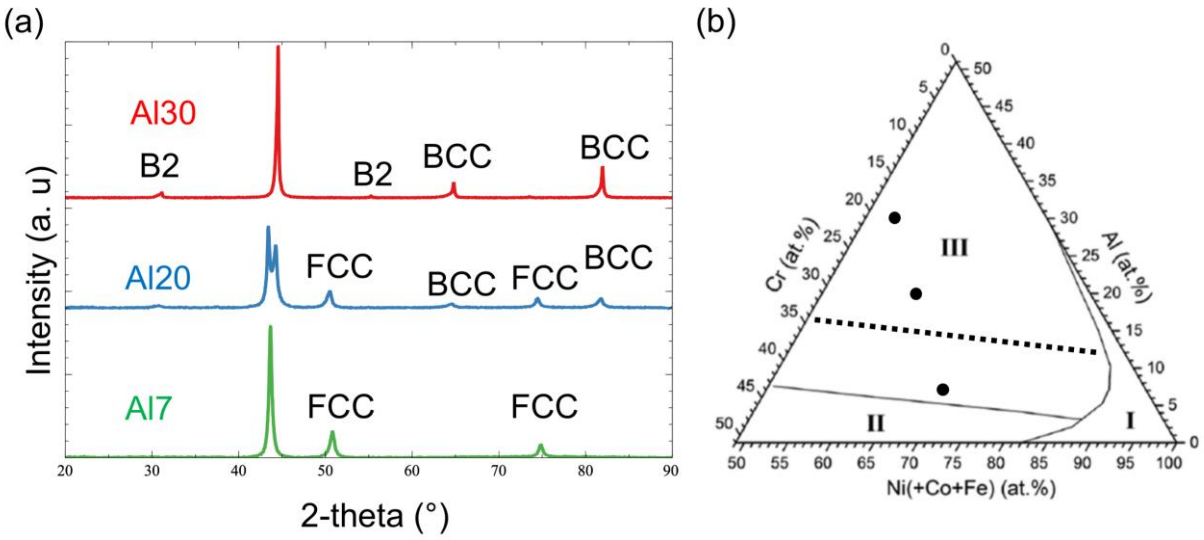

Figure 7: (a) XRD patterns of the as-sintered alloys for the three compositions. (b) Schematic oxide map for Ni-Cr-Al at 1100°C (adapted from [1]). The three dots correspond to the three compositions studied.

3.2.1. Ageing at 900°C

Figure 8 displays the normalized mass gain of the samples after 200h and 500h. In general, for high temperature materials, the formation of a protective oxide layer is pursued. In this case, a parabolic evolution of the mass gain is expected and a parabolic constant k_p is calculated. In the present study, two data points are not sufficient to accurately calculate the k_p. However, a first rough estimation gives $k_p \backsimeq 10^{-13}$ $g^2.cm^{-4}.s^{-1}$ in the case of Al_{20}. Unfortunately, since most studies concerning the oxidation of NiCrAl alloys are carried out at 1000°C and higher, direct comparisons of k_p values are not relevant. The aspect of the curves is encouraging at first glance; the following characterizations will allow us to more accurately evaluate the oxidation behavior of sintered HEAs. Finally, the mass gain increases with the Al content after 200h and after 500h. The Al_7 mass gain between 200h and 500h is 0.02 mg/cm^2, which is barely significant.

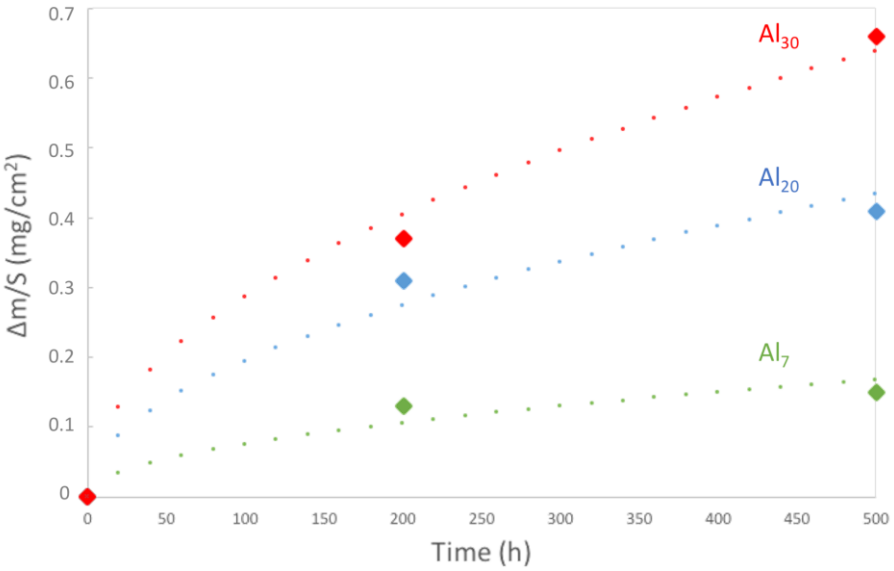

Figure 8: Normalized mass gain as a function of time for the three alloys aged at 900°C in laboratory air.

Figure 9 summarizes the results obtained by means of SEM concerning the Al_{20} aged 500h at 900°C in laboratory air. The surface exhibits mainly needle-shaped oxides (Fig. 9a), which is the typical structure of θ-Al_2O_3. EDS measurements summarized in Fig. 9c confirm the nature of the oxide layer. Some minority regions do not exhibit needles. EDS measurements reveal that the corresponding layer is also an Al oxide. Note that some spallation is noticeable on the surface (Fig. 9b). Cross-section analyses reveal the formation of a 4-µm Al-lean band. Interestingly enough, Figure 9e shows that the Al profile concentrations do not display the gradient evolution typical of an ongoing diffusion-governed mechanism. The system may have reached a first equilibrium after 500h at 900°C. EDS mappings confirm that the only oxides formed during ageing are Alumina. There are no traces of chromium oxides. The two main phases: Fe,Cr-rich FCC and Ni,Al-rich BCC are still present in the substrate far from the surface.

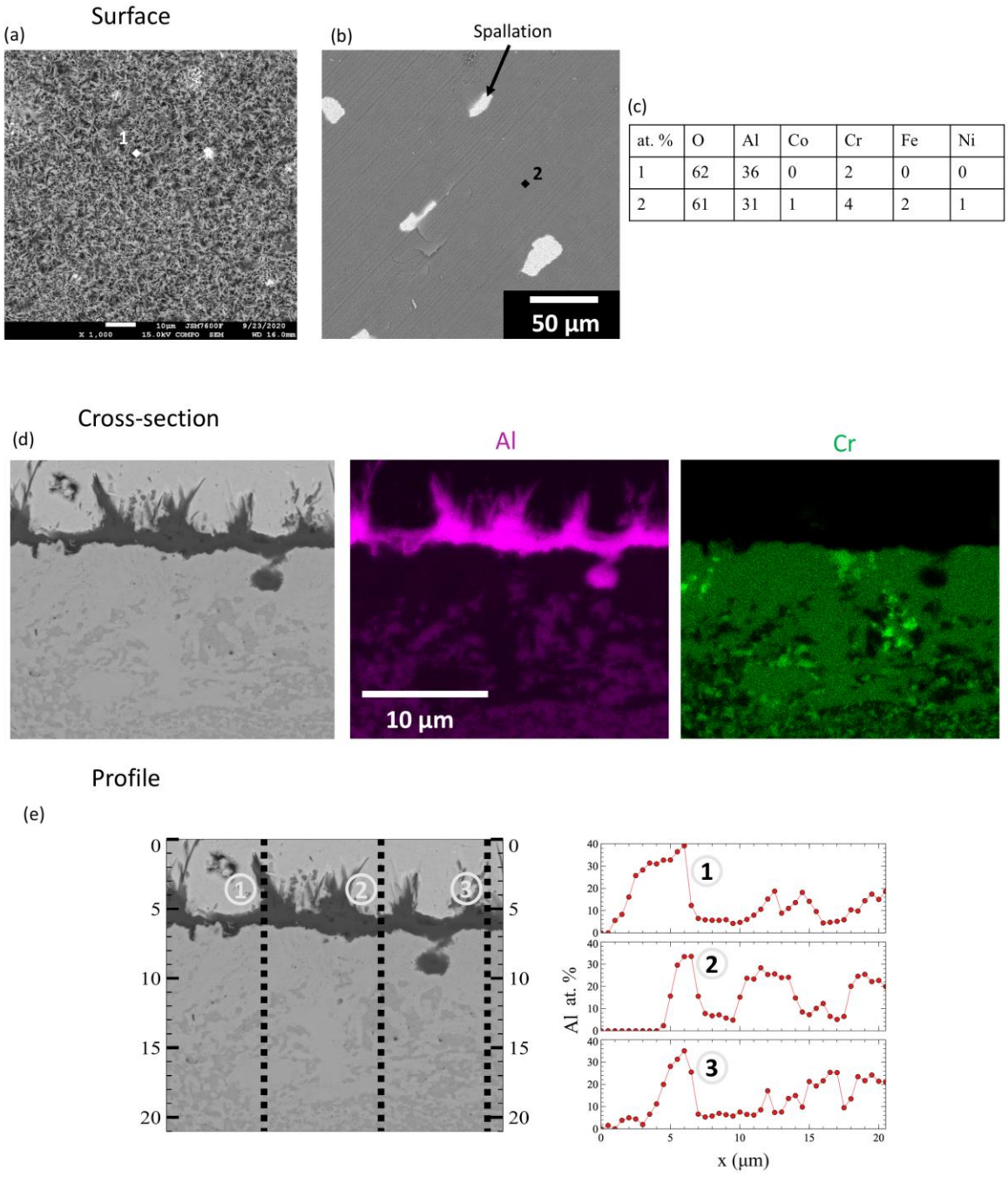

at. %	O	Al	Co	Cr	Fe	Ni
1	62	36	0	2	0	0
2	61	31	1	4	2	1

Figure 9: SEM (BSE) results concerning the Al_{20} alloy after 500h at 900°C. (a) representative picture of the surface, (b) picture illustrating spallation, (c) table of EDS measurements corresponding to the points represented in (a) and (b). (d) cross section and Al, Cr EDS mapping. (e) Al profile concentration along 3 lines of the alloy after high temperature oxidation.

Figure 10 summarizes the results obtained by means of SEM concerning the Al_7 aged 500h at 900°C in laboratory air. The surface exhibits mainly a dense oxide layer, which is the typical morphology of α-Al_2O_3. Note that some spallation is noticeable on the surface (Fig. 10b), although this spallation is of lesser magnitude than in the preceding Al_{20} case. Cross-section analyses reveal that the oxide layer is a dense layer whose thickness is inferior to 1 µm. Given the density of α-Al_2O_3 of 3.97 g/cm^2, the mass gain measured on the Al_7 sample aged 500h at 900°C indeed corresponds to a layer thinner than 1 µm (see Figure 8). Note that Fig. 10d was obtained with a different SEM device; EDS mappings are not available for this sample. EDS measurements confirm that the only oxides formed during ageing are Alumina. There are no traces of chromium oxides. Far from the surface, the main FCC phase seems unaltered. Some dark spots, already noticeable before ageing, are identified as chromium carbides.

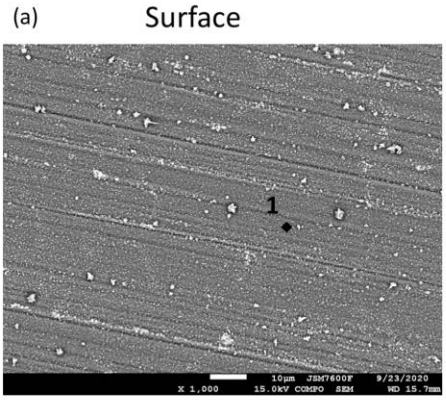

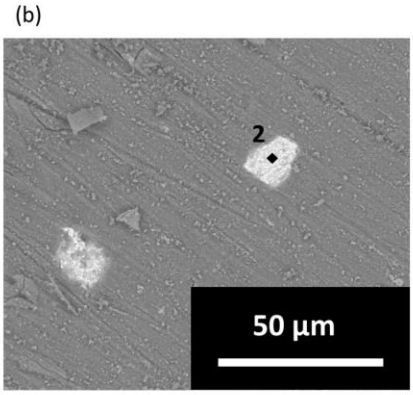

(c)

at. %	O	Al	Co	Cr	Fe	Ni
1	68	31	0	0	0	1
2	11	9	19	19	20	20
3	57	39	1	2	1	0

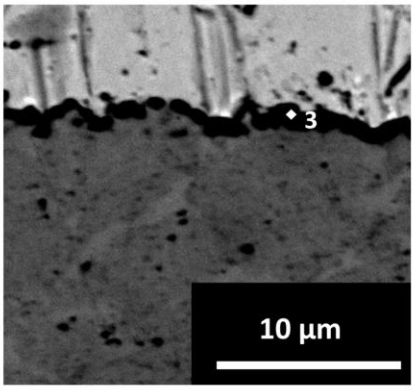

Figure 10: SEM (BSE) results concerning the Al_7 alloy after 500h at 900°C. (a) surface, (b) surface picture illustrating spallation. (c) table of EDS measurements corresponding to the points represented in (a), (b) and (d). (d) cross section.

Figure 11 summarizes the results obtained by means of SEM concerning the Al_{30} aged 500h at 900°C in laboratory air. The surface exhibits mainly needle-shaped oxides, which is the typical morphology of θ-Al_2O_3. As compared to Al_{20}, the number of needles is much higher. It is not possible to accurately measure the layer under the needles. However, some EDS measurements reveal the presence of Nitrogen. In addition, severe spallation is noticeable on the surface, especially near the edges of the sample (Fig. 11b). Cross-section analyses and EDS mappings reveal a very complex system after 500h at 900°C. Figure 11f corresponds to a schematic representation of the system drawn up from the EDS mappings, EDS measurements and XRD patterns. The top layer corresponds to a combination of θ-Al_2O_3 and α-Al_2O_3. The main feature of the second layer is its high Cr content. Given the small size of each region, it is difficult to precisely determine the amount oxygen in each particular layer. This second layer could correspond to Chromium oxide or Cr-rich FCC. Note that the actual crystalline structure of this layer is a pure speculation; this being said, in the Al_{20} system, the Cr-rich phases often correspond to FCC phases. Interestingly enough, the second layer position seems to correspond to the initial metal surface. Further investigations, such as gold deposition before ageing, could confirm this suggestion. The third layer seems to correspond to a combination of AlN and

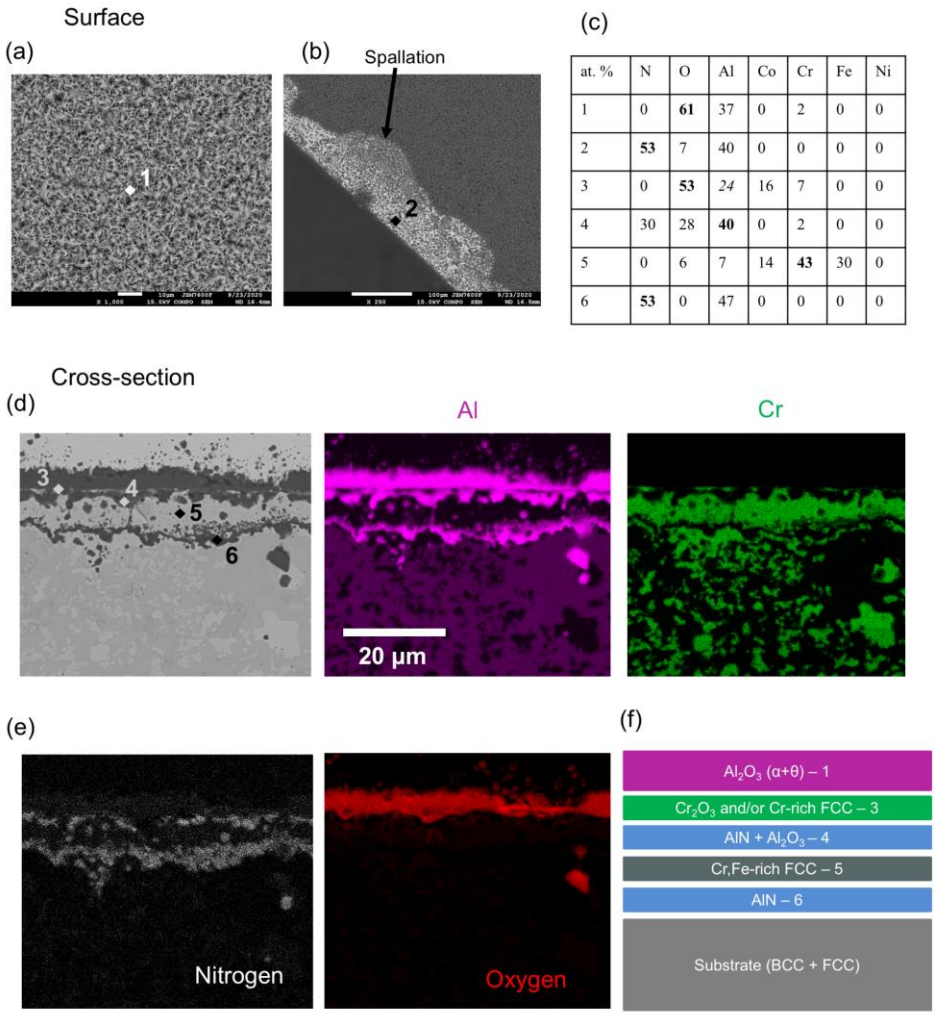

at. %	N	O	Al	Co	Cr	Fe	Ni
1	0	**61**	37	0	2	0	0
2	**53**	7	40	0	0	0	0
3	0	**53**	*24*	16	7	0	0
4	30	28	**40**	0	2	0	0
5	0	6	7	14	**43**	30	0
6	**53**	0	47	0	0	0	0

Figure 11: SEM (BSE) results concerning the Al_{30} alloy after 500h at 900°C. (a) Surface, (b) picture illustrating spallation, (c) table of EDS measurements. (d) cross sections and Al, Cr EDS mappings. (e) N and O EDS mappings. (f) Schematic representation of the system after 500h at 900°C.

Al_2O_3. The fourth layer is similar to the second, but its Fe content is higher while its O content is lower. The last layer before the substrate seems to correspond to an $Al_{50}N_{50}$ aluminum nitride. Far from the surface, the microstructure of the substrate appears to be simpler than before ageing. Only two contrasts are noticeable. Once again, the lighter contrast corresponds to a Fe,Cr-rich phase whose crystalline structure is likely to be FCC.

Figure 12a exhibits the XRD patterns after 200h at 900°C for the three alloys. The main phases resulting from the oxidation are two kinds of alumina, α-Al_2O_3 and θ-Al_2O_3, and Aluminum nitride AlN. According to the literature, θ-Al_2O_3 is a rhombohedral transition alumina which forms between 900°C and 1000°C whereas α-Al_2O_3 is a stable oxide phase which forms above 1000°C. The α-Al_2O_3 alumina usually forms a dense, compact layer which further protects the

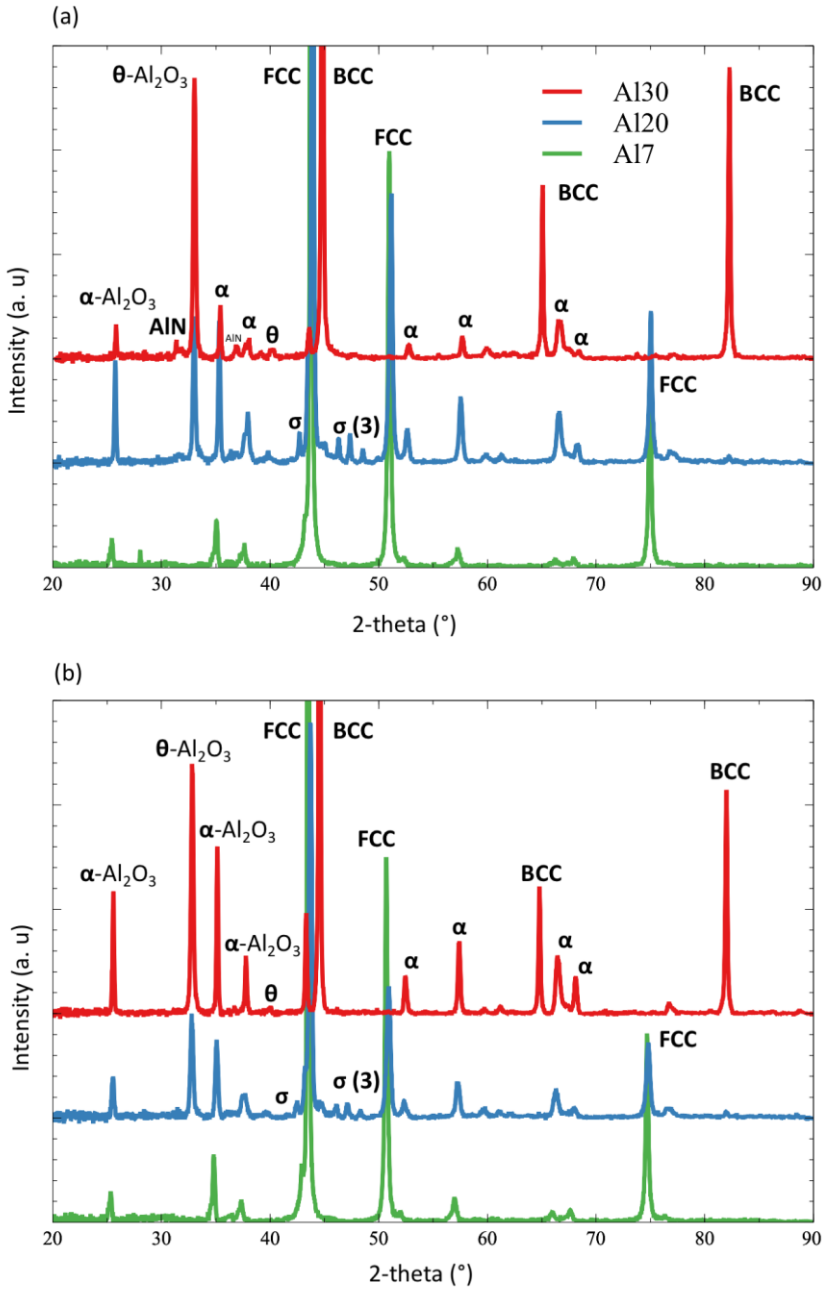

Figure 12: XRD patterns of the three alloys after (a) 200h and (b) 500h at 900°C.

alloys from aggressive atmosphere. Al_7 seems to exhibit only α-Al_2O_3 whereas Al_{20} and Al_{30} exhibit a combination of α-Al_2O_3 and θ-Al_2O_3. In addition, the Al_{30} composition seems to favor the θ-Al_2O_3 and AlN formation instead of α-Al_2O_3. Indeed, the α/θ peak ratios are vastly in favor of the θ-Al_2O_3 in the case of Al_{30} as compared to the Al_{20} case. Hence, the XRD results are in perfect agreement with the SEM observations. The combined XRD and SEM results lead us to conclude that no Cr_2O_3 is formed in the HEA samples after 200h or 500h at 900°C. Note that the sigma phase appears in the Al_{20} alloy only. Figure 12b shows the XRD patterns after 500h at 900°C for the three alloys. The observations are similar to those formulated in reference to Figure 8a. However, after 500h, no traces of AlN remain for Al_{30}: the oxide layer might be thick enough and the AlN deep enough to elude observation by XRD. In the case of Al30, longer exposure time seems to favor the formation of α-Al_2O_3 since the α/θ peak ratio increases. Interestingly enough, the (200) BCC peak at 65.2 2-theta is no longer noticeable on the Al_{20} patterns. However, the (111) FCC peak at 43.3 2-theta is noticeable on the Al_{30} patterns despite being absent from the as-sintered sample.

3.2.2. Ageing at 1100°C

The XRD pattern of the Al_{20} sample after 200h at 1100°C is displayed in Figure 13. As compared to ageing at 900°C, the θ-Al_2O_3 and the sigma peaks are no longer noticeable. Instead, Aluminum nitride and chromium carbide $Cr_{23}C_6$ peaks have appeared. However, the main oxidation product at 1100°C is clearly α-Al_2O_3. The formation of carbides does not likely result from the reaction of the sample with air but rather from the dissolution of Cr-rich sigma. This observation can put into perspective our previous discussion concerning the formation of carbides in as-sintered samples in Chapter V. Carbide formation seems mainly hindered by the formation of sigma phase. We can also note that the (200) BCC peak at 65.2 2-theta is not noticeable in this pattern. Unfortunately, information concerning the influence of temperature on the crystallite size of the substrate cannot be deduced from this pattern. Indeed, near the

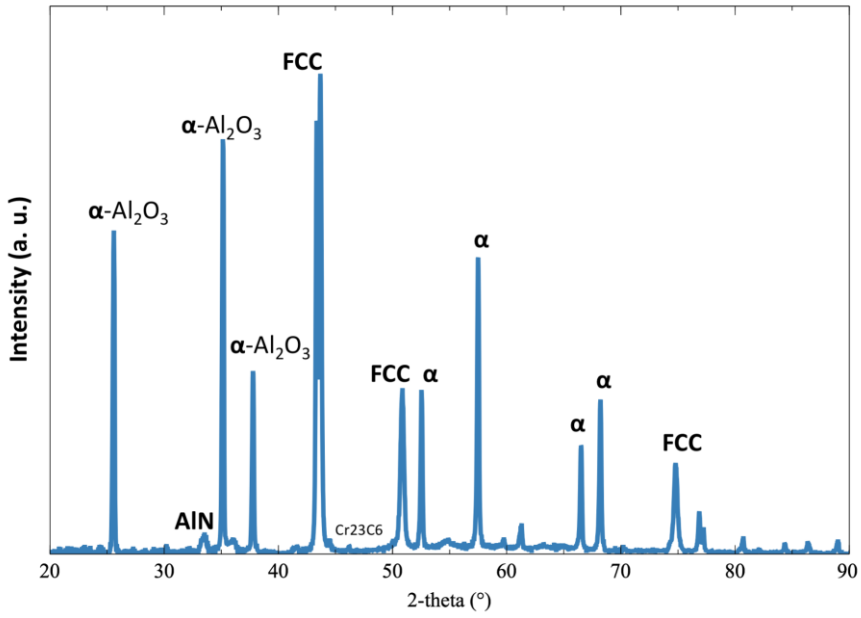

Figure 13: XRD patterns of the Al_{20} sample after 200h at 1100°C.

surface, the crystallite size is significantly increased because of a growth mechanism enhanced by strain hardening. Here, the strain hardening results from the polishing step performed during sample preparation, prior to high temperature ageing.

Figure 14 summarizes the results obtained by means of SEM concerning the Al_{20} aged 200h at 1100°C in laboratory air. The surface presented in Figure 14a is very different from the surface obtained after 500h at 900°C in the Al_{20} (α and θ) or Al_7 (only α) samples. Here, the peculiar shape of the oxide layer may result from the transformation of θ-Al_2O_3 into α-Al_2O_3. Indeed, Grabke *et al.* stated that θ-Al_2O_3 begins to form first, as soon as the target temperature is reached [6]. The growth of α-Al_2O_3 starts afterward and is slower. The peculiar, wavy shape could also result from the difference between the volume of the newly formed Al_2O_3 and the initial metallic substrate [7]. Cross section analyses confirm the formation of α-Al_2O_3 as the main oxidation product. In this case, AlN is not noticeable. The medium grey regions near the oxide layer correspond to a Cr,Al,Co,O-rich phase but is too thin to be accurately described (see label 3 in Fig. 14d). In addition, the Al-lean band is also present in this sample but, contrary to the ageing at 900°C, some Al,Ni-rich precipitates remain in the matrix. Moreover, one can note

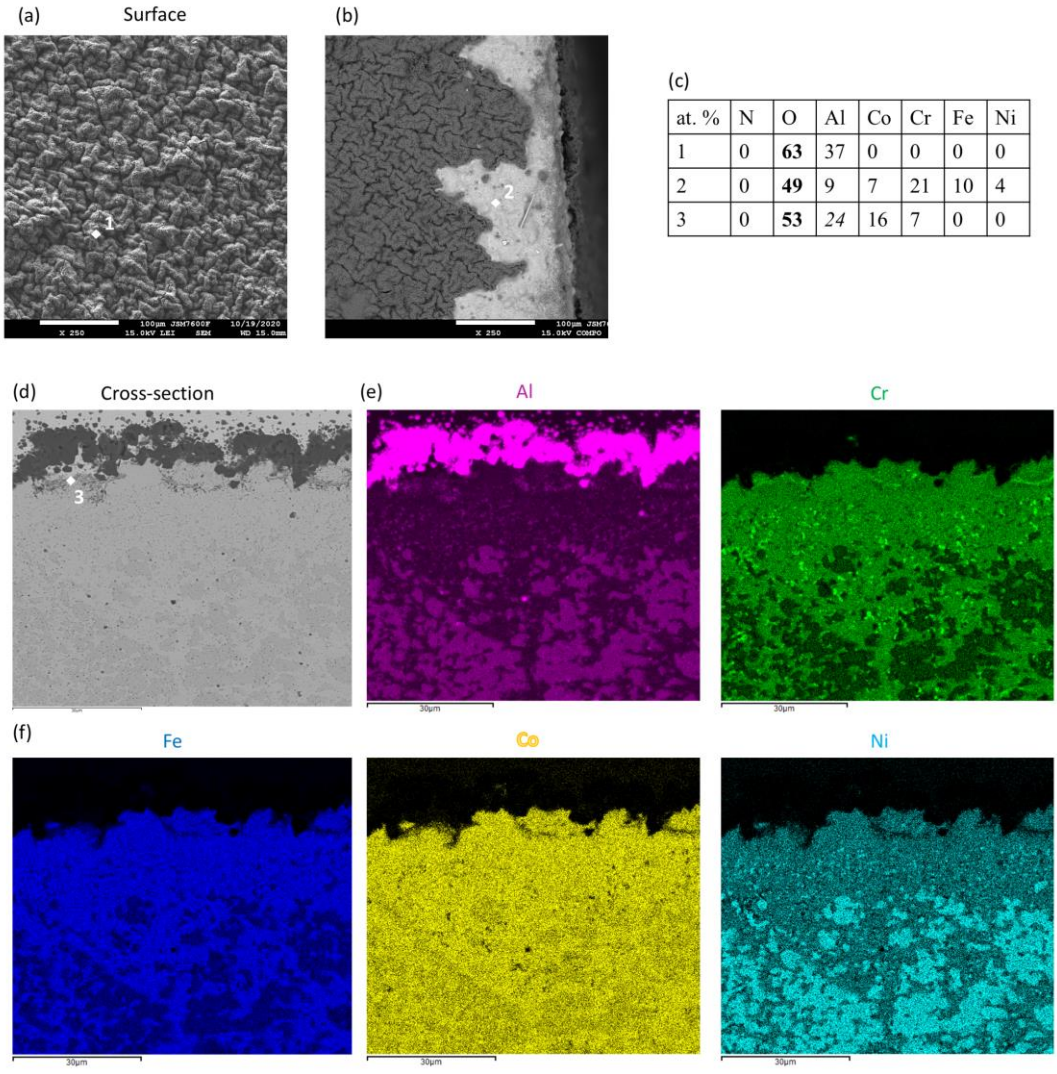

(c)

at. %	N	O	Al	Co	Cr	Fe	Ni
1	0	**63**	37	0	0	0	0
2	0	**49**	9	7	21	10	4
3	0	**53**	*24*	16	7	0	0

Figure 14: SEM (BSE) results concerning the Al_{20} alloy after 200h at 1100°C. (a) surface, (b) picture illustrating spallation, (c) table of EDS measurements. (d) cross sections, (e) Al and Cr EDS mappings, (f) Fe, Co and Ni EDS mappings.

some Ni depletion on the Al-lean band from the Ni EDS mapping. In fact, it seems that an upward flux of Cr and Fe is compensated by a downward flux of Ni. This trend is particularly visible in the case of Al_{20} at 1100°C but seems present in the cases of Al_{20} and Al_{30} at 900°C as well. Finally, a significant number of black dots are noticeable on the cross section, corresponding to either Al-rich regions (likely Al_2O_3) or Cr-rich regions (likely $Cr_{23}C_6$).

4. Conclusion

Concerning the thermal stability of mechanically activated and Spark Plasma Sintered high entropy alloys, the samples studied were found to exhibit remarkable stability, especially in terms of the size of crystallites and the aspect of the microstructure. This stability may result from the significant amount of oxides originating in the commercial powder. Indeed, if nano-oxides are located at the grain boundaries, it is reasonable to expect that crystallites and grain growth would be hindered. The experimental sigma phase formation at the annealing temperature is reliably predicted by the Calphad approach with ThermoCalc database. Equimolar AlCoCrFeNi leads irremediably to the formation of sigma as soon as the temperature reaches its stability domain.

Concerning the high temperature oxidation resistance of the mechanically activated High Entropy Alloys studied, the Al content was found to influence the amount and, indirectly, the nature of oxidation products (alumina types). However, the crystalline structure does not seem to have a significant effect. In all three compositions, the amount of chromium oxide was always found to be almost negligible. Our results do not therefore allow us to determine the border between group II and III of the Giggins and Pettit classification as applied to HEAs at 900°C. Nevertheless, the comparison of HEA behavior with the Ni-Cr-Al classification is not necessarily relevant. Indeed, the work of Giggins and Pettit was performed for short ageing durations (1h to 30h) at higher temperatures (between 1000°C and 1200°C). If a comparison between conventional alloys and HEAs has to be made, our preliminary results obtained at 900°C only demonstrate that the oxide layers of $Al_xCoCrFeNi$ are mainly two types of alumina and that the formation of aluminum nitride seems to be a particularity of these alloys.

In all three compositions, the alloy undergoes spallation during oxidation or during the cooling outside the furnace. Three reasons could explain this spallation:

- a difference between the volume of the newly formed Al_2O_3 and the initial metallic substrate. Indeed, the Pilling Bedworth ratio reaches $R_{PB}(Al_2O_3/Al) = 1.28$. This difference induces high residual stress in the oxide layer. When the oxide layer reaches a critical thickness, stress relaxation by spallation occurs [7].
- the formation of pores at the metal/oxide interface, which decreases the adherence of the oxide layer. The formation of the transition alumina occurs by means of rapid cationic diffusion; hence it severely depletes Al from the substrate. At the same time, other metallic cations fill the Al vacancies. This double flux leads to the formation of pores and spallation follows [6].

- a difference between the coefficients of thermal expansion in the substrate and in the aluminum oxide, which is maximal for the Al_7 composition. Indeed, the CTE value for alumina is estimated at 7.10^{-6} K^{-1} whereas the CTE value for Al_7 FCC substrate is approximately 16.10^{-6} K^{-1} and drops to 13.10^{-6} K^{-1} for the Al_{30} BCC phase [8]. However, we noted the formation of an Al-lean band occurring during oxidation near the surface. The actual composition of the substrate is generally close to the Al_7 composition. During the cooling of the samples, a major difference in CTE values often leads to spallation.

Obviously, the spallation observed could result from a combination of the aforementioned mechanisms. The comparison of oxide layer thicknesses is usually a relevant indicator to evaluate the reasons behind the spallation. However, in the present study, two cases exhibit specific and complex mechanisms involving Nitrogen (Al_{30} and Al_{20} at 1100°C). Hence, thickness comparison is not sufficient to identify one major reason.

Finally, the Al_7 composition is the only one which exhibits the desired protective α-Al_2O_3. This behavior could be explained by a faster formation of Al_2O_3 since the transformation of θ- to α-Al_2O_3 is known to be accelerated by an increased content of Fe and Cr. Indeed, the transient formation of Fe and Cr oxides favors the nucleation of α-Al_2O_3 [9]. The Al_7 composition exhibits the highest level in Cr and Fe among the three alloys (23.25 at. % versus 20 and 17.5%). This suggestion could be confirmed by investigating the early stages of the oxidation.
This composition had already shown interesting mechanical properties, as reported in the literature, and its high temperature oxidation properties were found to be promising in the present study. These results remain to be confirmed by a more thorough investigation. In further studies, the composition could also be fine-tuned to prevent spallation.

References

[1] T.M. Butler, M.L. Weaver, Oxidation behavior of arc melted AlCoCrFeNi multi-component high-entropy alloys, J. Alloys Compd. 674 (2016) 229–244. https://doi.org/10.1016/j.jallcom.2016.02.257.

[2] J. Dąbrowa, G. Cieślak, M. Stygar, K. Mroczka, K. Berent, T. Kulik, M. Danielewski, Influence of Cu content on high temperature oxidation behavior of AlCoCrCuxFeNi high entropy alloys (x = 0; 0.5; 1), Intermetallics. 84 (2017) 52–61. https://doi.org/10.1016/j.intermet.2016.12.015.

[3] J. Dąbrowa, G. Cieślak, M. Stygar, M. Zajusz, M. Jawańska, A. Gil, J. Jedliński, K. Mroczka, K. Matsuda, T. Kulik, M. Danielewski, Oxidation Behavior of Alx(CoCrFeNi)100-x High-Entropy Alloys Under Thermal-Cycling Conditions, Oxid. Met. (2021). https://doi.org/10.1007/s11085-021-10048-5.

[4] C.S. Giggins, F.S. Pettit, Oxidation of Ni - Cr - Al Alloys Between 1000° and 1200°C, J. Electrochem. Soc. 118 (1971) 1782. https://doi.org/10.1149/1.2407837.

[5] J. Lu, L. Li, H. Zhang, Y. Chen, L. Luo, X. Zhao, F. Guo, P. Xiao, Oxidation behavior of gas-atomized AlCoCrFeNi high-entropy alloy powder at 900－1100 °C, Corros. Sci. 181 (2021) 109257. https://doi.org/10.1016/j.corsci.2021.109257.

[6] H.J. Grabke, Oxidation of NiAl and FeAl, Intermetallics. 7 (1999) 1153–1158.

https://doi.org/10.1016/S0966-9795(99)00037-0.

[7] A.M. Huntz, P.Y. Hou, R. Molins, Study by deflection of the oxygen pressure influence on the phase transformation in alumina thin films formed by oxidation of Fe3Al, Mater. Sci. Eng. A. 467 (2007) 59–70. https://doi.org/10.1016/j.msea.2007.02.089.

[8] H.-P. Chou, Y.-S. Chang, S.-K. Chen, J.-W. Yeh, Microstructure, thermophysical and electrical properties in AlxCoCrFeNi (0≤x≤2) high-entropy alloys, Mater. Sci. Eng. B. 163 (2009) 184–189. https://doi.org/10.1016/j.mseb.2009.05.024.

[9] D.B. Lee, G.Y. Kim, J.G. Kim, The oxidation of Fe3Al–(0, 2, 4, 6%)Cr alloys at 1000°C, Mater. Sci. Eng. A. 339 (2003) 109–114. https://doi.org/10.1016/S0921-5093(02)00112-0.

ECOLE DOCTORALE
CARNOT - PASTEUR

Titre : Étude expérimentale et modélisation multi-échelle du comportement de poudres métalliques mécaniquement activées : des systèmes binaires aux alliages à haute entropie.

Mots clés : Alliage à haute entropie ; Métallurgie des poudres ; Broyage à haute énergie ; Activation mécanique ; Frittage SPS ; Dynamique moléculaire

Résumé : Les alliages métalliques sont généralement constitués d'un élément principal associé à d'autres éléments présents en plus faible quantité (e.g. alliages à base de fer ou de nickel). En 2004, le concept d'alliages à haute entropie (AHE) est proposé. Il s'agit d'alliages sans élément majeur. L'un des principaux défis de ce domaine en plein essor concerne la compréhension de la relation méthode d'élaboration / microstructure / propriétés.
La plupart des AHE sont élaborés par fusion à l'arc, en passant par une phase liquide pour obtenir le mélange. Dans ce travail, nous proposons d'étudier une méthode innovante basée sur la métallurgie des poudres (voie solide), en combinant activation mécanique et frittage SPS (Spark Plasma Sintering). L'activation mécanique augmente la réactivité subséquente des poudres et permet d'avoir un matériau homogène après frittage.
Nous avons étudié des AHE composés de Al, Co, Cr, Fe et Ni afin d'évaluer l'influence du procédé d'élaboration sur le matériau final. Les produits ont été caractérisés expérimentalement par Diffraction des rayons X, Microscopie Électronique à balayage, Sonde Atomique Tomographique… En parallèle, des études fondamentales ont été réalisées par une modélisation multi-échelle / multi-physique, incluant la thermodynamique calculatoire (méthode Calphad) et des simulations par dynamique moléculaire. Le but était de déterminer les propriétés microstructurales en fonction des paramètres du procedé.

Title: Experimental investigation and multi-scale modelling of the behavior of mechanically activated metallic powders: from binary systems to High Entropy Alloys.

Keywords: High entropy alloy; Powder metallurgy; High energy milling; Mechanical activation; SPS sintering; Molecular Dynamics

Abstract: Generally, metal alloys consist of a main element associated with other elements present in smaller quantities (e.g iron or nickel alloys). In 2004, the concept of High Entropy Alloys (HEAs) was suggested. HEAs are alloys without major element. One of the main challenges of this dynamic field of research is understanding the relationship between development method / microstructure / properties. Most HEAs are produced by arc melting, via a liquid phase to obtain the mixture. In the present work, we propose to study an innovative method based on powder metallurgy. The elaboration of HEAs has been carried out by a solid-state process, combining mechanical activation and SPS (Spark Plasma Sintering). Mechanical activation enhances the subsequent reactivity and leads to a homogeneous material after sintering. We studied HEAs composed of Al, Co, Cr, Fe and Ni in order to evaluate the influence of the elaboration process on the final material. The products were experimentally characterized by X-ray Diffraction, Scanning Electron Microscopy, Atomic Tomographic Probe...
In parallel, fundamental studies on the influence of the process on the AHEs were carried out by multi-scale/multi-physics modelling, including computational thermodynamics (Calphad method) and molecular dynamics simulations. The aim was to determine the microstructural properties as a function of the process parameters.

UBFC UNIVERSITE BOURGOGNE FRANCHE-COMTE
Université Bourgogne Franche-Comté
32, avenue de l'Observatoire
25000 Besançon